

Scientists help families search
for Mexico's disappeared *p. 1369*

Clustering of extreme
tornado outbreaks *p. 1419*

Roads fragment the
world *p. 1423*

Science

\$15
16 DECEMBER 2016
sciencemag.org

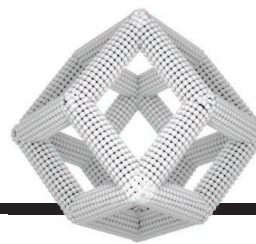
AAAS

A GEOLOGIST'S BEST FRIEND

Mantle chemistry and
massive diamond
formation tie the knot
p. 1403



CONTENTS



1378, 1410, & 1414

Perfecting platinum

16 DECEMBER 2016 • VOLUME 354 • ISSUE 6318



1366

NEWS

IN BRIEF

1356 News at a glance

IN DEPTH

1359 ANTISENSE RESCUES BABIES FROM KILLER DISEASE

Spinal muscular atrophy drug may herald treatments for other genetic brain illnesses *By M. Wadman*

1361 IN CANADA, CASE SPURS CONCERN OVER MISCONDUCT SECRECY

Government, universities should name offenders, critics say *By A. Komnenic*

1362 COST OF CARBON CAPTURE DROPS, BUT DOES ANYONE WANT IT?

Lure of technologies could fade with Trump administration
By R. F. Service

1363 NEW BIRD FLU STRAIN BRINGS DEATH AND QUESTIONS

H5N8 is killing birds around Europe and the Middle East but appears harmless to humans *By K. Kupferschmidt*

1364 TRUMP TEAM TARGETS KEY CLIMATE METRIC

"Social cost of carbon" to get a critical look from incoming administration
By D. Malakoff, R. F. Service, and W. Cornwall

FEATURES

1366 SOME LIKE IT HOT

Iran's Lut Desert—Earth's hottest—is devoid of plants but somehow sustains a vibrant ecosystem *By R. Stone*

1369 AFTER THE VANISHING

Savvy anthropologists mix science and legal skills to help the families of Mexico's disappeared *By L. Wade*

► PODCAST

INSIGHTS

POLICY FORUM

1372 U.S. SEAFOOD IMPORT RESTRICTION PRESENTS OPPORTUNITY AND RISK

Marine mammal protections require increased global capacity
By R. Williams et al.

PERSPECTIVES

1375 HOW HIGH WILL THE SEAS RISE?

Coastal defense measures must be flexible in the face of rising sea level estimates *By M. Oppenheimer and R. B. Alley*

1377 STARVING THE ENEMY

Plants respond to pathogen infection by relocating sugar from bacterial colonization sites *By P. N. Dodds and E. S. Lagudah*

► REPORT P. 1427

1378 TOWARD SUSTAINABLE FUEL CELLS

Improved fuel-cell catalysts require much less platinum for the same performance *By I. E. L. Stephens et al.*

► REPORTS PP. 1410 & 1414

1380 UNDERSTANDING INDUCED SEISMICITY

Observational data sets provide a clearer picture of the causes of induced seismicity *By D. Elsworth et al.*

► REPORT P. 1406

1382 JOHN D. ROBERTS (1918–2016)

One of the great leaders of modern chemistry during the field's most exciting time *By G. M. Whitesides*

BOOKS ET AL.

1383 THE CALCULATORS

Two tomes uncover how women broke down barriers to explore the universe
By C. Christian

1384 THE AFTERMATH OF AIDS IN CHINA

A candid history uncovers the country's stumbles and successes in the fight against the devastating virus
By K. Harper

LETTERS

1385 EDITORIAL RETRACTION

By J. Berg

1385 PRIORITIZING GOOD DIETS

By D. A. Cleveland

1386 INDIRECT IMPACTS OF CLIMATE CHANGE

By R. J. Smithers and M. Blicharska

1386 ERRATA

DEPARTMENTS

1355 EDITORIAL

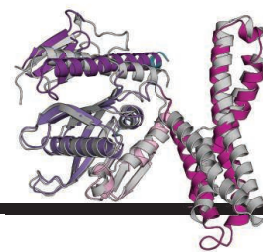
Science's rightful place
By Jeremy Berg

1494 WORKING LIFE

Living up to my mentors
By Barbara Gastel

Science Staff	1354
New Products	1445
Science Careers	1446

CONTENTS



1437

Terminating translation

16 DECEMBER 2016 • VOLUME 354 • ISSUE 6318

RESEARCH

IN BRIEF

1387 From *Science* and other journals

REVIEW

1390 ANTIBIOTIC RESISTANCE

Mechanisms of bacterial persistence during stress and antibiotic exposure
A. Harms et al.

REVIEW SUMMARY; FOR FULL TEXT:
dx.doi.org/10.1126/science.aaf4268

REPORTS

1391 PHOTOCHEMISTRY

Enantioselective photochemistry through Lewis acid-catalyzed triplet energy transfer
T. R. Blum et al.

VOLCANOLOGY

1395 Seismic constraints on caldera dynamics from the 2015 Axial Seamount eruption
W. S. D. Wilcock et al.

1399 Inflation-predictable behavior and co-eruption deformation at Axial Seamount
S. L. Nooner and W. W. Chadwick Jr.

1403 GEOCHEMISTRY

Large gem diamonds from metallic liquid in Earth's deep mantle
E. M. Smith et al.

1406 INDUCED SEISMICITY

Fault activation by hydraulic fracturing in western Canada
X. Bao and D. W. Eaton

► PERSPECTIVE P. 1380



1395 &
1399



1423

ELECTROCATALYSIS

1410 Biaxially strained PtPb/Pt core/shell nanoplate boosts oxygen reduction catalysis
L. Bu et al.

1414 Ultrafine jagged platinum nanowires enable ultrahigh mass activity for the oxygen reduction reaction
M. Li et al.

► PERSPECTIVE P. 1378

1419 TORNADOES

More tornadoes in the most extreme U.S. tornado outbreaks
M. K. Tippett et al.

1423 CONSERVATION

A global map of roadless areas and their conservation status
P. L. Ibisch et al.

1427 PLANT PATHOLOGY

Regulation of sugar transporter activity for antibacterial defense in *Arabidopsis*
K. Yamada et al.

► PERSPECTIVE P. 1377

1431 RIBOSOMES

The cryo-EM structure of a ribosome-Ski2-Ski3-Ski8 helicase complex
C. Schmidt et al.

1434 STRUCTURAL BIOLOGY

The structure and flexibility of conical HIV-1 capsids determined within intact virions
S. Mattei et al.

1437 STRUCTURAL BIOLOGY

Translational termination without a stop codon
N. R. James et al.

1441 PROTEIN ENGINEERING

Engineering extrinsic disorder to control protein activity in living cells
O. Dagliyan et al.

ON THE COVER



Standing at ~7-centimeters tall, this 404.2-carat rough diamond was recovered from the Lulo mine, Angola, in February 2016. Evidence from the interior of such large gem diamonds suggests that these diamonds grow from an iron-nickel metallic liquid in Earth's deep convecting mantle. The presence of metal in regions of the deep mantle has broad implications for Earth's geologic evolution. See page 1403. Photo: © SPOA/Orel SIMON

SCIENCE (ISSN 0036-8075) is published weekly on Friday, except the last week in December, by the American Association for the Advancement of Science, 1200 New York Avenue, NW, Washington, DC 20005. Periodicals mail postage (publication No. 484460) paid at Washington, DC, and additional mailing offices. Copyright © 2016 by the American Association for the Advancement of Science. The title SCIENCE is a registered trademark of the AAAS. Domestic individual membership and subscription (51 issues): \$165 (\$74 allocated to subscription). Domestic institutional subscription (51 issues): \$1522; foreign postage extra: Mexico, Caribbean (surface mail) \$55; other countries (air assist delivery) \$89. First class, airmail, student, and emeritus rates on request. Canadian rates with GST available upon request. GST #R1254 88122. Publications Mail Agreement Number 1069624. Printed in the U.S.A. Change of address: Allow 4 weeks, giving old and new addresses and 8-digit account number. Postmaster: Send change of address to AAAS, P.O. Box 96178, Washington, DC 20090-6178. Single-copy sales: \$15.00 current issue, \$20.00 back issue prepaid includes surface postage; bulk rates on request. Authorization to photocopy material for internal or personal use under circumstances not falling within the fair use provisions of the Copyright Act is granted by AAAS to libraries and other users registered with the Copyright Clearance Center (CCC) Transactional Reporting Service, provided that \$35.00 per article is paid directly to CCC, 222 Rosewood Drive, Danvers, MA 01923. The identification code for Science is 0036-8075. Science is indexed in the Reader's Guide to Periodical Literature and in several specialized indexes.

Editor-in-Chief Jeremy Berg

Executive Editor Monica M. Bradford **News Editor** Tim Appenzeller

Deputy Editors Lisa D. Chong, Andrew M. Sugden(UK), Valda J. Vinson, Jake S. Yeston

Research and Insights

DEPUTY EDITOR, EMERITUS Barbara R. Jasny **SR. EDITORS** Caroline Ash(UK), Gilbert J. Chin, Julia Fahrenkamp-Uppenbrink(UK), Pamela J. Hines, Stella M. Hurlley(UK), Paula A. Kiberstis, Marc S. Lavine(Canada), Ian S. Osborne(UK), Beverly A. Purnell, L. Bryan Ray, H. Jesse Smith, Jelena Stajic, Peter Stern(UK), Phillip D. Szurmi, Sacha Vignieri, Brad Wible, Laura M. Zahn **ASSOCIATE EDITORS** Brent Grocholski, Priscilla Kelly, Keith T. Smith **ASSOCIATE BOOK REVIEW EDITOR** Valerie B. Thompson **LETTERS EDITOR** Jennifer Sills **LEAD CONTENT PRODUCTION EDITORS** Harry Jach, Lauren Kmec **CONTENT PRODUCTION EDITORS** Amelia Beyna, Jeffrey E. Cook, Chris Filiatreau, Cynthia Howe, Barbara P. Ordway, Catherine Wolner **SR. EDITORIAL COORDINATORS** Carolyn Kyle, Beverly Shields **EDITORIAL COORDINATORS** Aneera Dobbins, Joi S. Granger, Jeffrey Hearn, Lisa Johnson, Maryrose Madrid, Anita Wynn **PUBLICATIONS ASSISTANTS** Nida Masilius, Dona Mathieu, Le-Tonya Mayne Flood, Shannon McMahon, Scott Miller, Jerry Richardson, Alice Whaley(UK), Gwen Grant(UK), Brian White **EXECUTIVE ASSISTANT** Anna Bashkirova **ADMINISTRATIVE SUPPORT** Janet Clements(UK), Lizanne Newton(UK), Sarah Harrison(UK)

News

NEWS MANAGING EDITOR John Travis **INTERNATIONAL EDITOR** Richard Stone **DEPUTY NEWS EDITORS** Elizabeth Culotta, David Grimm, Eric Hand, David Malakoff, Leslie Roberts **CONTRIBUTING EDITOR** Martin Enserink(Europe) **SR. CORRESPONDENTS** Daniel Clery(UK), Jeffrey Mervis, Elizabeth Pennisi **NEWS WRITERS** Adrian Cho, Jon Cohen, Jennifer Couzin-Frankel, Carolyn Gramling, Jocelyn Kaiser, Catherine Maticic, Kelly Servick, Robert F. Service, Erik Stokstad(Cambridge, UK), Paul Voosen, Meredith Wadman **INTERNS** Jessica Boddy, Rachael Lallensack **CONTRIBUTING CORRESPONDENTS** John Bohannon, Warren Cornwall, Ann Gibbons, Mara Hvistendahl, Sam Kean, Eli Kintisch, Kai Kupferschmidt(Berlin), Andrew Lawler, Mitch Leslie, Eliot Marshall, Virginia Morell, Dennis Normile(Shanghai), Tania Rabesandratana(London), Emily Underwood, Gretchen Vogel(Berlin), Lizzie Wade(Mexico City) **CAREERS** Donisha Adams, Rachel Bernstein(Editor), Maggie Kuo **COPY EDITORS** Julia Cole, Dorie Cheylen, Jennifer Levin(Chief) **ADMINISTRATIVE SUPPORT** Jessica Adams

Executive Publisher Rush D. Holt

Publisher Bill Moran **Chief Digital Media Officer** Rob Covey

DIRECTOR, BUSINESS STRATEGY AND PORTFOLIO MANAGEMENT Sarah Whalen **DIRECTOR, PRODUCT AND CUSTOM PUBLISHING** Will Schweitzer **PRODUCT DEVELOPMENT ASSOCIATE** Hannah Heckner **BUSINESS SYSTEMS AND FINANCIAL ANALYSIS** Director Randy Yi **SENIOR SYSTEMS ANALYST** Nicole Mehmedovich **DIRECTOR, BUSINESS OPERATIONS & ANALYSIS** Eric Knott **MANAGER, BUSINESS OPERATIONS** Jessica Tierney **SENIOR BUSINESS ANALYST** Cory Lipman **BUSINESS ANALYSTS** David Garrison, Michael Hardesty Meron Kebede, Sandy Kim **FINANCIAL ANALYST** Drew Sher **DIRECTOR, COPYRIGHTS LICENSING SPECIAL PROJECTS** Emilie David **PERMISSIONS ASSOCIATE** Elizabeth Sandler **RIGHTS, CONTRACTS, AND LICENSING ASSOCIATE** Lili Kiser **RIGHTS & PERMISSIONS ASSISTANT** Alexander Lee

MARKETING DIRECTOR Elise Swinehart **ASSOCIATE MARKETING DIRECTOR** Stacey Burke Bowers **MARKETING ASSOCIATE** Steven Goodman **CREATIVE DIRECTOR** Scott Rodgersen **SENIOR ART ASSOCIATES** Paula Fry **ART ASSOCIATE** Kim Huynh

FULFILLMENT SYSTEMS AND OPERATIONS membership@aaas.org **MANAGER, MEMBER SERVICES** Pat Butler **SPECIALISTS** Terrance Morrison, Latashia Russell **MANAGER, DATA ENTRY** Mickie Napoleoni **DATA ENTRY SPECIALISTS** Brenden Aquilino, Fiona Giblin **MARKETING ASSOCIATE** Isa Sesay-Bah

DIRECTOR, INSTITUTIONAL LICENSING David Celano **PUBLISHER RELATIONS, EASTERN REGION** Keith Layson **PUBLISHER RELATIONS, WESTERN REGION** Ryan Rexroth **ASSOCIATE DIRECTOR, INSTITUTIONAL LICENSING OPERATIONS** Iquo Edim **SENIOR OPERATIONS ANALYST** Lana Guzman **MANAGER, AGENT RELATIONS & CUSTOMER SUCCESS** Judy Lillibridge

WEB TECHNOLOGIES PORTFOLIO MANAGER Trista Smith **TECHNICAL MANAGER** Chris Coleman **PROJECT MANAGER** Nick Fletcher **DEVELOPERS** Elissa Heller, Ryan Jensen, Jimmy Marks, Brandon Morrison

DIGITAL MEDIA DIRECTOR OF ANALYTICS Enrique Gonzales **DIGITAL REPORTING ANALYST** Eric Hossinger **SR. MULTIMEDIA PRODUCER** Sarah Crespi **MANAGING DIGITAL PRODUCER** Alison Crawford **PRODUCER** Liana Birke **VIDEO PRODUCER** Chris Burns, Nguyễn Khởi Nguyễn **DIGITAL SOCIAL MEDIA PRODUCER** Brice Russ

DIRECTOR OF OPERATIONS PRINT AND ONLINE Lizabeth Harman **DIGITAL/PRINT STRATEGY MANAGER** Jason Hillman **QUALITY TECHNICAL MANAGER** Marcus Spiegler **PROJECT ACCOUNT MANAGER** Tara Kelly **DIGITAL PRODUCTION MANAGER** Lisa Stanford **ASSISTANT MANAGER DIGITAL/PRINT** Rebecca Doshi **SENIOR CONTENT SPECIALISTS** Steve Forrester, Antoinette Hodal, Lori Murphy, Anthony Rosen **CONTENT SPECIALISTS** Jacob Hedrick, Kimberley Oster **ADVERTISING OPERATIONS SPECIALIST** Ashley Jeter

DESIGN DIRECTOR Beth Rakouskas **DESIGN EDITOR** Marcy Atarod **SENIOR DESIGNER** Chrystal Smith **DESIGNER** Christina Aycock **GRAPHICS MANAGING EDITOR** Alberto Cuadra **GRAPHICS EDITOR** Garvin Grullón **SENIOR SCIENTIFIC ILLUSTRATORS** Chris Bickel, Katharine Sutliff **SCIENTIFIC ILLUSTRATOR** Valerie Altounian **INTERACTIVE GRAPHICS EDITOR** Jia You **SENIOR GRAPHICS SPECIALISTS** Holly Bishop, Nathalie Cary **PHOTOGRAPHY MANAGING EDITOR** William Douthitt **PHOTO EDITOR** Emily Petersen

DIRECTOR, GLOBAL COLLABORATION, CUSTOM PUBLICATIONS, ADVERTISING Bill Moran **EDITOR, CUSTOM PUBLISHING** Sean Sanders: 202-326-6430 **ASSISTANT EDITOR, CUSTOM PUBLISHING** Jackie Oberst: 202-326-6463 **ASSOCIATE DIRECTOR, ADVERTISING MARKETING** Justin Savyers: 202-326-7061 science_advertising@aaas.org **ADVERTISING SUPPORT MANAGER** Karen Foote: 202-326-6740 **ADVERTISING PRODUCTION OPERATIONS MANAGER** Deborah Tompkins **SR. PRODUCTION SPECIALIST/GRAPHIC DESIGNER** Army Hardcastle **SR. TRAFFIC ASSOCIATE** Christine Hall **SALES COORDINATOR** Shirley Young **ASSOCIATE DIRECTOR, COLLABORATION, CUSTOM PUBLICATIONS/CHINA/TAIWAN/KOREA/SINGAPORE** Xiaoying Chiu: +86-186 0082 9345, xchu@aaas.org **COLLABORATION/CUSTOM PUBLICATIONS/JAPAN** Adarsh Sandhu: +81532-81-5142 asandhu@aaas.org **EAST COAST/E. CANADA** Laurie Faraday: 508-747-9395, FAX 617-507-8189 **WEST COAST/W. CANADA** Lynne Stickrod: 415-931-9782, FAX 415-520-6940 **MIDWEST** Jeffrey Dembksi: 847-498-4520 x3005, Steven Loecher: 847-498-4520 x3006 **UK EUROPE/ASIA** Roger Goncalves: TEL/FAX +41 43 243 1358 **JAPAN** Katsuyoshi Fukamizu(Tokyo): +81-3-3219-1577 kfukamizu@aaas.org **DIRECTOR, COLLABORATION AND PUBLISHING SERVICES CHINA/TAIWAN** Yan Xiang: +86-186 0082 9345, xyiang@aaas.org

DIRECTOR, GLOBAL ADVERTISING AND SALES Tracy Holmes: +44 (0) 1223 326525, FAX +44 (0) 1223 326532 tholmes@science-int.co.uk **CLASSIFIED** advertise@sciencecareers.org **U.S. SALES** Tina Burks: 202-326-6577, Nancy Toema: 202-326-6578 **EUROPE/ROW SALES** Sarah Lelarge **SALES ASSISTANT KAC** Grace Japan Hironoyuki Mashiki(Kyoto): +81-75-823-1109 hnmashiki@aaas.org **CHINA/TAIWAN** Yan Xiang: +86-186 0082 9345 xyiang@aaas.org **MARKETING MANAGER** Allison Pritchard **MARKETING ASSOCIATE** Aimee Aponte

AAAS BOARD OF DIRECTORS, Chair Geraldine L. Richmond **PRESIDENT** Barbara A. Schaaf **PRESIDENT-ELECT** Susan Carol Field **TREASURER** David Evans **SHAW CHIEF EXECUTIVE OFFICER** Rush D. Holt **BOARD** Cynthia M. Beall, May R. Berenbaum, Charles J. Bustamante, Stephen P.A. Fodor, Claire M. Fraser, Michael S. Gazzaniga, Laura H. Greene, Elizabeth Loftus, Mercedes Pascual

SUBSCRIPTION SERVICES For change of address, missing issues, new orders and renewals, and payment questions: 866-434-AAAS (2227) or 202-326-6417, FAX 202-842-1065. Mailing addresses: AAAS, P.O. Box 96178, Washington, DC 20090-6178 or AAAS Member Services, 1200 New York Avenue, NW, Washington, DC 20005

INSTITUTIONAL SITE LICENSES 202-326-6730 **REPRINTS:** Author Inquiries 800-635-7181 **COMMERCIAL INQUIRIES** 803-359-4578 **PERMISSIONS** 202-326-6765, permissions@aaas.org **AAAS Member Services** 202-326-6417 or <http://membercentral.aaas.org/discourts>

Science serves as a forum for discussion of important issues related to the advancement of science by publishing material on which a consensus has been reached as well as including the presentation of minority of conflicting points of view. Accordingly, all articles published in Science—including editorials, news and comment, and book reviews—are signed and reflect the individual views of the authors and not official points of view adopted by AAAS or the institutions with which the authors are affiliated.

INFORMATION FOR AUTHORS See pages 624 and 625 of the 5 February 2016 issue or access www.sciencemag.org/authors/science-information-authors

SENIOR EDITORIAL BOARD

Gary King, *Harvard University*, Susan M. Rosenberg, *Baylor College of Medicine*, Ali Shilatfard, *Northwestern University Feinberg School of Medicine*

BOARD OF REVIEWING EDITORS

(Statistics board members indicated with \$)

Adriano Aguzzi, *U. Hospital Zurich*
Takuzo Aida, *U. of Tokyo*
Leslie Aiello, *Wenner-Gren Foundation*
Judith Allen, *U. of Edinburgh*
Sonia Altizer, *U. of Georgia*
Sebastian Amigorena, *Institut Curie*
Meinrat O. Andreae, *Max-Planck Inst. Mainz*
Paola Arlotta, *Harvard U.*
Johan Auwerx, *EPFL*
David Awschalom, *U. of Chicago*
Clare Baker, *University of Cambridge*
Nenad Ban, *ETH Zurich*
Franz Bauer, *Pontificia Universidad Católica de Chile*
Ray H. Baughman, *U. of Texas, Dallas*
David Baum, *U. of Wisconsin*
Carlo Beenakker, *Leiden U.*
Kamran Behnia, *ESPCI-ParisTech*
Yasmine Belkaid, *NIAID, NIH*
Philip Benfey, *Duke U.*
May Berenbaum, *U. of Illinois*
Gabriele Bergers, *U. of California, San Francisco*
Bradley Bernstein, *Massachusetts General Hospital*
Peer Bork, *EMBL*
Bernard Bourdon, *Ecole Normale Supérieure de Lyon*
Chris Bowler, *Ecole Normale Supérieure*
Ian Boyd, *U. of St. Andrews*
Emily Brodsky, *U. of California, Santa Cruz*
Ron Brookmeyer, *U. of California Los Angeles (\$)*
Christian Büchel, *U. Hamburg-Eppendorf*
Joseph A. Burns, *Cornell U.*
Carter Tribble Butts, *U. of California, Irvine*
Gyorgy Buzsaki, *New York U. School of Medicine*
Blanche Capel, *Duke U.*
Mats Carlsson, *U. of Oslo*
Ib Chorkendorff, *U. of Denmark*
David Clapham, *Children's Hospital Boston*
Joel Cohen, *Rockefeller U., Columbia U.*
James J. Collins, *MIT*
Robert Cook-Deegan, *Duke U.*
Lisa Coussens, *Oregon Health & Science U.*
Alan Cowman, *Walter & Eliza Hall Inst.*
Robert H. Crabtree, *Yale U.*
Roberto Croce, *Vrije Universiteit*
Janet Currie, *Princeton U.*
Jeff L. Dangl, *U. of North Carolina*
Tom Daniel, *U. of Washington*
Frans de Waal, *Emory U.*
Stanislas Dehaene, *Collège de France*
Robert Desimone, *MIT*
Claude Desplan, *New York U.*
Sandra Diaz, *Universidad Nacional de Cordoba*
Dennis Discher, *U. of Pennsylvania*
Gerald W. Dorn II, *Washington U. School of Medicine*
Jennifer A. Doudna, *U. of California, Berkeley*
Bruce Dunn, *U. of California, Los Angeles*
William Dunphy, *Caltech*
Christopher Dye, *WHO*
Todd Ehlers, *U. of Tuebingen*
David Ehrhardt, *Carnegie Inst. of Washington*
Tim Elston, *U. of North Carolina at Chapel Hill*
Jennifer Elisseeff, *Johns Hopkins U.*
Gerhard Ertl, *Fritz-Haber-Institut, Berlin*
Barry Everitt, *U. of Cambridge*
Ernst Fehr, *U. of Zurich*
Anne C. Ferguson-Smith, *U. of Cambridge*
Michael Feuer, *The George Washington U.*
Toren Finkel, *NHLBI, NIH*
Kate Fitzgerald, *U. of Massachusetts*
Peter Fratzl, *Max-Planck Inst.*
Elaine Fuchs, *Rockefeller U.*
Daniel Geschwind, *UCLA*
Karl-Heinz Glassmeier, *TU Braunschweig*
Ramón González, *Rice U.*
Elizabeth Grove, *U. of Chicago*
Nicolas Gruber, *ETH Zurich*
Kip Guy, *St. Jude's Children's Research Hospital*
Teekjip Ha, *U. of Illinois at Urbana-Champaign*
Wolf-Dietrich Hardt, *ETH Zurich*
Christian Haass, *Ludwig Maximilians U.*
Sharon Hammes-Schiffer, *U. of Illinois at Urbana-Champaign*
Michael Hasselmo, *Boston U.*
Martin Heimann, *Max-Planck Inst. Jena*
Yka Helariutta, *U. of Cambridge*
James A. Hendler, *Rensselaer Polytechnic Inst.*
Janet G. Hering, *Swiss Fed. Inst. of Aquatic Science & Technology*
Kai-Uwe Hinrichs, *U. of Bremen*
David Hodell, *U. of Cambridge*
Lora Hooper, *UT Southwestern Medical Ctr. at Dallas*
Tamas Horvath, *Yale University*
Raymond Huey, *U. of Washington*
Fred Hughson, *Princeton U.*
Auke Ijspeert, *EPFL Lausanne*
Stephen Jackson, *USGS and U. of Arizona*
Steven Jacobsen, *U. of California, Los Angeles*
Seema Jayachandran, *Northwestern U.*
Kai Jonsson, *EPFL Lausanne*
Peter Jonas, *Inst. of Science & Technology (IST) Austria*
Matt Kaeberlein, *U. of Washington*
William Kaelin Jr., *Dana-Farber Cancer Inst.*
Daniel Kahne, *Harvard U.*
Daniel Kammen, *U. of California, Berkeley*
Abby Kanner, *U. of California, Los Angeles*
Hitoshi Kawakatsu, *U. of Tokyo*
Masashi Kawasaki, *U. of Tokyo*
V. Naray Kim, *Seoul National U.*
Robert Kingston, *Harvard Medical School*

Etienne Kochlin, *Ecole Normale Supérieure*
Alexander Kolodkin, *Johns Hopkins U.*
Thomas Langer, *U. of Cologne*
Mitchell A. Lazar, *U. of Pennsylvania*
David Lazer, *Harvard U.*
Thomas Lecuit, *IDM*
Virginia Lee, *U. of Pennsylvania*
Stanley Lemon, *U. of North Carolina at Chapel Hill*
Ottoline Leyser, *Cambridge U.*
Wendell Lim, *U.C. San Francisco*
Marcia C. Linn, *U. of California, Berkeley*
Jianguo Liu, *Michigan State U.*
Luis Liz-Marzan, *CIC biomaGUNE*
Jonathan Losos, *Harvard U.*
Ke Lu, *Chinese Acad. of Sciences*
Christian Lüscher, *U. of Geneva*
Laura Machesky, *CRUK Beatson Inst. for Cancer Research*
Aime Magurran, *U. of St. Andrews*
Oscar Marin, *CSIC & U. Miguel Hernández*
Charles Marshall, *U. of California, Berkeley*
C. Robertson McClung, *Dartmouth College*
Rodrigo Medellín, *U. of Mexico*
Graham Medley, *U. of Warwick*
Jane Memmott, *U. of Bristol*
Tom Misteli, *NCI*
Yasushi Miyashita, *U. of Tokyo*
Mary Ann Moran, *U. of Georgia*
Richard Morris, *U. of Edinburgh*
Alison Moutter-Reif, *NC State U. (\$)*
Thomas Murray, *The Hastings Center*
Daniel Neuman, *U. of California, Berkeley*
Kitty Nijmeijer, *U. of Twente*
Helga Nowotny, *European Research Advisory Board*
Rachel O'Reilly, *Warwick U.*
Joe Orenstein, *U. of California Berkeley & Lawrence Berkeley National Lab*
Harry Orr, *U. of Minnesota*
Pilar Ossorio, *U. of Wisconsin*
Andrew Oswald, *U. of Warwick*
Isabella Pagano, *Istituto Nazionale di Astrofisica*
Margaret Palmer, *U. of Maryland*
Steve Palumbi, *Stanford U.*
Jane Parker, *Max-Planck Inst. of Plant Breeding Research*
Giovanni Parmigiani, *Dana-Farber Cancer Inst. (\$)*
John H. J. Petrini, *Memorial Sloan-Kettering Cancer Center*
Samuel Pfaff, *Salk Institute for Biological Studies*
Kathrin Plath, *U. of California, Los Angeles*
Joshua Plotkin, *U. of Pennsylvania*
Albert Polman, *FOM Institute AMOLF*
Philippe Poulin, *CNRS*
Jonathan Pritchard, *Stanford U.*
Wim van der Putten, *Netherlands Institute of Ecology*
David Randall, *Colorado State U.*
Sarah Reisman, *Caltech*
Felix Rey, *Institut Pasteur*
Trevor Robbins, *U. of Cambridge*
Jim Roberts, *Fred Hutchinson Cancer Research Ctr.*
Amy Rosenzweig, *Northwestern University*
Mike Ryan, *U. of Texas, Austin*
Mitsunori Sakata, *Kyoto U.*
Shimon Saitouchi, *Kyoto U.*
Miguel Salmeron, *Lawrence Berkeley National Lab*
Jürgen Sandkühler, *Medical U. of Vienna*
Alexander Schier, *Harvard U.*
Vladimir Shalaev, *Purdue U.*
Robert Siliciano, *Johns Hopkins U.*
Denis Simon, *Arizona State U.*
Uri Simonsohn, *U. of Pennsylvania*
Alison Smith, *Johns Hopkins U.*
Richard Smith, *U. of North Carolina (\$)*
John Speakman, *U. of Aberdeen*
Allan C. Spradling, *Carnegie Institution of Washington*
Jonathan Sprent, *Garvan Inst. of Medical Research*
Eric Steig, *U. of Washington*
Paula Stephan, *Georgia State U. and National Bureau of Economic Research*
Molly Stevens, *Imperial College London*
Ira Tabas, *Columbia U.*
Sarah Teichmann, *Cambridge U.*
John Thomas, *North Carolina State U.*
Shubha Tole, *Jata Institute of Fundamental Research*
Christopher Tyler-Smith, *The Wellcome Trust*
Sanger Inst.
Herbert Virgin, *Washington U.*
Bert Vogelstein, *Johns Hopkins U.*
David Wallace, *Weizmann Inst. of Science*
Ian Walmsey, *U. of Oxford*
Jane-Ling Wang, *U. of California, Davis (\$)*
David Waxman, *Fudan U.*
Jonathan Weissman, *U. of California, San Francisco*
Chris Wikle, *U. of Missouri (\$)*
Ian A. Wilson, *The Scripps Res. Inst. (\$)*
Timothy D. Wilson, *U. of Virginia*
Rosemary Wyse, *Johns Hopkins U.*
Jan Zaenen, *Leiden U.*
Kenneth Zaret, *U. of Pennsylvania School of Medicine*
Jonathan Zehr, *U. of California, Santa Cruz*
Len Zon, *Children's Hospital Boston*
Maria Zuber, *MIT*

BOOK REVIEW BOARD

David Bloom, *Harvard U.*, Samuel Bowring, *MIT*, Angela Creager, *Princeton U.*, Richard Swedder, *U. of Chicago*, Ed Wasserman, *DuPont*

Science's rightful place

In his first inaugural address, U.S. President Obama said, “We’ll restore science to its rightful place...” He subsequently used this phrase to frame a number of activities across his administration.* While I, like many in the scientific community, was pleased with this declaration, I found the term “rightful place” to be thought-provoking.

The word “rightful” is usually taken to mean legitimate or morally appropriate. Yet, the word “right” has multiple meanings; it can mean morally good or justified, as noted above, but it can also mean true or correct as fact. It is the latter meaning that is essential for the position of science in government.

The scientific method has proved to be the best method for determining what is factually correct. Facts are important because they are robust and provide foundations on which intellectual constructs and technologies can be built. Consider, for example, investigations by Albert Michelson and Edward Morley on the speed of light. To their surprise, they discovered, with great precision, that the speed of light was the same in all directions. This became a pillar for Hendrik Lorentz’s and Albert Einstein’s work leading to formulation of the theory of special relativity. Today, it provides the framework for a vast amount of modern technology, such as Global Positioning Systems.

The ability for science to get the facts right also has profound implications for health care. While I was a professor at Johns Hopkins University School of Medicine during the 1990s, the AIDS epidemic continued to accelerate in the absence of effective treatments. There were serious discussions of how to manage the crisis as hospital beds filled with AIDS patients, with projections that the capacity to handle the situation would soon be overwhelmed. The identification of human immunodeficiency virus (HIV) as the cause of AIDS, the demonstration that two enzyme activities (reverse transcriptase and protease) were essential for the vi-

ability of the virus, and the development of combination therapies that included inhibitors of both enzymes stopped acceleration of the epidemic in developed countries. Remarkably, it was recently reported that individuals in the United States infected with HIV are now more likely to die from smoking-related diseases than from AIDS. The adverse health effects of tobacco, of course, had previously been established by scientific

investigations, but those results were met with denial of the facts and considerable political resistance, delaying policy changes and societal benefits.

American surgeon Bernard Fisher nicely framed the importance of the scientific method for getting the facts on which policies and practices can be based. In the 1960s, Fisher questioned the notion of radical, deforming operations as the best way to treat breast cancer. On the basis of laboratory results, he believed that breast cancer could be a systemic rather than a local disease. From this basic science insight, Fisher proposed that some breast cancer surgeries failed to prevent metastasis because the cancer had already spread at the time

of surgery. He led a clinical trial comparing radical mastectomy with more limited surgery in the face of considerable opposition, including accusations of unethically risking patients’ lives. The trial found no significant difference in the results of the two approaches. Fisher described his approach to mediating scientific discussions with the statement, “In God we trust; all others require data.”

The United States will face many issues related to climate change, medical and public health challenges including vaccines and other technologies, and the roles of computers and artificial intelligence tools in society, among other national and global matters. In 2017, let respect for data and rigorous analysis establish the rightful place for science in the new U.S. administration.

—Jeremy Berg



Editor-in-Chief,
Science Journals.
jberg@aaas.org



“...let respect for data and rigorous analysis establish the rightful place for science...”

*www.whitehouse.gov/blog/2016/06/21/100-examples-putting-science-its-rightful-place

“We’re living on soft signals. They might be asking questions to see how good the arguments are.”

Patent policy specialist **Robert Cook-Deegan** of **Arizona State University in Tempe**, on the danger of using the queries of judges at the 6 December hearing on CRISPR intellectual property rights to anticipate their decision.

IN BRIEF

Data mount linking Zika, birth defects



Colombian authorities are giving pregnant women mosquito nets to minimize Zika virus transmission.

Two studies this week strengthen the link between Zika virus infection of pregnant women and a range of serious birth defects. Researchers in Colombia have identified more than 147 babies in the country infected with Zika and born with microcephaly since January, they reported in the *Morbidity and Mortality Weekly Report*, a publication of the U.S. Centers for Disease Control and Prevention. That is more than twice as many as the Colombian ministry of health reported publicly (<http://scim.ag/ColombiaZika>). The news may help solve a puzzle: After Brazil, Colombia has been hardest hit by Zika, yet it appeared to have far fewer microcephaly cases per capita. It now appears that incomplete reporting may explain some of the disparity. A second study, in *The New England Journal of Medicine*, reported that among 182 pregnant women in Rio de Janeiro, Brazil, who tested positive for Zika virus, 46% experienced “adverse outcomes” affecting their babies. The problems included miscarriage, infant brain hemorrhages, and four cases of microcephaly. Among women infected during their first trimester, 55% had adverse outcomes. Similar problems were identified in 52% of women infected in their second trimester and 29% of women infected in their third trimester. http://scim.ag/_ZikaRio

AROUND THE WORLD

Cracks in U.S. spending freeze

WASHINGTON, D.C. | Congress has extended the current spending freeze on all U.S. agencies until 28 April 2017. But it spared several research-related projects at the National Institutes of Health (NIH), the Census Bureau, the National Oceanic and Atmospheric Administration (NOAA), and NASA. President Barack Obama signed the latest so-called continuing resolution (CR) Friday night to avert a government shut-down. The CR grants NIH \$352 million as a down payment on projects included in the 21st Century Cures Act, also signed into law this week. It allows the Census Bureau to test new approaches to the decennial census in 2020 that could shave \$5 billion off a projected cost of \$20 billion. NASA gets to continue building a new rocket and astronaut capsule for humans to return to the International Space Station and the moon, and possibly explore Mars. And NOAA gets the OK to continue building a series of polar-orbiting weather satellites, the first of which is scheduled to go up in late 2017.

Shortcut for stem cell therapies

WEST PALM BEACH, FLORIDA | Major changes may be ahead for how the U.S. Food and Drug Administration (FDA) evaluates stem cell therapies. The mammoth biomedical bill known as the 21st Century Cures Act, which was signed into law this week, includes a section addressing regenerative medicine that prompted



Law may ease way for stem cell-based therapies.

buzz at last week's annual World Stem Cell Summit. The new law could lessen the regulatory hurdles imposed by FDA by designating stem cell therapies as "regenerative advanced therapy." Products that qualify would be eligible for several existing shortcuts in the FDA review process. They include an accelerated approval pathway that allows a drug to reach the market based on what are called intermediate clinical trial endpoints—measures like imaging data or markers in blood that may be predictive of survival or other long-term disease outcomes. Those can mean fewer, shorter, or smaller trials. However, critics of the measure worry that speedier approvals on less evidence could put experimental therapies on the market before they're proven effective. <http://scim.ag/CURESstem>

Debating an embryo rule

LONDON | Should scientists be allowed to study embryos cultured in the lab beyond 14 days after fertilization? U.K.-based biologists and ethicists met last week to debate the topic at a daylong workshop held by the London-based nonprofit the Progress Educational Trust. Biologists in the United Kingdom and many other countries have not been allowed to culture human embryos in the laboratory longer than 14 days—which has never posed a constraint because it wasn't possible to keep embryos alive longer than about a week anyway. But earlier this year, two teams reignited the debate when they succeeded in keeping embryos alive for 13 days. Developmental biologist Magdalena Zernicka-Goetz of the University of Cambridge in the United Kingdom, who led one of the teams, noted that an extension would bring scientific gains, such as understanding the development of the central nervous system. But philosopher Mary Warnock, who chaired a committee in the 1980s that shaped current regulations, urged caution; researchers should first learn what they can from embryos 5 to 14 days old, she said; that might also help build a case for benefits from older embryos in the future. <http://scim.ag/14dayruledebate>

State water war kills weather bill

WASHINGTON, D.C. | A decades-long feud between three southern states over water last week killed a bill in the U.S. Congress that was poised to bolster the nation's weather forecasting capabilities, including support for seasonal predictions and commercial alternatives to collecting data (*Science*, 9 December, p. 1212). The bill,

Researchers sequenced the whole genome of the tiger tail seahorse.

The genes that make seahorses so weird

Seahorses are bizarre little ocean anomalies, from their tube-shaped snouts to their prehensile tails. Perhaps their most unusual trait: It's the males that give birth. Now, a research team has begun to investigate the genetic basis for these evolutionary oddities, by sequencing and analyzing the genome of a male tiger tail seahorse (*Hippocampus comes*) and comparing it with the DNA of other bony fish species. The seahorse species, the team reported this week in *Nature*, evolved at a faster rate than its ancestors. Though it is unclear why, the rapid pace has led to key genetic changes: For example, *H. comes* lacks most of the genes that influence enamel development; instead of teeth, its jaws have fused into a tubular snout and tiny mouth, suitable for slurping up food from the sea floor. And although most fish depend on their sense of smell for survival, *H. comes* has relatively few smell-related genes. *H. comes* and its brethren seahorses also lack the genes for pelvic fins—which might explain their elongated tail and bony body armor. But *H. comes* does have an abundance of one gene: Dubbed Pastrisacin, the gene is associated with male pregnancy, and the seahorse genome contains six copies of it.

which passed the Senate on 1 December and had broad bipartisan support, was widely expected to pass the House of Representatives as well. But in the most recent version, Senator Bill Nelson (D-FL) added a call for a study of the water management of the Apalachicola River and its tributaries, a river system shared by Georgia, Florida, and Alabama; the states have battled over its management for decades, and the addition drew a heated response from Georgia representatives. The bill was not brought up for a vote before the House adjourned for the remainder of the year. It will likely return next year, and scientists will continue to push for a deal, says Tony Busalacchi, president of the University Corporation for Atmospheric

Research based in Boulder, Colorado, which has advocated for the bill for 4 years. <http://scim.ag/waterforecast>

PubPeer wins comments battle

DETROIT, MICHIGAN | A Michigan appeals court last week handed PubPeer, a website that allows anonymous reviews of technical papers, a key win in its legal battle with a researcher who claims the site cost him a job and sullied his reputation. In 2014, Fazlul Sarkar, a cancer researcher at Wayne State University in Detroit, Michigan, sued anonymous commenters at the site for defamation, claiming their posts alleging misconduct cost him a lucrative position at the University of Mississippi and demanding

that PubPeer release the names of his accusers. In 2015, a judge ruled that all but one of the commenters could remain anonymous; the American Civil Liberties Union appealed that decision on behalf of PubPeer. Now, three judges on the Michigan Court of Appeals have reversed the 2015 decision, stating that Sarkar could continue to pursue a defamation case, but “is not entitled to unmask the identities of any speakers on pubpeer.com with respect to those claims due to the anonymity protections afforded by the First Amendment.”

Scientists are unmuzzled

OTTAWA | Scientists working for the Canadian government this week successfully negotiated a clause in their new contract that guarantees their right to speak to the public and media about science and their research without first seeking approval from their managers. Under the previous prime minister, Stephen Harper, many government-employed scientists complained that they were forbidden from discussing their research without approval. Justin Trudeau's Liberal government, which came to power last year, has reversed many of those restrictive

communication policies. But the scientists' professional union, which represents about 15,000 researchers, says it wants to ensure that those rights are protected in the future. The deal, announced on 12 December and the first of its kind in the world, states that “employees shall have the right to express themselves on science and their research ... without being designated as an official media spokesperson.” It also includes an agreement for the union and government to work together to develop broader science integrity policies and guidelines. <http://scim.ag/Canadamuzzle>

NEWSMAKERS

Physicist accused of plagiarism

French physicist and philosopher **Étienne Klein**, one of the country's best known scientists and popularizers of science, has been accused of appropriating passages from other scientists, philosophers, and famous writers in his work, including novelists Émile Zola and Stefan Zweig. Klein, who leads a lab for material sciences at the Alternative Energies and Atomic Energy Commission in Saclay, France, has written numerous popular science books and hosts

a weekly radio show; in September, he was named president of the Institute of High Studies for Science and Technology, which seeks to buttress public trust in the scientific enterprise. But many passages from his recent Albert Einstein biography appear to have been lifted almost verbatim from other sources, the weekly news magazine *L'Express* reported in November; in a subsequent article, the magazine also cited other examples of alleged plagiarism in his work. Klein, responding on his own website, said he had made mistakes but that he hasn't knowingly committed plagiarism. <http://scim.ag/EtienneKlein>

Three Qs

Representative **John Culberson** (R-TX) has a big voice in setting the budgets of NASA, the National Science Foundation (NSF), and other science agencies as chair of a congressional spending panel. Last week, he talked with *Science* about the future of U.S. science policy, including the White House Office of Science and Technology Policy (OSTP). <http://scim.ag/CulbersonQA>

Q: Would you like to see any changes to OSTP?

A: I'd be hard-pressed to identify any tangible, specific accomplishments or achievements of the office. It's important that we make government as efficient as possible. I think the president obviously needs a science adviser. But there are other places where he can get good advice. NSF is the nation's leader in scientific research, and NASA is responsible for preserving America's leadership in space exploration. ... I don't know that [OSTP] needs a large staff or a big operation.

Q: Have you talked to the transition team of President-elect Donald Trump about your plans for missions to the jovian moon Europa and Alpha Centauri?

A: Right now they are focused on filling the top positions within the administration. But I've had good conversations with them on the need to make sure that the U.S. space program is the best on Earth and that it will be an American spacecraft that discovers life on another world and achieves interstellar travel.

Q: There has been talk of moving earth sciences out of NASA.

A: At this point that is very speculative. There's strong support in Congress for keeping a close eye on planet Earth and understanding our complex planet. It will continue to be a topic of ongoing discussion. But nobody in the earth sciences community should be concerned in the least.

A spinning, star-eating black hole

Earlier this year, astronomers saw a flash in the sky tens of times brighter than our entire Milky Way galaxy. At the time, many thought it was the brightest supernova ever detected. But new data suggest it's something much more exotic. The flash was spotted in 2015 by the All-Sky Automated Survey for Supernovae, a network of small telescopes in Chile and Hawaii that monitors the sky for fast-changing objects. Astronomers assumed it was a superluminous supernova, which may occur when a massive star collapses under its own gravity, spewing out a bright fireball of hot dust and gas. But additional data on the event, gathered from sources ranging from the European Southern Observatory's Very Large Telescope in Chile to the Hubble Space Telescope, point to a very different origin for the bright flash: the dying gasp of a star that strayed too close to the supermassive black hole at the center of its galaxy. It may then have been ripped apart by the black hole's extreme gravitational field, the researchers suggest this week in *Nature Astronomy*, in an extremely rare phenomenon called a tidal disruption event.



A supermassive black hole shreds a star in this artist's illustration.



Laboring to breathe and near death as a baby, Cameron Harding, nearly 3, receives a drug that keeps his motor neurons alive, allowing him significant muscle movement.

BIOMEDICINE

Antisense rescues babies from killer disease

Spinal muscular atrophy drug may herald treatments for other genetic brain illnesses

By **Meredith Wadman**

Biomedical researchers tackling genetic diseases dream of tracing a clean, straight line from discovering a mutation to understanding a disease's mechanism to developing a curative drug. The messy complexities of biology have often frustrated that hope. But building on a deep understanding of the basic biology of a disease, they have now taken just such a path to what appears to be an unprecedented advance in treating spinal muscular atrophy (SMA), a progressive, fatal neurological disorder that kills its most severely affected victims as babies or toddlers. The therapy, called nusinersen, is poised to win regulatory approval within weeks or months, and it may well be a harbinger of successes with other grave, inherited neurological disorders, from Huntington disease to subsets of amyotrophic lateral sclerosis (ALS).

"This is a huge win for our field," says molecular neuroscientist J. Paul Taylor of St. Jude Children's Research Hospital in Memphis, Tennessee, who is not involved with the drug or with the companies behind it. "There has never been a disease-altering therapy for a neurodegenerative disease."

As one of a long, but often disappointing, class of drug candidates called antisense, which use snippets of genetic sequence to

correct errors in the conversion of RNA into proteins, nusinersen could open the way to similar treatments for other neurodegenerative diseases. "Nusinersen is a game changer," says Loren Eng, the president of the SMA Foundation in New York City and the mother of a 16-year-old with the disease. "It's a drug that treats a disease that has never been treated before. It's also a model for how to make drugs and get them across the finish line early."

SMA, the most common genetic cause of death in childhood, inexorably destroys the motor neurons of the spinal cord and brainstem. These cells allow movement, including swallowing and breathing. About one in 50 adults is an asymptomatic carrier of the recessive genetic defect that causes it, a flaw in the gene *SMN1*—for "survival motor neuron 1." In children who inherit two copies of the defect—between one in 8000 and one in 12,000 infants—the SMN protein is largely missing, which leads to the death of motor neurons. Toddlers with the most severe form of the disease ultimately suffocate when their respiratory muscles give out.

Children with milder forms of SMA can survive into adulthood, but must cope with progressive and often immobilizing weakness. The disease course depends on how many copies they carry of a very slightly different gene, *SMN2*, that produces a modest amount of the SMN protein. Most of the time

that protein degrades quickly, because after transcribing *SMN2*, cells splice out a key bit of protein-coding genetic sequence, so-called exon 7, producing a truncated version.

But nusinersen, a snippet of modified nucleic acid akin to RNA, can keep those vital motor neurons alive. Its short sequence complements part of a messenger RNA (mRNA) precursor produced by *SMN2*, binding to the molecule there and altering its processing so that exon 7 is included and the gene's full-length, functional protein is made (see graphic, p. 1360).

The drug's efficacy seems clear from strongly positive, though unpublished, results from two late-stage clinical trials. On 7 November, a trial of the drug in 84 wheelchair-bound children was stopped on the grounds that the treatment's benefits were so obvious that it was unethical to deny the antisense therapy to the 42 untreated children in the control arm. On measures including 33 tests of movement such as sitting, standing, and taking steps, investigators found a "highly statistically significant improvement" in the treated children. In July, a similar trial in 121 infants with the most severe form of the disease, who would otherwise die within several years, was similarly stopped in order to allow the 41 babies in the control group to begin receiving nusinersen. Soon thereafter, the U.S. Food and Drug Administration (FDA) and the

European Medicines Agency granted the drug fast-track review status.

Nusinersen clearly saved Cameron Harding of Charleston, South Carolina, who was diagnosed with SMA at 5 weeks old after his parents noticed that their newborn son couldn't move and was struggling to breathe. He began receiving the drug in a clinical trial at 7 weeks old and continues to do so. Late this month he will turn 3 years old. Over that time, he has gone from lying immobile to moving his arms to grasping toys to sitting up unsupported to standing with support and, lately, barreling around in a light-weight wheelchair he propels with his arms. "He absolutely would not be alive without the medication. He wouldn't have lasted 6 months," says Cameron's father, Rob Harding.

Cameron is still improving, he adds. "We were very afraid he would reach a plateau and that was going to be it. But he continues to get stronger."

Other antisense drugs have had far less success over the past 2 decades, with only a handful earning marketing approval. The most recent was the most controversial. In September, Sarepta Therapeutics of Cambridge, Massachusetts, won approval from FDA for eteplirsen, which aims to treat boys with a particular mutation causing another progressive and ultimately fatal inherited condition: Duchenne muscular dystrophy. At the molecular level, eteplirsen does the opposite of nusinersen: It removes an exon that disrupts the reading of an mRNA precursor for a protein, dystrophin, that muscles need. But the resulting protein is truncated and only partially functional. Critics charged that FDA approved the drug only because of pressure from politicians and parents of affected children, overruling its staff advisers and relying on at-best-equivocal trial results.

Although no one expects similar battles over nusinersen given its striking clinical results, it is not a perfect drug. It produced no serious side effects in the trials, but it cannot rescue motor neurons that are already dead, meaning that it cannot restore motor function for older SMA patients. Indeed, the goal is to begin treatment even before babies develop symptoms, and calls for universal newborn screening are expected to follow the drug's approval. "The earlier we treat the better the effect, and the longer we treat the better the effect," says Stanley Crooke, CEO of Ionis Pharmaceuticals, the company in Carlsbad, California, that developed nusinersen and has subsequently licensed it to Biogen in Cambridge.

Eng, who with her husband, Dinakar Singh, has channeled more than \$110 million into SMA research through the foundation the couple launched in 2003, says that

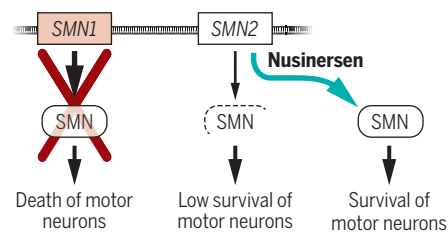
the tale of nusinersen demonstrates how "it takes a village" of scientists, physicians, companies, nonprofits, and families to efficiently develop a successful drug. Their foundation, for example, helped fund Adrian Krainer, a biochemist and RNA-splicing expert at the Cold Spring Harbor Laboratory in New York. Eight years after the discovery of the *SMN* genes in 1995, Krainer set the stage for the development of nusinersen when he engineered a synthetic snippet of genetic code that tweaked the splicing of *SMN2*'s mRNA precursor, so that the final RNA included exon 7.

A game-changing drug

An RNA-like molecule called nusinersen can treat spinal muscular atrophy (SMA) by boosting production of a key protein.

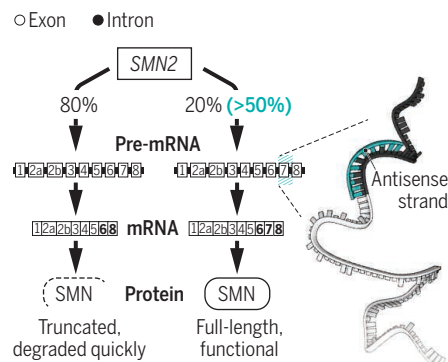
Exploiting a second gene

In SMA, the *SMN1* gene is faulty. A related gene, *SMN2*, typically makes little functional protein, but nusinersen increases production enough to sustain motor neurons.



Fixing the message

By binding to a messenger RNA (mRNA) precursor, nusinersen boosts the fraction of mRNAs with a key segment, exon 7, needed for a functional protein.



At another point, Eng persuaded Taiwanese researchers to share at reasonable cost a mouse model of SMA with which nusinersen and other drug candidates could be tested. Later, she introduced leaders at Ionis to executives at Biogen. And by the time the drug was ready for all-important phase III trials, the foundation, SMA advocacy and support groups, and physicians had persuaded enough parents of SMA patients to participate in a trial in which their children might not get the actual drug—a sham arm

was considered necessary to prove the drug's value to regulators.

Because antisense drugs do not cross the blood-brain barrier, the drug was injected near the base of the spine into fluid that bathes the brain and spinal cord, where the afflicted motor neurons are located. In the sham arms, babies and children chosen at random simply received needle pricks in their spine. "It was very difficult to see sham injection-controlled trials," Krainer says. But, he adds, the phase III trial results are "the best news one could hope to get."

A paper in *The Lancet* last week describing an earlier phase II trial of nusinersen demonstrates that such spinal injections reach their targets. Autopsy samples from several infants who died during the trial revealed that the drug had traveled to the targeted brain and spine motor neurons. In samples of the infants' spinal tissue, levels of full-length SMN protein were elevated compared with untreated babies.

To sustain nusinersen's benefits, SMA patients will likely need to receive spinal injections two or three times a year. But that may not keep symptoms that result from the lack of SMN in other tissues and organs from emerging, because the drug does not travel beyond the brain and spinal cord.

Still, the success of nusinersen and its delivery method into neurons has enthused those who work on other inherited neurodegenerative diseases caused by genetic defects that could, in theory, be overcome by antisense drugs that manipulate RNA processing. "There is more excitement now about antisense therapy," says Walter Koroshetz, a Huntington disease expert who is the director of the National Institute of Neurological Disorders and Stroke in Bethesda, Maryland. "If the problem of getting antisense access to the neurons and glia has been solved, then there's potential for a bunch of genetically determined diseases to get effective treatments."

Ionis is already in clinical trials with similarly delivered antisense drugs for Huntington disease and a form of ALS. Its drugs are also being tested in animal models of Rett and Angelman syndromes, rare neurological disorders whose mutations are amenable to an antisense approach.

Jeffrey Rothstein, a neuroscientist at the Johns Hopkins University School of Medicine in Baltimore, Maryland, who was not involved with the trials of nusinersen, sees its success as an object lesson in the importance of understanding the underpinnings of a disease. "It's a powerful story of moving from superb preclinical science to the development of this drug," he says. "This proves that when you get at the initial insult you can really change the course of the disease." ■

In Canada, case spurs concern over misconduct secrecy

Government, universities should name offenders, critics say

By **Ana Komnenic**, *Retraction Watch*

In early 2013, scientists working in a laboratory led by a prominent cancer researcher at the University of British Columbia (UBC) in Vancouver, Canada, were getting worried. They were unable to reproduce results from several of the researcher's experiments, and suspected some of the original work was fraudulent.

An investigation by UBC ultimately confirmed their fears: In 2014, investigators identified 29 instances of scholarly misconduct, 16 of them "serious," including falsification and fabrication of data, according to university correspondence obtained by Retraction Watch. Investigators found that the tainted work had been included in 12 papers published in six journals between 2005 and 2012 and had drawn financial support from more than a dozen government and private funders.

To the dismay of some scientists familiar with the case, however, UBC never publicly released the damning report or named the researcher, who has since left the institution. Canadian policy does not require the university or federal funding agencies to disclose the researcher's name. And a spokesperson for the university says its hands are tied by British Columbia's privacy laws, which prohibit it from disclosing personal information unless it is "clearly" in the public interest. But critics say the case highlights a troubling lack of transparency in Canada's system for policing scientific misconduct. Some believe the secrecy allows unreliable papers to remain in circulation, and could enable researchers to continue to raise funds from donors and investors who may not be aware of misconduct findings.

The university is "obviously trying to limit dissemination of information," and that is a "huge mistake," says UBC biochemist Ivan Sadowski, a member of the three-person team that made the misconduct findings.

The researcher at the center of the case is Sandra Dunn, according to the UBC documents. (Repeated attempts to contact Dunn

were unsuccessful.) For nearly 15 years, Dunn ran a lab at UBC's Experimental Medicine Program, where she worked on new treatments for aggressive brain and breast cancers. Dunn, once featured on an expert panel organized by the Canadian Breast Cancer Foundation, secured at least CAD\$1.1 million in government funding between 2009 and 2015. She left the university in 2015, after UBC concluded its investigation, to run Phoenix Molecular Designs, a



Officials at the University of British Columbia say privacy laws prevent them from naming scientists found to have committed misconduct.

company based in Richmond, Canada, that she founded in 2012. The company says it develops cancer therapies, and lists charities—including one supported by the parents of a child who died of cancer—among its "partners and supporters."

Many of Dunn's past and current private funders may not be aware of UBC's misconduct findings. The UBC correspondence lists 15 outside funders that directly or indirectly supported Dunn's work, and recommended that UBC contact them "as necessary." Retraction Watch tried to contact the funders; of the 10 that responded, only one—the C¹⁷ foundation in Edmonton, Canada—said it was aware of UBC's investigation. Some of those who had not been notified said they would not expect to be informed, as they had not directly funded Dunn. And one current funder, the Michael Cuccione Foundation in Vancouver, said

that UBC had not contacted it about the investigation, but that it was not concerned by the findings. The foundation has supported Dunn for years, says Executive Director Gloria Cuccione, and she has done "unbelievable work."

None of the 12 papers identified by investigators has been retracted, but one journal, *Molecular Pharmacology*, recently published an "expression of concern" about one of the papers, citing UBC's investigation. *Breast Cancer Research*, a journal that published two of the papers, confirmed that UBC had informed it of the investigation's findings.

Although UBC has no legal obligation to publicly disclose details of its misconduct investigations, it is required to notify federal funding agencies of misconduct findings against researchers that the agencies have supported. The agencies can then decide whether releasing the name

is in the public interest. In 2011, agencies started requiring all funding applicants to consent to having their names publicized if they committed a serious breach of agency policy. Dunn's funding predated the 2011 policy, however, and so far the policy has not led the agencies to publicly name any offending scientists (although one agency recently named an offender under a different set of rules).

Some Canadian researchers would like to see their funding agencies follow the lead of the U.S. Department of Health and Human Service's Office of Research Integrity, which does name researchers it concludes have committed misconduct. (The U.S. National Science Foundation does not.)

Current practices in Canada are "nothing but a cover-up with the excuse of privacy laid on top of it," argues Amir Attaran, a law professor and biologist at the University of Ottawa.

Research institutions face a tricky task in balancing the need for public transparency with the right to privacy, says Paul Hébert of the University of Montreal in Canada. Misconduct findings can be "extremely disruptive," he says, and there's a danger that colleagues of the offending researcher can be "painted with the same brush." Still, Hébert would like to see Canada improve its misconduct monitoring system. As it stands, he says, there is too little transparency and "no policing. ... Universities as research institutes investigate themselves." ■

This story is the product of a collaboration between Science and Retraction Watch.



A recent retrofit of the Boundary Dam coal plant in Canada captures CO₂ and stores it underground.

ENERGY POLICY

Cost of carbon capture drops, but does anyone want it?

Lure of technologies could fade with Trump administration

By Robert F. Service

Coal without the climate-warming carbon dioxide (CO₂) it emits so abundantly may be within reach, thanks to new substances that would sharply lower the cost of capturing carbon from power plant exhaust. But the technology's moment may have passed, as low natural gas prices in the United States make new coal-fired power plants uneconomical and the administration of President-elect Donald Trump dismisses the threat of climate change.

By 2025, so-called "third-generation" materials, some of which were detailed earlier this month at a meeting of the Materials Research Society in Boston, should bring the cost of filtering out CO₂ from today's \$100 per ton to \$20 per ton, according to officials at the U.S. Department of Energy (DOE). That would put carbon capture and sequestration (CCS) within striking distance of being economically feasible under several tax credit plans being considered by the U.S. Congress. "I think we're going to get there," says Lynn Brickett, who heads the carbon capture technology program at DOE's National Energy Technology Laboratory in Pittsburgh, Pennsylvania.

Yet the political landscape is shifting. Trump has said he wants to pull out of last year's Paris climate deal, which commits nations to reducing CO₂ emissions through measures like CCS. And

although he talks about bringing coal back, his stated support for fracking and oil and gas exploration on public lands could help keep natural gas prices low and doom any coal renaissance. "It's hard to know where this is going to go," says James Van Nostrand, an energy policy expert at West Virginia University in Morgantown.

First-generation carbon capture materials are already being tested widely at coal power plants around the globe, but they are expensive to use. Most are alkaline substances called amines, dissolved into water to prevent them from becoming gooey when they absorb CO₂. When exhaust bubbles through the liquid, the acidic CO₂ molecules latch onto the amines. The liquid is piped to another chamber and heated to between 120°C and 150°C to release the captured CO₂, which is pressurized and piped underground; the amines can then be reused. The pumping and heating steal up to 30% of the energy produced by a coal-fired power plant, reduc-

ing its efficiency and raising its electricity price. Second-generation facilities capture and reuse waste heat, among other things, but their costs are still too high, Brickett says.

Third-generation materials are much more efficient. Take, for instance, the pale yellow, organic liquids being developed by Phillip Koech, a chemist at the Pacific Northwest National Laboratory (PNNL) in Richland, Washington. They still rely on amines to suck out the CO₂, but the amines are dissolved at much higher concentrations in a water-free liquid—eliminating the need to heat that part of the brew. Koech says that one such compound, abbreviated 2-EAMP, gives up its CO₂ at 60°C. That means a plant's waste heat could provide almost enough warmth, potentially cutting the energy penalty of carbon capture in half from 30% to 15%. Like other amines, the PNNL material evaporates over time, Koech says. Once his team solves this issue, he hopes DOE will test it in a pilot-scale facility.

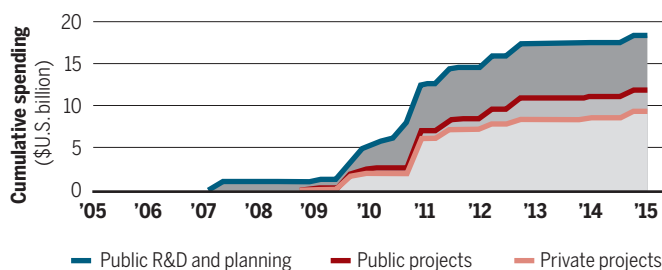
Other third-generation approaches do away with liquids altogether. For example, solid powders, made of porous materials called metal organic frameworks (MOFs), would capture CO₂ from flue gas and, like amines, let it go with added heat. But because MOFs contain no liquid, less heat is needed. An alternative requires no heat at all: polymer membranes that contain MOFs or other porous solid particles. They allow CO₂ to pass through while blocking other exhaust gases, such as nitrogen oxides and oxygen.

It's not yet clear how to push flue exhaust through a silo packed with MOF powders, or whether small research-scale membranes can be scaled up to work in a power plant. "This is an engineering problem now," says Tom McDonald, the CEO of Mosaic Materials, a company based in Berkeley, California, that is trying to turn powdery MOF CO₂ absorbers into a viable technology.

Bills pending in Congress could provide incentives to overcome such obstacles. Companies can currently receive tax credits of \$10 per ton of CO₂ pumped underground into depleted oil fields to force out additional oil. They receive \$20 per ton if that CO₂ is injected into deep saline aquifers, a more permanent form of sequestration. Those tax credits are capped at \$75 million, and companies have already claimed about 60% of the pot. This summer, companion bills were introduced in the

Global slowdown

A sharp injection of public and private money into carbon capture and sequestration projects and R&D that began early this decade has since plateaued.



U.S. House of Representatives and Senate to lift the caps and boost the tax credits for both types of injection to \$35 and \$50 per ton of CO₂, respectively. “That’s getting close to the point where it would make CCS cost effective, and develop a market,” says Howard Herzog, a chemical engineer and carbon capture specialist at the Massachusetts Institute of Technology in Cambridge.

Last week, despite lobbying efforts, Congress failed to include the new CCS tax credits in an end-of-the-year spending bill. Proponents hope to add them to a tax reform measure early next year.

The CCS tax credit extension was launched against the backdrop of President Barack Obama’s Clean Power Plan (CPP)—a key component of the U.S. commitment to the Paris climate deal. The CPP ramps up restrictions on CO₂ emissions and could force CCS retrofits on existing coal plants. That encouraged broad bipartisan support for beefing up the tax credits, which would then make coal with CCS more affordable.

But besides vowing to “cancel” the Paris agreement, Trump last week named Scott Pruitt, Oklahoma’s attorney general, to head the Environmental Protection Agency (EPA)—even though Pruitt is leading the efforts to sue EPA over the CPP. Van Nostrand thinks the plan “for all practical purposes is dead.” If so, pressure to retrofit existing coal plants with CCS technologies would disappear, says Michael Webber, deputy director of the Energy Institute at the University of Texas in Austin. At the same time, Webber adds, new coal plants will remain scarce, because of low U.S. natural gas prices.

Even if CCS efforts sputter in the United States, they will play an important role internationally, as long as other countries work to keep their commitments under the Paris agreement. Today there are 15 large-scale CCS projects in operation with the capacity to capture up to 28 million metric tons of CO₂ per year. This needs to increase to 6 billion metric tons per year by 2050 if the world is to adhere to the Paris goals of keeping temperature rises below 2°C, according to the International Energy Agency (IEA), because many developing countries’ reliance on coal-fired power is still growing. Yet, an IEA report released last month warns of a meager pipeline of CCS projects. “The current pace of CCS deployments is out of step with the Paris ambitions,” the IEA report concludes.

If the climate agreement holds, pressure will continue to mount on countries to implement CCS, Van Nostrand says. The new technologies will ease the way. “In order for coal to have a future you have to have a breakthrough in CCS,” he says. ■

INFECTIOUS DISEASE

New bird flu strain brings death and questions

H5N8 is killing birds around Europe and the Middle East but appears harmless to humans

By Kai Kupferschmidt

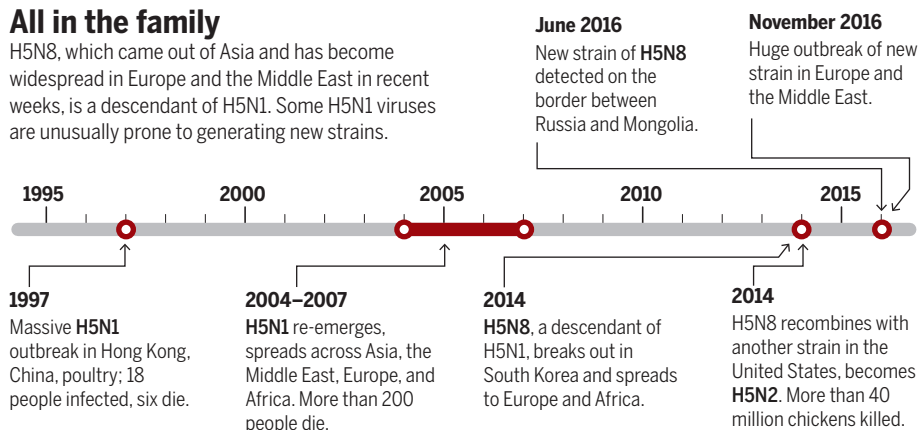
In Germany, the ducks started dying in November. Workers wearing face masks and rubber gloves collected dozens of Eurasian coots, tufted ducks, and other species along the shoreline of Lake Constance in the country’s south. Soon, reports of dead birds began emerging from elsewhere in Europe, and then from North Africa and the Middle East. Chickens and other domesticated birds also fell ill; hundreds of thousands have been culled to halt the epidemic. Its cause: the latest

terdam, the Netherlands. “A few decades ago, domestic birds were free of influenza virus except for occasional epidemics.”

This is the second time H5N8 has spread far and wide. In 2014, migrating birds carried the virus from the Korean peninsula north to Russia, then west to Europe, and east to North America. But this year, the virus has spread farther and faster into Europe and Africa than it did 2 years ago. And compared with its predecessor, Kuiken says, “this virus is more pathogenic for more wild bird species.” The Eurasian wigeon, for instance, a common duck spe-

All in the family

H5N8, which came out of Asia and has become widespread in Europe and the Middle East in recent weeks, is a descendant of H5N1. Some H5N1 viruses are unusually prone to generating new strains.

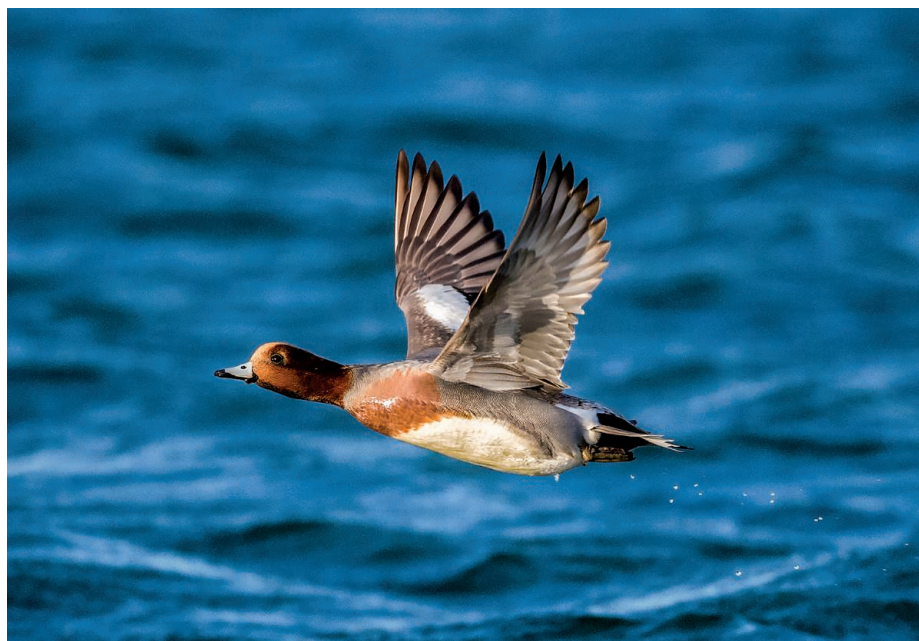


deadly avian influenza virus, H5N8, which researchers had also reported from Russia in the summer.

H5N8, a distant descendant of the H5N1 virus that devastated flocks across much of the world and killed hundreds of people more than a decade ago, is another testament to the flu virus’s unending ability to shift shapes and traits. The good news is that so far, H5N8 does not seem to infect humans. But its rapid spread and increasing deadliness to birds have mystified experts. And it underscores that avian influenza, once an occasional crisis, is now endemic in the burgeoning flocks of Asia, from which it periodically spreads in migrating birds. “This is really a new situation,” says Thijs Kuiken, a pathologist at Erasmus University Medical Center in Rot-

terdam, the Netherlands. “A few decades ago, domestic birds were free of influenza virus except for occasional epidemics.”

The increased lethality makes the virus’s rapid spread a puzzle. The new H5N8 counts as highly pathogenic avian influenza. Yet viruses that use migratory animals to spread are generally less pathogenic; after all, they’re not going anywhere if their host isn’t healthy enough to travel. “You would expect H5N8 to have a phenotype like LPAI [low pathogenic avian influenza] in wild birds to be able to spread so well,” Kuiken says. At the moment, scientists can only speculate about the unusual pattern, Kuiken says. One possibility might be that the virus is more benign during



The Eurasian wigeon is one of many bird species stricken by the H5N8 influenza virus.

its long-haul travel, then becomes highly pathogenic as soon as it arrives in a dense bird population, he says.

The virus's distant progenitor, H5N1, burst onto the global stage during a massive poultry outbreak in Hong Kong, China, in 1997. Eighteen people were also infected, and six died. More H5N1 outbreaks struck Asia in 2003 and 2004, and the virus later spread to Europe and Africa, triggering worries that it might unleash a human pandemic. That didn't happen, but by now more than 400 people have died from H5N1 after coming into contact with infected birds.

One particular group of H5N1 viruses, dubbed clade 2.2.3.4, has an uncanny ability to change its makeup by swapping the gene for an important surface protein called neuraminidase (the "N" in strain names like H5N1) with that of another flu virus. Those exchanges spawned H5N8 as well as other viruses. When H5N8 spread to the United States in 2014, it quickly morphed into H5N2 and caused an outbreak in which more than 40 million birds were killed.

"We suspect that it is something virologic that allows this virus to be a bit more promiscuous in terms of its neuraminidase," says influenza virologist Richard Webby of St. Jude Children's Research Hospital in Memphis, Tennessee. Webby is waiting for permits to import samples so that he can try to start answering this and other questions about H5N8 in the lab.

Reassuringly, the current H5N8 strain does not seem to affect mammals, according to scientists at the Friedrich Loeffler Institute on the island of Riems in Germany who have tried to infect mice and ferrets. Still, Webby cautions that small changes in the genome can have big consequences in flu. "It could be one or two amino acids away from changing that behavior."

Even if the current outbreak is beaten back, avian influenza is unlikely to just disappear. Poultry production in Asia and parts of Africa has increased dramatically in recent years, and influenza viruses have become permanently established in some stocks, Kuiken says. The next threat may be H5N6, which can sicken humans and is already widespread in poultry in China, according to a recent paper in *Cell Host & Microbe*. In that study, researchers sampled live poultry markets and poultry farms in 39 Chinese cities and found that H5N6 has become the dominant subtype in some places.

Wherever domestic and wild birds interact—for instance, when domestic ducks graze on rice paddy fields—H5N6 and others have many opportunities to jump hosts and start on a worldwide trek. "Because the poultry production is only going to be increasing in the coming years, we may expect that spillover of avian influenza from poultry to wild birds is going to happen more often," Kuiken says. "This isn't going to stop anytime soon." ■

"This virus is more pathogenic for more wild bird species."

Thijs Kuiken, Erasmus University Medical Center

CLIMATE POLICY

Trump team targets key climate metric

"Social cost of carbon" to get a critical look from incoming administration

By David Malakoff, Robert F. Service, and Warren Cornwall

President-elect Donald Trump has made no secret of his intention to dramatically reshape U.S. climate and energy policy. He has said he intends to name staunch allies of the fossil fuel industry to lead the Environmental Protection Agency and the state and energy departments, and promised to walk away from international climate agreements. And last week a provocative leaked memo hinted at another likely element of the incoming administration's plan for weakening climate regulations: tweaking an obscure but increasingly utilized economic measure that tallies the costs and benefits of controlling carbon pollution.

The memo, which included 74 questions from Trump's Department of Energy (DOE) transition team to agency officials, caused a stir because it asked for the names of agency employees involved in developing climate policy. The transition team was silent on why it asked for the names, and DOE officials ultimately refused to provide them. But the move spurred fears that the new administration would seek to fire or punish those employees, and it drew condemnation from science advocacy groups and some lawmakers in Congress. "It harkens back to an era when politicians sought out individuals for partisan politics with little basis of any wrongdoing," said Representative Bill Foster (D-IL), a physicist who spent 22 years at DOE's Fermi National Accelerator Laboratory in Batavia, Illinois. "These Cold War-era tactics threaten to undo the decades of progress we have made on climate change and to dissuade a new generation of scientists from tackling our world's biggest problems."

Many of the other questions have a technical flavor, asking about DOE's role in developing the nitty-gritty statistical and economic data that often underpin regulatory efforts. One set of inquiries, for ex-



President-elect Donald Trump has promised to aid the coal and other fossil fuel industries, in part by rolling back climate regulations.

ample, focuses on an economic measure called the social cost of carbon (SCC), which attempts to quantify the economic damage associated with carbon emissions and the climate change they drive. It is meant to tally the cost of impacts such as coastal erosion, reduced harvests, and increased disease, and it provides crucial guidance about how much society should pay now to avoid future damage from carbon emissions. As economist Michael Greenstone of the University of Chicago in Illinois, who served as a senior economic official in the Obama administration, puts it, “If you want to be hostile to climate regulations, the SCC is kind of a pivot joint.”

As a result of a 2008 court case, federal agencies typically consider the SCC in analyzing the costs and benefits of new regulations. And although the SCC alone doesn't determine whether a new rule moves forward, the measure has played a role in developing some 100 new regulations. They address issues including vehicle fuel efficiency, pollution from coal-fired power plants, and energy efficiency standards for home appliances. The SCC “has become increasingly important in the federal regulatory arena because carbon emissions are pervasive throughout the economy,” says Richard Newell, president of Resources for the Future, a think tank in Washington, D.C., and the co-chair of a panel at the National Academies of Sciences, Engineering, and Medicine that will soon issue a report on the measure.

That report is likely to confirm that calculating the SCC, which melds projections about likely impacts of climate change with economic assumptions, isn't easy. Govern-

ment and academic scholars have debated the best methods for years, and researchers have developed three major computer models dedicated to the task. In 2010, a working group assembled by President Barack Obama's administration recommended that agencies set the SCC at \$21 per ton of carbon, and in 2013 the administration boosted the number to \$36 per ton, citing increasingly dire predictions about the global impacts of climate change.

Not surprisingly, opponents of regulation have accused the Obama administration of manipulating SCC values to justify costly new rules. For example, critics have panned the administration's estimate that its Clean Power Plan to reduce power plant pollution would produce climate benefits of up to \$29 billion in 2030, compared with costs of just \$8.4 billion. One of the leading SCC skeptics—Thomas Pyle, president of the Institute for Energy Research, an industry-affiliated think tank in Washington, D.C.—is leading the DOE transition team that asked questions about how the measure is developed and used. Shortly before being named to that post, Pyle predicted in a statement that, under Trump, “the SCC will likely be reviewed and the latest science brought to bear. If the SCC were subjected to the latest science, it would certainly be much lower than what the Obama administration has been using.”

There are at least two major ways a new administration could tweak the SCC to produce lower values, analysts say. One is to change the discount rate—a value, expressed as a percent, that attempts to quantify what society would spend today to avoid damage in the future. “The discount rate is

the most important question,” but it is also “extremely controversial,” says William Nordhaus, an economist at Yale University, who has written extensively about the SCC. Currently, the Obama administration asks agencies to calculate the SCC using a range of discount rates, from 2.5% to 5%, and it has tended to rely on the lower rates, which produce higher SCC values. For example, in 2020 the SCC is \$62 per ton at a 2.5% rate, but \$12 per ton at 5%. So moving to a higher rate makes rules appear less beneficial.

Another is to change the geographic scope of the calculation. Currently, the Obama administration takes into account the potential global benefits of any new regulation, not just the benefits within the United States. It says that's because climate change is a global problem. But some economists question that approach, arguing it overstates the benefits. An effort to narrow the scope of the SCC could fit in with Trump's nationalistic leanings, notes Ted Gayer, an economist at the Brookings Institution in Washington, D.C., who has been critical of the global approach. “If you put it in the perspective of the Trump campaign and ‘America first,’ it makes sense,” Gayer says.

Although a Trump administration could tweak the SCC, it is unlikely to be able to completely eliminate it, Greenstone says. “This is not the first time people have come hunting for the social cost of carbon,” he says. Industry groups have challenged it in court, but judges have tended to find the concept sound. “For reasons of law and science, it looks like a very bumpy, windy road to me to greatly reduce the social cost of carbon.” ■



SOME LIKE IT HOT

Iran's Lut Desert—Earth's hottest—is devoid of plants but somehow sustains a vibrant ecosystem

By **Richard Stone**; Photography by **Bahman Izadi**

During the 1920s and 1930s, Viennese physician and adventurer Alfons Gabriel fell under the spell of Iran's Lut Desert. Gabriel had crisscrossed arid parts of the Middle East, Pakistan, and Afghanistan by camel, observing and mapping areas into which few dared venture—lands with names such as Dasht-i-Naumid (the Desert without Hope) and Dasht-i-Margo (the Desert of Death). But a “confused mass of impassable tangled dunes” stymied his efforts to probe the interior of the Lut Desert, a tract of sand and fantastical rock formations in southeastern Iran that was said to be the hottest place on Earth.

In March 1937, Gabriel finally conquered the central Lut—and barely made it out alive. He described his experiences a year later in a spellbinding talk to the Royal Geographical

Society in London. Late one afternoon, Gabriel recounted, “the landscape darkened under red clouds ... and a noise like the roaring of the sea began.” The dust storm raged into the night. “For several anxious hours we lay, motionless and helpless, outstretched on the ground.” Later, the voyagers were disoriented by mirages that were most vivid when the air was coolest, just before sunrise. Near the end of the 3-week journey, even their parched camels had had enough: “Their legs trembled; they panted, knelt down, and sometimes crept along on their knees.”

The allure of the Lut persists. Last month, a convoy of five SUVs carried 10 researchers and their guides, along with cameras, instruments, and hundreds of liters of water and fuel, into the heart of the desert. These modern explorers from Iran, the United States, and Europe were drawn not so much by the exotic landscape as by the puzzle of its un-

usual ecosystem. Many researchers had assumed that the Lut Desert is too hostile to sustain life, says Hossein Akhane, a plant biologist at the University of Tehran. The interior of the desert, an area nearly as big as West Virginia, is mostly devoid of plant life. But adventurers and the occasional scientist who traveled into the Lut had spotted diverse animal life, including insects, reptiles, and desert foxes. How that food web holds together without plants has been a mystery.

A morbid, and possibly unique, phenomenon may be the answer. Dead birds are a frequent sighting in the desert. A few years ago, scientists in Iran began wondering whether migratory birds stray into the Lut and, overcome by the intense heat, fall from the sky like manna, forming the base of a food web. The expedition, organized by Akhane and Bahman Izadi, head of an environmental nonprofit in Shiraz, Iran, and a Lut explorer,

The Lut Desert's fantastical landscape harbors creatures that eke out a living from hidden water and the occasional windfall.



set out to test the idea. Colleagues warned that in the fall, right after the heat of summer, the team might not find enough living things to tell. Creatures that burrowed or migrated to escape the heat would not have had time to venture back into the desert.

Instead, the team confirmed the existence of a vibrant ecosystem and saw compelling signs that migratory birds do help nourish it. They also found that the bone-dry landscape conceals what they are calling a “hidden sea”: a surprisingly shallow layer of salty groundwater that may also help sustain life.

The Lut Desert also offers a less uplifting lesson—at least for people living on the knife edge of sustainability in arid regions. Climate change models predict that as temperatures rise, tracts of the Middle East that are naturally uninhabitable—not survivable without air conditioning—will expand. Those areas may come to resemble the transition zone between settlements on the Lut’s edges and its supremely hostile core.

AFTER GABRIEL'S PIONEERING VENTURE, the scientific literature on the Lut Desert remained sparse. One point was settled, though: Gabriel had noted that a contemporary, the German geographer Gustav Stratil-Sauer, “was of the opinion that the hottest region of the earth was not, as hitherto supposed, to be found in Sind, or Abyssinia, or in the Death Valley of California, but in the southern Lut.” In 2005, an infrared radiometer on NASA’s Aqua satellite measured a ground temperature of 70.7°C (159.3°F) at one spot in the Lut—the hottest satellite

reading of ground temperature ever. And in April 2014, Morteza Djamali, a paleoecologist at the Mediterranean Institute of Marine and Terrestrial Biodiversity and Ecology in Marseille, France, and his colleagues ventured into the central Lut to install a temperature logger at the same spot. In an experience worthy of Alfred Hitchcock, a swarm of locusts descended, picking nearby bird carcasses clean, cannibalizing each other, and biting the researchers. “I can imagine that a lonely traveler could be killed by these small creatures” in a few days, Djamali says.

The hardship paid off, Djamali says. In July, the thermometer, planted 30 centimeters above the surface in the shade of a wooden cylinder, registered 61°C—some 5°C higher than the official shade record

set in Death Valley in 1913. Bands of heat-absorbing black sand, primarily magnetite, together with topography that limits air movement help explain the blazing temperatures, Djamali says.

That same year Akhani paid his first visit to the Lut, a quick scouting trip. A specialist in salt-loving plants, which grow in salty seeps in a few spots in the desert, he also had noticed the birds’ carcasses and wondered what role they might play in the ecosystem. Cobbling together backing from the Iranian National Science Foundation, the Saeedi Institute for Advanced Studies at Kashan University in Iran, and other sources, he assembled a team of specialists from Iran and abroad that will spend the next 5 years prizing scientific secrets from the desert.

Empty quarter

Few scientists had probed the heart of the Lut Desert.



THE TEAM SET OFF LAST MONTH on its maiden expedition, departing from Shahdad, an oasis on the Lut’s western edge, and heading

due north before arcing south in a path that bisected the desert (see map, left). In some areas, yardangs, wind-sculpted rock formations several meters tall, sprouted from the desert like mushrooms.

Heftier formations called kaluts reminded Akhani of “the ruins of an old city.” Relics of what Djamali calls a “complex geoclimatic history,” some are made of sandstone, whereas others were eroded from the beds of saline and playa lakes that dotted the landscape some 10 million years ago. The topography, whimsical or majestic, is a major reason

the United Nations Educational, Scientific and Cultural Organization inscribed the Lut Desert on its World Heritage List last July. (Iran hopes it will beckon intrepid ecotourists.) Along their 700-kilometer journey, the researchers sampled soil and biota at 37 sites before emerging from the desert east of Bam, a city that suffered catastrophic damage from a 2003 earthquake.

One day, the team struck out on foot into a canyon called Zabone Mar, which means “snake’s tongue.” By satellite, the canyon,

ran, collected carcasses of several migratory species. Why the birds make a fatal detour into the desert is a puzzle, he says. Even outside the canyon dead migratory birds were plentiful, and they often bore signs of having been scavenged by foxes. “I think that’s their main food source,” AghaKouchak says.

Insects, too, are critical to the Lut’s food web. Many nibble on plants on the desert’s periphery and are in turn eaten by spiders, reptiles, and foxes in the Lut’s interior, supplementing the nutrients in the ill-fated birds, says expedition member Hossein

so dry that microwaves were radiating from deeper layers of soil or even rocks, falsely indicating shallow moisture.

Last month, in the heart of the desert, the team’s convoy entered “a flat landscape, as far as you can see,” the hydrologist says. A short distance onto the plain, one of the trucks broke through several centimeters of hard, crusty soil and sank, up to its axles—in mud. After another SUV pulled out the stricken vehicle, “you could actually see water” where the tires had been. “It was hard to believe,” AghaKouchak says, “but the area is really, really wet.”

He thinks the moisture comes from distant mountains that ring the table-flat playa. Occasional rainfalls in the spring and early fall drain into the flat basin, he says. According to the team’s guides, other areas of the Lut have similar features. Back at UC Irvine, AghaKouchak will attempt to correlate the local knowledge with satellite moisture data to map the extent of the hidden sea.

NO ONE LIVES in the heart of the Lut, and after a 6-year-long drought in Iran, settlements on the desert’s fringes are in retreat. That may foreshadow the fate of other parts of the Middle East as global warming pushes summer temperatures still higher, says Elfatih Eltahir, an environmental engineer at the Massachusetts Institute of Technology in Cambridge.

Last year, in *Nature Climate Change*, Eltahir and a colleague defined a naturally uninhabitable climate as one in which the heat index—temperature adjusted for humidity—exceeds 35°C for more than six straight hours. “What we are talking about are really extreme conditions,” Eltahir says. “If a human being is exposed to that, very likely that person would die.”

In summer, areas of the Persian Gulf already exceed that threshold and would be unbearable without air-conditioning. Barring “significant mitigation,” the uninhabitable areas near the Persian Gulf are likely to expand, including arid but still habitable regions of Iran. “Lut would be a good lab to study what an extreme environment would look like,” AghaKouchak says.

To probe such questions more deeply, Akhiani’s team plans to return in the spring. Among other things, they will bring more sophisticated instruments for measuring soil moisture and set up camera traps to study the ecology of the desert fox and other creatures in more detail. They also hope to decipher at a molecular level how the life forms adapt to broiling heat, Akhiani says. In 2018, they may even attempt a summer expedition.

“If we go then, we probably need to bring a physician,” says AghaKouchak, who has- tens to add, “I can’t wait to go back.” ■



The remains of birds that blundered into the desert (top) apparently help support an ecosystem of animals including Rüppell’s foxes (bottom left) and geckos (bottom right), along with numerous insects.

about 15 meters wide with walls reaching 30 meters high, looks like a bifurcated tongue. “I noticed a weird noise,” recalls expedition member Amir AghaKouchak, a hydrologist at the University of California (UC), Irvine. A continuous, soft crackling emanated from the walls. He speculates that the sound was the rock expanding as temperatures soared from nightly lows near 0°C up to fall daily maximums of about 40°C. “I just stopped and listened to this beautiful music.”

Or perhaps it was a siren call: The canyon is a death trap. Within its walls, the researchers found the remains of dozens of migratory birds. The birds may have sought shelter in the canyon’s shade, but without water they would have quickly perished, AghaKouchak says. Mahmoud Ghasempouri, an ornithologist at Tarbiat Modares University in Teh-

Rajaei, curator of Lepidoptera—moths and butterflies—at the Stuttgart State Museum of Natural History in Germany. Yet some live in the heart of the desert. When Rajaei set up light traps at night, he was surprised to count large numbers of moth species. “What do they do there? What do they eat there?” he asks. How the fly larvae he found in a pool of hypersaline water survive is another enigma, he says. And so is the question of how the Lut’s denizens stay hydrated.

The answer may lie just below the surface. Before the expedition began, AghaKouchak had scrutinized satellite sensor data from the Lut. To his surprise, microwaves emanating from the ground suggested that in some parts of the oven-hot desert, the soil is moist. Perplexed, AghaKouchak consulted a colleague, who proposed that the Lut’s soil is



Celia García Velázquez has spent 5 years searching for her son Alfredo, who disappeared in Veracruz state. She has helped excavate the largest clandestine grave found in Mexico.

AFTER THE VANISHING

Savvy anthropologists mix science and legal skills to help the families of Mexico's disappeared

By **Lizzie Wade**, in Veracruz, Mexico; Photography by **Félix Márquez**

On 18 July 2011, Celia García Velázquez's son Alfredo disappeared. The 33-year-old lived in a town called Chiconquiaco in the Mexican state of Veracruz, and at the time of his disappearance he was running for president of his municipality against a candidate supported by the country's most powerful political party. "Everybody knew him," says García Velázquez, a stout woman with hair the color of a lion's mane and a blast of bright pink lipstick. One day Alfredo went to Xalapa, the capital of Veracruz state, to sort out the paperwork for a car he'd bought. Like so many young men in Veracruz these days—more than 700 since 2006—he never made it home.

"I need to know what happened," García Velázquez says to 15 people gathered in a classroom overlooking the courtyard of a church in this port city. Her voice breaking, she says, "How is it possible that someone can disappear like that, as if he never existed?"

The group nods. They, too, have family members who have disappeared. Many here are mothers looking for their sons. Others are searching for brothers or cousins; one woman seeks six loved ones. They are part of the Solecito collective, a group of more than 100 people searching for the disappeared. And they are getting help from a new source: forensic anthropologists.

Veracruz, like many states in Mexico, is experiencing an epidemic of disappearances.

Since the beginning of the drug war in 2006, more than 28,000 people have gone missing across the country, according to Mexico's National Registry of Missing or Disappeared Persons. (That is likely an underestimate, as many disappearances go unreported because families fear retaliation.) Some are kidnapped by drug cartels and either killed or forced into labor or human trafficking. Human Rights Watch, a nonprofit based in New York City, says that many others are abducted by the police and military, and that the government does little to investigate. The 15 people in the classroom this weekend have come for help searching for their disappeared.

At the front of the classroom is anthropologist Roxana Enríquez Farias, who in 2013

founded a nonprofit organization called the Mexican Forensic Anthropology Team (EMAF) based in Mexico City. EMAF anthropologists often serve as expert witnesses, evaluating state investigations of disappearances. But on this November weekend, Enríquez Farias is explaining to the families themselves the steps of a search for the disappeared, and how to use their amateur searches to pressure the authorities into action. “We want to build the base [of knowledge] that will support their right to truth and justice,” Enríquez Farias explains.

“Until a few years ago, we scientists didn’t think about the families [of victims],” says Lorena Valencia Caballero, a forensic anthropologist at the National Autonomous University of Mexico in Mexico City who is not part of the group. But as the disappearances

ON MOTHER’S DAY THIS YEAR, Solecito organized a rally to bring attention to the disappearances and protest government inaction. As the group listened to a prayer, young men moved into the crowd and discreetly slipped folded papers to several Solecito members. They were photocopies of a hand-drawn map of a Veracruz neighborhood called Colinas de Santa Fe, with crudely drawn directions to an empty field. There, someone had drawn a cluster of crosses labeled *cuerpos*—“bodies.”

The members of Solecito weren’t sure what to do with the information. Where had it come from? What could grieving civilians do about a potential mass grave? After weeks of deliberation, they decided to start digging. So they contacted Enríquez Farias.

Enríquez Farias had come face-to-face

remove the layers of earth deposited over a grave, how physical anthropologists measure bones to determine the gender of a skeleton, and which family members can provide the most useful samples for DNA identifications.

But she steered clear of giving the searchers explicit instructions. “We don’t teach them techniques. We teach fundamentals,” she says. Once families understand the principles, “they can evaluate the techniques,” including those they see the police using, and judge whether evidence is being lost.

That approach wins approval from forensic bioarchaeologist Derek Congram of the University of Toronto in Canada. Trying to turn families into practicing scientists overnight would be impossible as well as “irresponsible,” he says.

In August, Solecito began to dig, under the watchful eye of the local police and prosecutor’s office. “We use rudimentary methods, but they’re effective,” says Lucy Díaz, one of Solecito’s founders. Searchers look for places where the earth has a different texture or color than the surrounding ground, or where plants have been cleared. Then they plunge a 2-meter-long metal rod into the earth, bring it up, and sniff the tip for the stench of decomposition. If they smell death, they dig.

Since August, the group has uncovered 107 graves, containing 124 skulls and myriad other remains, all in the area indicated by the map. It is the largest mass grave discovered in Mexico so far. “It’s not a clandestine grave. It’s a clandestine cemetery,” Díaz said at a scientific meeting in October. The graves, she says, are at least 1.6 meters deep, and most of the bodies are buried in garbage bags. The majority are men, many still blindfolded. A few show gunshot wounds.

Such burials are sensitive because state agents might have been involved in some disappearances. Human Rights Watch documented 249 disappearances between 2007 and 2013, and found that the Mexican police or military were involved in 149 of them.

But Solecito’s initiative spurred the government to send forensic investigators from Mexico’s federal police force, known as the Scientific Police, to the cemetery. Solecito locates the bodies, but once a grave is found, the investigators document everything in and around it—clothing, bandages, and even the occasional work identification card, Díaz says—and remove the remains for lab analysis.

It’s slow going: So far, 52 of 107 graves have been fully processed. Solecito expects an update from the Scientific Police in January 2017, perhaps including the first identifications. (The National Security Commission, which oversees the Scientific Police, did not respond to interview requests.)



Workshop attendees piece together a puzzle outlining the steps of a forensic investigation.

mounted into a humanitarian crisis, EMAF’s work became “exceedingly necessary,” she says. “It now falls to anthropologists to help the families understand how we determine age, what are the stage[s] of decomposition, how do organized crime groups behave—a thousand things they should never have had to learn.”

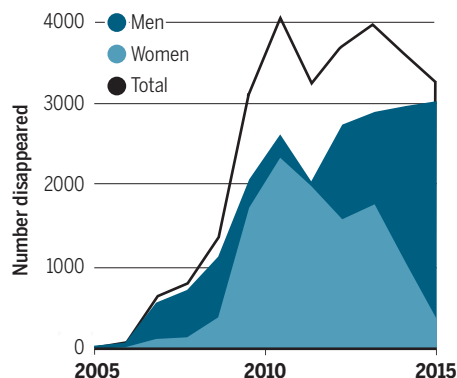
“It’s a brilliant strategy” when authorities are not sensitive to families’ needs, says forensic anthropologist Nicholas Márquez-Grant of Cranfield University in the United Kingdom. When he met families of the disappeared in Mexico this fall, “I could see that many relatives were completely lost.” He hopes EMAF’s model can be replicated in other countries, such as Iraq, where families are left by the wayside in disappearance investigations.

with Mexico’s disappearance problem while working as a forensic archaeologist in the prosecutor’s office of Ciudad Juárez, the border city across the Rio Grande River from El Paso, Texas. From 2008 to 2012, when the city had the highest murder rate in the world, she excavated clandestine graves to help identify victims. She began to see how her scientific expertise could help bring justice to victims. That inspired her to found EMAF, which now employs seven scientists and two student volunteers and is funded by grants from international agencies.

Before Solecito went out to dig up graves this summer, Enríquez Farias came here and gave the group a workshop on forensic anthropology. “They were preparing themselves for what they would find,” she says. She explained how archaeologists examine and

Counting the missing

Disappearances in Mexico spiked after the drug war began in 2006, and have now reached about 28,000, although this official tally is likely an underestimate.



After searching for her son independently for 5 years, García Velázquez joined Solecito in August, when she heard about the cemetery. She hopes Alfredo isn't there, that he's still alive somewhere—perhaps held by his political rivals, or forced to work for a drug cartel. But she knows that even if her son isn't buried in Colinas de Santa Fe, someone else's son is. She helps excavate in the cemetery twice a week. "It's horrible. It hurts your heart," she says. But she believes that if she and other family members don't take action, the bodies will stay in the ground, lost and unidentified, forever.

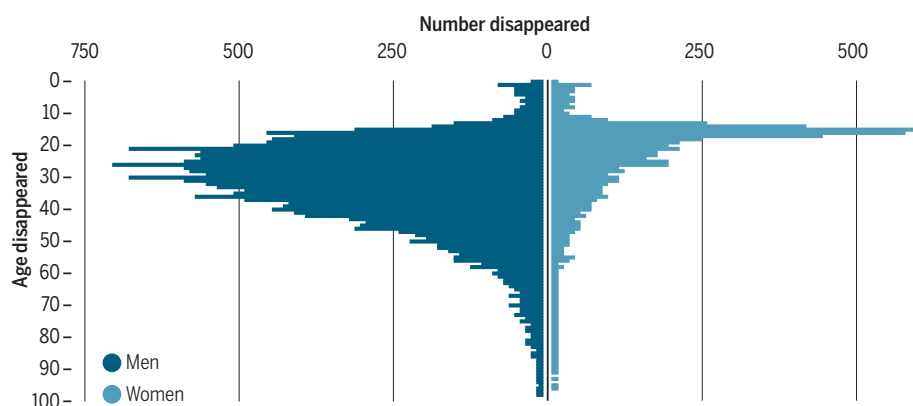
ENRÍQUEZ FARIAS ADMIRES the bravery of the searchers but worries their work won't result in justice. The problem, she says, is that local prosecutors aren't doing the basic investigation of cases that could lead to hypotheses about who is likely to be buried at Colinas de Santa Fe. That means authorities can't efficiently compare DNA from the remains to probable family members, or even use basic investigative strategies like matching the clothes a missing person was last seen wearing to clothes found in the cemetery. "The investigation isn't just going and looking for bodies. There are steps before that," Enríquez Farias says.

Congram sees a parallel in Spain, where families in recent years have pushed investigators like him to search for loved ones who disappeared during the country's civil war in the 1930s. "There was a rush to go out and dig up bodies," he says, but it hasn't provided much closure. "A lot of bodies were coming up without background research being done." One site where he worked yielded more than 400 bodies, but so far, "not one of them is identified."

Everybody in the classroom that November day has notified prosecutors by filing missing person reports, sometimes against the wishes of other family members, who

Who vanishes

Teenage girls and young men are at the highest risk of disappearance. Some are killed and others are conscripted into forced labor and human trafficking.



fear becoming targets themselves. Most have also provided a description of the disappeared, plus a list of their friends. Some have given blood and hair samples for DNA analysis. But no one is sure what investigators did with that information, if anything.

So in this latest workshop, Enríquez Farias shows families how to pressure prosecutors to tackle their cases. She invites Ibeté Estrada Gazga, a lawyer with the Institute for Security and Democracy, a nonprofit in Mexico City, to the front. Prosecutors "have a constitutional obligation to investigate," Estrada Gazga explains. Families can check progress by requesting a copy of the prosecutor's case file, she tells the group. If the file shows that nothing has happened, a judge can order the prosecutor to return to the case.

Later, Enríquez Farias says she's surprised at the direction her work has taken. "At first we thought that just doing exhumations or DNA analyses would be enough." She sighs. "It's always so much more complicated." For example, in one of EMAF's cases in another state, they eventually won the

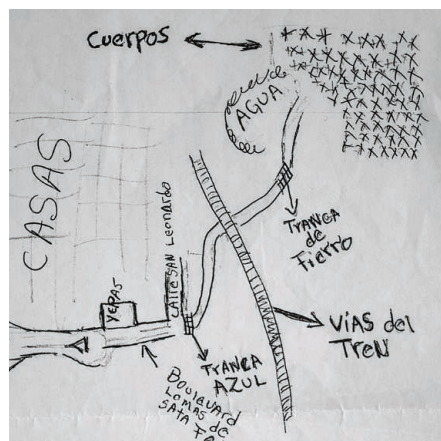
right to exhume a body to confirm a DNA identification. But the cemetery is in such disarray—one private grave held three extra bodies—that after three attempts, EMAF has yet to locate the body in question.

Then there are the legal issues: EMAF anthropologists don't excavate unofficially with Solecito, because their opinion might then be seen as biased and be discredited in a trial, Enríquez Farias says. "If the legal context doesn't exist, the anthropology goes down the drain," she says. Instead, families must request EMAF's services as expert witnesses. She hopes that together, families and EMAF can prod the state into investigating. "Our mission is to build a different kind of country."

Congram agrees that "families bringing up the dead can be a way of shaming the government to fulfill its obligations." But he thinks EMAF anthropologists could go into the field independently, as has happened in other countries. For example, a nonprofit foundation in Guatemala independently identified bodies of people who disappeared during the country's civil war. Its analyses ultimately were accepted in court.

As the workshop draws to a close, Liliana González, an anthropology student volunteering with EMAF, writes in big letters at the front of the classroom, "What is science?" People call out: "Chemistry!" "Physics!" "Anthropology!" And what are scientists looking for? "Knowledge!" That's right, Enríquez Farias says. "Science is a search for knowledge. But not just any knowledge. It has to be the truth."

García Velázquez leaves the church that weekend more determined than ever to discover her piece of that truth, starting with obtaining a copy of her case file. "The workshop was excellent," she says. The next time the state throws up an obstacle, "we'll remember what they taught us." And no matter what, she'll keep digging. ■



This hand-drawn map directed Solecito to the mass grave in Colinas de Santa Fe. They have uncovered more than 100 bodies since August.

POLICY FORUM

MARINE CONSERVATION

U.S. seafood import restriction presents opportunity and risk

Marine mammal protections require increased global capacity

By Rob Williams,^{1,2*} Matthew G. Burgess,^{3*} Erin Ashe,^{1,2} Steven D. Gaines,³ Randall R. Reeves⁴

On 1 January 2017, the U.S. National Oceanic and Atmospheric Administration (NOAA) will enact a new rule (1) requiring countries exporting seafood to the United States to demonstrate that their fisheries comply

with the U.S. Marine Mammal Protection Act (MMPA). The United States is the world's largest seafood importer (2); the MMPA is among the world's strongest marine mammal protection laws; and most of the world's ~125 marine mammal species are affected by fisheries bycatch (accidental entanglement in fishing gear) (3). This regulation could thus have significant conservation benefits, potentially spilling over to other areas of

marine governance, if it is accompanied by substantial investments to boost scientific and compliance capacity in developing countries. Otherwise, it risks having little effect besides inflicting economic hardship on already poor communities.

Bycatch is the greatest human threat to small cetaceans (4) and some populations of large whales (5). Bycatch played a major role in the recent extinction of the Yangtze River dolphin, or baiji (*Lipotes vexillifer*) (6), and there is high risk that it will soon cause the extinction of the vaquita (*Phocoena sinus*), a porpoise endemic to the northern Gulf of California (7). Marine mammals are entangled in many of the most common fishing gears, including gillnets, pelagic longlines, purse seines, pots, and traps (8).

The MMPA—adopted in 1972—prohibits intentionally harming marine mammals in



A California sea lion has drowned in a deep water drift net. A new regulation sets limits on marine mammal bycatch in U.S. fish imports similar to U.S. fisheries' limits.

U.S. fishing activities, and it requires bycatch to be kept within the limits of what marine mammal populations can sustain—known as “potential biological removal” (PBR) (9). To ensure accountability, the MMPA mandates periodic estimation of marine mammal population sizes (and uncertainty) to set PBR, monitoring of bycatch rates, and implementation of mitigation measures, such as gear modifications or fishery closures when PBR is exceeded. These requirements apply to U.S. fisheries both inside and outside national waters, except where superseded by an international fishery management treaty to which the United States is a party (1). The MMPA has resulted in dramatic improvements in the status of many marine mammal populations, including Eastern Tropical Pacific dolphins, harbor porpoises, and California sea lions (10).

The new regulation effective 1 January 2017 requires that any fishery or aquaculture enterprise exporting products to the United States meets standards equivalent in effectiveness to those the MMPA requires of U.S. fisheries, in terms of both monitoring and bycatch mitigation, in all waters where harvest occurs (1). Exporting countries must prove compliance for each exporting fishery not exempted by NOAA due to remote likelihood of marine mammal impacts (e.g., freshwater fisheries and most nonsalmon aquaculture) (1). Noncompliant products [including those from illegal, unreported, and unregulated (IUU) fishing] can neither be exported directly, nor reexported, to the United States, and NOAA reserves the right to require intermediary countries processing noncompliant products to certify the origins of similar compliant products to be

allowed to export these to the United States (1). Countries will be given a (maximum) 5-year grace period to achieve and document compliance before import restrictions come into force (1).

Although leveling the playing field for U.S. fishers is clearly part of the rationale (8), this new regulation could be a game-changer if it inspires widespread compliance. With over 120 countries exporting seafood to the United States (8) (table S1), it could expand the highest available standard of protection for marine mammals caught in commercial fisheries (including most large whales, many small cetaceans, and some pinnipeds). Although some of the most critically endangered marine mammals—found in coastal and estuarine waters of Africa, Asia, and Latin America—face their most serious threats from artisanal fisheries, which do not export (11), they too could benefit indirectly from improvements in marine mammal monitoring. Because many fisheries with high marine mammal bycatch are also overfishing their target stocks (11, 12), efforts to comply with the current rule could spill over into broader fishery reforms having ecological and economic benefits.

However, some countries may choose not to comply, and many developing countries may be unable to comply due to lack of monitoring and enforcement capacity (13). Widespread noncompliance would blunt any conservation benefits, and import bans could inflict significant economic hardship on some already poor countries.

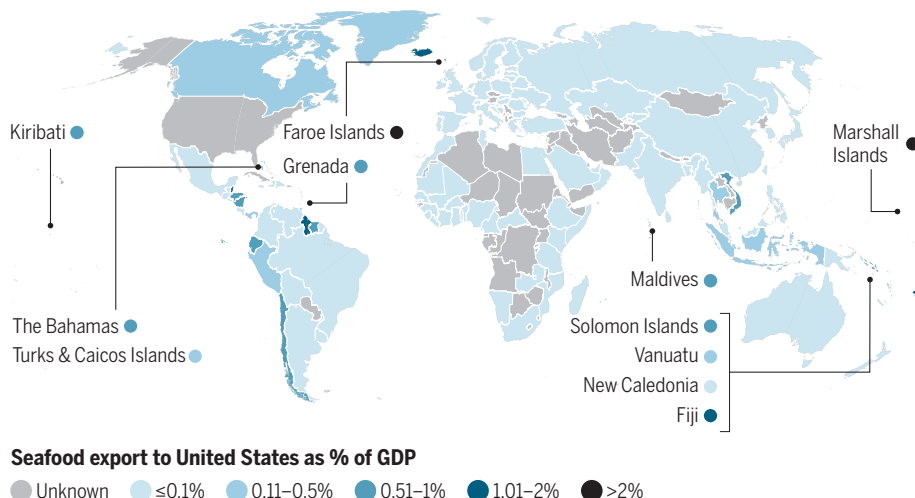
To reduce these risks, we urge the international community to support capacity-building efforts in the most economically vulnerable countries. We urge the U.S. government to promote rigorous compliance in larger, capacity-rich countries through collaborative diplomacy—an intent NOAA has signaled (1).

In gross economic terms, the largest seafood exporters to the United States are large countries in Asia (China, Indonesia, Vietnam, Thailand, and India) and Latin America (Chile, Ecuador, and Mexico) as well as Canada (table S1). These countries export many products (table S2), some of which NOAA deems likely to be exempt (e.g., tilapia and farmed shrimp), others not (e.g., lobster and tuna not caught in purse seines) (8).

How the new rule is applied to China and how China chooses to respond could be pivotal in many respects. China is the world's largest seafood producer (2), is likely the world's largest seafood re-exporter, and is the largest seafood exporter to the United States (8). Reforms in Chinese fisheries would thus have far-reaching benefits. Because China is also likely to be the largest alternate market

Annual seafood exports to the United States by country

Annual seafood exports (14), as a fraction of the country's annual GDP (15). Plants and algae, freshwater species, farmed products besides salmon, reptiles, and amphibians are excluded because of probable exemption (see table S2).



for products facing U.S. import bans, any certification requirements placed on its supply chain might indirectly increase compliance incentives for other countries.

The countries most economically dependent on seafood exports to the United States (see the figure) are small Latin American countries (e.g., Guyana, Belize, Ecuador, Honduras, Suriname, and Nicaragua), Small Island Developing States (SIDS) (e.g., Marshall Islands, Fiji, Kiribati, Maldives, Grenada, Bahamas, and Solomon Islands), and a few developed countries [Faroe Islands (of Denmark), Iceland, and Chile]. Seafood exports to the United States (excluding some clearly exempt categories, table S2) make up 0.5% or more of GDP in the 16 countries listed above (as much as 5 to 6% in the Marshall Islands and Faroe Islands) and in Vietnam (14, 15).

Most of these countries' U.S. exports are dominated by a small number of products (14) (table S2). Some of the products may be exempted [e.g., tuna from purse seines in the Pacific Islands (1)], but many seem likely to be affected [e.g., wild-caught shrimp from Guyana, tuna from Suriname and Grenada, cod from Iceland, and farmed salmon from the Faroe Islands and Chile (8)]. Bans on these exports could have severe economic impacts if comparable demands and prices are unavailable in other markets.

The small Latin American countries and most of the SIDS that would be potentially affected are relatively poor and likely to need rapid and substantial improvements in scientific and management capacity to be able to comply at U.S.-equivalent standards within the 5-year grace period (13). Efforts to comply will need to be driven from within the countries themselves, but history suggests that outside support and funding could increase the chances of success (16).

Compliance with the new import regulation requires capacity to monitor marine mammal abundance and bycatch rates, and to implement bycatch mitigation measures where necessary. Abundance monitoring is a significant gap—only ~5% of the ocean has been surveyed well enough to detect the presence of rare cetacean species or trends in common ones (17). Estimating marine mammal abundance throughout a country's Exclusive Economic Zone generally requires large, costly surveys (18). But regional coordination can exploit an economy of scale by allowing countries to share costs, ships, trained observers, analytical expertise, and data. Coordination also promotes regional planning and management. The Agreement on the Conservation of Small Cetaceans of the Baltic and North Seas (ASCOBANS) provides an example of such regional cooperation in monitoring that NOAA specifically cites as adequate for meeting the new import standards (1).

Bycatch mortality is best monitored by placing trained observers on a representative sample of boats, but there are also rapid assessment methods that estimate bycatch mortality rates roughly from interview surveys (19). If bycatch is found to be

exceeding allowable harm limits, mitigation workshops could allow stakeholders to design locally adapted strategies to reduce bycatch with minimal impact on fishing yield (20). Strategies can include changing the fishing timing, location, or gear, or the use of acoustic "pingers" to deter marine mammals from nets. IUU fishing remains a challenge, but emerging satellite technologies are rapidly expanding options to monitor and coordinate enforcement (21).

The international community can support each of these efforts through both funding and building scientific capacity. The United States will need to lead in providing such support. But other countries, foundations, and intergovernmental organizations may also be willing to help some of the small Latin American countries and SIDS, which face high economic stakes but have relatively few fisheries requiring reform. ■

REFERENCES AND NOTES

- National Oceanic and Atmospheric Administration (NOAA), *Fed. Regist.* **81**(157), 54390 (2016).
- Food and Agricultural Organization of the United Nations, "Fishery Commodities and Trade" (FAO, Rome, 2016); http://bit.ly/FAO_fishstat.
- R. R. Reeves, K. McClellan, T. B. Werner, *Endanger. Species Res.* **20**, 71 (2013).
- A. J. Read, *J. Mammal.* **89**, 541 (2008).
- P. O. Thomas, R. R. Reeves, R. L. Brownell, *Mar. Mamm. Sci.* **32**, 682 (2016).
- S. T. Turvey et al., *Biol. Lett.* **3**, 537 (2007).
- L. Rojas-Bracho, R. R. Reeves, *Endanger. Species Res.* **21**, 77 (2013).
- NOAA, Final Environmental Assessment, Regulatory Impact Review, and Final Regulatory Flexibility Analysis for a Proposed Rule to Implement Provisions of Section 101(a)(2)(A) of the Marine Mammal Protection Act for Imports of Fish and Fish Products (NOAA, 2016); <http://bit.ly/NOAAImportRule>.
- P. R. Wade, *Mar. Mamm. Sci.* **14**, 1 (1998).
- J. Roman et al., *Ann. N. Y. Acad. Sci.* **1286**, 29 (2013).
- R. L. Lewison et al., *Proc. Natl. Acad. Sci. U.S.A.* **111**, 5271 (2014).
- C. Costello et al., *Proc. Natl. Acad. Sci. U.S.A.* **113**, 5125 (2016).
- C. Mora et al., *PLOS Biol.* **7**, e1000131 (2009).
- National Marine Fishery Service, "Monthly trade data by product, country/association" (NMFS, 2016); <http://bit.ly/NMFS2f19>.
- World Bank, "World Development Indicators" (World Bank, 2016); <http://bit.ly/WBank2f0B>.
- M. C. Lemos, A. Agrawal, *Annu. Rev. Environ. Resour.* **31**, 297 (2006).
- K. Kaschner, N. J. Quick, R. Jewell, R. Williams, C. M. Harris, *PLOS ONE* **7**, e44075 (2012).
- P. S. Hammond et al., *Biol. Conserv.* **164**, 107 (2013).
- J. Moore et al., *Biol. Conserv.* **143**, 795 (2010).
- T. Werner, S. Kraus, A. Read, E. Zollett, *Mar. Technol. Soc. J.* **40**, 50 (2006).
- D. J. McCauley et al., *Science* **351**, 1148 (2016).

ACKNOWLEDGMENTS

R.W. thanks the Pew Fellows in Marine Conservation program for supporting his work. M.G.B. and S.D.G. acknowledge funding from the Waitt Foundation and the Ocean Conservancy. R.W., E.A., and R.R.R. thank Synchronicity Earth and the U.S. Marine Mammal Commission for supporting related work.

SUPPLEMENTARY MATERIALS

www.sciencemag.org/content/354/6318/1372/suppl/DC1

¹Oceans Initiative, Seattle, WA 98102, USA. ²Sea Mammal Research Unit, Scottish Oceans Institute, University of St. Andrews, St. Andrews KY16 8LB, Scotland UK. ³Sustainable Fisheries Group, Bren School of Environmental Science and Management, and Marine Science Institute, University of California, Santa Barbara, CA 93106, USA. ⁴Okapi Wildlife Associates, Hudson, Quebec J0P 1H0, Canada. *These authors contributed equally to this work. Email: rmcw@st-andrews.ac.uk

CLIMATE CHANGE

How high will the seas rise?

Coastal defense measures must be flexible in the face of rising sea level estimates

By **Michael Oppenheimer¹** and
Richard B. Alley²

Recent estimates suggest that global mean sea level rise could exceed 2 m by 2100. These projections are higher than previous ones and are based on the latest understanding of how the Antarctic Ice Sheet has behaved in the past and how sensitive it is to future climate change. They pose a challenge for scientists and policy-makers alike, requiring far-reaching decisions about coastal policies to be made based on rapidly evolving projections with large, persistent uncertainties. An effective approach to managing coastal risk should couple research priorities to policy needs, enabling judicious decision-making while focusing research on key questions.

In a recent study, DeConto and Pollard used a model that combines ice-fracture processes with inferences from paleoclimatic data to estimate the Antarctic contribution to global sea level rise by 2100. For a high emissions scenario, they found this contribution to be as high as 78 to 150 cm (mean value 114 cm) (1). For the same scenario, the Intergovernmental Panel on Climate Change (IPCC) Fifth Assessment Report (AR5) gave an Antarctic contribution of only –8 to +14 cm (mean value 4 cm) (2). Combining AR5 estimates for thermal expansion, mountain glaciers, the Greenland Ice Sheet, and land water storage with the Antarctic contribution from (1) yields a mean value of 184 cm for the total global sea level rise and an uncertainty range that extends above 2 m. Additional processes may increase or decrease local changes, but major coastal effects would occur almost everywhere (3).

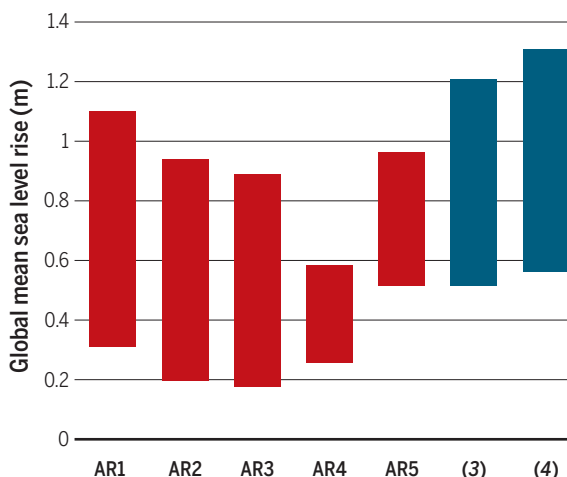
These and other scientific developments (1, 3, 4) are emerging too fast to be captured by the comprehensive IPCC assessments, which are published every 6 to 7 years. Policy-makers are left without a means to contextualize recent estimates, which remain

highly uncertain. Taking an engineering approach and defending against the highest projections available at a given time, plus a margin of error, can be prohibitively expensive. But ignoring such estimates could prove disastrous.

Furthermore, flood defenses take a lot of time and political will to implement. The construction of the Thames storm surge barrier and the ongoing strengthening of the Netherlands' sea defenses were both stimulated by a catastrophic 1953 storm in which more than 2000 people perished. Yet, the process

The fall and rise of projected sea level rises

Sea level projections from models for year 2100 have changed markedly since the IPCC published its First Assessment Report (AR1) in 1990. Recent projections (3, 4) are based on ice models and other approaches that may capture the ice sheet contribution better than in the past, but large uncertainties remain. For details see (15).



of political consensus building, planning, finance, and construction took almost 30 years before the Thames barrier was complete (5)—and that was fast compared with some large infrastructure projects. Waiting another few decades to decide on specific adaptations in the hope that scientific predictions will become firmer may put completion off until the last quarter of this century. At that time, actual sea level rise could be approaching 2 m, with a much larger rise still to come.

CHANGING ESTIMATES

In the early 1980s, U.S. EPA projected a sea level rise of 144 to 217 cm by 2100 (6). From the late 1980s to the late 1990s, developments in numerical modeling of ice sheets undercut the notion that ice sheet instability would cause such rapid ice loss and sea level rise (7). Other sources of sea level change, particularly thermal expansion and mountain glacier retreat, dominated projections. The resulting estimates of total sea level rise were lower than before, as reflected by the projection in IPCC's AR1 of 31 to 110 cm (see the figure).

Fast forward another decade to IPCC's Fourth Assessment Report (AR4), and the field was in chaos due to emerging observations of the ice sheets. These led AR4's authors to refrain from a complete estimate of sea level rise because they could not constrain the effect of warming on ice sheet flow (8). Improved remote sensing and on-the-ground capability captured spectacular episodes of change, such as the collapse of most of the Antarctic Peninsula's floating Larsen B Ice Shelf and resulting acceleration

of its tributary glaciers, acceleration of West Antarctica's Thwaites and Pine Island Glaciers, and ice loss in Greenland. These events were driven by similar dynamical processes that were not represented in ice sheet models, confounding attempts to project. Also troubling was the discovery that a few glaciers and ice streams on the periphery of East Antarctica are vulnerable to warming, adding additional meters to potential sea level rise beyond 2100 (1). These findings drove rapid improvements in ice sheet modeling and a renewed interest in paleoclimate analogs of a warming world, enabling IPCC to begin to quantify these uncertainties in AR5, although the models were still evolving. Since AR5, various improvements have been proposed for representing the ice sheet contribution to global mean sea level projections (3, 4).

SOLVING THE ICE FLOW PROBLEM

The main reason for the difficulties in predicting sea level change is a limited understanding of ice flow. In many locations on the Greenland and Antarctic ice sheets, ice that is too thick to float rests on a bed below sea level. The ice thins as it flows toward the coast until it crosses the grounding line to form floating ice shelves. The latter, still attached to the main ice sheet, are restrained from flowing faster by friction at their sides or by local seafloor highs. Warming ocean water or air can thin ice shelves, reducing this lat-

Model projections suggest that global sea level could rise by 2 m or more by 2100. Such a rise would permanently submerge parts of coastal cities and regions unless costly defensive action, such as building sea walls, is taken. It would also vastly increase the area flooded temporarily during coastal storms. The image shows water crashing over the seawall in downtown Cedar Key, Florida, during Tropical Storm Andrea in 2013.

eral and basal friction and speeding the flow of nonfloating ice into the ocean. This may trigger an unstable retreat of the grounding line in some cases. Recent advances in theory and modeling have produced credible descriptions of aspects of this behavior, which are now routinely incorporated into regional and continental-scale ice sheet models used in projections. But the complexities of the ice sheet bed and ice interaction with the neighboring ocean make reliable prediction of unstable retreat very challenging.

At the same time, improved analyses of paleoclimate proxies indicate strongly that the sea surface was 6 to 9 m higher than today during the Last Interglacial (~130,000 to 116,000 years ago) (9). These high sea levels can only be explained through mass loss from the ice sheets in response to a sustained forcing that is likely to be exceeded before 2100 under high emissions pathways. The rate of this rise was geologically rapid but cannot be resolved to the century-or-less scale that is of greatest economic concern today.

Projections that sea level rise over the course of this century would remain below 1 m (2) hinged on the assumption that ice-shelf friction and other processes will continue to limit the rate of ice loss. However, beyond some threshold, especially if surface meltwater wedges open crevasses, the ice shelves may break off entirely to leave cliffs that calve icebergs directly. Taller cliffs are less stable. The tallest modern ice cliffs often persist months or longer between major calving events, but the larger stresses from taller cliffs might cause faster failure and retreat (10). Retreat of Thwaites Glacier in West Antarctica after future ice-shelf loss could generate such a high and potentially very unstable cliff. The study by DeConto and Pollard projected the onset of rapid ice sheet retreat around much of West Antarctica during this century after warming caused abundant meltwater in surface crevasses; the maximum retreat rate in these projections depends on uncertain assumptions, and a faster sea level rise might be possible (1).

¹Department of Geosciences and the Woodrow Wilson School, Robertson Hall 448, Princeton University, Princeton, NJ 08544, USA. ²Earth and Environmental Systems Institute and Department of Geosciences, 517 Deike Building, Pennsylvania State University, University Park, PA 16802, USA. Email: omichael@princeton.edu



RESEARCH PRIORITIES

Measurements of the Antarctic Ice Sheet and its surroundings continue to be sparse and difficult. Insufficient data limit physical understanding, in turn preventing accurate modeling. And, even under idealized conditions, efficiently solving the full fluid dynamic (Stokes) equations for ice flow presents numerical challenges. Recent reports (11, 12) outline an integrated research program that targets these large uncertainties to understand by how much and how fast the sea level may rise. The Thwaites Glacier region appears to be the most likely place for rapid ice loss to drive sea level rise, motivating a combined modeling and observation effort to accurately characterize its bed, ice, ocean, and atmosphere.

Major retreat of Thwaites Glacier might not occur, or it might occur while maintaining an ice shelf at a rate that would be geologically rapid but not necessarily fast compared with societal ability to plan and adjust. But it is also possible that very fast retreat occurs, challenging adaptation capacity worldwide. High emissions scenarios foresee climate forcing well beyond that which occurred over the time span of the instrumental record. Models constrained against this record may therefore not capture future behavior. Even the paleoclimatic record may not capture both the size and rate of future warming, motivating the need for process understanding. Ice-shelf loss and cliff failure are most evident now along the Antarctic Peninsula and in Greenland. Process studies should also be conducted in these places.

POLICY IN THE INTERIM

There are better options for policy-makers than to play wait-and-see. Measures specifi-

cally designed with an eye toward evolving predictions include building defenses such as those in the Netherlands, which can be augmented over time (13); building structures resilient to periodic flooding; and retreat from exposed areas combined with enhancement of natural defenses such as wetlands. In flood-prone areas, perverse incentives, such as submarket insurance premiums, should be eliminated while substituting reduced premiums and other incentives contingent on property owners taking adaptive measures before disaster occurs. These measures would reduce the large expense now incurred for disaster relief and rebuilding.

Scientists can contribute to improving the basis for policy judgments by presenting policy-makers with projections that are as fully probabilistic as possible while also characterizing deep uncertainties, rather than just them handing the worst-case or most-likely estimates. Coastal protection is a risk management issue, and risks cannot be fully managed outside a probabilistic context. ■

REFERENCES AND NOTES

1. R. M. DeConto, D. Pollard, *Nature* **531**, 591 (2016).
2. J. A. Church et al., in *Climate Change 2013: The Physical Science Basis. Contribution of Working Group I to the Fifth Assessment Report of the Intergovernmental Panel on Climate Change*, T. F. Stocker et al., Eds. (Cambridge Univ. Press, Cambridge/New York, 2013), chap. 13.
3. R. E. Kopp et al., *Earth's Future* **2**, 383 (2014).
4. M. Mengel, A. Levermann, K. Frieler, A. Robinson, B. Marzeion, R. Winkelmann, *Proc. Natl. Acad. Sci. U.S.A.* **113**, 2597 (2016).
5. O. A. Sayvetz, "A decision-making framework to support flood adaptation policy in New York City," thesis, Princeton University (2015).
6. S. J. Hoffman, D. Keyes, J. G. Titus, 1983, *Projecting Future Sea Level Rise: Methodology, Estimates to the Year 2100, and Research Needs* (Environmental Protection Agency, Washington, DC, 1983).
7. J. A. Church, J. M. Gregory, in *Climate Change 2001: The Scientific Basis. Contribution of Working Group I to the Third Assessment Report of the Intergovernmental Panel on*



PLANT IMMUNITY

Starving the enemy

Plants respond to pathogen infection by relocating sugar from bacterial colonization sites

By Peter N. Dodds and Evans S. Lagudah

Plants are energy storage factories. Photosynthetic cells convert energy from sunlight to sugars that are transported to growing tissues via both extracellular and intercellular trafficking pathways. Many pathogens have evolved mechanisms to infect the nutrient-rich niche of plant tissues and exploit these sugar pipelines. Some pathogens manipulate sugar transport to enhance their access to carbohydrate. For example, *Xanthomonas* bacteria deliver transcription-activator-like effector proteins into leaf cells. These proteins induce expression of SWEET family sugar transporters to release sucrose into the apoplastic (extracellular) space where the bacteria grow (1). On page 1427 of this issue, Yamada *et al.* (2) show that, in return, plants can also regulate sugar transporters, to redistribute the sugars away from the infection niche, removing the pathogens' energy source and limiting their proliferation.

Plants respond to infection through an innate immunity system that uses both extracellular and intracellular receptors to detect pathogen components and trigger responses (3). Pattern recognition receptors (PRRs) expressed on the cell surface include flagellin-sensing 2 (FLS2), which recognizes bacterial flagellin, and chitin elicitor receptor kinase 1 (CERK1), which responds to chitin, a component of fungal cell walls (4). These receptor kinase molecules signal through interaction with the helper receptor kinase brassinosteroid insensitive 1-associated receptor kinase 1 (BAK1), which initiates a mitogen-activated protein kinase cascade and leads to responses including induction of defense gene expression, reactive oxygen species production, and stomatal closure.

Yamada *et al.* treated *Arabidopsis* plants with flg22, a fragment of bacterial flagellin recognized by FLS2, and found that hexose uptake from the apoplast increased as part of the induced defense response. This was mediated by the plasma membrane hexose sugar transporter 13 (STP13). Indeed, the *STP13* gene was expressed in leaf epidermal

and mesophyll cells after flg22 treatment, but in addition, the transporter seems to be directly activated by phosphorylation. The authors observed STP13 interaction with several PRRs, including FLS2, as well as with the co-receptor BAK1, suggesting that it may be targeted by PRR signaling complexes. Indeed, the STP13 carboxyl-terminal cytoplasmic domain was an *in vitro* phosphorylation substrate of BAK1. A phosphomimic mutation of the target residue (threonine 485) resulted in enhanced glucose and fructose uptake rates for the transporter.

Yamada *et al.* further found that mutation of STP13 (and the constitutive hexose transporter STP1) increased hexose concentrations in leaf apoplast after flg22 treatment and enhanced growth of the pathogen *Pseudomonas syringae*. This was true even for a nonpathogenic *hrc* mutant strain that is incapable of delivering effectors into host cells. Expression of STP13-green fluorescent protein decreased bacterial growth, demonstrating the defensive value of induced hexose uptake in response to infection. However, an STP13 mutant with an altered BAK1 phosphorylation site failed to complement this phenotype, suggesting the importance of direct protein activation in the response. Overall, these findings show STP13-mediated hexose uptake as a basal pathogen resistance induced as part of pattern-mediated immunity. Cell wall invertase activity, which converts apoplastic sucrose into hexoses (glucose and fructose), was also induced by flg22, so the overall effect of this response is to remove a sugar source from the pathogen environment by sequestering it inside the host cells (see the figure). In addition to the nutritional effect on bacteria, Yamada *et al.* also observed increased induction of the type III secretion system in *P. syringae* infecting double *stp1stp13* mutant plants, suggesting that STP13 function may also contribute to suppressing bacterial virulence.

Partitioning of sugars between the leaf cell and apoplast may also be important for other pathogen interactions. One example is the enhanced infection of an *Arabidopsis stp13* mutant by the fungus *Botrytis cinerea* (5). Overexpression of STP13 reduced infection levels, suggesting a reliance on apoplastic sugars by this pathogen. However, no effects were observed for another fungus, *Alternaria*

Climate Change, J. T. Houghton *et al.*, Eds. (Cambridge Univ. Press, Cambridge/New York, 2001), chap. 11.

8. IPCC, 2007: Summary for Policymakers, in *Climate Change 2007: The Physical Science Basis. Contribution of Working Group I to the Fourth Assessment Report of the Intergovernmental Panel on Climate Change*, S. Solomon *et al.*, Eds. (Cambridge Univ. Press, Cambridge/New York, 2007).
9. R. E. Kopp, F. J. Simons, J. X. Mitrovica, A. C. Maloof, M. Oppenheimer, *Nature* **462**, 863 (2009).
10. R. B. Alley *et al.*, *Annu. Rev. Earth Planet. Sci.* **43**, 207 (2015).
11. National Academies of Sciences, *A Strategic Vision for NSF Investments in Antarctic and Southern Ocean Research* (National Academies of Sciences, Washington, DC, 2015).
12. Royal Society London Workshop Report from West Antarctica and future sea-level rise: A workshop to identify priorities for research and collaboration in West Antarctica (Royal Society, London, 2016); www.istar.ac.uk/wp-content/uploads/sites/5/sites/5/2016/05/West-Antarctica-Royal-Society-Meeting-Report-final.pdf.
13. Delta Commission, "Working together with water. A living land builds for its future" (Findings of the Deltacommissie, 2008); www.deltacommissie.com/doc/deltareport_full.pdf.
14. S. Jevrejeva, A. Grinsted, J. C. Moore, *Environ. Res. Lett.* **9**, 1 (2014).
15. Model-based ranges of sea level projections by 2100 for high emissions scenarios from each IPCC assessment report were derived from figure 1 of (14). The upper end of the bar for AR1 has been modified to reflect the values actually published in AR1, rather than a sensitivity test published subsequently. The upper end of the bar for AR2 has been modified to reflect aerosol emissions in the IS92e scenario, rather than the constant-aerosol sensitivity test published in AR2 and reproduced in (14). In AR4, the numerical range given was qualified by the phrase "model-based range excluding future rapid dynamical changes in ice flow" to indicate that the value at the upper end of the AR4 bar is not a reasonable approximation of an upper bound to sea level rise. For AR5, the bar represents the 17 to 83% probability range. AR1 to AR3 used 1990 as the base year, whereas AR4 and AR5 used base periods 1980 to 1999 and 1986 to 2005, respectively. Two other recent estimates are shown (3, 4), both using the 1986 to 2005 base period and an ice sheet treatment differing from AR5; neither account for the findings of DeConto and Pollard (1). Both estimates are for the 5 to 95% probability range. For (3), the 17 to 83% range is 62 to 100 cm. AR5 did not report a 5 to 95% range, and (4) did not report a 17 to 83% range.

ACKNOWLEDGMENTS

The authors are grateful to K. Keller and R. Kopp for insightful comments on an earlier version of this manuscript.

10.1126/science.aak9460

Commonwealth Scientific and Industrial Research Organisation, Agriculture and Food, Canberra, ACT 2601, Australia. Email: peter.dodds@csiro.au

brassicicola. Both of these are necrotrophic pathogens that kill host tissues to provide nutritional substrate. Other fungi have a biotrophic lifestyle, relying on maintaining living host tissue for nutrition, and may have an opposite requirement for sugar partitioning. Biotrophic rust and mildew fungi produce specialized structures called haustoria that penetrate host cell walls to extract nutrients (6). Mildew fungi grow on the leaf surface, and their only contact with the plant cell is through haustoria formed in leaf epidermal cells. Rust fungi grow in leaf intercellular spaces, but nevertheless, haustorial contact with leaf cells appears to be their main source of nutrients. Rust haustoria specifically express a proton pump adenosine triphosphatase and proton hexose symporter to drive hexose uptake from the extrahaustorial space (7). Thus, in contrast to *P. syringae*, which acquires nutrients and propagates in the apoplastic environment, intracellular hexoses are probably the primary source of carbohydrate for these pathogens. Interestingly, a natural mutation in the wheat STP13 ortholog that abolishes hexose transport activity is the basis of an important quantitative resistance gene (*Lr67*) present in some lines of wheat that is effective against rust and mildew pathogens (8). Expression of wheat STP13 increases during rust or mildew infections, which could be a strategy of the pathogen to increase sugar availability within the

infected cells. Likewise, expression of the grapevine STP13 homolog (VvHT5) increases during powdery mildew and downy mildew infection, and accumulates in phloem unloading cells (9), suggesting a role in increasing sugar supply to the infected leaves.

Sugar partitioning is clearly an important parameter affecting plant-pathogen interactions. Yamada *et al.* provide useful insights to test the role of STP13 in interactions with other *Arabidopsis* pathogens, particularly the biotrophic mildews. The biotrophic maize pathogen *Ustilago maydis* relies on sucrose rather than hexoses as primary assimilate (10), so other transport processes may be important during its infection. There are several families of sugar transporters in plants with different roles and substrate specificities (11), and these may provide opportunities for generating useful disease resistance phenotypes, such as that observed for *Lr67* in wheat. ■

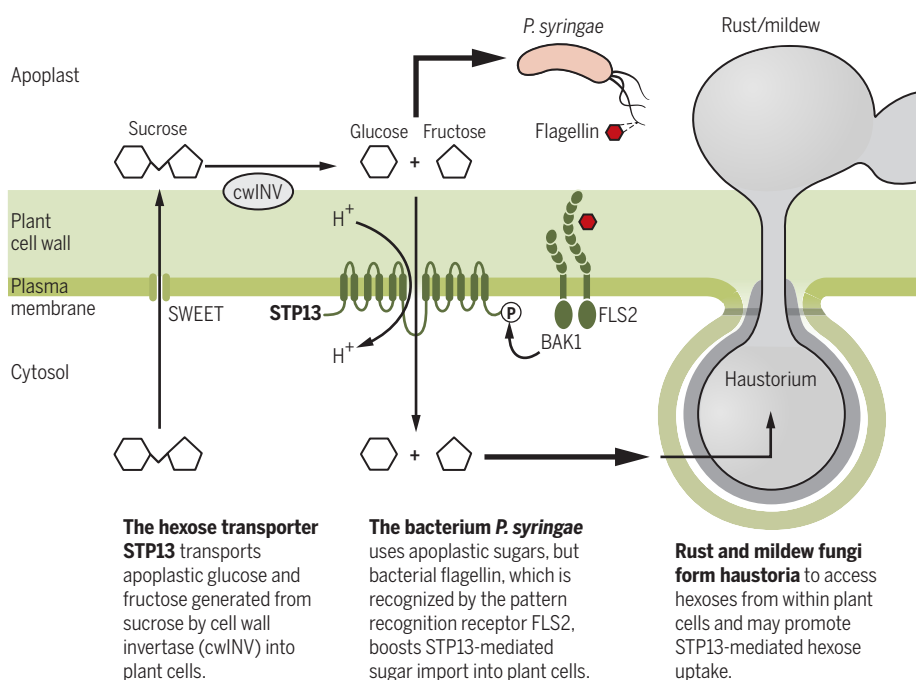
REFERENCES

1. J. Boch, U. Bonas, T. Lahaye, *New Phytol.* **204**, 823 (2014).
2. K. Yamada *et al.*, *Science* **354**, 1427 (2016).
3. P. N. Dodds, J. R. Rathjen, *Nat. Rev. Genet.* **11**, 539 (2010).
4. D. Couto, C. Zipfel, *Nat. Rev. Immunol.* **16**, 537 (2016).
5. P. Lemonnier *et al.*, *Plant Mol. Biol.* **85**, 473 (2014).
6. M. J. Harrison, *J. Exp. Bot.* **50**, 1013 (1999).
7. R. T. Voegelé, K. W. Mendgen, *Euphytica* **179**, 41 (2011).
8. J. W. Moore *et al.*, *Nat. Genet.* **47**, 1494 (2015).
9. M. A. Hayes *et al.*, *Plant Physiol.* **153**, 211 (2010).
10. R. Wahl *et al.*, *PLOS Biol.* **8**, e1000303 (2010).
11. L. Q. Chen *et al.*, *Annu. Rev. Biochem.* **84**, 865 (2015).

10.1126/science.aal4273

Competing for sugar

Sucrose is exported from leaf cells into the extracellular space (apoplast) for transport to other parts of the plant. Plants and pathogens compete for apoplastic sugars.



CATALYSIS

Toward sustainable fuel cells

Improved fuel-cell catalysts require much less platinum for the same performance

By Ifan Erfyl Lester Stephens, Jan Rossmeisl, Ib Chorkendorff

A quarter of humanity's current energy consumption is used for transportation (1). Low-temperature hydrogen fuel cells offer much promise for replacing this colossal use of fossil fuels with renewables; these fuel cells produce negligible emissions and have a mileage and filling time equal to a regular gasoline car. However, current fuel cells require 0.25 g of platinum (Pt) per kilowatt of power (2) as catalysts to drive the electrode reactions. If the entire global annual production of Pt were devoted to fuel cell vehicles, fewer than 10 million vehicles could be produced each year, a mere 10% of the annual automotive vehicle production. Lowering the Pt loading in a fuel cell to a sustainable level requires the reactivity of Pt to be tuned so that it accelerates oxygen reduction more effectively (3). Two reports in this issue address this challenge (4, 5).

Strategies for tuning the activity of Pt catalysts are based on the premise that pure Pt binds the oxygen-containing reaction intermediates too strongly. State-of-the-art fuel cells use Pt-Ni or Pt-Co cathode catalysts (2). The solute metal (Ni or Co) leaches out from the surface layer into the acid electrolyte, leaving behind a Pt overlayer. Ni and Co atoms are smaller than Pt atoms and therefore exert a compressive strain on the Pt surface atoms. Compression weakens the binding to the oxygen-containing reaction intermediates (6). A mild weakening increases the catalytic activity of Pt for oxygen reduction.

On page 1410 of this issue, Bu *et al.* (4) report Pt-Pb nanoplatelets for use as oxygen-reduction electrocatalysts. The catalytic activity of the platelets is high (4.3 A/mg at 0.9 V; see the figure) in a liquid half cell (an electrochemical cell that allows catalysts to be probed under well-defined conditions). The superior performance of the nanoplatelets is somewhat counterintuitive because Pb atoms are larger than Pt atoms and should therefore

brassicicola. Both of these are necrotrophic pathogens that kill host tissues to provide nutritional substrate. Other fungi have a biotrophic lifestyle, relying on maintaining living host tissue for nutrition, and may have an opposite requirement for sugar partitioning. Biotrophic rust and mildew fungi produce specialized structures called haustoria that penetrate host cell walls to extract nutrients (6). Mildew fungi grow on the leaf surface, and their only contact with the plant cell is through haustoria formed in leaf epidermal cells. Rust fungi grow in leaf intercellular spaces, but nevertheless, haustorial contact with leaf cells appears to be their main source of nutrients. Rust haustoria specifically express a proton pump adenosine triphosphatase and proton hexose symporter to drive hexose uptake from the extrahaustorial space (7). Thus, in contrast to *P. syringae*, which acquires nutrients and propagates in the apoplastic environment, intracellular hexoses are probably the primary source of carbohydrate for these pathogens. Interestingly, a natural mutation in the wheat STP13 ortholog that abolishes hexose transport activity is the basis of an important quantitative resistance gene (*Lr67*) present in some lines of wheat that is effective against rust and mildew pathogens (8). Expression of wheat STP13 increases during rust or mildew infections, which could be a strategy of the pathogen to increase sugar availability within the

infected cells. Likewise, expression of the grapevine STP13 homolog (VvHT5) increases during powdery mildew and downy mildew infection, and accumulates in phloem unloading cells (9), suggesting a role in increasing sugar supply to the infected leaves.

Sugar partitioning is clearly an important parameter affecting plant-pathogen interactions. Yamada *et al.* provide useful insights to test the role of STP13 in interactions with other *Arabidopsis* pathogens, particularly the biotrophic mildews. The biotrophic maize pathogen *Ustilago maydis* relies on sucrose rather than hexoses as primary assimilate (10), so other transport processes may be important during its infection. There are several families of sugar transporters in plants with different roles and substrate specificities (11), and these may provide opportunities for generating useful disease resistance phenotypes, such as that observed for *Lr67* in wheat. ■

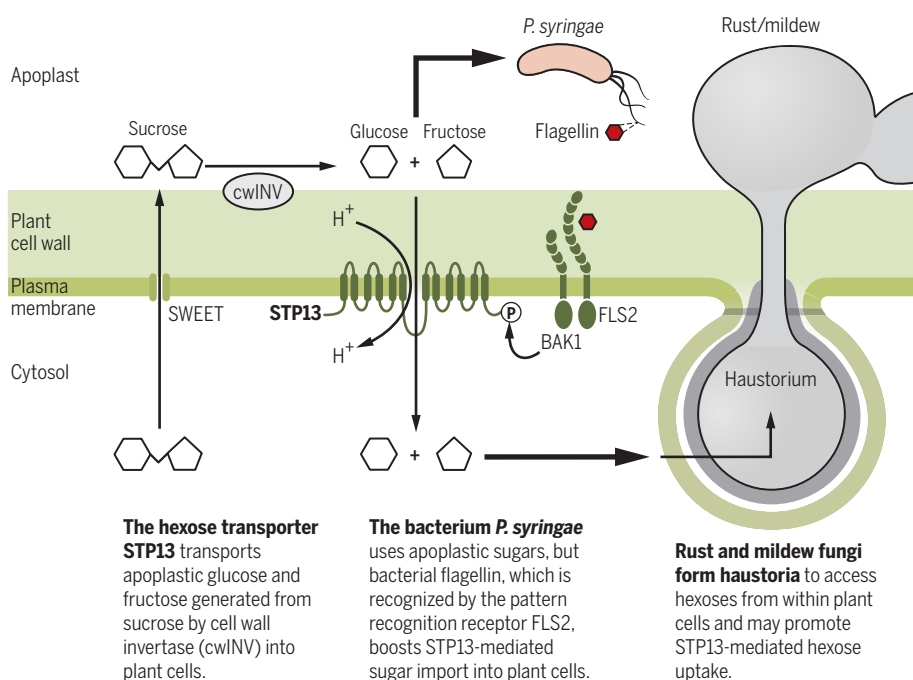
REFERENCES

1. J. Boch, U. Bonas, T. Lahaye, *New Phytol.* **204**, 823 (2014).
2. K. Yamada *et al.*, *Science* **354**, 1427 (2016).
3. P. N. Dodds, J. R. Rathjen, *Nat. Rev. Genet.* **11**, 539 (2010).
4. D. Couto, C. Zipfel, *Nat. Rev. Immunol.* **16**, 537 (2016).
5. P. Lemonnier *et al.*, *Plant Mol. Biol.* **85**, 473 (2014).
6. M. J. Harrison, *J. Exp. Bot.* **50**, 1013 (1999).
7. R. T. Voegelé, K. W. Mendgen, *Euphytica* **179**, 41 (2011).
8. J. W. Moore *et al.*, *Nat. Genet.* **47**, 1494 (2015).
9. M. A. Hayes *et al.*, *Plant Physiol.* **153**, 211 (2010).
10. R. Wahl *et al.*, *PLOS Biol.* **8**, e1000303 (2010).
11. L. Q. Chen *et al.*, *Annu. Rev. Biochem.* **84**, 865 (2015).

10.1126/science.aal4273

Competing for sugar

Sucrose is exported from leaf cells into the extracellular space (apoplast) for transport to other parts of the plant. Plants and pathogens compete for apoplastic sugars.



CATALYSIS

Toward sustainable fuel cells

Improved fuel-cell catalysts require much less platinum for the same performance

By Ifan Erfyl Lester Stephens, Jan Rossmeisl, Ib Chorkendorff

A quarter of humanity's current energy consumption is used for transportation (1). Low-temperature hydrogen fuel cells offer much promise for replacing this colossal use of fossil fuels with renewables; these fuel cells produce negligible emissions and have a mileage and filling time equal to a regular gasoline car. However, current fuel cells require 0.25 g of platinum (Pt) per kilowatt of power (2) as catalysts to drive the electrode reactions. If the entire global annual production of Pt were devoted to fuel cell vehicles, fewer than 10 million vehicles could be produced each year, a mere 10% of the annual automotive vehicle production. Lowering the Pt loading in a fuel cell to a sustainable level requires the reactivity of Pt to be tuned so that it accelerates oxygen reduction more effectively (3). Two reports in this issue address this challenge (4, 5).

Strategies for tuning the activity of Pt catalysts are based on the premise that pure Pt binds the oxygen-containing reaction intermediates too strongly. State-of-the-art fuel cells use Pt-Ni or Pt-Co cathode catalysts (2). The solute metal (Ni or Co) leaches out from the surface layer into the acid electrolyte, leaving behind a Pt overlayer. Ni and Co atoms are smaller than Pt atoms and therefore exert a compressive strain on the Pt surface atoms. Compression weakens the binding to the oxygen-containing reaction intermediates (6). A mild weakening increases the catalytic activity of Pt for oxygen reduction.

On page 1410 of this issue, Bu *et al.* (4) report Pt-Pb nanoplatelets for use as oxygen-reduction electrocatalysts. The catalytic activity of the platelets is high (4.3 A/mg at 0.9 V; see the figure) in a liquid half cell (an electrochemical cell that allows catalysts to be probed under well-defined conditions). The superior performance of the nanoplatelets is somewhat counterintuitive because Pb atoms are larger than Pt atoms and should therefore

exert tensile strain. According to conventional wisdom, such an effect should strengthen the binding to the reaction intermediates (6), impeding the kinetics of oxygen reduction. However, transmission electron microscopy images suggest that the core of the Pt-Pb nanoplatelets imposes tensile strain in some directions and compressive strain in others (4). As a result, some surface sites are under mild compression; these sites dominate the activity for oxygen reduction. This finding is somewhat analogous to our own research on alloys of Pt with rare earth metals. We have found that the larger rare earth atoms distort the compound away from a closely packed structure, inducing a compressive strain to the surface (7).

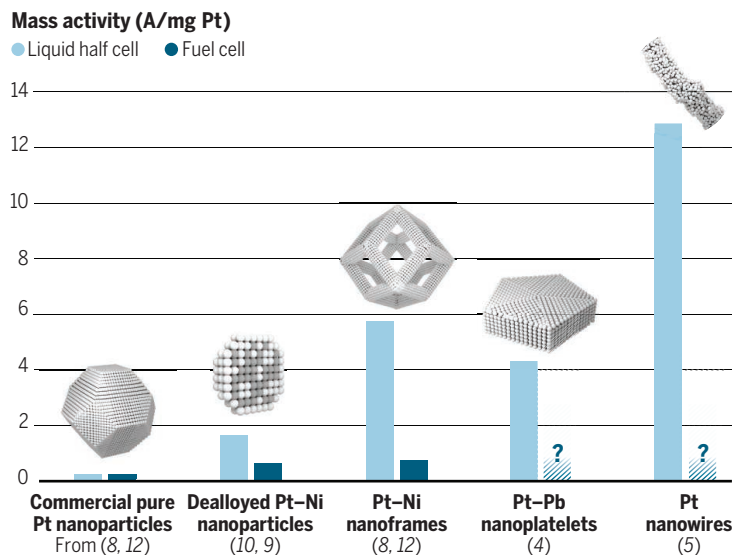
On page 1414, Li *et al.* report their investigations of Pt nanowires. Whereas earlier studies have reported partially dealloyed Pt-Ni catalysts (8–10), Li *et al.* completely leach Ni out of Pt-Ni nanowires, resulting in jagged nanowires of pure Pt. The surface area and surface-specific catalytic activity of the nanowires are both exceptionally high, yielding a record-breaking mass activity of 13.6 A/mg Pt at 0.9 V in a liquid half cell (see the figure). X-ray absorption spectroscopy measurements, supported by simulations, suggest that the Pt-Pt distance in the nanowires is shorter than in bulk Pt. The simplest explanation for the high oxygen reduction activity of the nanowires is that the surface is under compressive strain (8).

Both the Pt nanowires and the Pt-Pb nanoplatelets show negligible activity losses under accelerated degradation tests at room temperature. Such resistance to degradation is surprising, given that strained Pt structures are thermodynamically destabilized relative to unstrained Pt. It remains to be shown, however, how well these catalysts will operate in real fuel cells, as opposed to the idealized conditions of liquid half cells.

Liquid half cells are simple to optimize, require low amounts of catalysts, and are thus well suited for laboratory-scale studies. Catalyst activity is typically benchmarked at 0.9 V because at higher current densities, the reaction is limited by the poor O₂ transport in liquid half cells. In the case of commercial pure Pt nanoparticles, which are relatively inactive, there is excellent agree-

From model studies to real devices

Novel Pt-based catalysts, including those reported by Bu *et al.* and Li *et al.* in this issue, perform better than commercial pure Pt nanoparticles in model liquid half cells (15). The next challenge is to translate the full extent of this superior performance to fuel cells.



ment between liquid half cells and fuel cells at 0.9 V (11), but this is not always the case for more active catalysts (see the figure) (2).

For instance, Stamenkovic and co-workers' Pt-Ni nanoframes have a mass activity of 5.7 A/mg at 0.9 V in a liquid half cell; such high catalytic activity was unprecedented in 2014, when their work was published (8). Preliminary, unoptimized experiments on Pt-Ni nanoframes in a fuel cell yielded an activity of 0.76 A/mg (see the figure) (12); to the best of our knowledge, this is the highest activity reported for any catalyst in a fuel cell. The nanoframes clearly offer high activity in a fuel cell but, thus far, have not captured the superior performance promised by the experiments in liquid half cells. This illustrates the challenges in translating advances from model studies to technological application.

Furthermore, fuel cells are operated at high current densities in order to maximize power; this requires the overall cell potential to be below 0.9 V. The benefit of using very active catalysts at such high current densities is currently under debate. Recent reports suggest that a high power output is more easily sustained in a fuel cell loaded with catalysts with a large electrochemically active surface area, rather than those with an intrinsically high catalytic activity (2). To this end, the high surface area of Li *et al.*'s Pt nanowires may be particularly beneficial.

The reason for this phenomenon encountered close to maximum power is unclear. At high overpotentials (that is, distance from equilibrium potential), Pt-based catalysts

seem to reach a limiting surface-specific current density of ~0.1 A/cm² (13). Kongkanand and Mathias have suggested that this is due to poor transport through the ionomer phase that covers each catalyst particle (2). We propose another possibility: At sufficiently large overpotentials, the barriers associated with electrochemical charge transfer processes should become negligible. Thus, the kinetics for the reaction cannot be accelerated further. At this point, the catalyst reaches a limiting value of the current density. The overpotential required to reach this current density falls with increased catalyst activity. Different catalysts operating beyond this limiting overpotential should exhibit the same surface-specific activity.

Improvements in catalyst design have already allowed Pt loadings in fuel cells to be lowered substantially. This progress has been reached on the basis of model studies that have elucidated fundamental bottlenecks at the electrochemical interface and shown how they can be overcome. Scientists should extend this approach to the investigation of well-defined catalysts at the high current densities at which fuel cells are operated (14). The resulting insights will help to translate the spectacular gains in activity and stability represented by the latest generation of fuel cell catalysts to real devices. ■

REFERENCES AND NOTES

1. International Energy Outlook 2016 (U.S. Energy Information Administration, 2016).
2. A. Kongkanand, M. F. Mathias, *J. Phys. Chem. Lett.* **7**, 1127 (2016).
3. M. K. Debe, *Nature* **486**, 43 (2012).
4. L. Bu *et al.*, *Science* **354**, 1410 (2016).
5. M. Li *et al.*, *Science* **354**, 1414 (2016).
6. P. Strasser *et al.*, *Nature Chem.* **2**, 454 (2010).
7. M. Escudero-Escribano *et al.*, *Science* **352**, 73 (2016).
8. C. Chen *et al.*, *Science* **343**, 1339 (2014).
9. B. H. Han *et al.*, *Energy Environ. Sci.* **8**, 258 (2015).
10. C. H. Cui, L. Gan, M. Heggen, S. Rudi, P. Strasser, *Nature Catal. B-Environ.* **56**, 9 (2005).
11. H. A. Gasteiger, S. S. Kocha, B. Sompalli, F. T. Wagner, *Appl. Catal. B-Environ.* **56**, 9 (2005).
12. V. Stamenkovic, N. Markovic, 2015 DOE Hydrogen and Fuel Cells Program Review: Nanosegregated Cathode Catalysts with Ultra-Low Platinum Loading (U.S. Department of Energy, 2015).
13. J. P. Owejan, J. E. Owejan, W. B. Gu, *J. Electrochem. Soc.* **160**, F824 (2013).
14. C. M. Zalitis, D. Kramer, A. R. Kucernak, *Phys. Chem. Chem. Phys.* **15**, 4329 (2013).
15. All data shown are for 0.9 V versus a reversible hydrogen electrode. Experimental parameters such as temperature and scan rate may have differed between the experiments.

Department of Physics, Technical University of Denmark, 2800 Kgs. Lyngby, Denmark. E-mail: ibchork@fysik.dtu.dk

GEOPHYSICS

Understanding induced seismicity

Observational data sets provide a clearer picture of the causes of induced seismicity

By Derek Elsworth,¹ Christopher J. Spiers,² Andre R. Niemeijer²

Fluid injection-induced seismicity has become increasingly widespread in oil and gas-producing areas of the United States (1–3) and western Canada. It has shelved deep geothermal energy projects in Switzerland and the United States (4), and its effects are especially acute in Oklahoma, where seismic hazard is now approaching the tectonic levels of parts of California. Unclear in the highly charged debate over expansion of shale gas recovery has been the role of hydraulic fracturing (fracking) in causing increased levels of induced seismicity. Opponents to shale gas development have vilified fracking as directly responsible for this increase in seismicity. However, this purported causal link is not substantiated; the predominant view is that triggering in the midwestern United States is principally a result of massive reinjection of energy-coproduced wastewaters. On page 1406 of this issue, Bao and Eaton (5) identify at least one example of seismicity developed from hydraulic fracturing for shale gas in the Alberta Basin.

Energy supply in the United States has changed dramatically over the past decade. In an energy-hungry world, the shale gas revolution has been heralded both as salvation and as damnation. This position has resulted from unlocking the massive store of gas and oil held in deep, ultralow-permeability shale reservoirs. The successful development of both horizontal drilling and massive hydraulic fracturing has been key to foment this revolution.

On the positive side, this new and abundant supply of gas and liquid hydrocarbons has contributed to a sea change in the U.S.

¹Energy and Mineral Engineering and Geosciences, G3 Center and EMS Energy Institute, Pennsylvania State University, University Park, PA 16802, USA. ²HPT Laboratory, Department of Earth Sciences, Utrecht University, Budapestlaan 4, 3484 CD, Utrecht, Netherlands. Email: elsworth@psu.edu



Hydraulic fracturing at the Bakken Formation in North Dakota. A mixture of water and fracking fluids are pumped into the ground.

energy outlook, with North America effectively becoming energy-independent (6). On the downside, some identify gas-for-coal substitution as only deferring the inevitable hard choice of transitioning from fossil fuel to sustainable energy, noting the impact of cheap gas in impeding penetration of true renewables into the marketplace (7). Concerns about rural industrialization, fears of the impact on groundwater resources, dangers inherent in surface transportation of fracturing water and hydrocarbons, the proliferation of pipeline networks, and risks of induced seismicity have all fueled the debate.

Part of this debate, on the causality of induced seismicity, is informed by the analyses of Shirzaei *et al.* (8) and by Bao and Eaton (5). Their treatments of observational data specifically address the role of massive wastewater injection in triggering seismicity (8) and whether the much smaller injections involved in hydraulic fracturing (5) may have similar impact.

Induced seismicity in the midwestern United States has grown lockstep with the increase in coproduced waters pumped from near-exhausted conventional oil reservoirs. Disposal of the sometimes four barrels or so of brine produced for every single barrel of oil is typically achieved through reinjection into deep saline aquifers (see the figure). The resulting inflation of deep saline aquifers is the principal, obvious culprit for increased seismicity. Increased fluid pressures reduce

the strength of faults transecting the disposal aquifers, which may already be on the point of tectonic reactivation. However, the evidence is often circumstantial and equivocal.

By contrast, Shirzaei *et al.* (8) provide a direct link between observations of seismicity and wastewater injection with constraints on surface deformation derived from InSAR (Interferometric Synthetic Aperture Radar). These observations allow the authors to match a straightforward model for the elastic inflation of the porous, disposal aquifer to the deformation signature of uplift at the surface. Predictions of the fluid injection-induced changes in stress causing the surface deformation are then combined with a model of fault failure to infer the observed seismicity. The constraint afforded by the InSAR-measured deformations is the key to establishing causality between reinjection and the observed seismicity—removing ambiguity in linking wastewater production to seismicity and thus opening the way to mitigation.

A misperception is that increased hydraulic fracturing for shale gas is the culprit for the increase in induced seismicity seen in North America. Rather, it is the reinjected disposal of the large volumes of coproduced brines from conventional hydrocarbon reservoirs that are principally implicated (8). Although the much smaller (but appreciable) volumes of fracturing fluid have also contributed to smaller seismic events, the evidence directly linking observed seismicity to active

hydraulic fracturing is generally ambiguous. However, Bao and Eaton provide compelling evidence directly linking a magnitude-3.9 event in Alberta to hydraulic fracturing of a gas shale. Seismicity initiated several weeks after the initiation of hydraulic fracturing and continued for 4 months after pumping had stopped. Although Bao and Eaton's analysis lacks the geodetic (InSAR) constraint for the case of wastewater disposal (8), the role of hydraulic fracturing—and its interaction with large faults that also intersect basement rocks underneath the reservoir—seems clear. Most interesting is that seismic failure occurred on two strands of a fault, but in response to very different triggers.

The first event was triggered when elevated pore fluid pressures from the injected fracking fluids diffused outward to reactivate a tectonically primed strand of a deep fault cutting basement rocks. This strand failed once a sufficient portion was weakened, a mechanism identical to triggering from wastewater injection (8). However, the second triggering mechanism had much greater reach from the hydraulic fracture. In this case, failure was driven by elevating the far-field stress beyond the immediate region inflated by the blade-like hydraulic fractures (see the figure

inset). This implies two distinct mechanisms for seismicity: (i) a proximal region where pore fluid pressures are elevated and failure is driven by a reduction of the strength of the fault, with the stress state in the local rock mass remaining essentially unchanged, and (ii) an encapsulating aureole, which is as yet unpenetrated by pore pressure diffusion but where increased rock stress drives fault failure while fault strength remains largely unaffected. These two different styles of failure act on similar time scales but are characterized by different length scales.

For now, management strategies for mitigating seismicity associated with wastewater injection have a reasonable basis. Elevated pore pressures contributing to seismicity are reduced if injection rates are curtailed, if injection is distributed over multiple wells across the aquifer, or if injection wells are carefully located away from tectonically primed deep faults. However, solutions are less simple for hydraulic fracturing, in which wells must be located within the hydrocarbon reservoir with no possibility to relocate and the size, reach, fluid-conductivity, and ultimate effectiveness of the fracturing treatment all depend on a high fluid injection rate.

The constrained analysis of wastewa-

ter reinjection provided by Shirzaei *et al.* (8) helps clarify the debate over causality between injection and induced seismicity, and the observations by Bao and Eaton (5) dispel the notion that events resulting from hydraulic fracturing are always small. These studies provide important steps toward answering the key question in the induced seismicity debate: What is the size of the probable maximum event (9) based on sound and established scientific principles? Only through such mechanistic understanding can induced seismicity be fully understood and mitigated. ■

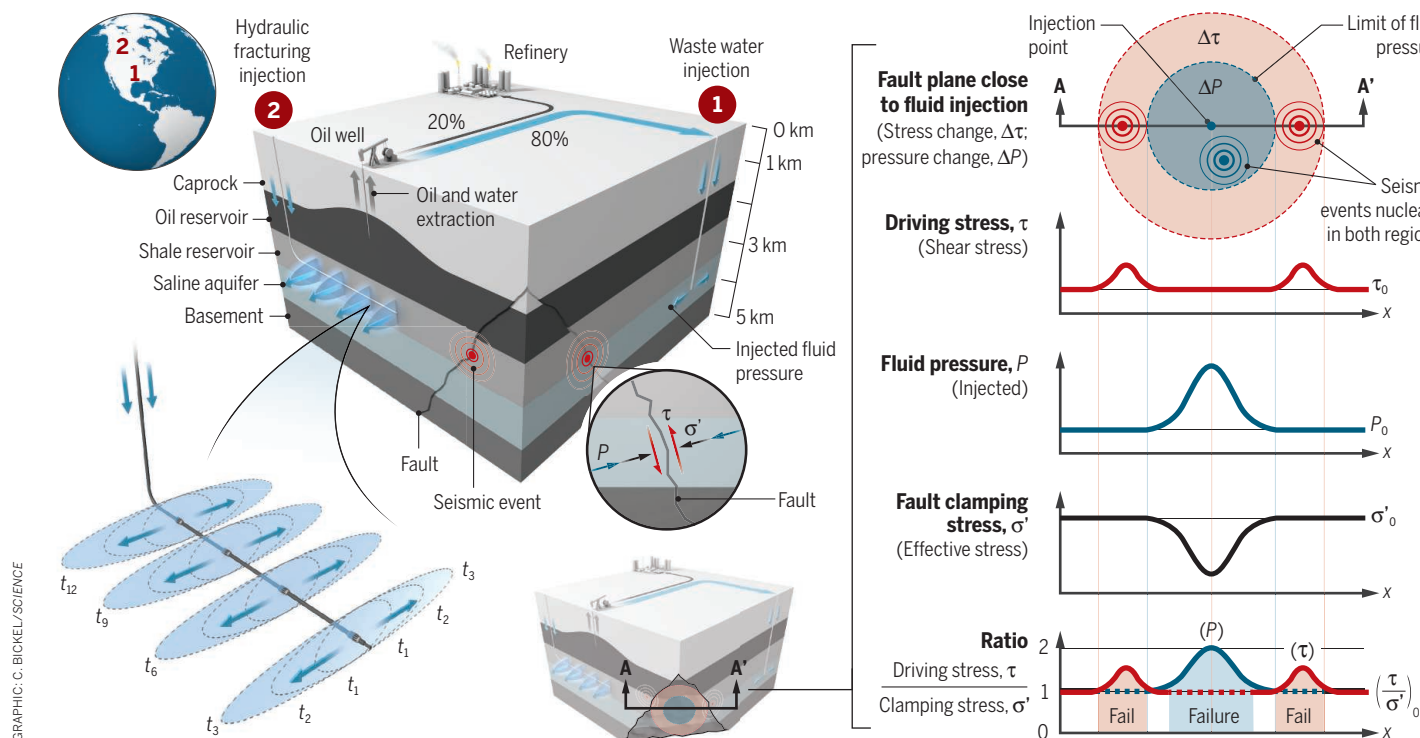
REFERENCES

1. N.J. van der Elst, H.M. Savage, K. Keranen, G.A. Abers, *Science* **341**, 164 (2013).
2. K. Keranen, M. Weingarten, G.A. Abers, B. Bekins, S. Ge, *Science* **345**, 448 (2014).
3. M. Weingarten, S. Ge, J.W. Godt, B.A. Bekins, J.L. Rubenstein, *Science* **348**, 1336 (2015).
4. "Quake fears stall energy extraction project," *New York Times*, 13 July 2009; www.nytimes.com/2009/07/14/business/energy-environment/14drill.html.
5. X. Bao, D.W. Eaton, *Science* **354**, 1406 (2016).
6. M. Egan, "After 40-year ban, U.S. starts exporting crude oil," *CNN Money* (29 January 2016); money.cnn.com/2016/01/29/investing/us-oil-exports-begin.
7. H. McJeon *et al.*, *Nature* **514**, 482 (2015).
8. M. Shirzaei *et al.*, *Science* **353**, 1416 (2016).
9. A. McGarr, *J. Geophys. Res.* **119**, 1008 (2014).

10.1126/science.aal2584

Induced seismicity

A vertical well taps a conventional oil reservoir whereas a horizontal well accesses a shale reservoir for gas. Wastewater reinjection into a saline aquifer (shown in 1) and the injection of fracturing fluid (principally water) into the shale reservoir (shown in 2) have the same impact in elevating fluid pressures and driving the stress state on a deeply penetrating fault to failure. In cross section A-A', injection of fluid near the fault causes slip by contrasting mechanisms in both the near-field and the far-field. The net effect of these two mechanisms is to elevate driving stress above the clamping stresses in these two concentric regions, and to potentially induce seismic slip.



RETROSPECTIVE

John D. Roberts (1918–2016)

One of the great leaders of modern chemistry during the field's most exciting time

By George M. Whitesides

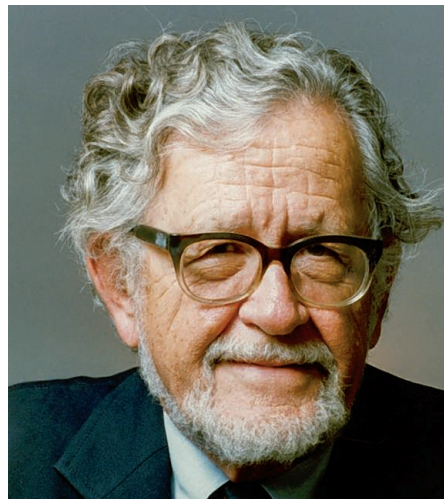
John D. (“Jack”) Roberts, Professor of Chemistry, Emeritus, at the California Institute of Technology (Caltech), died on 29 October at the age of 98. Roberts led organic chemistry’s transition from a field that studied what reactions did to one that also studied how reactions happened. He was an explorer with boundless curiosity who was untiring in his efforts to bring new and useful ideas, tools, and experimental designs to chemistry. He thrived on convincing chemists that his opinions on both science and scientific standards were correct (or at least worth arguing about, usually strenuously). He was not the only parent of physical-organic chemistry, but he was its best teacher.

Roberts began his independent career in the time immediately after World War II. Before the war, chemistry had been concerned primarily with combining small molecules to make larger, more complicated ones. The war had produced a flood of new ideas and instrumental techniques in physical chemistry, ranging from theories of electronic structure to new spectroscopic tools. Organic synthetic chemistry and physical/analytical chemistry were culturally distinct, and interactions between them were limited. The war also resulted in the formation of the similarly distinct petrochemical industry and system of U.S. research universities that quickly came to support academic science.

Roberts was completely indifferent to these boundaries between scientific ideologies. He went where his curiosity led him, and if there were obstacles that might have deterred others (for example, if he understood nothing about the subject), he simply charged on (boldly, or incautiously, depending upon one’s point of view). When he discovered a good new idea, or a new technique, he did everything he could to teach other chemists about it. He became simultaneously an organic chemist, a physical chemist, an academic scientist, an inveterate teacher, and an active industrial consultant.

As a scientist, his greatest contribution was to the formation of physical-organic

chemistry, the field that studies organic reactions using combinations of physical and synthetic methods. In addition to introducing methods of simple quantum mechanics and new forms of spectroscopy [especially nuclear magnetic resonance (NMR)] to the field, Roberts showed how to infer the existence and structure of “transitory intermediates”: molecular structures that exist fleetingly (and are often, even now, invisible to direct observation) between the starting materials and products. In doing so, he made clear that focusing only on stable, long-lived reactants and products misses much of what



goes on during the course of chemical reactions. The understanding of reaction mechanisms and intermediates that Roberts and others developed has been invaluable both in improving synthesis and in understanding the critical reaction networks making up processes ranging from metabolism in living cells to the formation of hydrocarbon fuels in petroleum refineries.

Roberts taught by doing, but he also taught by teaching. He wrote a number of books—from a widely used first-year organic chemistry text to short books on NMR spectroscopy and molecular-orbital theory (which he claimed to have dictated in his car while commuting). These books introduced the philosophy of physical-organic chemistry to both students and senior scientists.

Born in 1918 in Los Angeles, California, Roberts received his B.A. (1941) and Ph.D. (1944) degrees from the University of Cali-

fornia, Los Angeles (UCLA). After short appointments at UCLA, Harvard, and MIT, he moved to Caltech in 1952, where he spent the remainder of his career. After 1980, he became vice president, provost, and dean of the faculty at Caltech, but he continued to teach courses for many years.

I joined his research group as a graduate student in 1960, when his research career was in its most active phase. Roberts was an unwavering supporter of young scientists (and, long before others, of women in science). He worked tirelessly and invisibly—insofar as he could manage it—to support and encourage younger colleagues. During the time I was a student, I almost never saw him in person (he later told me that I was a porcupine best left alone), but he devoted countless hours to editing my work. I would write a draft of a paper, he would correct it in word-for-word detail (in red pen), I would rewrite it, he would correct it again, and so on, seemingly *ad infinitum*. This style of directing graduate research was splendid for improving scientific standards, logic, grammar, style, and punctuation. It was even better as a lesson in the scientific method and, perhaps best of all, for building a (partially illusory) sense of independence. Years later, no longer a beginner, I wrote a report for a U.S. National Academy of Sciences committee, and Roberts was the reviewer. As in the past, we went through six or seven rounds of detailed editing (his, of course, in red pen) before he was satisfied. One comes to realize that—as a writer or scientist—one can have no better friend and teacher than a demanding editor.

Roberts loved to argue, and did not discriminate between arguments in private and in public. For decades, he was the voice of conscience in the U.S. National Academy of Sciences and in other musty halls of Washington, DC, science. His arguments were always elitist. To him, only “quality” mattered. There could be no compromise on standards (and, fortunately, he had a clear and unwavering view of what these standards should be). His arguments were also loud. He was hard of hearing, and he loved combat. Every discussion proceeded at high volume. But it was always worth thinking about what he said.

Jack Roberts was someone who was almost impossible not to love. To deal with—even for those of us who knew him well—he was gruff, argumentative, difficult or impossible to convince, and stubborn to a fault. He was also extraordinarily generous (he never took credit for a student’s idea), incorrigibly curious, addicted to new ideas, warm and loyal to his friends, devoted to his family, students, and colleagues, and deeply and genuinely protective of science and its institutions. ■

Department of Chemistry and Chemical Biology,
Harvard University, Cambridge, MA 02138, USA.
Email: gwhitesides@gmwhgroup.harvard.edu



BOOKS *et al.*

HISTORY OF SCIENCE

The calculators

Two tomes uncover how women broke down barriers to explore the universe

By Carol Christian

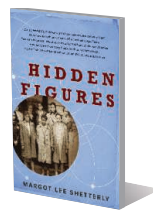
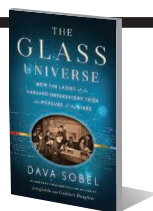
As testimony to the tenacity and bravery of clever women, and the courage of some laboratory managers and directors, the 20th century saw the emergence of women as significant participants in astronomy and space engineering.

In the opening pages of *The Glass Universe*, Dava Sobel recounts how, in the wake of her husband's death in 1882, Mary Anna Palmer Draper was determined to ensure that his legacy as a trailblazer in the field of astrophotography was not forgotten. With the encouragement of Edward Charles Pickering, director of the Harvard College Observatory, she established the Henry Draper Memorial, which would support an ambitious new program that sought to classify several thousand stars from a catalog of photographs captured on glass plates. She thus became a benefactor of the observatory, providing funds and eventually a telescope, to ensure that her husband's spectroscopic work was continued. In doing so, Draper—herself an active participant in her husband's research—set in motion events that would firmly establish a role for women in modern astrophysics.

In the year of Henry Draper's untimely passing, Pickering had issued a plea requesting the help of amateur astronomical observ-

The Glass Universe
How the Ladies of the
Harvard Observatory Took
the Measure of the Stars
Dava Sobel
Viking, 2016. 352 pp.

Hidden Figures
The American Dream and
the Untold Story of the Black
Women Mathematicians Who
Helped Win the Space Race
Margot Lee Shetterly
Morrow, 2016. 367 pp.



ers, who would be responsible for performing calculations on the observatory's nighttime observations. Noting the aptitude and untapped potential of the gentler sex, he had enlisted the assistance of six women “computers” by February 1883.

Sobel capably demonstrates how Pickering's cadre of women computers not only standardized the stellar brightness scale to levels fainter than the unaided eye could see but also characterized the detailed appearance of stellar spectra on plates that recorded hundreds of observations at a time. Williamina Fleming, for example, originally employed as Pickering's maid, created an extensive empirical classification scheme based on the visual appearance of the spectra. The scheme was later augmented by Antonia Maury, none other than Henry Draper's niece. Astronomers at the time were skeptical of the use of photography as a robust astronomical medium, but the women's careful analysis helped the field of astrophotography become a cornerstone of stellar astronomy.

Later, we meet Cecilia Payne, an English woman who read chemistry and physics at Cambridge University. Payne arrived at the observatory in 1923, where she would eventually determine that stars are 99% hydrogen,

Aerospace engineer Mary Jackson (played by Janelle Monáe) consults a colleague in *Hidden Figures*, in theaters 25 December 2016.

an important breakthrough counter to conventional wisdom at the time. Payne would go on to become the first woman to obtain a Ph.D. in astronomy from Radcliffe College (now part of Harvard) in 1925.

Sobel interweaves the diverse personalities and backgrounds of these and other women with stories about the evolution of the field of astronomy as a whole, including the establishment of the American Astronomical Society, and the International Astronomical Union's struggle to maintain and then reestablish international research collaborations across national boundaries during World War II (an effort in which the Harvard Observatory was a major player, according to Sobel).

Hidden Figures, by Margot Lee Shetterly, picks up where *The Glass Universe* leaves off, highlighting a group of African American women who made important early contributions to the space race during and after World War II. The book follows the career of Dorothy Vaughan, a former high school mathematics teacher, and her fellow female computers in the all-black West Area Computing Unit of Langley Memorial Aeronautical Laboratory, who were recruited from around the country to provide computation support for the war effort in the early 1940s.

Contrasting the headline-grabbing exploits of Tuskegee airmen with the understated but no less impressive contributions of the “colored computers,” Shetterly reveals how the women earned the respect and admiration of their colleagues. “They wore their professional clothes like armor,” she writes. “They wielded their work like weapons, warding off the presumption of inferiority because they were Negro or female.”

The women continued their work after the war, during the period when rocketry was born and competition with the Soviet Union was fierce. A film about their contributions to NASA's Project Mercury and the Apollo 11 mission based on Shetterly's book is set to be released on 25 December (1).

Besides being captivating reads, these two books chronicle stories of overlooked contributions of women in space science, astrophysics, and engineering in the 20th century. Both are a testimony to personal perseverance and ingenuity. Such histories enrich our understanding of the value of tapping diverse individuals to advance knowledge in any field. ■

REFERENCES

1. *Hidden Figures*, Theodore Melfi, director. Fox 2000 Pictures, 2016.

10.1126/science.aaj2225

PUBLIC HEALTH

The aftermath of AIDS in China

A candid history uncovers the country's stumbles and successes in the fight against the devastating virus

By **Kristin Harper**

By the mid-1990s, the terror of the early AIDS epidemic had subsided in many western countries, as antiretroviral therapy transformed the once-deadly disease into a chronic condition. In China, however, the AIDS epidemic was just getting started. Slipping across the nation's southern borders via injection drug use, the virus went largely undetected until it exploded among tens of thousands of plasma sellers in rural China. Up to that point, many Chinese leaders had naively hoped that the absence of "social evils," such as prostitution and illegal drugs, would prevent the infection from taking root in the country. *HIV/AIDS in China: Beyond the Numbers* is a fascinating account of how the AIDS epidemic forced these leaders into action.

This slim volume is full of quotes from researchers, policy-makers, and clinicians who were on the front lines of the epidemic. On the first page, Zunyou Wu (director of the National Centre for AIDS/STD Control and Prevention at China's CDC) and Elizabeth Pisani (King's College London) state, "[E]veryone involved felt that it was important to give an honest account of these events; they all recognise that the lessons of the past have contributed in important ways to the strength and success of China's response at present."

As promised, the pages that follow are remarkable for their candor, detailing many shortfalls on the part of the Chinese government. A slow response to the plasma seller outbreak, for example, meant that even though the first HIV cases were detected in this group in the mid-1990s, many of the infected were still undiagnosed and untreated when the story broke in the national and international news around the year 2000.

The book also details how rank-and-file researchers and patient advocates went to heroic lengths to prevent new infections. We learn, for example, how the organizers of a national training workshop that took place early in the epidemic instructed shocked participants to head outside to practice talking to sex workers; how one deputy director at the All-China Women's Federation took advantage of her boss's absence to apply for HIV prevention funds



Chinese nursing students hold ribbons in honor of World AIDS Day in 2011.

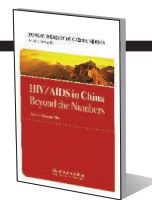
from the World Bank; and how virologist Laiyi Kang narrowly escaped arrest for instituting an experiment that provided free condoms in the bathrooms of a high-end hotel in Shanghai.

The book describes how, eventually, senior leaders took notice of the successes that these AIDS pioneers had carefully documented. When the Chinese government did decide to support prevention and treatment efforts in earnest, it did so with all of its weight. The government's spending on AIDS skyrocketed from a mere US\$2 million in 2000 to \$600 million in 2015. And between 2010 and 2014, health officials reduced the number of steps between HIV screening and treatment from 4 to 1, thus increasing the percentage of individuals with a confirmed HIV infection who had initiated antiretrovirals from 40% to 90%. Most recently, in February of this year, the

HIV/AIDS in China Beyond the Numbers

Zunyou Wu, Ed.

People's Medical
Publishing House, 2016. 191 pp.



government announced that anyone with a confirmed HIV diagnosis can seek free treatment immediately, regardless of CD4 cell count.

This account of China's transformation from HIV laggard to leader will be valuable to other countries seeking to meet the Joint United Nations Programme on HIV/AIDS 90-90-90 target (i.e., by the year 2020, 90% of people living with HIV will know their status, 90% of people with HIV will receive sustained antiretroviral therapy, and 90% of people receiving antiretroviral therapy will achieve viral suppression). In particular, countries dependent on donor funds may want to take note of the Chinese government's insistence on using international assistance to meet national objectives rather than donors' objectives and on satisfying grantors' reporting requirements with a single, centralized data platform built to meet national needs and reduce paperwork.

As the authors acknowledge, though, many features of China's system may be difficult for other nations to replicate. Few countries have such a strong central government, and whereas today over 99% of funds for HIV programs in China come from domestic sources, many AIDS-stricken countries do not have the resources to ramp up funding in this way.

As the authors point out, it remains to be seen how China will adapt to the changing HIV landscape; to what extent its top-down government will be able to partner with grass-roots community groups to reach at-risk populations; and whether the stigma that impedes prevention and treatment efforts can be reduced. However, this book offers a vivid history of China's response to HIV from the pathogen's emergence until the present, and it joins the relatively thin ranks of books that offer first-person accounts of important eras in public health. This is a must-read book for anyone interested in HIV, infectious diseases more generally, or global health. ■

10.1126/science.aal0205

The reviewer is at Harper Health and Science Communications, LLC, Seattle, WA 98117, USA. Email: kristin.nicole.harper@gmail.com

LETTERS



Edited by **Jennifer Sills**

Editorial retraction

AN INVESTIGATION BY Imperial College into the *Science* Research Article “The protein LEM promotes CD8⁺ T cell immunity through effects on mitochondrial respiration” (1), which was the subject of an Editorial Expression of Concern in December 2015 (2), has now concluded that duplications and use of incorrect Western blots occurred during the preparation of several figures in the paper. The investigation also found that examples of the original Western blots and accompanying experimental details had been lost. The investigation found that the problematic figures had been prepared solely by corresponding author Ashton-Rickardt and he accepted full responsibility for them. In agreement with the recommendation of the investigation, *Science* is therefore retracting the Research Article.

Jeremy Berg

Editor-in-Chief

REFERENCES

1. I. Okoye et al., *Science* **348**, 995 (2015).
2. M. McNutt, *Science* **350**, 1482 (2015).

10.1126/science.aal5242

Prioritizing good diets

IN HER PERSPECTIVE “Plating up solutions” (16 September, p. 1202), T. Garnett identifies “policy reluctance to interfere with the market, risk votes, or displeasure powerful corporations” as a major obstacle to addressing the problems inherent in our food system. Garnett identifies values as key to overcoming the policy obstacle and solving these problems.

The problems that Garnett enumerates persist because two sets of conflicting diets, and associated values and policies, have been institutionalized: those that facilitate equitable food systems and healthy people and environments, and those that create inequity, noncommunicable diseases, environmental degradation, and corporate profit (1). For example, the U.S. Department of Agriculture supports programs to increase consumption of fruits and vegetables but also subsidizes commodity foods that are correlated with increased risk of cardiometabolic disease, especially among the poor and minority groups (2). U.S. colleges increasingly focus on combating growing student food insecurity with food aid and education (3), but also support fast-food franchises and contracts with soda companies that fuel poor health, food insecurity (4), and

U.S. colleges contract with soda companies even as they try to facilitate good health.

environmental damage. [They then claim that proceeds from these sales enhance sustainability (5, 6).]

Efforts to prioritize good diets over bad ones meet active resistance. When the U.S. Dietary Guidelines Advisory Committee made recommendations in 2015 for diets that support human and environmental health, the Obama Administration did not accept them, most likely because of pressure from the food industry (7). To advance good diets, the values on which diets are based must be openly discussed, and decisions must prioritize equity and human and environmental health over economic profit. We must make young people aware of the conflict between their values of autonomy and social justice and the manipulation of their food choices by industry (8, 9). Research showing the importance of diet in slowing and reversing negative trends in health and the environment could motivate policy changes. Publicizing this research could help garner the public and government support necessary to counter food industry resistance (7) and its influence on scientific research (10).

David A. Cleveland

Environmental Studies Program and Department of Geography, University of California, Santa Barbara, CA 93106-4160, USA.
Email: cleveland@es.ucsb.edu

REFERENCES

1. J. L. Harris et al., “Food advertising targeted to Hispanic and Black youth: Contributing to health disparities” (The Rudd Center For Food Policy and Obesity, University of Connecticut, 2015); www.uconnruddcenter.org/files/Pdfs/272-7_Rudd_Targeted_Marketing_Report_Release_081115%5B1%5D.pdf.
2. K. R. Siegel et al., *JAMA Intern. Med.* **176**, 1124 (2016).
3. S. M. Martinez, K. Maynard, L. D. Ritchie, “Student Food Access and Security Study” (University of California, Global Food Initiative, Oakland, CA, 2016); www.ucop.edu/global-food-initiative/best-practices/food-access-security/index.html.
4. T. M. Horacek et al., *Public Health Nutr.* **16**, 1186 (2013).
5. University of California, Los Angeles, Purchasing and Accounts Payable, “Purchase & Sponsorship Contract for Pouring Rights” (2013); www.purchasing.ucla.edu/news/purchase-sponsorship-contract-for-pouring-rights.
6. University of California, Santa Barbara, “Business and Financial Services, Procurement Services, Sustainability” (2016); www.bfs.ucsb.edu/procurement/sustainability.
7. C. Gonzalez Fischer, T. Garnett, “Plates, pyramids and planet—Developments in national healthy and sustainable dietary guidelines: A state of play assessment” (2016); www.fcrn.org.uk/fcrn-publications/reports/plates-pyramids-and-planet-%E2%80%93-developments-national-healthy-and-sustainable.
8. C. J. Bryan et al., *Proc. Natl. Acad. Sci. U.S.A.* **113**, 10830 (2016).
9. University of California, San Francisco Center for Vulnerable Populations at San Francisco General Hospital and Trauma Center, and Youth Speaks, “The Bigger Picture” (2016); <http://youthspeaks.org/thebiggerpicture/home/>.
10. D. Schillinger, J. Tran, C. Mangurian, C. Kearns, *Ann. Intern. Med.* **107**, 1616-1634 (2016).

10.1126/science.aak9923

Indirect impacts of climate change

THE VAST MAJORITY of research on climate change impacts on biodiversity has focused on direct impacts, as reviewed by B. R. Scheffers *et al.* ("The broad footprint of climate change from genes to biomes to people," Review, 11 November, p. 719). However, the indirect effects of climate change on biodiversity will likely be far more damaging, given their scale, scope, and speed, especially those that affect already highly-modified landscapes and seascapes (1). These indirect impacts may arise from changes in people's values (such as an increasing desire for national self-sufficiency), socioeconomic drivers (such as escalating global food prices), and policies and use of land and resources that accelerate habitat loss and fragmentation (such as intensification of water management and agriculture).

Scheffers *et al.* focus on the importance of conserving large intact areas and on promoting "human-assisted evolution" through the "managed movement

of individuals or gametes between populations." However, the greater need is to influence land and resource managers' reactive responses to extreme weather events and proactive responses to climate change in ways that help sustain and restore natural processes on which biodiversity and our future well-being depend. This could be achieved by promoting targeted ecosystem-based adaptation actions (2, 3) such as the creation of buffer zones around habitats; habitat conservation, restoration, and creation; and management of the matrix between habitat patches. Species translocation should be a last resort, given the possible adverse impacts on nontarget species and potentially limited wider benefits for biodiversity and ecosystem services, as well as high economic costs and low success rates (4).

**Richard J. Smithers^{1*} and
Malgorzata Blicharska²**

¹Ricardo Energy and Environment, Harwell, Oxon, OX11 0QR, UK. ²Department of Earth Sciences, Uppsala University, 75 236, Uppsala, Sweden.

*Corresponding author.
Email: richard.smithers@ricardo.com

REFERENCES

1. R. J. Smithers *et al.*, *England Biodiversity Strategy Climate Change Adaptation Principles* (Defra, London, 2008).
2. K. R. Jones *et al.*, *Biol. Conserv.* **194**, 121 (2016).
3. T. H. Oliver *et al.*, *Biol. Conserv.* **193**, 17 (2016).
4. T. H. Oliver *et al.*, *J. Appl. Ecol.* **49**, 1247 (2012).

10.1126/science.aal4402

ERRATA

Erratum for the Report "Self-organization of river channels as a critical filter on climate signals" by C. B. Phillips and D. J. Jerolmack, *Science* **354, aal4272 (2016).** Published online 2 December 2016; 10.1126/science.aal4272

Erratum for the Report "Large wind ripples on Mars: A record of atmospheric evolution" by M. G. A. Lapotre *et al.*, *Science* **354, aal4197 (2016).** Published online 2 December 2016; 10.1126/science.aal4197

Erratum for the Technical Comment "Comment on 'Principles of connectivity among morphologically defined cell types in adult neocortex'" by A. L. Barth *et al.*, *Science* **353, aaj2094 (2016).** Published online 23 September 2016; 10.1126/science.aaj2094

Erratum for the Report "Large-scale magnetic fields at high Reynolds numbers in magnetohydrodynamic simulations" by H. Hotta *et al.*, *Science* **353, aai8684 (2016).** Published online 2 September 2016; 10.1126/science.aai8684

AAAS Travels

CHINA by Rail June 6-20, 2017

Sacred Mountains, Grand Canal & Ancient Cities including seven World Heritage sites!

China's high speed rail network offers a terrific and innovative way to explore the Middle Kingdom, making sacred mountain ranges and ancient cities accessible and amazing to behold, including the Terra Cotta Warriors! Discover a China that is off the beaten path with our superb leader team while exploring many fantastic sites! \$4,195 pp + air.

For a detailed brochure, call (800) 252-4910
All prices are per person twin share + air



BETCHART EXPEDITIONS Inc.
17050 Montebello Rd, Cupertino, CA 95014
Email: AAASInfo@betchartexpeditions.com
www.betchartexpeditions.com

FOCUS ON CAREERS

CHINA



South China: A rising power in science

After emerging as a trade superpower, China aims to become a leading force in scientific research and applications ranging from cosmology and spaceflight to genomics and medicine. Universities across south China are stepping up the recruitment of scientists with advanced degrees gained in Europe or the United States. This strategy has yielded prestigious science prizes and papers, and generated the growth of scientific research clusters in the region.

See the full story on page 1448.

Upcoming Features

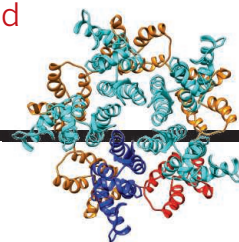
Faculty Careers—February 10
Postdoc Careers—March 17
Postdoc Careers—August 25

Produced by the Science/AAAS Custom Publishing Office

RESEARCH

High-resolution cryo-electron tomography structures of the HIV-1 capsid

Mattei et al., p. 1434



IN SCIENCE JOURNALS

Edited by Stella Hurtley

TORNADOES

Blowing harder and more often

The frequency of tornado outbreaks (clusters of tornadoes) and the number of extremely powerful tornado events have been increasing over nearly the past half-century in the United States. Tippett *et al.* found that tornado outbreaks have become more common since the 1970s. This increase seems to have been driven by consistent changes in the meteorological environment that make tornadoes more likely to form. However, the changes are not necessarily those that one would expect from climate change, which makes it difficult to predict whether this trend will continue. —HJS

Science, this issue p. 1419



Twin tornadoes over farmland in Kansas, USA

AUTOIMMUNITY

A joint effect of bacteria and genetics

Although rheumatoid arthritis is an autoimmune disease, scientists have long suspected that bacterial infections (and in particular, periodontal infections) may play a role in its pathogenesis. König *et al.* now demonstrate that a particular periodontal pathogen called *Aggregatibacter actinomycetemcomitans* (Aa) induces changes in neutrophil function. These lead to hypercitrullination of host proteins, which is also observed in the joints of patients with rheumatoid arthritis. Moreover, an association

between the presence of *HLA-DRB1* allele and increased risk of rheumatoid arthritis was only observed in patients exposed to Aa. Thus, the combination of this allele and Aa exposure could identify high-risk patients. —YN

Sci. Transl. Med. **8**, 369ra176 (2016).

GEOCHEMISTRY

Diamonds rock their metal roots

Massive diamonds are rare, expensive, and captivating. These diamonds now appear to be distinctive not only in their size but also in their origin. Smith *et al.* probed mineral inclusions from these very large diamonds and

found abundant slivers of iron metal surrounded by reducing gases. This suggests that the large diamonds grew from liquid metal in Earth's mantle. The inclusions also provide direct evidence of a long-suspected metal precipitation reaction that requires a more reducing mantle. —BG

Science, this issue p. 1403

CONSERVATION

Too many roads

Roads have done much to help humanity spread across the planet and maintain global movement and trade. However, roads also damage wild areas and rapidly contribute to habitat

degradation and species loss. Ibisch *et al.* cataloged the world's roads. Though most of the world is not covered by roads, it is fragmented by them, with only 7% of land patches created by roads being greater than 100 km². Furthermore, environmental protection of roadless areas is insufficient, which could lead to further degradation of the world's remaining wildernesses. —SNV

Science, this issue p. 1423

PHOTOCHEMISTRY

Asymmetric catalysis by tuning triplets

Triplet excited states manifest a distinct mode of reactivity

associated with their unpaired electrons. However, modulating this reactivity to select just one of two mirror-image products, or enantiomers, is difficult. Blum *et al.* found that Lewis acid coordination lowered the energy of a compound's triplet state, which allowed it to be accessed using an optically excited sensitizer. Because the Lewis acid was essential for triplet formation, it could also direct the reaction pathway toward a single enantiomer. —JSY

Science, this issue p. 1391

INDUCED SEISMICITY Triggered quakes get unconventional

The big earthquakes induced by human activity are mostly linked with disposal of wastewater. However, Bao and Eaton implicate hydraulic fracturing (or fracking) as the culprit in western Canada (see the Perspective by Elsworth). Fracking near Fox Creek, Alberta, reactivated faults, clustering earthquakes along the old fault traces. Fracking does not appear to cause large earthquakes in many other areas that are prone to induced seismicity. Understanding the underlying causes of seismicity in different localities is vital for developing sound regulation to limit damaging earthquakes. —BG

Science, this issue p. 1406;
see also p. 1380

VOLCANOLOGY Volcano monitoring goes into the deep

Axial Seamount is a large and active submarine volcano along the Juan de Fuca mid-ocean ridge off the coast of the western United States. Eruptions in 1998 and 2011 were followed by periods of magma recharge, making it an ideal location to include in the Ocean Observatories Initiative Cabled Array. Wilcock *et al.* present real-time seismic data from the most recent eruption in April 2015 that allow the tracking of

magma before and during eruption. Nooner and Chadwick show that eruptions are predictable on the basis of deformation data. As magma pools underneath it, Axial Seamount inflates and erupts when the inflation hits a threshold. Both studies elucidate the dynamics of submarine volcanoes, which vastly outnumber their aboveground counterparts. —BG

Science, this issue p. 1395, p. 1399

PLANT PATHOLOGY Dueling for sugars

Bacteria thrive on sugar. So do plant cells. Yamada *et al.* now show how the fight for sugar plays out in the extracellular spaces around plant cells when pathogenic bacteria are invading the plant (see the Perspective by Dodds and Lagudah). In the model plant *Arabidopsis*, part of the defense response incited by the presence of pathogenic bacteria includes transcriptional and posttranscriptional regulation of sugar transporters. The resulting uptake of monosaccharides from the extracellular space makes life a little bit more difficult for the invading bacteria. —PJH

Science, this issue p. 1427;
see also p. 1377

RIBOSOMES Getting rid of faulty mRNA

The cell monitors the health of its mRNAs, destroying those that are faulty or damaged. Destruction by the exosome complex prevents them from being used to synthesize deranged and potentially dangerous proteins. Schmidt *et al.* determined the structure of the Ski helicase complex, which guides RNAs to the exosome complex destruction machinery in association with a mRNA-bound ribosome. The end of the mRNA is threaded from the ribosome into the heart of the helicase, whence the message would be channeled into the maw of the exosome complex. —GR

Science, this issue p. 1431

IN OTHER JOURNALS

Edited by **Caroline Ash**
and **Jesse Smith**

STELLAR ASTROMETRY

A star passing close to the solar system

The Gaia astrometry satellite has greatly improved measurements of the position and motion of nearby stars. Berski and Dybczyński searched the Gaia data for the star that will pass closest to the Sun. They found that Gliese 710, a small faint star, will pass within $13,000 \pm 6,000$ astronomical units (one astronomical unit is roughly the distance from Earth to the Sun). That will be well within the Oort Cloud, a collection of small bodies on the outskirts of our solar system. Some of those bodies will be knocked inward, generating large numbers of new comets. Earth is safe for now, though; the encounter will happen in 1.3 million years. —KTS

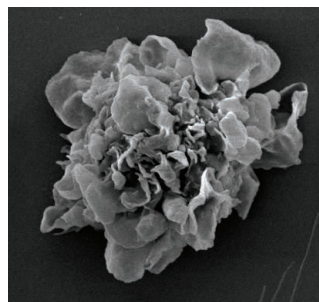
Astron. Astrophys. **595**, L10 (2016).

Many new comets could be produced by the passage of the small star Gliese 710 through the Oort Cloud.

CELL BIOLOGY

Crawling cells need to explore

As it crawls, a cell explores the space in front of it by extending protrusions. These are formed by the branching of actin filaments in the cytoskeleton at the leading edge that push the cell membrane outward. Leithner *et al.* disrupted actin branching in crawling leukocytes and observed profound changes in cell shape. The cells were able to move but were unable to change direction or navigate, whereas wild-type cells oriented in response to chemical gradients and navigated obstacles.



Actin filaments allow cells to explore.

Thus, although actin filament branching is not required to move a crawling cell forward, it is essential for generating the protrusions necessary to explore and navigate a complex three-dimensional environment. —SH

Nat. Cell Biol. **18**, 1253 (2016).

CANCER ETIOLOGY

Poor clock management and cancer

For most people, sleeping and waking on a regular schedule is an aspiration rather than a reality. Unfortunately, it is becoming clear that chronic disruption of the circadian clock, or "social jet lag," can pose health risks. Kettner *et al.* studied mice to explore how jet lag affects liver function experimentally by varying the times at which lights were switched on and off each week. Despite a healthy diet, the jet-lagged mice gained weight and developed fatty liver disease, which progressed to fibrosis and in some cases to hepatocellular carcinoma, a form of liver cancer. The livers of these mice showed

ALSO IN SCIENCE JOURNALS

Edited by Stella Hurtley

ANTIBIOTIC RESISTANCE

Defying the onslaught of antibiotics

Bacterial persistence during and after antibiotic treatment is increasingly recognized to be as challenging as the evolution of genetic resistance in the clinic. Most bacteria, including most pathogens, have an innate ability to enter dormant stages as a bet-hedging strategy to ensure survival of stress. The tactics and mechanistic details are legion. Harms *et al.* review the triggers and signaling involved in bacterial persistence, the important role of toxin/antitoxin modules in persistence, and how persister cells revive. On a more optimistic note, our recent understanding of the mechanisms underlying persistence opens the way to finding adjuvant drugs for antibiotics. —CA

Science, this issue p. 1390

ELECTROCATALYSIS

An activity lift for platinum

Platinum is an excellent but expensive catalyst for the oxygen reduction reaction (ORR), which is critical for fuel cells. Alloying platinum with other metals can create shells of platinum on cores of less expensive metals, which increases its surface exposure, and compressive strain in the layer can also boost its activity (see the Perspective by Stephens *et al.*). Bu *et al.* produced nanoplates—platinum-lead cores covered with platinum shells—that were in tensile strain. These nanoplates had high and stable ORR activity, which theory suggests arises from the strain optimizing the platinum-oxygen bond strength. Li *et al.* optimized both the amount of surface-exposed platinum and the specific activity. They made nanowires with a nickel oxide core and a platinum shell, annealed them to the metal alloy, and then leached

out the nickel to form a rough surface. The mass activity was about double the best reported values from previous studies. —PDS

Science, this issue p. 1410, p. 1403; see also p. 1378

PROTEIN ENGINEERING

Engineering control of cellular proteins

The ability to switch proteins between active and inactive conformations can give insight into their function. Dagliyan *et al.* present a method to insert domains that control protein activity. They computationally identified protein loops that are coupled to the active site. Sensory domains inserted into these loops could modulate protein activity when their conformation was changed by light or ligand binding. The authors engineered domains into three different classes of proteins involved in cell signaling and found that switching the proteins between active and inactive states could control the shape and movement of living cells. —VV

Science, this issue p. 1441

STRUCTURAL BIOLOGY

Rescuing stalled ribosomes

A small percentage of bacterial mRNAs lack a stop codon. Ribosomes stall at the end of such mRNAs, and the buildup of stalled ribosomes can be lethal. The primary rescue mechanism, in which translation continues on a piece of RNA that contains a stop codon, is a drug target. However, bacteria have another backup plan. James *et al.* present structures that show that ArfA (alternative rescue factor A) substitutes for a stop codon by binding in the ribosomal mRNA channel and recruiting RF2 (release factor 2). It mediates conformational changes

required for RF2 to catalyze peptide release. —VV

Science, this issue p. 1437

CLIMATE CHANGE

The seas will rise, but by how much?

As Earth's climate warms, sea levels are projected to rise as a result of the expansion of ocean waters and melting of glaciers and ice sheets. But uncertainties over the magnitude of the rise make it difficult to develop appropriate policies. In a Perspective, Oppenheimer and Alley highlight recent studies that project higher sea levels by 2100 than the most recent assessment report of the Intergovernmental Panel on Climate Change. The main factor leading to these higher estimates is a larger projected contribution from the Antarctic ice sheet. Policy-makers would do well to develop flexible flood defense approaches that can be adapted as the scientific understanding of Antarctic ice loss evolves. —JFU

Science, this issue p. 1375

VASCULAR DISEASE

Preventing vascular calcification

The arterial calcification that develops in patients with the genetic disease ACDC (arterial calcification due to deficiency of CD73) leads to peripheral ischemia. Cells from these patients have increased levels of an enzyme that degrades pyrophosphate, a compound that inhibits calcification. Jin *et al.* found that cells from ACDC patients had decreased pyrophosphate levels and increased activity of the mTOR pathway, which promotes calcification. These cells formed calcified teratomas when injected into mice. Teratoma calcification was reduced by treating the mice with a mTOR inhibitor or a drug

that resembles pyrophosphate, suggesting new treatment options for this disease. —AV

Sci. Signal. **9**, ra121 (2016).

STRUCTURAL BIOLOGY

Structural insights into capsid flexibility

Viral capsids are protein structures that enclose the genetic material of viruses. Previous structural studies of the HIV-1 capsid have relied on recombinant, cross-linked, or mutant capsid proteins. Mattei *et al.* now report subnanometer-resolution cryo-electron tomography structures of the HIV-1 capsid from intact virions. These structures confirm the hollow cone shape of the capsid and allow for the specific placement of each individual capsid hexamer and pentamer within the lattice structure. The structures also reveal the flexible nature of the capsid, which likely helps it to accommodate interactions with host cell factors. —KLM

Science, this issue p. 1434

REVIEW SUMMARY

ANTIBIOTIC RESISTANCE

Mechanisms of bacterial persistence during stress and antibiotic exposure

Alexander Harms, Etienne Maisonneuve, Kenn Gerdes*

BACKGROUND: The escalating crisis of multidrug resistance is raising fears of untreatable infections caused by bacterial “superbugs.” However, many patients already suffer from infections that are effectively untreatable due to innate bacterial mechanisms for persistence. This phenomenon is caused by the formation of specialized persister cells that evade antibiotic killing and other stresses by entering a physiologically dormant state, irrespective of whether they possess genes enabling antibiotic resistance. The recalcitrance of persister cells is a major cause of prolonged and recurrent courses of infection that can eventually lead to complete antibiotic treatment failure. Regularly growing bacteria differentiate into persister cells stochastically at a basal rate, but this phenotypic conversion can also be induced by environmental cues indicative of imminent threats for the bacteria. Size and composition of the persister subpopulation in bacterial communities are largely controlled by stress signal-

ing pathways, such as the general stress response or the SOS response, in conjunction with the second messenger (p)ppGpp that is almost always involved in persister formation. Consequently, persister formation is stimulated under conditions that favor the activation of these signaling pathways. Such conditions include bacterial biofilms and hostile host environments, as well as response to damage caused by sublethal concentrations of antibiotics.

ADVANCES: The limited comprehensive understanding of persister formation and survival is a critical issue in controlling persistent infections. However, recent work in the field has uncovered the molecular architecture of several cellular pathways underlying bacterial persistence, as well as the functional interactions that generate heterogeneous populations of persister cells. These results confirm the long-standing notion that persistence is intimately connected to slow growth or dormancy in the sense that

a certain level of physiological quiescence is attained. Most prominently, the central role of toxin-antitoxin (TA) modules has been explained in considerable detail. In the model organism *Escherichia coli* K-12, two major pathways of persister formation via TA modules are both controlled by (p)ppGpp and involve toxin HokB and a panel of mRNA endonuclease toxins, respectively. Whereas activation of the membrane-associated toxin HokB depends on the enigmatic

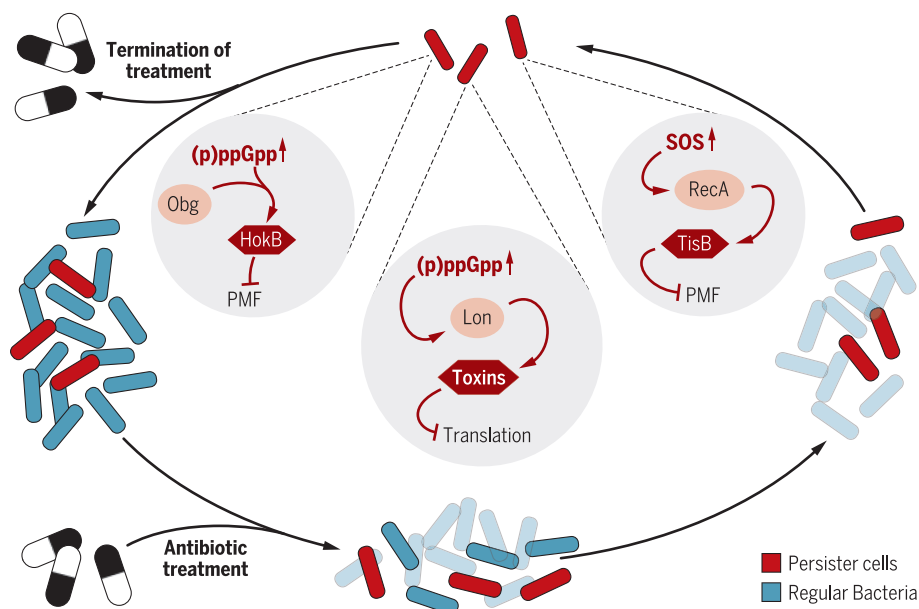
ON OUR WEBSITE

Read the full article at <http://dx.doi.org/10.1126/science.aaf4268>

guanosine triphosphatase (GTPase) Ogb and causes persister formation by abolishing the proton-motive force, mRNA endonuclease toxins are activated through antitoxin degradation by

protease Lon and globally inhibit translation. In addition to these two pathways, toxin TisB is activated in response to DNA damage by the SOS response and promotes persister formation in a manner similar to HokB. Beyond TA modules, many additional factors (such as cellular energy metabolism or drug efflux) have been found to contribute to persister formation and survival, but their position in particular molecular pathways is often unclear. Altogether, this diversity of mechanisms drives the formation of a highly heterogeneous ensemble of persister cells that displays multistress and multidrug tolerance as the root of the recalcitrance of persistent infections.

OUTLOOK: Though recent advances in the field have greatly expanded our understanding of the molecular mechanisms underlying persister formation, important facets have remained elusive and should be addressed in future studies. One example is the upstream signaling input into the pathways mediating bacterial persister formation (e.g., the nature of the pacemaker driving stochastic persister formation). Similarly, it is often not well understood how—beyond the general idea of dormancy—persister cells can survive the action of lethal antibiotics. Finally, one curious aspect of the persister field is recurrent inconsistency between the results obtained by different groups. We speculate that these variations may be linked to subtle differences in experimental procedures inducing separate yet partially redundant pathways of persister formation. It is evident that the elucidation of this phenomenon may not only consolidate progress in the field but also offer the chance to gain insights into the molecular basis and control of bacterial persistence. ■



Bacterial persisters defy antibiotic treatment. Persister cells are phenotypic variants of regularly growing bacteria and survive lethal antibiotic treatment in a nongrowing, dormant state. Upon termination of treatment, the resuscitation of persister cells can replenish the population. Our Review focuses on the diverse molecular mechanisms that underlie bacterial persister formation and drive the heterogeneity of these cells. PMF, proton-motive force.

Center of Excellence for Bacterial Stress Response and Persistence (BASP), Department of Biology, Ole Maaløes Vej 5, DK-2200 Copenhagen, Denmark.

*Corresponding author. Email: kgerdes@bio.ku.dk
Cite this article as A. Harms et al., *Science* 354, aaf4268 (2016). DOI: 10.1126/science.aaf4268

REVIEW

ANTIBIOTIC RESISTANCE

Mechanisms of bacterial persistence during stress and antibiotic exposure

Alexander Harms, Etienne Maisonneuve, Kenn Gerdes*

Bacterial persister cells avoid antibiotic-induced death by entering a physiologically dormant state and are considered a major cause of antibiotic treatment failure and relapsing infections. Such dormant cells form stochastically, but also in response to environmental cues, by various pathways that are usually controlled by the second messenger (p)ppGpp. For example, toxin-antitoxin modules have been shown to play a major role in persister formation in many model systems. More generally, the diversity of molecular mechanisms driving persister formation is increasingly recognized as the cause of physiological heterogeneity that underlies collective multistress and multidrug tolerance of persister subpopulations. In this Review, we summarize the current state of the field and highlight recent findings, with a focus on the molecular basis of persister formation and heterogeneity.

Antibiotic-resistant infections are presently a leading cause of anxiety surrounding public health policy (1). Typically, the current escalation in the acquisition of genetic resistance determinants has been seen as the main driver of this phenomenon. But this is only part of the story. Bacterial persistence is increasingly recognized as another major cause of antibiotic treatment failure and relapsing infections (2–4). Unlike antibiotic resistance that denotes the inherited ability of bacteria to grow in the presence of an antibiotic, bacterial persistence is based on the formation of rare persister cells that transiently display phenotypic tolerance to antibiotic treatment (5). These specialized survivor cells evade antibiotic killing by entering a physiologically dormant state—that is, at the cost of essentially complete abrogation of bacterial growth. The presence of persister cells can be easily detected by the “biphasic killing” phenomenon of bacterial cultures exposed to bactericidal antibiotics: Characteristically, an initial, rapid drop in bacterial counts represents the death of the majority of the population, followed by a second phase with much slower kinetics that reflects the poor killing of persister cells (Fig. 1) (6). This tolerance of persister cells and their ability to reinitiate growth after the termination of antibiotic treatment are commonly seen as main causes for the persistent and relapsing course of many bacterial infections (2, 3). Despite considerable efforts and recent advances in the field, major hurdles to efficient strategies against persisters remain, including a lack of comprehensive understanding of which physiological properties and

molecular mechanisms underlie their formation, survival, and resuscitation (3, 5, 7, 8).

Clinical relevance of persisters

Bacterial infections have always been a scourge of mankind, but rates of morbidity and mortality related to these infections have declined over the past century, owing to lifestyle improvements as well as the discovery and extensive use of antibiotics. The prevailing crisis of antibiotic resistance has therefore raised fears that we are descending into a postantibiotic “era of untreatable infections” (9). Already today, however, many patients suffer from bacterial infections that defy massive, long-lasting, and repeated antimicrobial treatment regardless of genetically acquired antibiotic resistance. These infections are often chronic and are never fully cleared by antibiotic treatment because bacteria can persist in biofilms or other protected niches (10, 11). The recalcitrance of bacterial persister cells is well established as a cause for these prolonged and recurrent infections, leading to eventual treatment failure (2–4, 11). Clinical examples are urinary tract infections with uropathogenic strains of *Escherichia coli*; the notoriously recalcitrant infections with *Mycobacterium tuberculosis*; or opportunistic infections of implanted devices, open wounds, and other body lesions typically caused by biofilms of *Pseudomonas aeruginosa* or *Staphylococcus aureus* (10, 12).

Heterogeneous populations of persisters that display antibiotic tolerance, slow growth, and the ability to reinitiate infection after antibiotic treatment have been directly observed in diverse animal models of bacterial infection with *Salmonella*, uropathogenic *E. coli*, or *M. tuberculosis* (12–17). In vitro, bacterial persisters inside host cells exhibit greatly increased tolerance to antibiotic treatment (12, 15, 18), and the hostile environment in phagocytic vacuoles of macrophages directly in-

duces *Salmonella* persister formation (15). The standard treatment of chronic infections, which is based on the cyclic administration of high doses of antibiotics, is clearly linked to greatly increased persister levels of clinical isolates and has repeatedly been shown in vitro to rapidly select for mutants displaying particularly high rates of persister formation (18–26). Apart from problems with antibiotic tolerance itself, bacterial persisters have also been described as a “catalyst” for the emergence of genetic resistance (19) because different stress signaling pathways commonly involved in persister formation are known to enhance mutation rates and activate mobile genetic elements (27, 28).

Dormancy and the physiology of persisters

Bactericidal antibiotics poison essential cellular processes to cause lethal damage (29). The survival of persister cells is usually explained by their transition into a “dormant” state hallmarked by a reversible and substantial reduction of growth rate and metabolism that protects the cellular processes otherwise poisoned by bactericidal antibiotics (5, 7). In 1944, Joseph Bigger initially discovered persisters and described them as cells surviving antibiotic treatment in a “dormant, non-dividing phase” (30). More globally, it has been proposed that bacterial communities in all ecosystems generate dormant cells as a perseverant “seed bank” that enables the population to recover and repopulate the habitat after catastrophic events (31). Therefore, persisters are likely just one face of a more general bacterial strategy to cope with dynamic and latently hostile environments. This hypothesis is in line with the finding that bacterial killing—not only by antibiotics but also by environmental hazards such as acid stress,

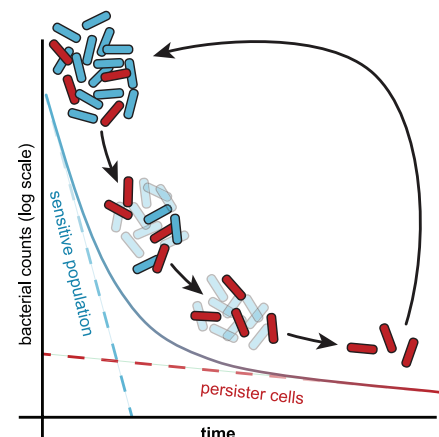


Fig. 1. Biphasic killing kinetics of bactericidal antibiotic treatment. A lethal dose of bactericidal antibiotic added at time zero rapidly eradicates the sensitive bulk of the population (blue) until only non-growing persister cells (red) that are killed at a slower rate remain. The slower killing has been interpreted to reflect the persister resuscitation rate, but this remains to be substantiated experimentally. The termination of antibiotic treatment enables the population to be replenished by resuscitation of surviving persisters.

Center of Excellence for Bacterial Stress Response and Persistence (BASP), Department of Biology, Ole Maaløes Vej 5, DK-2200 Copenhagen, Denmark.

*Corresponding author. Email: kgerdes@bio.ku.dk

toxic metals, or heat—displays biphasic kinetics (32).

However, it is clear that the nonreplicating state of persisters is not sufficient for survival because bacteriostatic conditions do not necessarily induce antibiotic tolerance (33, 34). One study using flow cytometry showed that most dormant cells were not antibiotic-tolerant, although persisters were strongly enriched in the physiologically dormant fraction of the population (35). It is therefore evident that “persisters are not simply non-growing cells” (36) but that persister formation involves specific qualitative changes of bacterial physiology to enable survival and resuscitation. Apart from persisters surviving in dormancy, the stochastic drop in expression of a prodrug-activating enzyme has been described as “dynamic persistence” characterized by transient antibiotic tolerance of growing bacteria (37). However, this mechanism of drug avoidance could also be seen as stochastically expressed resistance rather than as persister formation in the true sense.

Persister formation in bacterial populations

Genetic basis of a phenotypic conversion

Strong experimental evidence supports the notion that the signaling that controls bacterial persistence and the mechanisms directly mediating persister formation are genetically encoded (5, 7, 20, 38–42). An alternative model—“persistence as stuff happens”—explains persisters as accidentally nongrowing cells arising from “errors and glitches” (i.e., random cell malfunctioning) (43) but conflicts with the growing literature on defined molecular pathways as the basis of bacterial persistence. The genetic heritability of these pathways enables the frequency of persister formation to adapt to the incidence of antibiotic treatment. For example, recurrent antibiotic treatment is clearly linked to raised levels of persisters in clinical isolates and can rapidly select for increased persistence up to population-wide tolerance in vitro (18–26, 44). However, persister formation also has a pleiotropic fitness cost that selects for reduced levels of persistence in the absence of antibiotic treatment, though the evolution along this path appears to be rather slow, at least under laboratory conditions (15, 22, 23). In natural populations, the forces driving the evolution of persister frequencies seem to be highly variable because persister levels differ widely between different species and strains (23, 45–47).

Stochastic and responsive persister formation

Bacterial persister formation is driven by a combination of stochastic and responsive mechanisms that allow organisms to respond when harmful conditions are sometimes, but not always, preceded by a stress signal (48). Stochastic persister formation is typically interpreted as bet-hedging—that is, an evolutionary strategy relying on phenotypic heterogeneity to maximize the fitness of an isogenic population in dynamic environments (49, 50). This concept implies that some persister cells have formed before the onset of lethal antibiotic treatment. Direct observations from single-

cell microfluidics and flow cytometry show that cells surviving antibiotic treatment had largely been part of a preexisting dormant subpopulation of exponentially growing *E. coli* (6, 34, 35, 51, 52). Furthermore, bacteria can respond to environmental cues by quantitatively and qualitatively modulating the rate of phenotypic conversion into persister cells, a concept known as responsive diversification (53). As a simple example, the application of sublethal levels of virtually any stress, including antibiotic treatment, has been shown to stimulate bacterial persister formation (26, 41, 54, 55).

Cellular signaling upstream of persister formation

Both stochastic and responsive persister formation are controlled by the same panel of signaling pathways. These include conserved components, such as (p)ppGpp signaling, that are integral to nearly all persister formation, whereas other pathways, such as the SOS response or hypoxia signaling, have mostly modulatory roles (Fig. 2).

Stringent response and (p)ppGpp signaling

Guanosine tetraphosphate (ppGpp) and guanosine pentaphosphate (pppGpp) collectively act in the “stringent response” as the ubiquitous second messenger and “alarmone” (p)ppGpp that is typically produced in response to nutrient starvation and other stresses to reprogram cellular physiology from growth to metabolic homeostasis and survival functions (56, 57). In *E. coli*, (p)ppGpp synthetase RelA is activated by amino acid starvation and heat shock, whereas carbon, nitrogen, phosphate, iron, and fatty acid starvation activate the (p)ppGpp synthetase activity of the bifunctional synthetase/hydrolase enzyme SpoT. Once produced, (p)ppGpp modulates bacterial physiology

by transcriptional reprogramming and the direct adjustment of target protein activities (56–58). Across diverse organisms and experimental models, mutants unable to produce (p)ppGpp often show reduced levels of persister formation. For example, *relA spoT* mutants of *E. coli* and *Pseudomonas aeruginosa* exhibit defective persister formation during exponential growth, in biofilms, and in the stationary phase (33, 40, 51, 59, 60). The magnitude of this phenotype is highly context-dependent, confirming that complementary signaling plays important roles in guiding persister formation. Similarly, (p)ppGpp signaling has been repeatedly implicated in persister formation and antibiotic tolerance in Gram-positive organisms such as *Enterococcus faecalis* or *S. aureus* (61, 62). However, the molecular basis of this contribution remains to be elucidated, and one recent study was unable to detect an effect of (p)ppGpp signaling on the persistence of *S. aureus* under their experimental conditions (63).

Bacterial persister formation can be triggered by a seemingly stochastic activation of (p)ppGpp signaling in rare cells during exponential growth (51) and by environmental conditions that stimulate the production of (p)ppGpp (e.g., in biofilms or during the stationary phase) (Fig. 2). Bacterial biofilms are surface-associated multicellular communities that are characteristically embedded in a thick extracellular matrix and are prevalent in the environment as well as during infections (10, 11). Though the physical structure of biofilms shields the bacterial community from hostile conditions, including immune responses, many antibiotics readily penetrate into the biofilm core (11, 64). Therefore, the notorious recalcitrance of biofilms to antibiotic treatment and their propensity to relapse have largely been attributed to the high amounts of persisters that form inside a structure (11, 64, 65). Biofilms typically harbor 100- to

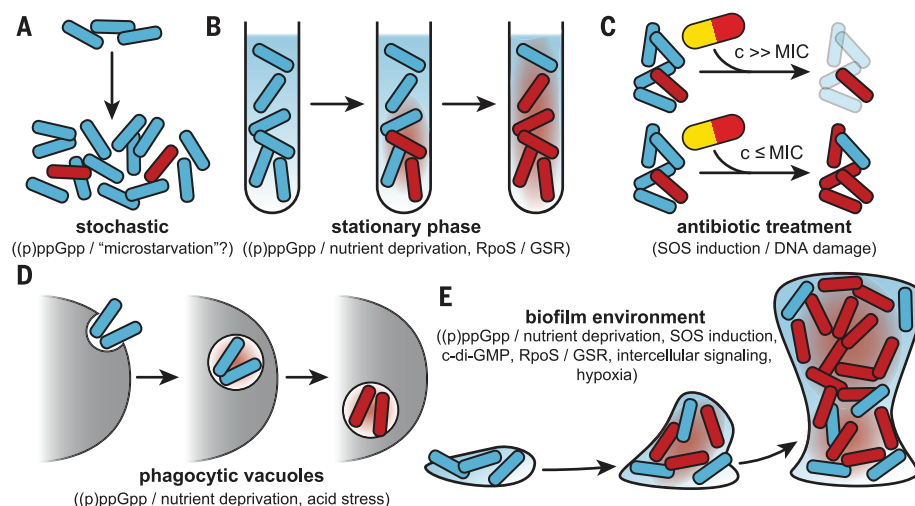


Fig. 2. Environmental cues and cellular signals underlying persister formation. Beyond a basis of stochastic persister formation (A), different environmental cues activate bacterial signaling to induce the formation of persister cells (red) from regular growing cells (blue). For example, the transition into bacterial persistence is strongly induced by the stationary phase (B), sublethal antibiotic treatment (C), and phagocytosis by immune cells (D), as well as in biofilms (E). GSR, general stress response; c, concentration; MIC, minimum inhibitory concentration.

1000-fold more persisters than planktonic cultures (2, 51, 65, 66). These high rates of persister formation depend on (p)ppGpp as well as on other signaling processes, including diverse stress responses such as SOS induction, hypoxia, or the sessility-associated second messenger cyclic di-guanylate (commonly known as cyclic di-GMP) (51, 59, 66–68). The stationary phase of bacterial cultures is also hallmarked by a quiescent and highly stress-tolerant physiology induced by the integration of (p)ppGpp signaling and various stress response pathways dominated by the RpoS regulon (69, 70). Consequently, stationary-phase cultures can easily harbor 10^3 to 10^4 times more persisters than exponentially growing cultures (26, 51, 65, 71, 72). A special case of persisters are those whose formation is induced by diauxic transitions between using a preferred carbon source and using an alternative one. During such lag periods, (p)ppGpp production is combined with catabolite derepression (i.e., signaling through the second messenger cyclic adenosine monophosphate) (38, 53, 73).

RpoS and the general stress response

The default pathway of a given bacterium to respond to adverse conditions is known as the general stress response. In many proteobacteria such as *E. coli* and *P. aeruginosa*, this response largely relies on transcriptional reprogramming via the alternative sigma factor RpoS (74). In *E. coli*, the general stress response can be induced in the stationary phase by nutrient deprivation and/or (p)ppGpp, temperature stress, biofilm formation, extreme pH, oxidative stress, and several other cues (70). Beyond globally enhancing stress tolerance of the population, RpoS is also a regulator of bacterial persister formation (Fig. 2). The dual role of RpoS in controlling population-wide stress tolerance and persister formation in single cells results in divergent phenotypes of *rpoS* knockouts: Under conditions that would induce the general stress response, these mutants can display increased or decreased tolerance, depending on the experimental setup (55, 66, 75–77), whereas the low levels of RpoS in exponentially growing *E. coli* do not seem to relevantly contribute to persister formation (33, 74).

The SOS response

The SOS regulon comprises genes mostly involved in DNA repair and is induced in response to DNA damage caused by stochastic cell malfunctioning or various conditions such as oxidative stress, extreme pH, blocked DNA replication, and antibiotic treatment (78). More specifically, the SOS response is ultimately induced by the RecA protein that is activated by single-stranded DNA generated from the processing of damaged DNA (78). The role of the SOS response in bacterial persistence is twofold: first as a pathway of complementary stress signaling that modulates persister formation and second as a provider of diverse DNA repair functions that are important for persister resuscitation (see below). Consistently, SOS-deficient mutants usually exhibit a considerable drop in the number of surviving

persisters, particularly upon treatment with DNA-damaging agents (26, 41, 67, 75, 79). However, it is often not clear which of the two roles of the SOS response is responsible for this phenotype.

Bacterial communication

Since bet-hedging and responsive diversification optimize the fitness of a clonal population by managing the investment of community resources into phenotypically distinct subpopulations, it is not surprising that bacterial communities coordinate persister formation with the help of intercellular signaling molecules (Fig. 2). For example, quorum sensing of pyocyanine or acyl-homoserine lactone and the stress-inducible quorum-sensing peptide CSP (competence-stimulating peptide) can induce persister formation of *P. aeruginosa* and *Streptococcus mutans*, respectively (80, 81). Similarly, the widespread bacterial signaling molecule indole can modulate persister formation of *E. coli*, though the molecular mechanism of indole sensing is still a matter of debate (8, 82).

Persister heterogeneity

The original concept of persister dormancy as a state in which antibiotic targets are generally inactive implied that persister cells should exhibit a rather homogeneous profile of multidrug tolerance. However, direct experimentation typically revealed divergent profiles of antibiotic tolerance and susceptibility among persisters in a given culture (38, 45, 46, 83). True multidrug-tolerance was detected for only a small proportion of persister cells, but one may speculate that the heterogeneity of persisters enables survival of the population under a wide range of harmful conditions, as expected from the concept of bet-hedging. The differential tolerance and cross-tolerance patterns of cells within the persister subpopulations result from physiological differences among the persister cells, probably reflecting different molecular mechanisms of their formation. Mutations affecting bacterial persister formation often compromise tolerance to different antibiotics unevenly, which has also been observed with persisters induced by special growth conditions or genetic manipulations (33, 38, 41, 66, 84). For example, persisters tolerant to β -lactams and fluoroquinolones are induced by broadly similar cellular signaling in the diauxic transition model of *E. coli*, but full β -lactam tolerance required higher levels of (p)ppGpp than fluoroquinolone tolerance (38).

Persister formation by TA modules Biology of toxins and antitoxins

Bacterial toxin-antitoxin (TA) modules are genetic elements composed of a toxin protein that inhibits bacterial growth by interfering with essential cellular processes and an antitoxin that prevents or impairs the functionality of the toxin until this inhibition is abrogated in response to cellular signaling (85, 86). TA modules are classified according to the nature of the antitoxin and its mechanism of action, but thus far, only type I and type II TA modules have been widely studied in the context of persister formation. Whereas

the antitoxins of type I TA modules inhibit toxin expression as antisense RNAs (87, 88), the antitoxins of type II TA modules are proteins that inactivate their cognate toxins in direct protein-protein interactions (85, 86). Type I toxins are usually small proteins that form pores in bacterial membranes to collapse the proton-motive force and halt adenosine triphosphate (ATP) synthesis, but they can also act via different mechanisms (87). The molecular activities of type II toxins are highly diverse, but most are translation inhibitors (85). For example, type II toxins can impair translation as ribosome-dependent or -independent mRNA endonucleases (RelE or MazF families, respectively); cleave rRNA or tRNA molecules (VapC family); or inactivate elongation factors, tRNA, and tRNA synthetases by posttranslational modification (Doc, TacT, and HipA families, respectively) (85, 86, 89, 90).

TA modules in stress and persister formation

Activation of TA modules requires sufficient expression of the toxin component and a disruption of the toxin/antitoxin balance in favor of the toxin. Type I and II TA modules are usually controlled by a combination of transcriptional and post-transcriptional regulation, as well as antitoxin degradation in response to cellular signaling (87, 91). In *E. coli*, the *tisB/istR* and *hokB/sokB* type I TA modules are activated by the SOS response and (p)ppGpp signaling, respectively (40, 41). Type II antitoxins are usually degraded by the protease Lon in response to (p)ppGpp signaling or oxidative stress, although degradation by ClpP has also been described (51, 91–93).

Graded activation of TA modules in a way that does not completely abrogate bacterial growth enables cells to adjust growth rates and modify bacterial physiology to enhance stress tolerance (86, 94, 95). However, the activation of TA modules mostly exerts a robust switching into dormancy once free toxin levels have crossed a certain threshold, and this behavior is typically supported by transcriptional autoregulation (96, 97). The enforced expression of toxins of diverse type I or II TA modules often causes bacteriostatic growth inhibition that coincides with massively increased antibiotic tolerance, thus directly implicating TA modules in persister formation (39–41, 52, 81, 84, 98). Consistently, the transcriptomes of persister cells reveal an up-regulation of TA modules in *E. coli* and *M. tuberculosis* (52, 72, 84, 99). Furthermore, a considerable jump in antibiotic tolerance has been obtained by the treatment of *E. coli* with drugs that mimic the action of type I or II TA modules (100), and clones selected for increased persister levels often carry known or suspected gain-of-function mutants of TA modules (18, 20, 21, 24, 44). However, genetic screens have mostly failed to detect any strong effect of TA module loss-of-function mutants on persister frequencies under standard conditions (77, 81, 101, 102), indicating that persister formation by TA modules exhibits considerable functional redundancy. This hypothesis has been experimentally confirmed in *E. coli*, where the

consecutive deletion of 10 mRNA endonuclease TA modules showed the cumulative effects of different TA modules only after the first 5 had been knocked out (39).

Notably, single TA module knockouts occasionally display defects in persister formation, although these phenotypes are often very specific. For example, single knockouts in any mRNA endonuclease TA module had no effect on persister formation in exponentially growing *E. coli* (39). However, a mutant of *yafQ* (a RelE family mRNA endonuclease) displayed markedly reduced levels of persister cells in biofilms (103), and *mqsR* (another RelE homolog) or *relE* knockouts were impaired in the formation of long-time tolerant stationary-phase persisters (75). These results suggest that the roles of given TA modules in persister formation in natural environments may be highly context-dependent, and different TA modules may possibly be wired to distinct upstream signaling pathways (93, 104). Furthermore, it is clear that the different molecular mechanisms of distinct TA module toxins result in the formation of physiologically distinct persister cells. Consistently, the overexpression of different toxins induces distinct profiles of antibiotic tolerance (41, 52, 84, 105).

The observed accumulation of large numbers of TA modules—particularly in organisms that are adapted to dynamic environments including chronic, persistent infections—likely mediates both functional redundancy as well as the characteristic heterogeneity of persister cells. Typical examples for organisms that fit this pattern are *E. coli*, *M. tuberculosis*, and *Salmonella enterica* serovar Typhimurium (106). A recent dedicated study further showed that persister levels in different strains and species of the genus *Pseudomonas* correlate with the number of type II TA modules (47).

TA modules in the persistence of *E. coli* K-12

By far, the molecular basis of bacterial persister formation has been most intensively studied in the model organism *E. coli* K-12. This organism encodes at least ~30 TA modules: Of these, roughly half are type I and half are type II, with only few belonging to other types (85). A considerable number of these TA modules contribute to persister formation in three major pathways that have been elucidated in detail and provide useful examples for the molecular basis of bacterial persistence in general (Fig. 3).

mRNA endonucleases under control of (p)ppGpp and Lon

A set of 10 mRNA endonuclease type II TA modules in *E. coli* K-12 is under the control of (p)ppGpp, inorganic polyphosphate, and protease Lon in a linear, hierarchical signaling pathway (Fig. 3) (57). During rapid growth, this pathway is triggered in rare cells that contain high levels of (p)ppGpp as a result of seemingly random physiological fluctuations (57). Through competitive inhibition of the polyphosphate hydrolase PPX, (p)ppGpp causes the accumulation of polyphosphate produced by polyphosphate kinase PPK which, in turn, stim-

ulates protease Lon to degrade type II TA module antitoxins. Most importantly, the activation of 10 mRNA endonuclease TA modules inhibits global translation and thereby induces persister formation (39). Moreover, Lon degrades the HipB antitoxin of the HipBA type II TA module and hence frees the HipA toxin that inactivates aminoacyl-tRNA synthetase GltX by phosphorylation at its active site (92, 107). The resulting appearance of uncharged tRNAs at the ribosomal A site triggers RelA-dependent (p)ppGpp synthesis, presumably inducing a positive-feedback loop that causes sustained activation of the 10 mRNA endonucleases and HipA (34). In parallel, the mRNA endonuclease toxins limit the entry of uncharged tRNA into the ribosome through mRNA degradation and can thereby control the amplitude and duration of (p)ppGpp peaks via negative feedback (108). The critical role of the “master TA module” HipBA is highlighted by the repeated isolation of *hipBA* gain-of-function alleles upon

selection for increased persister formation of *E. coli* in vitro, as well as in clinical strains. These alleles caused substantially increased levels of persister formation (e.g., by interference with transcriptional autoregulation of the TA module) (18, 20, 109).

The SOS response and SOS-regulated TA modules

Among a diverse array of functions predominantly mediating DNA repair, the SOS response of *E. coli* controls the activation of two type I TA modules (*tisB/istR* and *symE/symR*), as well as two type II TA modules (*dinJ/yafQ* and *yafNO*) (67, 78). Whereas the SOS-dependent DNA repair functions seem to be generally essential for the survival of fluoroquinolone treatment (see below), the TisB toxin was found to be additionally required for the formation of highly fluoroquinolone-tolerant persisters by exponentially growing *E. coli* (41). TisB is a small protein that forms pores in

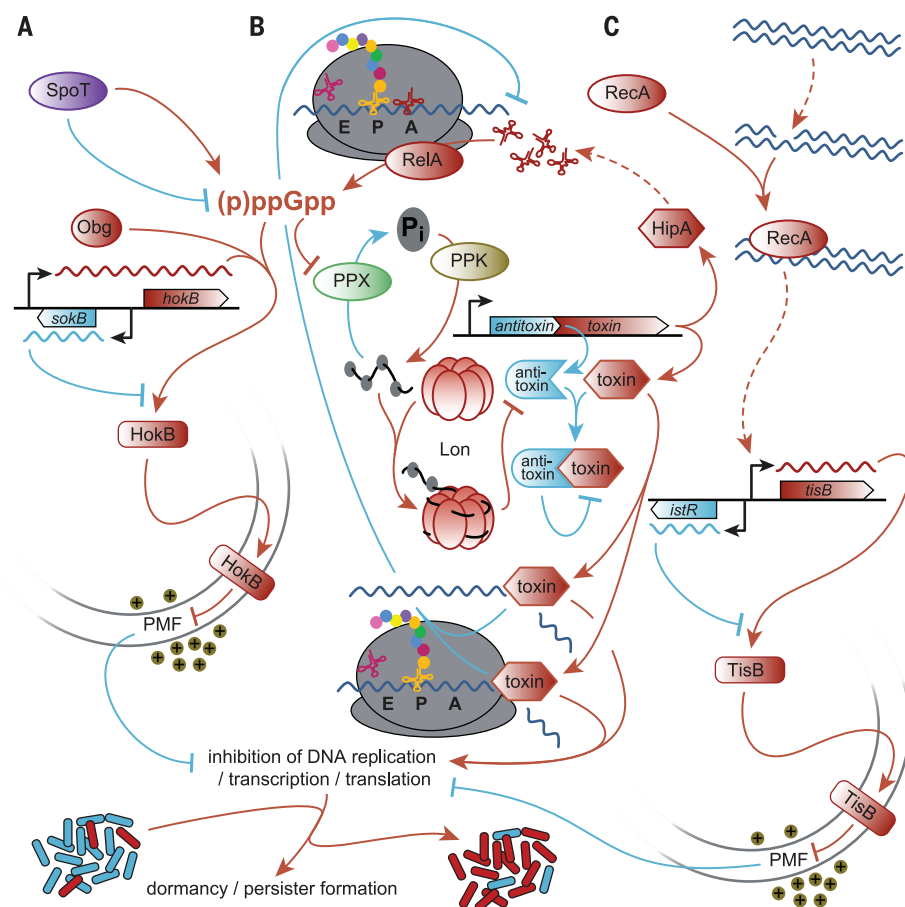


Fig. 3. Toxin-antitoxin modules and persister formation in *E. coli*. Three major pathways of persister formation in *E. coli* K-12 that rely on the activation of toxin-antitoxin (TA) modules are presented in detail, with mechanisms promoting and counteracting persister formation shown in red and blue, respectively. The Obg/HokB pathway (A) and the polyphosphate/Lon/mRNA interferase pathway (B) are under the control of (p)ppGpp signaling, whereas the TisB pathway (C) is activated upon strong SOS induction. Type I toxins HokB and TisB induce persister formation by abolishing the proton-motive force (PMF) as membrane-associated peptides, whereas the 10 mRNA endonuclease type II toxins interfere with ribosomal translation. Note that the latter pathway involves both positive feedback (via HipA) and negative feedback (via the drop of mRNA levels). E, P, and A denote ribosomal exit, peptidyl, and aminoacyl tRNA binding sites, respectively; Pi, inorganic phosphate.

the bacterial inner membrane and thereby disrupts the proton-motive force that inhibits ATP synthesis and induces dormancy (Fig. 3). Endogenously expressed TisB only affected tolerance to fluoroquinolones, whereas the overexpression of TisB caused multidrug tolerance (41). It therefore appears that the levels of SOS induction achieved by random activation in exponentially growing *E. coli* are insufficient to trigger TisB expression, possibly due to the lack of a positive-feedback loop like the one implemented by HipBA for the formation of mRNA endonuclease persisters (see above).

HokB toxin under the control of Obg and (p)ppGpp

Obg is an enigmatic, yet essential and highly conserved guanosine triphosphatase (GTPase) believed to adapt ribosome functioning, DNA replication, and stress responses to the energy status of the cell. A recent study showed that cellular levels of Obg determine the proportion of persister cells in the population (40). This property of Obg depended on the production of (p)ppGpp, which caused up-regulation of the type I toxin HokB in accord with Obg levels (40). Like TisB, HokB is a membrane-targeted type I toxin that disrupts the proton-motive force to impair ATP synthesis and induce dormancy (Fig. 3) (40).

TA modules in persistence of other bacteria

In *Salmonella* Typhimurium, different subsets of the at least 5 type I and 13 type II TA modules of this organism were shown to promote survival inside fibroblasts and epithelial cells, respectively

(110). Many of these TA modules were also activated by the acidic and nutrient-poor environment in vacuoles after phagocytosis by macrophages, which induced the formation of a heterogeneous set of multidrug-tolerant persisters in a manner dependent on (p)ppGpp signaling, Lon, and diverse type II TA modules (Fig. 3) (15). In contrast to the seemingly similar persister pathway of *E. coli* K-12, single TA module knockouts showed strong defects in persister formation in this model, suggesting that the activity of different TA modules may be linked by some kind of regulatory mechanism (15, 110). The notoriously persistent pathogen *M. tuberculosis* encodes at least ~80 TA modules, of which many have been shown to be functional in vivo and to differentially affect antibiotic tolerance or virulence in animal infection models (90, 111–113). Though the interplay of different TA modules in this repertoire is not understood at the global level, the synergistic contribution of some subsets to stress and drug tolerance under given conditions suggests a certain degree of functional specialization (112, 113).

Unlike these organisms, *P. aeruginosa* encodes comparatively few easily detectable TA modules for a generalistic organism that is obviously adapted to highly dynamic environments [six and eight predicted type II TA modules in strains PAO1 and PA14, respectively (114)]. Though persister levels in *Pseudomonas* seem to be generally linked to the abundance of type II TA modules (47), none of these has ever been demonstrated to participate in persister formation. Instead, published work suggests that *P. aeruginosa* largely relies on other strategies, such as the enforced activity of antioxidative defenses (see below)

and/or a pathway dependent on Ogb but, unlike in *E. coli*, lacking an obvious homolog of HokB (40, 59). Similarly, it was recently shown that the deletion of known TA modules in *S. aureus* did not affect bacterial persistence and that persisters formed by this organism exhibit decreased levels of ATP (63). It will be interesting to see what the molecular basis of the latter phenomenon is and, more generally, whether future studies may uncover a role of TA modules also for persister formation of *P. aeruginosa* and *S. aureus* (possibly involving yet undetected TA loci).

Other mechanisms of persister formation

Many factors beyond TA modules have been proposed to participate in persister formation, but the evidence for many of these is largely genetic, so that the phenotypic basis of antibiotic tolerance remains elusive. As an example, mutants affected in amino acid biosynthesis or metabolism have repeatedly been found to display altered (usually decreased) persister formation in diverse setups (33, 67, 81, 101, 109). However, it is unclear whether these phenotypes are simply caused by direct or indirect effects on (p)ppGpp signaling by RelA or whether other aspects of bacterial physiology are involved. Furthermore, diverse genes of the flagellar machinery have recently been implicated in aminoglycoside tolerance, but the molecular basis of this finding has not been resolved (102).

Inactivation of antibiotic targets

Aminoglycosides: Ribosomal translation

Aminoglycoside drugs kill bacteria by corrupting ribosomal translation to cause the production of toxic peptides, and drug uptake is known to require the proton-motive force (29). Ribosome hibernation, the formation of translationally inactive ribosome dimers, affects the bactericidal activity of aminoglycosides on both levels by inhibiting translation and consequently reducing the proton-motive force (Fig. 4). Consistently, ribosome hibernation has been found to be critical for the formation of aminoglycoside-tolerant persisters by several bacteria (115). Ribosome modulation factor, the main player in the ribosome hibernation process, is strongly expressed in *E. coli* persister cells, as well as in dormant *P. aeruginosa* biofilm cells (66, 84).

Fluoroquinolones: Topoisomerases and DNA replication

Fluoroquinolone antibiotics bind to DNA gyrase and topoisomerase IV in a way that promotes the formation of a ternary complex in which the enzyme is locked onto its DNA substrate and covalently bridges a DNA double-strand break, impairing DNA replication and gene expression. The bactericidal effect of fluoroquinolones is generally believed to be caused by the destabilization of these covalent complexes to release the free DNA ends—for example, by collision of these “roadblocks” with DNA-tracking complexes such as replisomes—resulting in chromosome fragmentation (116). Because ternary complex formation does not require enzymatic activity of the target enzyme, fluoroquinolone tolerance

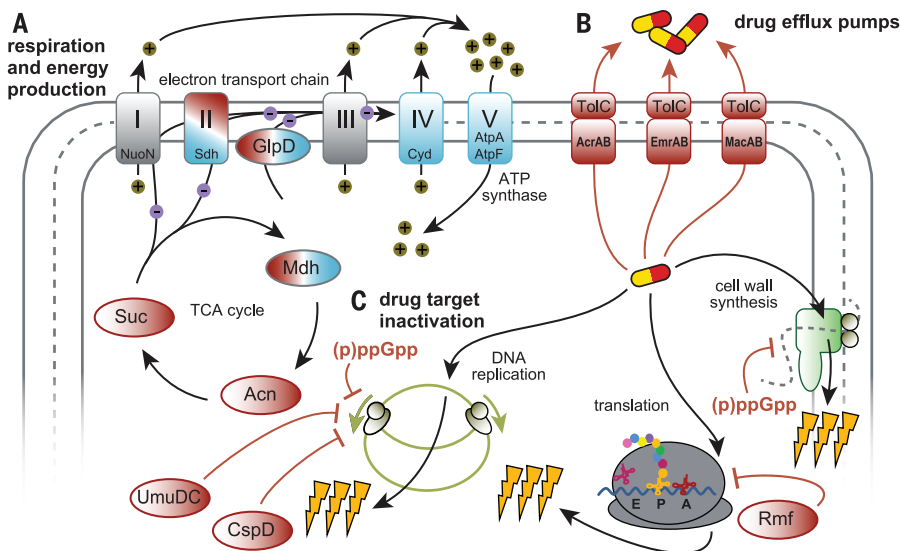


Fig. 4. Mechanisms of persister formation beyond TA modules. Diverse mechanisms beyond TA modules have been shown to contribute to bacterial persister formation. A nonexhaustive, exemplary set of factors involved in respiration and energy production (A), drug efflux pumps (B), and direct inactivation of antibiotic targets (C) are presented in this illustration. Note that mutants of complexes of the electron-transport chain (I to IV), ATP synthase (V), and different enzymes of the TCA cycle had divergent phenotypes in different studies or under different conditions (blue and red for increased and decreased persister formation, respectively). A *nuoN* mutant (at complex I of the electron-transport chain) displayed increased persister formation, but it is not known whether this phenotype is caused by a gain-of-function or loss-of-function mutation (22).

mechanisms may instead need to focus on the DNA side of antibiotic action. Consistently, several inhibitors of DNA replication (such as UmuDC or CspD) have been implicated in persister formation (42, 84), and (p)ppGpp itself also has dampening effects on transcription, as well as on DNA replication (56, 58, 117) (Fig. 4). Furthermore, the formation of fluoroquinolone-tolerant persisters has been studied in some detail for the carbon-source transition model (38, 73). These persisters are induced by (p)ppGpp signaling at a certain threshold level of this alarmone and require the transcriptional effects of (p)ppGpp and several nucleoid-associated proteins (73). However, the exact molecular basis of fluoroquinolone tolerance in this model remains unknown.

β-lactams: Peptidoglycan synthesis and cell growth

β-lactam antibiotics poison the cell wall synthesis machinery to induce a futile cycle of peptidoglycan synthesis and degradation that impairs cell wall integrity and results in osmotic lysis, particularly of growing cells (118). Apart from the general notion that persisters may survive *β*-lactam treatment because they do not replicate, a recent study unraveled a mechanism for the formation of ampicillin-tolerant persisters that links progressively increasing levels of (p)ppGpp to a broad shutdown of peptidoglycan synthesis (38) (Fig. 4).

Drug efflux pumps

A recent study showed that *E. coli* persister cells harbor higher levels of drug efflux pumps than the rest of the population and that these contribute to tolerance against *β*-lactams and quinolones by reducing intracellular antibiotic concentrations (Fig. 4) (119). The induction of efflux pumps has also been shown to contribute to antibiotic tolerance in other contexts; for instance, upon infection of host cells for mycobacteria (13) or as a component of indole-triggered persister formation in *E. coli* (8, 82).

Oxidant tolerance

The production of reactive oxygen species (ROS) and consequent damage to cellular macromolecules had been proposed as a common contributor to killing by diverse bactericidal antibiotics, but this view has been repeatedly challenged (29, 120, 121). Nevertheless, a study on *P. aeruginosa* showed that the survival of multidrug-tolerant persisters in biofilms of this organism was largely dependent on ROS detoxification enzymes under the control of (p)ppGpp signaling, and similar mechanisms may also operate in *E. coli* (59, 122).

Energy metabolism

A large body of evidence supports a connection between persister formation and the electron-transport chain, including the sources of electrons from the tricarboxylic acid (TCA) cycle and glycerol-3-phosphate dehydrogenase (GlpD) (Fig. 4). However, this notion is largely based on genetic experiments that detected usually decreased, but occasionally increased, frequencies of antibiotic-

tolerant persisters in strains carrying mutations or insertions in genes such as *glpD*, *ubiF*, *sdh*, *sucB*, *acnB*, *mdh*, and diverse others (22, 83, 102, 123–127). Phenotypes of decreased persistence were often very strong, consistently observed under diverse growth conditions, and frequently accompanied by increased sensitivity to a variety of stresses, ranging from extreme pH to heat or oxidants (123, 124). It therefore seems likely that these mutations generally impair cellular stress responses via metabolic deregulation, and defects in persister formation may be downstream of this phenomenon.

Persister resuscitation

On top of mere tolerance to the direct action of antibiotics, persister survival critically depends on the maintenance of cellular integrity throughout persistence and the resuscitation of cell functions from dormancy. Persister resuscitation is typically seen as a stochastic event that occurs randomly in time and has been interpreted in the context of a “scout model,” where the randomness of persister awakening allows the population to continuously probe the environment for favorable conditions (128). However, the frequency of persister resuscitation is also influenced by resource availability and other environmental variables such that exposure to preferred carbon sources, for example, can induce pronounced persister awakening (129). Molecular mechanisms underlying the exit from dormancy have remained rather elusive, with the exception of persisters formed by the activation of type II TA modules. For these, a specific mechanism of transcriptional autoregulation, conditional cooperativity, has been suggested to modulate the toxin/antitoxin balance in favor of resuscitation (85, 97), and the post-translational inactivation of toxins or the regeneration of corrupted targets may also contribute (89, 130).

Repair of DNA damage

Although the repair of damaged cellular macromolecules after antibiotic treatment is likely a general requirement of persister resuscitation, it has only been studied in the context of DNA damage. Two studies have shown that diverse components of the SOS regulon are involved in the repair of fluoroquinolone-induced DNA damage in stationary-phase persisters of *E. coli* (79, 131). Surprisingly, SOS induction caused by fluoroquinolone treatment was not different between persisters and nonpersisters, suggesting that the initial effects of the drug on the nucleoid were similar. Instead, survival of persisters depended on the abundance and activity of the DNA repair machinery primarily during the resuscitation phase, and enforced repression of the SOS response after fluoroquinolone treatment greatly reduced persister survival (79).

Overcoming persistence

Given that endurance is the key property of persisters as specialized survivor cells, it is unsurprising that their elimination is problematic for clinical situations. However, new insights into

the central principles of persister cell formation and tolerance have enabled a recent surge of ideas about how to deal with the phenomenon by, for example, enhancing drug uptake and preventing or reversing persister formation (8). The observation that persister formation usually depends on (p)ppGpp signaling has inspired the use of (p)ppGpp synthesis inhibitors, such as relacin, as adjuvant drugs for antibiotic treatment (132). Furthermore, the acyldepsipeptide antibiotic ADEP4 is notable for its ability to kill persister cells, irrespective of their dormant physiology. ADEP4 can enforce activation of the ClpP protease by uncoupling it from the requirement to use ATP, thereby subverting ClpP protease activity to target a wide range of essential targets, such as ribosomal proteins (133).

Concluding remarks and prospects

Recent studies shed new light on the molecular mechanisms underlying bacterial persistence, and—although many details remain to be resolved—diverse cellular pathways, including TA modules and metabolic rearrangements, are well established as mediators of persister formation. However, important aspects of the cellular decision-making process upstream of these mechanisms are still unclear, particularly in the context of seemingly random persister formation where the pacemaker of this stochasticity has remained elusive. More specifically, the question of whether this behavior is truly stochastic (i.e., simply following an amplification of noise) or equivalent to the induction of persister formation by external cues experienced by some cells in their local environment [e.g., “microstarvation” as a trigger of (p)ppGpp signaling (57)] is still to be resolved. Furthermore, many open questions persist regarding the actual basis of antibiotic tolerance downstream of established mediators of persister formation (i.e., regarding those aspects that are most critical for failure or success of clinical treatment). For example, it remains a riddle how exactly persisters that arise through inhibition of protein translation by mRNA endonucleases can be protected from fluoroquinolones that corrupt DNA topoisomerases. Similarly, it is currently unclear why tolerant persisters are still slowly killed during antibiotic treatment (e.g., as apparent from the slope of the second phase of biphasic killing experiments). Furthermore, the question of which molecular mechanisms control the timing of persister resuscitation remains to be resolved.

One curious aspect of the research on persister cells is the frequent lack of congruence in results reported by different laboratories. As an example, the persister pathway driven by (p)ppGpp, Lon, and mRNA endonucleases in *E. coli* (Fig. 3) has been the topic of some controversy. Several groups noted that, in their hands, a *lon* knockout had no effect on persister formation that could be attributed to the 10 mRNA endonucleases (131, 134), though others could readily reproduce the *lon* phenotype (75, 119). Similarly, the formation of fluoroquinolone-tolerant persisters of *E. coli* has repeatedly been explicitly noted to depend on the TisB toxin only in exponentially growing cells

(41, 79), but recent work in the stationary phase showed markedly decreased fluoroquinolone tolerance of a *tisB* mutant (75). Subtle differences in the experimental setup probably favor the formation of persisters by different pathways (83). Clearly, these discrepancies need to be resolved and understood, both as a means to learn more about the control of heterogeneous bacterial persister formation and also to facilitate the development of common concepts in the field.

REFERENCES AND NOTES

- World Health Organization (WHO), "Antimicrobial resistance: Global report on surveillance 2014 (WHO, 2014); www.who.int/drugresistance/documents/surveillance-report/en/.
- M. Fauvart, V. N. De Groot, J. Michiels, Role of persister cells in chronic infections: Clinical relevance and perspectives on anti-persister therapies. *J. Med. Microbiol.* **60**, 699–709 (2011). doi: [10.1099/jmm.0.030932-0](https://doi.org/10.1099/jmm.0.030932-0); pmid: [21459912](https://pubmed.ncbi.nlm.nih.gov/21459912/)
- N. Q. Balaban, K. Gerdes, K. Lewis, J. D. McKinney, A problem of persistence: Still more questions than answers? *Nat. Rev. Microbiol.* **11**, 587–591 (2013). doi: [10.1038/nrmicro3076](https://doi.org/10.1038/nrmicro3076); pmid: [24020075](https://pubmed.ncbi.nlm.nih.gov/24020075/)
- B. R. Levin, D. E. Rozen, Non-inherited antibiotic resistance. *Nat. Rev. Microbiol.* **4**, 556–562 (2006). doi: [10.1038/nrmicro1445](https://doi.org/10.1038/nrmicro1445); pmid: [16778840](https://pubmed.ncbi.nlm.nih.gov/16778840/)
- K. Lewis, Persister cells. *Annu. Rev. Microbiol.* **64**, 357–372 (2010). doi: [10.1146/annurev.micro.112408.134306](https://doi.org/10.1146/annurev.micro.112408.134306); pmid: [20528688](https://pubmed.ncbi.nlm.nih.gov/20528688/)
- N. Q. Balaban, J. Merrin, R. Chait, L. Kowalik, S. Leibler, Bacterial persistence as a phenotypic switch. *Science* **305**, 1622–1625 (2004). doi: [10.1126/science.1099390](https://doi.org/10.1126/science.1099390); pmid: [15308767](https://pubmed.ncbi.nlm.nih.gov/15308767/)
- E. Maisonneuve, K. Gerdes, Molecular mechanisms underlying bacterial persisters. *Cell* **157**, 539–548 (2014). doi: [10.1016/j.cell.2014.02.050](https://doi.org/10.1016/j.cell.2014.02.050); pmid: [24766804](https://pubmed.ncbi.nlm.nih.gov/24766804/)
- T. K. Wood, Combating bacterial persister cells. *Biotechnol. Bioeng.* **113**, 476–483 (2016). doi: [10.1002/bit.25721](https://doi.org/10.1002/bit.25721); pmid: [26264116](https://pubmed.ncbi.nlm.nih.gov/26264116/)
- D. M. Livermore, Has the era of untreatable infections arrived? *J. Antimicrob. Chemother.* **64** (suppl. 1), i29–i36 (2009). doi: [10.1093/jac/dkp255](https://doi.org/10.1093/jac/dkp255); pmid: [19675016](https://pubmed.ncbi.nlm.nih.gov/19675016/)
- T. Bjarnsholt, The role of bacterial biofilms in chronic infections. *APMIS Suppl.* **121**, 1–51 (2013). doi: [10.1111/apm.12099](https://doi.org/10.1111/apm.12099); pmid: [23635385](https://pubmed.ncbi.nlm.nih.gov/23635385/)
- L. Lebeaux, J. M. Ghigo, C. Beloin, Biofilm-related infections: Bridging the gap between clinical management and fundamental aspects of recalcitrance toward antibiotics. *Microbiol. Mol. Biol. Rev.* **78**, 510–543 (2014). doi: [10.1128/MMBR.00013-14](https://doi.org/10.1128/MMBR.00013-14); pmid: [25184564](https://pubmed.ncbi.nlm.nih.gov/25184564/)
- M. G. Blango, M. A. Mulvey, Persistence of uropathogenic *Escherichia coli* in the face of multiple antibiotics. *Antimicrob. Agents Chemother.* **54**, 1855–1863 (2010). doi: [10.1128/AAC.00014-10](https://doi.org/10.1128/AAC.00014-10); pmid: [20231390](https://pubmed.ncbi.nlm.nih.gov/20231390/)
- K. N. Adams et al., Drug tolerance in replicating mycobacteria mediated by a macrophage-induced efflux mechanism. *Cell* **145**, 39–53 (2011). doi: [10.1016/j.cell.2011.02.022](https://doi.org/10.1016/j.cell.2011.02.022); pmid: [21376383](https://pubmed.ncbi.nlm.nih.gov/21376383/)
- B. Claudi et al., Phenotypic variation of *Salmonella* in host tissues delays eradication by antimicrobial chemotherapy. *Cell* **158**, 722–733 (2014). doi: [10.1016/j.cell.2014.06.045](https://doi.org/10.1016/j.cell.2014.06.045); pmid: [25126781](https://pubmed.ncbi.nlm.nih.gov/25126781/)
- S. Helaine et al., Internalization of *Salmonella* by macrophages induces formation of nonreplicating persisters. *Science* **343**, 204–208 (2014). doi: [10.1126/science.1244705](https://doi.org/10.1126/science.1244705); pmid: [24408438](https://pubmed.ncbi.nlm.nih.gov/24408438/)
- G. Marina, N. Dhar, J. D. McKinney, Stress and host immunity amplify *Mycobacterium tuberculosis* phenotypic heterogeneity and induce nongrowing metabolically active forms. *Cell Host Microbe* **17**, 32–46 (2015). doi: [10.1016/j.chom.2014.11.016](https://doi.org/10.1016/j.chom.2014.11.016); pmid: [25543231](https://pubmed.ncbi.nlm.nih.gov/25543231/)
- P. Kaiser et al., Cecum lymph node dendritic cells harbor slow-growing bacteria phenotypically tolerant to antibiotic treatment. *PLoS Biol.* **12**, e1001793 (2014). doi: [10.1371/journal.pbio.1001793](https://doi.org/10.1371/journal.pbio.1001793); pmid: [24558351](https://pubmed.ncbi.nlm.nih.gov/24558351/)
- M. A. Schumacher et al., HipBA-promoter structures reveal the basis of heritable multidrug tolerance. *Nature* **524**, 59–64 (2015). doi: [10.1038/nature14662](https://doi.org/10.1038/nature14662); pmid: [26222023](https://pubmed.ncbi.nlm.nih.gov/26222023/)
- J. E. Michiels, B. Van den Bergh, N. Verstraeten, M. Fauvart, J. Michiels, *In vitro* emergence of high persistence upon periodic aminoglycoside challenge in the ESKAPE pathogens. *Antimicrob. Agents Chemother.* **60**, 4630–4637 (2016). doi: [10.1128/AAC.00757-16](https://doi.org/10.1128/AAC.00757-16); pmid: [27185802](https://pubmed.ncbi.nlm.nih.gov/27185802/)
- H. S. Moyed, K. P. Bertrand, *hipA*, a newly recognized gene of *Escherichia coli* K-12 that affects frequency of persistence after inhibition of murein synthesis. *J. Bacteriol.* **155**, 768–775 (1983). pmid: [6348026](https://pubmed.ncbi.nlm.nih.gov/6348026/)
- H. L. Torrey, I. Keren, L. E. Via, J. S. Lee, K. Lewis, High persister mutants in *Mycobacterium tuberculosis*. *PLoS ONE* **11**, e0155127 (2016). doi: [10.1371/journal.pone.0155127](https://doi.org/10.1371/journal.pone.0155127); pmid: [27176494](https://pubmed.ncbi.nlm.nih.gov/27176494/)
- B. Van den Bergh et al., Frequency of antibiotic application drives rapid evolutionary adaptation of *Escherichia coli* persistence. *Nat. Microbiol.* **1**, 16020 (2016). doi: [10.1038/nmicrobiol.2016.20](https://doi.org/10.1038/nmicrobiol.2016.20); pmid: [27572640](https://pubmed.ncbi.nlm.nih.gov/27572640/)
- K. Stepanyan et al., Fitness trade-offs explain low levels of persister cells in the opportunistic pathogen *Pseudomonas aeruginosa*. *Mol. Ecol.* **24**, 1572–1583 (2015). doi: [10.1111/mec.13127](https://doi.org/10.1111/mec.13127); pmid: [25721227](https://pubmed.ncbi.nlm.nih.gov/25721227/)
- A. Slattery, A. H. Victorsen, A. Brown, K. Hillman, G. J. Phillips, Isolation of highly persistent mutants of *Salmonella enterica* serovar Typhimurium reveals a new toxin-antitoxin module. *J. Bacteriol.* **195**, 647–657 (2013). doi: [10.1128/JB.01397-12](https://doi.org/10.1128/JB.01397-12); pmid: [23204462](https://pubmed.ncbi.nlm.nih.gov/23204462/)
- L. R. Mulcahy, J. L. Burns, S. Lory, K. Lewis, Emergence of *Pseudomonas aeruginosa* strains producing high levels of persister cells in patients with cystic fibrosis. *J. Bacteriol.* **192**, 6191–6199 (2010). doi: [10.1128/JB.01651-09](https://doi.org/10.1128/JB.01651-09); pmid: [20935098](https://pubmed.ncbi.nlm.nih.gov/20935098/)
- L. W. Gouneau et al., Selective target inactivation rather than global metabolic dormancy causes antibiotic tolerance in uropathogens. *Antimicrob. Agents Chemother.* **58**, 2089–2097 (2014). doi: [10.1128/AAC.02552-13](https://doi.org/10.1128/AAC.02552-13); pmid: [24449771](https://pubmed.ncbi.nlm.nih.gov/24449771/)
- A. A. Al Mamun et al., Identity and function of a large gene network underlying mutagenic repair of DNA breaks. *Science* **338**, 1344–1348 (2012). doi: [10.1126/science.1226683](https://doi.org/10.1126/science.1226683); pmid: [23224554](https://pubmed.ncbi.nlm.nih.gov/23224554/)
- N. R. Cohen, M. A. Lobritz, J. J. Collins, Microbial persistence and the road to drug resistance. *Cell Host Microbe* **13**, 632–642 (2013). doi: [10.1016/j.chom.2013.05.009](https://doi.org/10.1016/j.chom.2013.05.009); pmid: [23768488](https://pubmed.ncbi.nlm.nih.gov/23768488/)
- M. A. Kohanski, D. J. Dwyer, J. J. Collins, How antibiotics kill bacteria: From targets to networks. *Nat. Rev. Microbiol.* **8**, 423–435 (2010). doi: [10.1038/nrmicro2333](https://doi.org/10.1038/nrmicro2333); pmid: [20440275](https://pubmed.ncbi.nlm.nih.gov/20440275/)
- J. Bigger, Treatment of staphylococcal infections with penicillin by intermittent sterilisation. *Lancet* **244**, 497–500 (1944). doi: [10.1016/S0140-6736\(00\)74210-3](https://doi.org/10.1016/S0140-6736(00)74210-3)
- J. T. Lennon, S. E. Jones, Microbial seed banks: The ecological and evolutionary implications of dormancy. *Nat. Rev. Microbiol.* **9**, 119–130 (2011). doi: [10.1038/nrmicro2504](https://doi.org/10.1038/nrmicro2504); pmid: [21233850](https://pubmed.ncbi.nlm.nih.gov/21233850/)
- O. Gefen, N. Q. Balaban, The importance of being persistent: Heterogeneity of bacterial populations under antibiotic stress. *FEMS Microbiol. Rev.* **33**, 704–717 (2009). doi: [10.1111/j.1574-6976.2008.00156.x](https://doi.org/10.1111/j.1574-6976.2008.00156.x); pmid: [19207742](https://pubmed.ncbi.nlm.nih.gov/19207742/)
- D. K. Fung, E. W. Chan, M. L. Chin, R. C. Chan, Delineation of a bacterial starvation stress response network which can mediate antibiotic tolerance development. *Antimicrob. Agents Chemother.* **54**, 1082–1093 (2010). doi: [10.1128/AAC.01218-09](https://doi.org/10.1128/AAC.01218-09); pmid: [20086164](https://pubmed.ncbi.nlm.nih.gov/20086164/)
- E. Germain, M. Roghanian, K. Gerdes, E. Maisonneuve, Stochastic induction of persister cells by HipA through (p) ppGpp-mediated activation of mRNA endonucleases. *Proc. Natl. Acad. Sci. U.S.A.* **112**, 5171–5176 (2015). doi: [10.1073/pnas.1423536112](https://doi.org/10.1073/pnas.1423536112); pmid: [25848049](https://pubmed.ncbi.nlm.nih.gov/25848049/)
- M. A. Orman, M. P. Brynildsen, Dormancy is not necessary or sufficient for bacterial persistence. *Antimicrob. Agents Chemother.* **57**, 3230–3239 (2013). doi: [10.1128/AAC.00243-13](https://doi.org/10.1128/AAC.00243-13); pmid: [23629720](https://pubmed.ncbi.nlm.nih.gov/23629720/)
- K. Lewis, Persister cells and the riddle of biofilm survival. *Biochemistry (Moscow)* **70**, 267–274 (2005). doi: [10.1007/s10541-005-0111-6](https://doi.org/10.1007/s10541-005-0111-6); pmid: [15807669](https://pubmed.ncbi.nlm.nih.gov/15807669/)
- Y. Wakamoto et al., Dynamic persistence of antibiotic-stressed mycobacteria. *Science* **339**, 91–95 (2013). doi: [10.1126/science.1229858](https://doi.org/10.1126/science.1229858); pmid: [23288538](https://pubmed.ncbi.nlm.nih.gov/23288538/)
- S. M. Amato, M. P. Brynildsen, Persister heterogeneity arising from a single metabolic stress. *Curr. Biol.* **25**, 2090–2098 (2015). doi: [10.1016/j.cub.2015.06.034](https://doi.org/10.1016/j.cub.2015.06.034); pmid: [26255847](https://pubmed.ncbi.nlm.nih.gov/26255847/)
- E. Maisonneuve, L. J. Shakespeare, M. G. Jørgensen, K. Gerdes, Bacterial persistence by RNA endonucleases. *Proc. Natl. Acad. Sci. U.S.A.* **108**, 13206–13211 (2011). doi: [10.1073/pnas.1100186108](https://doi.org/10.1073/pnas.1100186108); pmid: [21788497](https://pubmed.ncbi.nlm.nih.gov/21788497/)
- N. Verstraeten et al., Ogb and membrane depolarization are part of a microbial bet-hedging strategy that leads to antibiotic tolerance. *Mol. Cell* **59**, 9–21 (2015). doi: [10.1016/j.molcel.2015.05.011](https://doi.org/10.1016/j.molcel.2015.05.011); pmid: [26051177](https://pubmed.ncbi.nlm.nih.gov/26051177/)
- T. Dörr, M. Vulić, K. Lewis, Ciprofloxacin causes persister formation by inducing the TisB toxin in *Escherichia coli*. *PLoS Biol.* **8**, e1000317 (2010). doi: [10.1371/journal.pbio.1000317](https://doi.org/10.1371/journal.pbio.1000317); pmid: [20186264](https://pubmed.ncbi.nlm.nih.gov/20186264/)
- Y. Kim, T. K. Wood, Toxins Hha and CspD and small RNA regulator Hfq are involved in persister cell formation through MqsR in *Escherichia coli*. *Biochem. Biophys. Res. Commun.* **391**, 209–213 (2010). doi: [10.1016/j.bbrc.2009.11.033](https://doi.org/10.1016/j.bbrc.2009.11.033); pmid: [19909729](https://pubmed.ncbi.nlm.nih.gov/19909729/)
- B. R. Levin, J. Concepción-Acevedo, K. I. Udekwe, Persistence: A copacetic and parsimonious hypothesis for the existence of non-inherited resistance to antibiotics. *Curr. Opin. Microbiol.* **21**, 18–21 (2014). doi: [10.1016/j.mib.2014.06.016](https://doi.org/10.1016/j.mib.2014.06.016); pmid: [25090240](https://pubmed.ncbi.nlm.nih.gov/25090240/)
- O. Fridman, A. Goldberg, I. Ronin, N. Shoshitaishvili, N. Q. Balaban, Optimization of lag time underlies antibiotic tolerance in evolved bacterial populations. *Nature* **513**, 418–421 (2014). doi: [10.1038/nature13469](https://doi.org/10.1038/nature13469); pmid: [25043002](https://pubmed.ncbi.nlm.nih.gov/25043002/)
- B. Stewart, D. E. Rozen, Genetic variation for antibiotic persistence in *Escherichia coli*. *Evolution* **66**, 933–939 (2012). doi: [10.1111/j.1558-5646.2011.01467.x](https://doi.org/10.1111/j.1558-5646.2011.01467.x); pmid: [22380453](https://pubmed.ncbi.nlm.nih.gov/22380453/)
- N. Hofsteenge, E. van Nimwegen, O. K. Silander, Quantitative analysis of persister fractions suggests different mechanisms of formation among environmental isolates of *E. coli*. *BMC Microbiol.* **13**, 25 (2013). doi: [10.1186/1471-2180-13-25](https://doi.org/10.1186/1471-2180-13-25); pmid: [23379956](https://pubmed.ncbi.nlm.nih.gov/23379956/)
- T. Vogwill, A. C. Comfort, V. Furió, R. C. MacLean, Persistence and resistance as complementary bacterial adaptations to antibiotics. *J. Evol. Biol.* **29**, 1223–1233 (2016). doi: [10.1111/jeb.12684](https://doi.org/10.1111/jeb.12684); pmid: [26999656](https://pubmed.ncbi.nlm.nih.gov/26999656/)
- M. Arnoldini, R. Mostowy, S. Bonhoeffer, M. Ackermann, Evolution of stress response in the face of unreliable environmental signals. *PLoS Comput. Biol.* **8**, e1002627 (2012). doi: [10.1371/journal.pcbi.1002627](https://doi.org/10.1371/journal.pcbi.1002627); pmid: [22916000](https://pubmed.ncbi.nlm.nih.gov/22916000/)
- I. G. de Jong, P. Haccou, O. P. Kuipers, Bet hedging or not? A guide to proper classification of microbial survival strategies. *BioEssays* **33**, 215–223 (2011). doi: [10.1002/bies.201000127](https://doi.org/10.1002/bies.201000127); pmid: [21254151](https://pubmed.ncbi.nlm.nih.gov/21254151/)
- E. Kussell, R. Kishony, N. Q. Balaban, S. Leibler, Bacterial persistence: A model of survival in changing environments. *Genetics* **169**, 1807–1814 (2005). doi: [10.1534/genetics.104.035352](https://doi.org/10.1534/genetics.104.035352); pmid: [15687275](https://pubmed.ncbi.nlm.nih.gov/15687275/)
- E. Maisonneuve, M. Castro-Camargo, K. Gerdes, (p)ppGpp controls bacterial persistence by stochastic induction of toxin-antitoxin activity. *Cell* **154**, 1140–1150 (2013). doi: [10.1016/j.cell.2013.07.048](https://doi.org/10.1016/j.cell.2013.07.048); pmid: [23993101](https://pubmed.ncbi.nlm.nih.gov/23993101/)
- D. Shah et al., Persisters: A distinct physiological state of *E. coli*. *BMC Microbiol.* **6**, 53 (2006). doi: [10.1186/1471-2180-6-53](https://doi.org/10.1186/1471-2180-6-53); pmid: [16768798](https://pubmed.ncbi.nlm.nih.gov/16768798/)
- O. Kotte, B. Volkmer, J. L. Radzikowski, M. Heinemann, Phenotypic bistability in *Escherichia coli*'s central carbon metabolism. *Mol. Syst. Biol.* **10**, 736 (2014). doi: [10.15252/msb.20135022](https://doi.org/10.15252/msb.20135022); pmid: [24987115](https://pubmed.ncbi.nlm.nih.gov/24987115/)
- Y. Wu, M. Vulić, I. Keren, K. Lewis, Role of oxidative stress in persister tolerance. *Antimicrob. Agents Chemother.* **56**, 4922–4926 (2012). doi: [10.1128/AAC.00921-12](https://doi.org/10.1128/AAC.00921-12); pmid: [22777047](https://pubmed.ncbi.nlm.nih.gov/22777047/)
- S. H. Hong, X. Wang, H. F. O'Connor, M. J. Benedik, T. K. Wood, Bacterial persistence increases as environmental fitness decreases. *Microb. Biotechnol.* **5**, 509–522 (2012). doi: [10.1111/j.1751-7915.2011.00327.x](https://doi.org/10.1111/j.1751-7915.2011.00327.x); pmid: [22221537](https://pubmed.ncbi.nlm.nih.gov/22221537/)
- V. Haurlyuk, G. C. Atkinson, K. S. Murakami, T. Tenson, K. Gerdes, Recent functional insights into the role of (p) ppGpp in bacterial physiology. *Nat. Rev. Microbiol.* **13**, 298–309 (2015). doi: [10.1038/nrmicro3448](https://doi.org/10.1038/nrmicro3448); pmid: [25853779](https://pubmed.ncbi.nlm.nih.gov/25853779/)
- U. Mechold, K. Potrykus, H. Murphy, K. S. Murakami, M. Cashel, Differential regulation by ppGpp versus pppGpp in *Escherichia coli*. *Nucleic Acids Res.* **41**, 6175–6189 (2013). doi: [10.1093/nar/gkt302](https://doi.org/10.1093/nar/gkt302); pmid: [23620295](https://pubmed.ncbi.nlm.nih.gov/23620295/)
- U. Kanjee, K. Ogata, W. A. Houry, Direct binding targets of the stringent response alarmone (pppGpp). *Mol. Microbiol.* **85**, 1029–1043 (2012). doi: [10.1111/j.1365-2958.2012.08177.x](https://doi.org/10.1111/j.1365-2958.2012.08177.x); pmid: [22812515](https://pubmed.ncbi.nlm.nih.gov/22812515/)
- D. Nguyen et al., Active starvation responses mediate antibiotic tolerance in biofilms and nutrient-limited bacteria. *Science* **334**, 982–986 (2011). doi: [10.1126/science.1211037](https://doi.org/10.1126/science.1211037); pmid: [22096200](https://pubmed.ncbi.nlm.nih.gov/22096200/)

60. D. Viducic *et al.*, Functional analysis of *spoT*, *relA* and *dksA* genes on quinolone tolerance in *Pseudomonas aeruginosa* under non-growing condition. *Microbiol. Immunol.* **50**, 349–357 (2006). doi: [10.1111/j.1348-0421.2006.tb03793.x](https://doi.org/10.1111/j.1348-0421.2006.tb03793.x); pmid: [16625057](https://pubmed.ncbi.nlm.nih.gov/16625057/)
61. A. O. Gaca, C. Colomer-Winter, J. A. Lemos, Many means to a common end: The intricacies of (p)ppGpp metabolism and its control of bacterial homeostasis. *J. Bacteriol.* **197**, 1146–1156 (2015). doi: [10.1128/JB.02577-14](https://doi.org/10.1128/JB.02577-14); pmid: [25605304](https://pubmed.ncbi.nlm.nih.gov/25605304/)
62. R. M. Corrigan, L. E. Bellows, A. Wood, A. Gründling, ppGpp negatively impacts ribosome assembly affecting growth and antimicrobial tolerance in Gram-positive bacteria. *Proc. Natl. Acad. Sci. U.S.A.* **113**, E1710–E1719 (2016). doi: [10.1073/pnas.1522179113](https://doi.org/10.1073/pnas.1522179113); pmid: [26951678](https://pubmed.ncbi.nlm.nih.gov/26951678/)
63. B. P. Conlon *et al.*, Persister formation in *Staphylococcus aureus* is associated with ATP depletion. *Nat. Microbiol.* **1**, 16051 (2016). doi: [10.1038/nmicrobiol.2016.51](https://doi.org/10.1038/nmicrobiol.2016.51)
64. P. S. Stewart, Antimicrobial tolerance in biofilms. *Microbiol. Spectr.* **3**, MB-0010-2014 (2015). pmid: [26185072](https://pubmed.ncbi.nlm.nih.gov/26185072/)
65. A. L. Spoering, K. Lewis, Biofilms and planktonic cells of *Pseudomonas aeruginosa* have similar resistance to killing by antimicrobials. *J. Bacteriol.* **183**, 6746–6751 (2001). doi: [10.1128/JB.183.23.6746-6751.2001](https://doi.org/10.1128/JB.183.23.6746-6751.2001); pmid: [11698361](https://pubmed.ncbi.nlm.nih.gov/11698361/)
66. P. S. Stewart *et al.*, Contribution of stress responses to antibiotic tolerance in *Pseudomonas aeruginosa* biofilms. *Antimicrob. Agents Chemother.* **59**, 3838–3847 (2015). doi: [10.1128/AAC.00433-15](https://doi.org/10.1128/AAC.00433-15); pmid: [25870065](https://pubmed.ncbi.nlm.nih.gov/25870065/)
67. S. P. Bernier *et al.*, Starvation, together with the SOS response, mediates high biofilm-specific tolerance to the fluoroquinolone ofloxacin. *PLOS Genet.* **9**, e1003144 (2013). doi: [10.1371/journal.pgen.1003144](https://doi.org/10.1371/journal.pgen.1003144); pmid: [23300476](https://pubmed.ncbi.nlm.nih.gov/23300476/)
68. A. Boehm *et al.*, Second messenger signalling governs *Escherichia coli* biofilm induction upon ribosomal stress. *Mol. Microbiol.* **72**, 1500–1516 (2009). doi: [10.1111/j.1365-2958.2009.06739.x](https://doi.org/10.1111/j.1365-2958.2009.06739.x); pmid: [19460094](https://pubmed.ncbi.nlm.nih.gov/19460094/)
69. J. M. Navarro Llorens, A. Tormo, E. Martínez-García, Stationary phase in Gram-negative bacteria. *FEMS Microbiol. Rev.* **34**, 476–495 (2010). doi: [10.1111/j.1574-6976.2010.00213.x](https://doi.org/10.1111/j.1574-6976.2010.00213.x); pmid: [20236330](https://pubmed.ncbi.nlm.nih.gov/20236330/)
70. R. Hengge, Stationary-phase gene regulation in *Escherichia coli*. *Ecosal Plus* 10.1128/ecosalplus.5.6.3 (2011). doi: [10.1128/ecosalplus.5.6.3](https://doi.org/10.1128/ecosalplus.5.6.3); pmid: [26442507](https://pubmed.ncbi.nlm.nih.gov/26442507/)
71. I. Keren, N. Kaldalu, A. Spoering, Y. Wang, K. Lewis, Persister cells and tolerance to antimicrobials. *FEMS Microbiol. Lett.* **230**, 13–18 (2004). doi: [10.1016/S0378-1097\(03\)00856-5](https://doi.org/10.1016/S0378-1097(03)00856-5); pmid: [14734160](https://pubmed.ncbi.nlm.nih.gov/14734160/)
72. I. Keren, S. Minami, E. Rubin, K. Lewis, Characterization and transcriptome analysis of *Mycobacterium tuberculosis* persisters. *mBio* **2**, e00100-11 (2011). doi: [10.1128/mBio.00100-11](https://doi.org/10.1128/mBio.00100-11); pmid: [21673191](https://pubmed.ncbi.nlm.nih.gov/21673191/)
73. S. M. Amato, M. A. Orman, M. P. Brynildsen, Metabolic control of persister formation in *Escherichia coli*. *Mol. Cell* **50**, 475–487 (2013). doi: [10.1016/j.molcel.2013.04.002](https://doi.org/10.1016/j.molcel.2013.04.002); pmid: [23665232](https://pubmed.ncbi.nlm.nih.gov/23665232/)
74. A. Battesti, N. Majdalani, S. Gottesman, The RpoS-mediated general stress response in *Escherichia coli*. *Annu. Rev. Microbiol.* **65**, 189–213 (2011). doi: [10.1146/annurev-micro-090110-102946](https://doi.org/10.1146/annurev-micro-090110-102946); pmid: [21639793](https://pubmed.ncbi.nlm.nih.gov/21639793/)
75. N. Wu *et al.*, Ranking of persister genes in the same *Escherichia coli* genetic background demonstrates varying importance of individual persister genes in tolerance to different antibiotics. *Front. Microbiol.* **6**, 1003 (2015). doi: [10.3389/fmicb.2015.01003](https://doi.org/10.3389/fmicb.2015.01003); pmid: [26483762](https://pubmed.ncbi.nlm.nih.gov/26483762/)
76. K. Murakami *et al.*, Role for *rpoS* gene of *Pseudomonas aeruginosa* in antibiotic tolerance. *FEMS Microbiol. Lett.* **242**, 161–167 (2005). doi: [10.1016/j.femsle.2004.11.005](https://doi.org/10.1016/j.femsle.2004.11.005); pmid: [15621433](https://pubmed.ncbi.nlm.nih.gov/15621433/)
77. S. Hansen, K. Lewis, M. Vulić, Role of global regulators and nucleotide metabolism in antibiotic tolerance in *Escherichia coli*. *Antimicrob. Agents Chemother.* **52**, 2718–2726 (2008). doi: [10.1128/AAC.00144-08](https://doi.org/10.1128/AAC.00144-08); pmid: [18519731](https://pubmed.ncbi.nlm.nih.gov/18519731/)
78. Z. Baharoglu, D. Mazel, SOS, the formidable strategy of bacteria against aggressions. *FEMS Microbiol. Rev.* **38**, 1126–1145 (2014). doi: [10.1111/1574-6976.12077](https://doi.org/10.1111/1574-6976.12077); pmid: [24923554](https://pubmed.ncbi.nlm.nih.gov/24923554/)
79. K. G. Volzing, M. P. Brynildsen, Stationary-phase persisters to ofloxacin sustain DNA damage and require repair systems only during recovery. *mBio* **6**, e00731-15 (2015). doi: [10.1128/mBio.00731-15](https://doi.org/10.1128/mBio.00731-15); pmid: [26330511](https://pubmed.ncbi.nlm.nih.gov/26330511/)
80. N. Möker, C. R. Dean, J. Tao, *Pseudomonas aeruginosa* increases formation of multidrug-tolerant persister cells in response to quorum-sensing signaling molecules. *J. Bacteriol.* **192**, 1946–1955 (2010). doi: [10.1128/JB.01231-09](https://doi.org/10.1128/JB.01231-09); pmid: [20097861](https://pubmed.ncbi.nlm.nih.gov/20097861/)
81. V. Leung, C. M. Lévesque, A stress-inducible quorum-sensing peptide mediates the formation of persister cells with noninherited multidrug tolerance. *J. Bacteriol.* **194**, 2265–2274 (2012). doi: [10.1128/JB.06707-11](https://doi.org/10.1128/JB.06707-11); pmid: [22366415](https://pubmed.ncbi.nlm.nih.gov/22366415/)
82. J. Kim, W. Park, Indole: A signaling molecule or a mere metabolic byproduct that alters bacterial physiology at a high concentration? *J. Microbiol.* **53**, 421–428 (2015). doi: [10.1007/s12275-015-5273-3](https://doi.org/10.1007/s12275-015-5273-3); pmid: [26115989](https://pubmed.ncbi.nlm.nih.gov/26115989/)
83. H. Luidalepp, A. Jöers, N. Kaldalu, T. Tenson, Age of inoculum strongly influences persister frequency and can mask effects of mutations implicated in altered persistence. *J. Bacteriol.* **193**, 3598–3605 (2011). doi: [10.1128/JB.00085-11](https://doi.org/10.1128/JB.00085-11); pmid: [21602347](https://pubmed.ncbi.nlm.nih.gov/21602347/)
84. I. Keren, D. Shah, A. Spoering, N. Kaldalu, K. Lewis, Specialized persister cells and the mechanism of multidrug tolerance in *Escherichia coli*. *J. Bacteriol.* **186**, 8172–8180 (2004). doi: [10.1128/JB.186.24.8172-8180.2004](https://doi.org/10.1128/JB.186.24.8172-8180.2004); pmid: [15576765](https://pubmed.ncbi.nlm.nih.gov/15576765/)
85. R. Page, W. Peti, Toxin-antitoxin systems in bacterial growth arrest and persistence. *Nat. Chem. Biol.* **12**, 208–214 (2016). doi: [10.1038/nchembio.2044](https://doi.org/10.1038/nchembio.2044); pmid: [26991085](https://pubmed.ncbi.nlm.nih.gov/26991085/)
86. K. Gerdes, E. Maisonneuve, Bacterial persistence and toxin-antitoxin loci. *Annu. Rev. Microbiol.* **66**, 103–123 (2012). doi: [10.1146/annurev-micro-092611-150159](https://doi.org/10.1146/annurev-micro-092611-150159); pmid: [22994490](https://pubmed.ncbi.nlm.nih.gov/22994490/)
87. R. Brielle, M. L. Pinel-Marie, B. Felden, Linking bacterial type I toxins with their actions. *Curr. Opin. Microbiol.* **30**, 114–121 (2016). doi: [10.1016/j.mib.2016.01.009](https://doi.org/10.1016/j.mib.2016.01.009); pmid: [26874964](https://pubmed.ncbi.nlm.nih.gov/26874964/)
88. K. Gerdes, E. G. Wagner, RNA antitoxins. *Curr. Opin. Microbiol.* **10**, 117–124 (2007). doi: [10.1016/j.mib.2007.03.003](https://doi.org/10.1016/j.mib.2007.03.003); pmid: [17376733](https://pubmed.ncbi.nlm.nih.gov/17376733/)
89. A. M. Cheverton *et al.*, A *Salmonella* toxin promotes persister formation through acetylation of tRNA. *Mol. Cell* **63**, 86–96 (2016). doi: [10.1016/j.molcel.2016.05.002](https://doi.org/10.1016/j.molcel.2016.05.002); pmid: [27264868](https://pubmed.ncbi.nlm.nih.gov/27264868/)
90. K. Winther, J. J. Tree, D. Tollervy, K. Gerdes, VapCs of *Mycobacterium tuberculosis* cleave RNAs essential for translation. *Nucleic Acids Res.* **10.1093/nar/gkw781** (2016). pmid: [27599842](https://pubmed.ncbi.nlm.nih.gov/27599842/)
91. I. Brzozowska, U. Zielenkiewicz, Regulation of toxin-antitoxin systems by proteolysis. *Plasmid* **70**, 33–41 (2013). doi: [10.1016/j.plasmid.2013.01.007](https://doi.org/10.1016/j.plasmid.2013.01.007); pmid: [23396045](https://pubmed.ncbi.nlm.nih.gov/23396045/)
92. S. Hansen *et al.*, Regulation of the *Escherichia coli* HipBA toxin-antitoxin system by proteolysis. *PLOS ONE* **7**, e39185 (2012). doi: [10.1371/journal.pone.0039185](https://doi.org/10.1371/journal.pone.0039185); pmid: [22720069](https://pubmed.ncbi.nlm.nih.gov/22720069/)
93. X. Wang, T. K. Wood, Toxin-antitoxin systems influence biofilm and persister cell formation and the general stress response. *Appl. Environ. Microbiol.* **77**, 5577–5583 (2011). doi: [10.1128/AEM.05068-11](https://doi.org/10.1128/AEM.05068-11); pmid: [21685157](https://pubmed.ncbi.nlm.nih.gov/21685157/)
94. H. Tamman, A. Ainelo, K. Ainsaar, R. Hörak, A moderate toxin, GraT, modulates growth rate and stress tolerance of *Pseudomonas putida*. *J. Bacteriol.* **196**, 157–169 (2014). doi: [10.1128/JB.00851-13](https://doi.org/10.1128/JB.00851-13); pmid: [24163334](https://pubmed.ncbi.nlm.nih.gov/24163334/)
95. B. W. Kwan *et al.*, The MqsR/MqsA toxin/antitoxin system protects *Escherichia coli* during bile acid stress. *Environ. Microbiol.* **17**, 3168–3181 (2015). doi: [10.1111/1462-2920.12749](https://doi.org/10.1111/1462-2920.12749); pmid: [25534751](https://pubmed.ncbi.nlm.nih.gov/25534751/)
96. E. Rotem *et al.*, Regulation of phenotypic variability by a threshold-based mechanism underlies bacterial persistence. *Proc. Natl. Acad. Sci. U.S.A.* **107**, 12541–12546 (2010). doi: [10.1073/pnas.1004333107](https://doi.org/10.1073/pnas.1004333107); pmid: [20616060](https://pubmed.ncbi.nlm.nih.gov/20616060/)
97. I. Cataudella, A. Trusina, K. Sneppen, K. Gerdes, N. Mitarai, Conditional cooperativity in toxin-antitoxin regulation prevents random toxin activation and promotes fast translational recovery. *Nucleic Acids Res.* **40**, 6424–6434 (2012). doi: [10.1093/nar/gks297](https://doi.org/10.1093/nar/gks297); pmid: [22495927](https://pubmed.ncbi.nlm.nih.gov/22495927/)
98. N. Vázquez-Laslop, H. Lee, A. A. Neyfakh, Increased persistence in *Escherichia coli* caused by controlled expression of toxins or other unrelated proteins. *J. Bacteriol.* **188**, 3494–3497 (2006). doi: [10.1128/JB.188.10.3494-3497.2006](https://doi.org/10.1128/JB.188.10.3494-3497.2006); pmid: [16672603](https://pubmed.ncbi.nlm.nih.gov/16672603/)
99. N. D. Walter *et al.*, Transcriptional adaptation of drug-tolerant *Mycobacterium tuberculosis* during treatment of human tuberculosis. *J. Infect. Dis.* **212**, 990–998 (2015). doi: [10.1093/infdis/jiv149](https://doi.org/10.1093/infdis/jiv149); pmid: [25762787](https://pubmed.ncbi.nlm.nih.gov/25762787/)
100. B. W. Kwan, J. A. Valenta, M. J. Benedikt, T. K. Wood, Arrested protein synthesis increases persister-like cell formation. *Antimicrob. Agents Chemother.* **57**, 1468–1473 (2013). doi: [10.1128/AAC.02135-12](https://doi.org/10.1128/AAC.02135-12); pmid: [23295927](https://pubmed.ncbi.nlm.nih.gov/23295927/)
101. V. N. De Groote *et al.*, Novel persistence genes in *Pseudomonas aeruginosa* identified by high-throughput screening. *FEMS Microbiol. Lett.* **297**, 73–79 (2009). doi: [10.1111/j.1574-6968.2009.01657.x](https://doi.org/10.1111/j.1574-6968.2009.01657.x); pmid: [19508279](https://pubmed.ncbi.nlm.nih.gov/19508279/)
102. Y. Shan, D. Lazinski, S. Rowe, A. Camilli, K. Lewis, Genetic basis of persister tolerance to aminoglycosides in *Escherichia coli*. *mBio* **6**, e00078-15 (2015). doi: [10.1128/mBio.00078-15](https://doi.org/10.1128/mBio.00078-15); pmid: [25852159](https://pubmed.ncbi.nlm.nih.gov/25852159/)
103. J. J. Harrison *et al.*, The chromosomal toxin gene *yafQ* is a determinant of multidrug tolerance for *Escherichia coli* growing in a biofilm. *Antimicrob. Agents Chemother.* **53**, 2253–2258 (2009). doi: [10.1128/AAC.00043-09](https://doi.org/10.1128/AAC.00043-09); pmid: [19307375](https://pubmed.ncbi.nlm.nih.gov/19307375/)
104. D. W. Holden, Persisters unmasked. *Science* **347**, 30–32 (2015). doi: [10.1126/science.1262033](https://doi.org/10.1126/science.1262033); pmid: [25554777](https://pubmed.ncbi.nlm.nih.gov/25554777/)
105. R. Singh, C. E. Barry III, H. I. Boshoff, The three RelE homologs of *Mycobacterium tuberculosis* have individual, drug-specific effects on bacterial antibiotic tolerance. *J. Bacteriol.* **192**, 1279–1291 (2010). doi: [10.1128/JB.01285-09](https://doi.org/10.1128/JB.01285-09); pmid: [20061486](https://pubmed.ncbi.nlm.nih.gov/20061486/)
106. D. P. Pandey, K. Gerdes, Toxin-antitoxin loci are highly abundant in free-living but lost from host-associated prokaryotes. *Nucleic Acids Res.* **33**, 966–976 (2005). doi: [10.1093/nar/gki201](https://doi.org/10.1093/nar/gki201); pmid: [15718296](https://pubmed.ncbi.nlm.nih.gov/15718296/)
107. E. Germain, D. Castro-Roa, N. Zenkin, K. Gerdes, Molecular mechanism of bacterial persistence by HipA. *Mol. Cell* **52**, 248–254 (2013). doi: [10.1016/j.molcel.2013.08.045](https://doi.org/10.1016/j.molcel.2013.08.045); pmid: [24095282](https://pubmed.ncbi.nlm.nih.gov/24095282/)
108. C. Tian *et al.*, Rapid curtailing of the stringent response by toxin-antitoxin module-encoded mRNases. *J. Bacteriol.* **198**, 1918–1926 (2016). doi: [10.1128/JB.00062-16](https://doi.org/10.1128/JB.00062-16); pmid: [27137501](https://pubmed.ncbi.nlm.nih.gov/27137501/)
109. H. S. Girgis, K. Harris, S. Tavaio, Large mutational target size for rapid emergence of bacterial persistence. *Proc. Natl. Acad. Sci. U.S.A.* **109**, 12740–12745 (2012). doi: [10.1073/pnas.1205124109](https://doi.org/10.1073/pnas.1205124109); pmid: [22802628](https://pubmed.ncbi.nlm.nih.gov/22802628/)
110. D. Lobato-Márquez, I. Moreno-Córdoba, V. Figueroa, R. Díaz-Orejías, F. García-del Portillo, Distinct type I and type II toxin-antitoxin modules control *Salmonella* lifestyle inside eukaryotic cells. *Sci. Rep.* **5**, 9374 (2015). doi: [10.1038/srep09374](https://doi.org/10.1038/srep09374); pmid: [25792384](https://pubmed.ncbi.nlm.nih.gov/25792384/)
111. A. Sala, P. Bordes, P. Genevieux, Multiple toxin-antitoxin systems in *Mycobacterium tuberculosis*. *Toxins (Basel)* **6**, 1002–1020 (2014). doi: [10.3390/toxins6031002](https://doi.org/10.3390/toxins6031002); pmid: [24662523](https://pubmed.ncbi.nlm.nih.gov/24662523/)
112. H. R. Ramage, L. E. Connolly, J. S. Cox, Comprehensive functional analysis of *Mycobacterium tuberculosis* toxin-antitoxin systems: Implications for pathogenesis, stress responses, and evolution. *PLOS Genet.* **5**, e1000767 (2009). doi: [10.1371/journal.pgen.1000767](https://doi.org/10.1371/journal.pgen.1000767); pmid: [20011113](https://pubmed.ncbi.nlm.nih.gov/20011113/)
113. P. Tiwari *et al.*, MazF ribonucleases promote *Mycobacterium tuberculosis* drug tolerance and virulence in guinea pigs. *Nat. Commun.* **6**, 6059 (2015). doi: [10.1038/ncomms7059](https://doi.org/10.1038/ncomms7059); pmid: [25608501](https://pubmed.ncbi.nlm.nih.gov/25608501/)
114. Y. Shao *et al.*, TADB: A web-based resource for Type 2 toxin-antitoxin loci in bacteria and archaea. *Nucleic Acids Res.* **39** (suppl. 1), D606–D611 (2011). doi: [10.1093/nar/gkq908](https://doi.org/10.1093/nar/gkq908); pmid: [20929871](https://pubmed.ncbi.nlm.nih.gov/20929871/)
115. S. L. McKay, D. A. Portnoy, Ribosome hibernation facilitates tolerance of stationary-phase bacteria to aminoglycosides. *Antimicrob. Agents Chemother.* **59**, 6992–6999 (2015). doi: [10.1128/AAC.01532-15](https://doi.org/10.1128/AAC.01532-15); pmid: [26324267](https://pubmed.ncbi.nlm.nih.gov/26324267/)
116. J. R. Pohlhaus, K. N. Kreuzer, Norfloxacin-induced DNA gyrase cleavage complexes block *Escherichia coli* replication forks, causing double-stranded breaks *in vivo*. *Mol. Microbiol.* **56**, 1416–1429 (2005). doi: [10.1111/j.1365-2958.2005.04638.x](https://doi.org/10.1111/j.1365-2958.2005.04638.x); pmid: [15916595](https://pubmed.ncbi.nlm.nih.gov/15916595/)
117. J. DeNapoli, A. K. Tehranchi, J. D. Wang, Dose-dependent reduction of replication elongation rate by (p)ppGpp in *Escherichia coli* and *Bacillus subtilis*. *Mol. Microbiol.* **88**, 93–104 (2013). doi: [10.1111/mmi.12172](https://doi.org/10.1111/mmi.12172); pmid: [23461544](https://pubmed.ncbi.nlm.nih.gov/23461544/)
118. H. Cho, T. Uehara, T. G. Bernhardt, Beta-lactam antibiotics induce a lethal malfunctioning of the bacterial cell wall synthesis machinery. *Cell* **159**, 1300–1311 (2014). doi: [10.1016/j.cell.2014.11.017](https://doi.org/10.1016/j.cell.2014.11.017); pmid: [25480295](https://pubmed.ncbi.nlm.nih.gov/25480295/)
119. Y. Pu *et al.*, Enhanced efflux activity facilitates drug tolerance in dormant bacterial cells. *Mol. Cell* **62**, 284–294 (2016). doi: [10.1016/j.molcel.2016.03.035](https://doi.org/10.1016/j.molcel.2016.03.035); pmid: [27105118](https://pubmed.ncbi.nlm.nih.gov/27105118/)
120. Y. Liu, J. A. Imlay, Cell death from antibiotics without the involvement of reactive oxygen species. *Science* **339**, 1210–1213 (2013). doi: [10.1126/science.1232751](https://doi.org/10.1126/science.1232751); pmid: [23471409](https://pubmed.ncbi.nlm.nih.gov/23471409/)

121. I. Keren, Y. Wu, J. Inocencio, L. R. Mulcahy, K. Lewis, Killing by bactericidal antibiotics does not depend on reactive oxygen species. *Science* **339**, 1213–1216 (2013). doi: [10.1126/science.1232688](https://doi.org/10.1126/science.1232688); pmid: [23471410](https://pubmed.ncbi.nlm.nih.gov/23471410/)
122. M. Khakimova, H. G. Ahlgren, J. J. Harrison, A. M. English, D. Nguyen, The stringent response controls catalases in *Pseudomonas aeruginosa* and is required for hydrogen peroxide and antibiotic tolerance. *J. Bacteriol.* **195**, 2011–2020 (2013). doi: [10.1128/JB.02061-12](https://doi.org/10.1128/JB.02061-12); pmid: [23457248](https://pubmed.ncbi.nlm.nih.gov/23457248/)
123. C. Ma *et al.*, Energy production genes *sucB* and *ubiF* are involved in persister survival and tolerance to multiple antibiotics and stresses in *Escherichia coli*. *FEMS Microbiol. Lett.* **303**, 33–40 (2010). doi: [10.1111/j.1574-6968.2009.01857.x](https://doi.org/10.1111/j.1574-6968.2009.01857.x); pmid: [20041955](https://pubmed.ncbi.nlm.nih.gov/20041955/)
124. W. Wang *et al.*, Transposon mutagenesis identifies novel genes associated with *Staphylococcus aureus* persister formation. *Front. Microbiol.* **6**, 1437 (2015). pmid: [26779120](https://pubmed.ncbi.nlm.nih.gov/26779120/)
125. M. A. Orman, M. P. Brynildsen, Inhibition of stationary phase respiration impairs persister formation in *E. coli*. *Nat. Commun.* **6**, 7983 (2015). doi: [10.1038/ncomms8983](https://doi.org/10.1038/ncomms8983); pmid: [26246187](https://pubmed.ncbi.nlm.nih.gov/26246187/)
126. J. S. Kim *et al.*, Fumarate-mediated persistence of *Escherichia coli* against antibiotics. *Antimicrob. Agents Chemother.* **60**, 2232–2240 (2016). doi: [10.1128/AAC.01794-15](https://doi.org/10.1128/AAC.01794-15); pmid: [26810657](https://pubmed.ncbi.nlm.nih.gov/26810657/)
127. A. L. Spoering, M. Vulic, K. Lewis, GlpD and PlsB participate in persister cell formation in *Escherichia coli*. *J. Bacteriol.* **188**, 5136–5144 (2006). doi: [10.1128/JB.00369-06](https://doi.org/10.1128/JB.00369-06); pmid: [16816185](https://pubmed.ncbi.nlm.nih.gov/16816185/)
128. S. S. Epstein, Microbial awakenings. *Nature* **457**, 1083 (2009). doi: [10.1038/4571083a](https://doi.org/10.1038/4571083a); pmid: [19242455](https://pubmed.ncbi.nlm.nih.gov/19242455/)
129. A. Jöers, N. Kaldalu, T. Tenson, The frequency of persisters in *Escherichia coli* reflects the kinetics of awakening from dormancy. *J. Bacteriol.* **192**, 3379–3384 (2010). doi: [10.1128/JB.00056-10](https://doi.org/10.1128/JB.00056-10); pmid: [20435730](https://pubmed.ncbi.nlm.nih.gov/20435730/)
130. M. A. Schumacher *et al.*, Role of unusual P loop ejection and autophosphorylation in HipA-mediated persistence and multidrug tolerance. *Cell Reports* **2**, 518–525 (2012). doi: [10.1016/j.celrep.2012.08.013](https://doi.org/10.1016/j.celrep.2012.08.013); pmid: [22999936](https://pubmed.ncbi.nlm.nih.gov/22999936/)
131. A. Theodore, K. Lewis, M. Vulic, Tolerance of *Escherichia coli* to fluoroquinolone antibiotics depends on specific components of the SOS response pathway. *Genetics* **195**, 1265–1276 (2013). doi: [10.1534/genetics.113.152306](https://doi.org/10.1534/genetics.113.152306); pmid: [24077306](https://pubmed.ncbi.nlm.nih.gov/24077306/)
132. E. Wexselblatt *et al.*, Relacin, a novel antibacterial agent targeting the Stringent Response. *PLOS Pathog.* **8**, e1002925 (2012). doi: [10.1371/journal.ppat.1002925](https://doi.org/10.1371/journal.ppat.1002925); pmid: [23028324](https://pubmed.ncbi.nlm.nih.gov/23028324/)
133. B. P. Conlon *et al.*, Activated ClpP kills persisters and eradicates a chronic biofilm infection. *Nature* **503**, 365–370 (2013). doi: [10.1038/nature12790](https://doi.org/10.1038/nature12790); pmid: [24226776](https://pubmed.ncbi.nlm.nih.gov/24226776/)
134. N. Chowdhury, B. W. Kwan, T. K. Wood, Persistence increases in the absence of the alarmone guanosine tetraphosphate by reducing cell growth. *Sci. Rep.* **6**, 20519 (2016). doi: [10.1038/srep20519](https://doi.org/10.1038/srep20519); pmid: [26837570](https://pubmed.ncbi.nlm.nih.gov/26837570/)

ACKNOWLEDGMENTS

This work was supported by the Danish National Research Foundation–funded Centre of Excellence BASP (grant DNRF120), a Novo Nordisk Foundation Laureate Research grant, and the European Research Council Advanced Investigator grant PERSIST (294517). A.H. is grateful for the support of C. Dehio and a European Molecular Biology Organization Long-Term Fellowship (ALTF 564-2016). The authors do not declare any competing interests.

10.1126/science.aaf4268

REPORTS

PHOTOCHEMISTRY

Enantioselective photochemistry through Lewis acid-catalyzed triplet energy transfer

Travis R. Blum, Zachary D. Miller, Desiree M. Bates, Ilia A. Guzei, Tehshik P. Yoon*

Relatively few catalytic systems are able to control the stereochemistry of electronically excited organic intermediates. Here we report the discovery that a chiral Lewis acid complex can catalyze triplet energy transfer from an electronically excited photosensitizer. We applied this strategy to asymmetric [2 + 2] photocycloadditions of 2'-hydroxychalcones, using tris(bipyridyl) ruthenium(II) as a sensitizer. A variety of electrochemical, computational, and spectroscopic data rule out substrate activation by means of photoinduced electron transfer and instead support a mechanism in which Lewis acid coordination dramatically lowers the triplet energy of the chalcone substrate. We expect that this approach will enable chemists to more broadly apply their detailed understanding of chiral Lewis acid catalysis to stereocontrol in reactions involving electronically excited states.

The ability to control the stereochemistry of organic reactions is a defining characteristic of contemporary synthetic chemistry. Because access to structurally well-defined organic molecules is important for progress in fields of research ranging from drug discovery to materials science, numerous chiral catalysts have been developed to control the enantioselectivity of a wide range of mechanistically diverse organic transformations. Photochemical reactions, however, have long proven to be challenging to conduct in an enantioselective fashion, particularly with substoichiometric stereocontrolling catalysts (1, 2). This represents a fundamental gap in synthetic methodology because the reactivity of electronically excited organic molecules is distinctive and often impossible to replicate using nonphotochemical techniques (3, 4).

Recently, a renewed interest in synthetic applications of photoinduced electron transfer (5) has resulted in the development of several strategies for performing highly enantioselective photocatalytic reactions. In general, these protocols have involved the photochemical generation of reactive intermediates by using an organic or transition metal photoredox catalyst; subsequently, a second chiral Lewis acid (6), Brønsted acid (7, 8), or organic catalyst (9, 10) influences the stereochemistry of ensuing reactions and affords highly enantioenriched products. The key bond-forming events in all of these photoredox reactions necessarily occur via photogenerated reactive intermediates in their electronic ground-state configurations. Although photoactivation provides a particularly convenient strategy for the generation of the open-shell radical and radical ion intermediates in-

involved in these reactions, similar reactive intermediates can be generated through a variety of nonphotochemical means (11). Stereochemical control over the distinctive reactivity of excited-state organic intermediates remains a largely unsolved challenge.

The difficulty of controlling electronically excited organic molecules with exogenous chiral catalysts is commonly attributed to the characteristically short lifetimes of the former, which arise from fast unimolecular vibrational and emissive deactivation pathways that are not available to ground-state reactive intermediates. Highly enantioselective catalytic reactions of photoexcited organic substrates have only recently been reported, using either chiral hydrogen-bonding organic sensitizers (12–16) or, more recently, chiral Lewis acid catalysts (17–20).

We were intrigued by this latter advance because Lewis acid catalysis offers a mature, well-understood platform for asymmetric synthesis. The ability to generalize a chiral Lewis acid strategy for excited-state photoreactions would offer a powerful tool for organic photochemistry. Bach and coworkers' seminal results in this area have demonstrated that chiral oxazaborolidines can be used to mediate asymmetric [2 + 2] photocycloadditions of enones (17–20) (Fig. 1A). These impressive proof-of-principle studies nevertheless rely on subtle changes in the absorption properties of the substrate that arise upon coordination to a Lewis acid (21). High levels of enantiomeric excess (ee) are only feasible if the catalyst-substrate complex can be photoexcited preferentially over the unbound, achiral substrate to minimize the participation of racemic background reactions. Because this approach requires a delicate balancing of the singlet excited-state properties of both the free substrate and the chiral Lewis acid-substrate complex (22), the range of substrates

that have been shown to date to provide high enantioselectivities when using Bach's chiral oxazaborolidine strategy is somewhat narrowly constrained to cyclic enones.

We envisioned an alternative approach in which a chiral Lewis acid would serve as a catalyst for triplet energy transfer from a racemic triplet sensitizer. The coordination of Lewis acids to enones can substantially perturb the energy of their singlet excited states, a phenomenon first documented by Lewis and colleagues several decades ago (23, 24). The effect of Lewis acid coordination on triplet energies, to the best of our knowledge, has not been the subject of similarly detailed exploration. We hypothesized that if coordination of a Lewis acid to an enone could produce a bathochromic shift in the energy of its singlet excited state, the same interaction might exert an analogous effect on its triplet state energy as well. If so, it should be possible to design a system in which triplet energy transfer from an appropriate sensitizer would become thermodynamically feasible only when a substrate enone is bound to a chiral Lewis acid cocatalyst (Fig. 1B).

In previous work, we have shown that chiral Lewis acids are effective in controlling the stereochemical course of reactions initiated by photoinduced electron transfer from an electronically excited $\text{Ru}^*(\text{bpy})_3^{2+}$ photocatalyst (where the asterisk indicates the excited state; bpy, 2,2'-bipyridine) (6). Among the most substantial benefits of this two-catalyst strategy is the ability to modify the structure of a chiral Lewis acid for optimal stereocontrol without deleteriously affecting the desirable photophysical properties of the sensitizer. This flexibility opens photochemical synthesis to the wide range of Lewis acid scaffolds that are known to be highly effective in other enantioselective reactions, and we have subsequently shown that the same strategy can be applied to a number of other reactions that exploit chiral Lewis acid-catalyzed photoredox activation (25, 26). We propose that this concept, when applied to the more difficult problem of catalytic energy transfer, can have similarly broad ramifications.

The feasibility of Lewis acid-catalyzed triplet energy transfer was initially tested by examining the effect of exogenous Lewis acids on photocatalytic reactions of 2'-hydroxychalcone (**2**) (Table 1). This substrate provides an ideal model system because the 2'-hydroxyaryl ketone moiety is predisposed toward association with a variety of Lewis acidic metals, and because the photochemical properties of **2** have been thoroughly characterized. In particular, **2** has been experimentally shown to possess a triplet state that is 54 kcal/mol higher in energy than its closed-shell singlet ground state (27). This triplet energy (E_T) is well outside of the range that should be reasonably accessible using $\text{Ru}(\text{bpy})_3^{2+}$ as a triplet sensitizer ($E_T = 46$ kcal/mol) (28). Indeed, an experiment in which **2** and diene **3** were irradiated with visible light in the presence of $\text{Ru}(\text{bpy})_3(\text{PF}_6)_2$ showed minimal evidence of productive photoreaction (entry 1). But when the same reaction was conducted in the presence of various oxophilic Lewis acid additives,

Department of Chemistry, University of Wisconsin–Madison, Madison, WI 53706, USA.

*Corresponding author. Email: tyoon@chem.wisc.edu

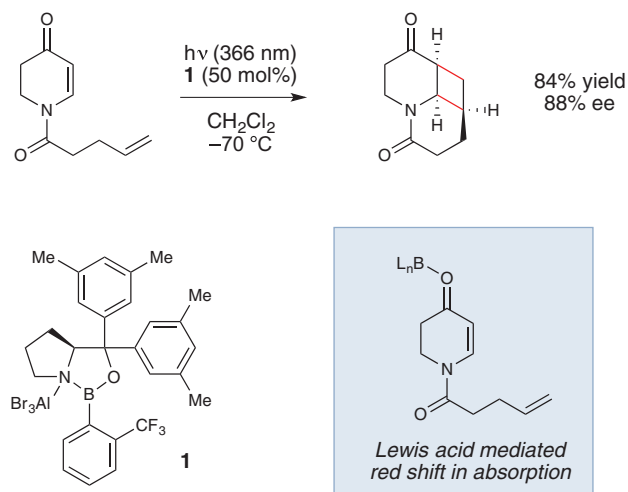
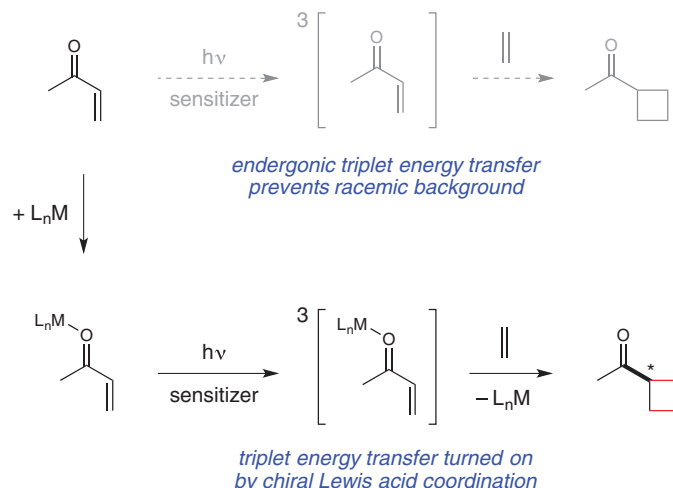
A Previous work: (Bach, ref 20)**B This work:** Lewis acid catalyzed energy transfer

Fig. 1. Enantioselective catalysis involving excited-state organic intermediates. (A) A prior example of enantioselective Lewis acid-catalyzed photoreaction involving direct photoexcitation of a chiral catalyst-substrate complex. (B) Design for Lewis acid catalysis of a triplet sensitization reaction. ee, enantiomeric excess; Me, methyl; L_nM, generic Lewis acidic metal-ligand complex; red lines, new bonds.

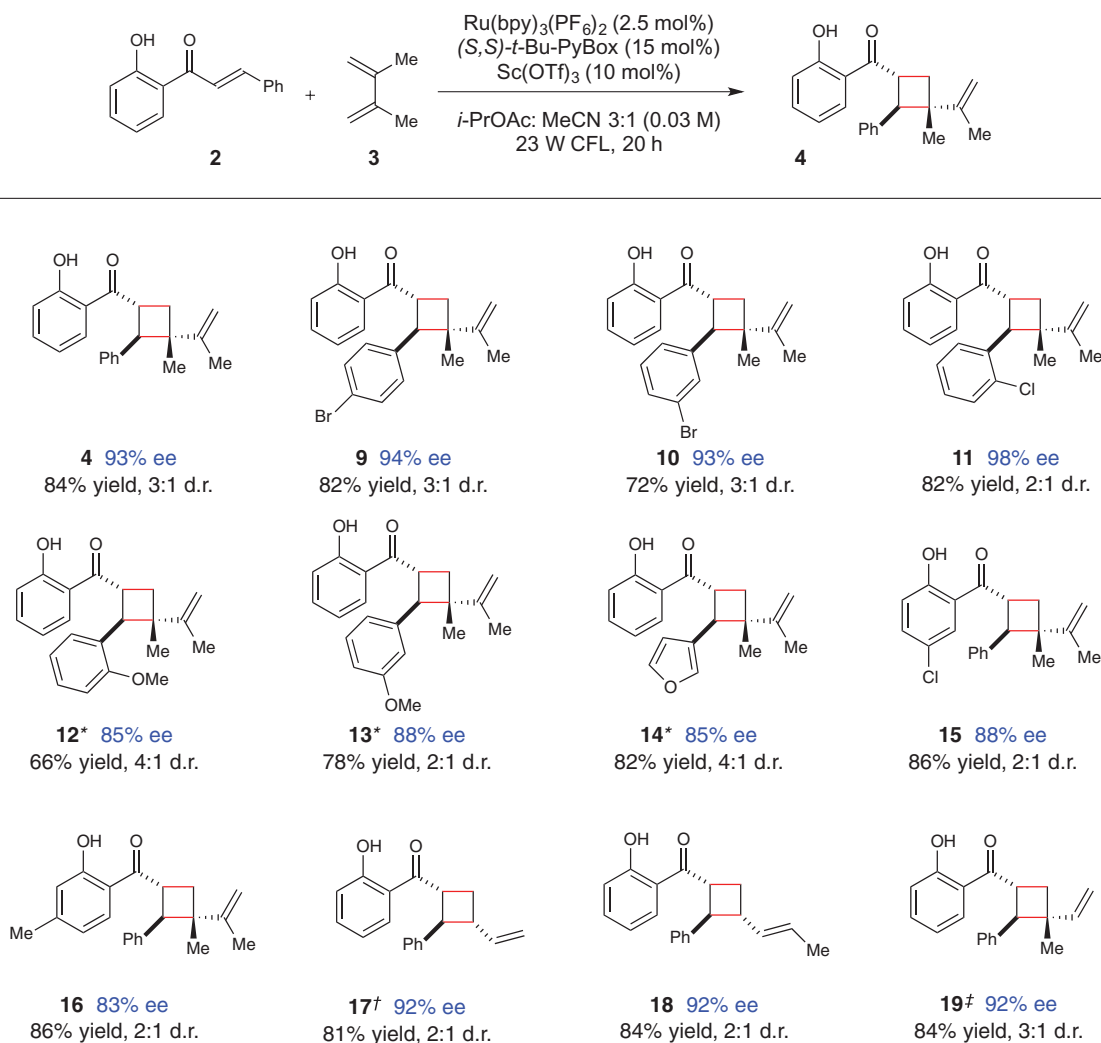
Fig. 2. Scope of the enantioselective catalytic [2 + 2] cycloaddition of 2'-hydroxychalcones.

Data reflect the averaged isolated yields from two reproducible experiments. Diastereomer ratios (d.r.) were determined by proton nuclear magnetic resonance (¹H NMR) analysis of the unpurified reaction mixture. Enantiomer ratios were determined using chiral supercritical fluid chromatography (SFC) or high-performance liquid chromatography (HPLC) analysis. Details are provided in the supplementary materials.

*Irradiation was conducted using a blue LED lamp instead of a 23 W CFL bulb (2 hours irradiation time).

†40 hours irradiation time.

‡Isolated as a 6:1 mixture of regioisomers. bpy, 2,2'-bipyridine; t-Bu, *tert*-butyl; Ph, phenyl; Ac, acetyl; OTf, triflate; h, hours.



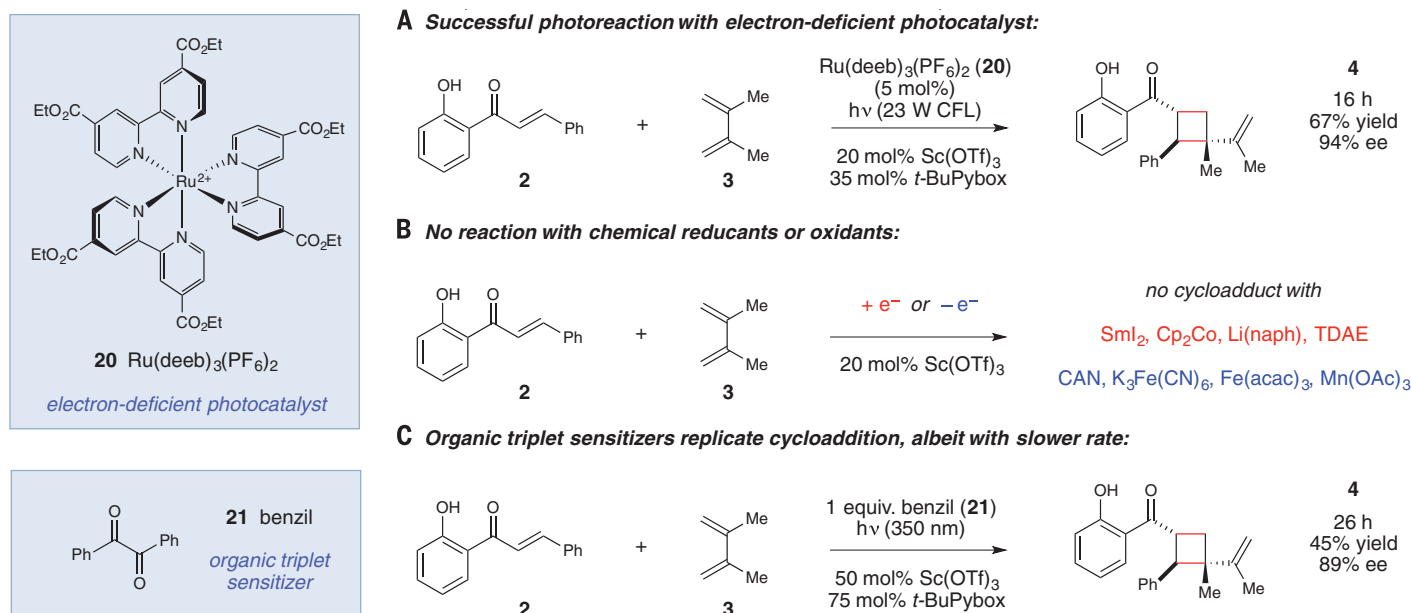
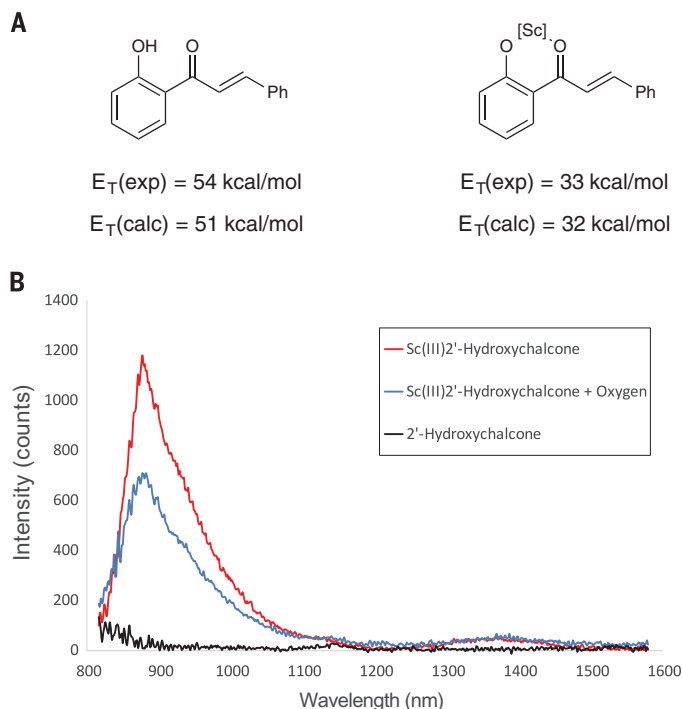


Fig. 3. Differentiation of electron transfer and energy transfer pathways. (A) Successful photocycloaddition using an electron-deficient photocatalyst rules out a mechanism involving initial enone photoreduction. (B) Experiments using chemical redox reagents fail to produce [2 + 2] cycloadducts. (C) An ultraviolet light-activated triplet sensitizer replicates reactivity with similar ee. Full details are given in the supplementary materials. Et, ethyl; deeb, 2,2'-bipyridinyl-4,4'-dicarboxylic acid diethyl ester; Cp_2Co , cobaltocene; $\text{Li}(\text{naph})$, lithium naphthalenide; TDAE, tetrakis(dimethylamino)ethylene; CAN, ammonium cerium(IV) nitrate; $\text{Fe}(\text{acac})_3$, iron(III) acetylacetonate.

Fig. 4. Computational and experimental evidence for a Lewis acid-promoted decrease in triplet energy (E_T). (A) Experimental (exp) and calculated (calc) S_0-T_1 gaps for 2'-hydroxychalcone **2** and its $\text{Sc}(\text{III})$ complex.

(B) Experimental near-IR emission data for 2'-hydroxychalcone **2** in the absence (black) and presence (red) of $\text{Sc}(\text{OTf})_3$. The emission is partially quenched in the presence of oxygen (blue).



we observed the formation of [2 + 2] cycloadduct **4** in good to moderate yields (entries 2 to 5). Control experiments indicated that the cycloaddition occurs only in the presence of both the photocatalyst and the Lewis acid cocatalyst, because no cycloadduct was observed when $\text{Ru}(\text{bpy})_3^{2+}$ was omitted or when the reaction was conducted in the dark (entries 6 and 7). Given the strict dependence on the presence of a Lewis acid, we

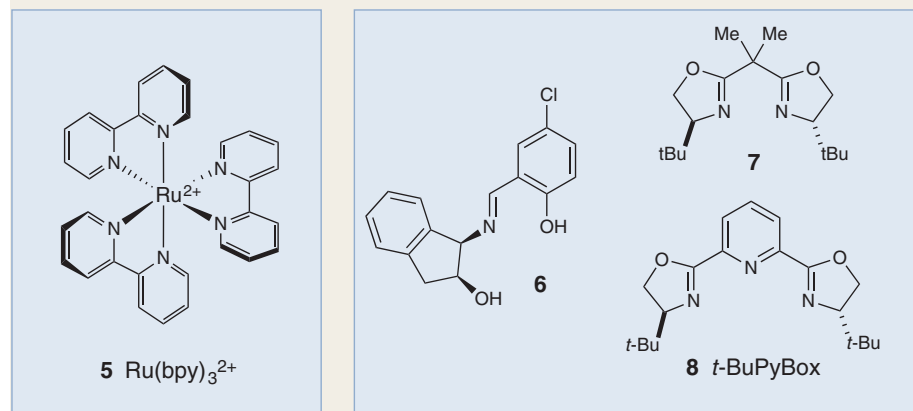
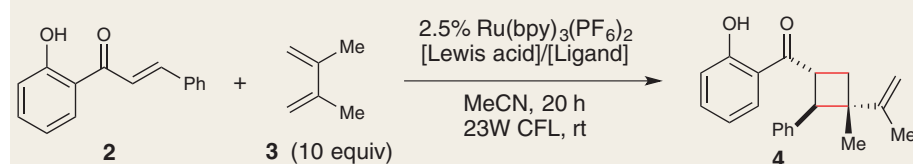
speculated that a highly enantioselective reaction might result from the use of a chiral Lewis acid complex. After investigating several classes of chiral ligands, we found that $\text{Sc}(\text{III})$ PyBox complexes generally worked well as chiral Lewis acid cocatalysts, and *t*-Bu-PyBox (*t*-Bu, *tert*-butyl) (**7**) in particular provided promising ee (entries 8 to 10). Subsequent optimization of standard reaction variables (**29**) afforded our optimized con-

ditions (entry 11), which produced cyclobutane **4** in high yields and excellent enantioselectivity. Last, we conducted an experiment using a 2:1 mixture of (*E*)- and (*Z*)-2'-hydroxychalcone as the substrate and found that the geometry of the alkene had no discernible impact on the stereoselectivity of the reaction, consistent with a stepwise triplet cycloaddition (entry 12).

This reaction is a rare example of an enantioselective catalytic intermolecular photocycloaddition (**16**) and, to the best of our knowledge, is the only example of a highly enantioselective cycloaddition of an acyclic excited-state enone. Studies exploring the synthetic scope of this transformation are outlined in Fig. 2 (**30**). Variation of the β -aryl moiety of the chalcone was well tolerated. Substrates with ortho, meta, and para substituents on this ring provided excellent ee and good yields (**9** to **11**). Chalcones with electron-rich β -aryl groups participated in an uncatalyzed background cycloaddition under compact fluorescent lamp (CFL) irradiation and therefore required irradiation with a monochromatic blue light-emitting diode (LED; emission maximum, 450 nm) light source for optimal enantioselectivities (**12** to **14**) (**31**). Heteroaryl groups were also easily accommodated using this method (**14**). Substitution of the hydroxyphenyl moiety was tolerated (**15** and **16**) so long as this substituent did not interfere with the putative binding site for the chiral Lewis acid. Last, a range of substituted and unsubstituted dienes also provided high ee and good yields (**17** to **19**), and unsymmetrical dienes offered good levels of regioselectivity (**18** and **19**).

Several lines of evidence support the hypothesis that this transformation involves substrate

Table 1. Optimization and control studies for Lewis acid-catalyzed enantioselective cycloadditions of 2'-hydroxychalcone. Yields were determined by ^1H NMR, using phenanthrene as a calibrated internal standard. Enantiomer ratios were determined by chiral SFC analysis. rt, room temperature; equiv, equivalent.



racemic photocatalyst

chiral stereodifferentiating ligand

Entry	Lewis acid	Ligand	Note	Yield	ee
1	None	None	—	<5%	—
2	$\text{Al}(\text{OTf})_3$ (1 equiv)	None	—	70%	—
3	$\text{Ti}(\text{OEt})_4$ (1 equiv)	None	—	29%	—
4	$\text{Y}(\text{OTf})_3$ (1 equiv)	None	—	15%	—
5	$\text{Sc}(\text{OTf})_3$ (1 equiv)	None	—	88%	—
6	$\text{Sc}(\text{OTf})_3$ (1 equiv)	None	No $\text{Ru}(\text{bpy})_3(\text{PF}_6)_2$	<5%	—
7	$\text{Sc}(\text{OTf})_3$ (1 equiv)	None	No light	<5%	—
8	$\text{Sc}(\text{OTf})_3$ (20 mol %)	6 (30 mol %)	—	52%	0%
9	$\text{Sc}(\text{OTf})_3$ (20 mol %)	7 (30 mol %)	—	64%	0%
10	$\text{Sc}(\text{OTf})_3$ (20 mol %)	8 (30 mol %)	—	75%	74%
11	$\text{Sc}(\text{OTf})_3$ (10 mol %)	8 (15 mol %)	3:1 <i>i</i> -PrOAc:MeCN	80%	93%
12*	$\text{Sc}(\text{OTf})_3$ (10 mol %)	8 (15 mol %)	3:1 <i>i</i> -PrOAc:MeCN	89%	93%

*Reaction conducted using a 2:1 ratio of (*Z*)- and (*E*)-2'-hydroxychalcone as the starting substrate.

activation by means of energy transfer rather than photoredox catalysis. First, Porco and coworkers have reported that redox activation of 2'-hydroxychalcones affords [4 + 2] cycloadducts upon reaction with dienes (32, 33), rather than the [2 + 2] cycloadducts produced in the photocatalytic protocol that we have developed. No traces of similar [4 + 2] Diels-Alder products were observed under our optimized photocatalytic conditions. We also independently investigated the possibility that this reactivity was the result of redox activation. Electrochemical characterization rules out photocatalytic one-electron oxidation as a mechanism of activation: No oxidation features below +1.60 V [versus saturated calomel electrode (SCE)] are observable in the cyclic voltammogram of **2**, either in the presence or absence of $\text{Sc}(\text{OTf})_3$ (OTf, triflate), indicating that $\text{Ru}^*(\text{bpy})_3^{2+}$

is too weak an oxidant (excited-state oxidation potential, $E_{\text{ox}}^* = +0.77$ V) to activate the chalcone substrate this way. We did, however, observe a reduction feature with a half-wave potential of -1.2 V (versus SCE) in the cyclic voltammogram of **2** that shifted to -0.47 V in the presence of $\text{Sc}(\text{OTf})_3$. Although photoreduction of the $\text{Sc}\cdot\text{2}$ complex by $\text{Ru}^*(\text{bpy})_3^{2+}$ (excited-state reduction potential, $E_{\text{red}}^* = -0.81$ V versus SCE) cannot be ruled out on the basis of these electrochemical data, we found that a variety of substantially less reducing Ru photocatalysts also successfully mediated this cycloaddition. For example, in an experiment replacing $\text{Ru}(\text{bpy})_3(\text{PF}_6)_2$ with its much more electron-deficient analog $\text{Ru}(\text{deeb})_3(\text{PF}_6)_2$ (deeb, 2,2'-bipyridinyl-4,4'-dicarboxylic acid diethyl ester) (**20**), from which photoreduction of the $\text{Sc}\cdot\text{2}$ complex would be endergonic ($E_{\text{red}}^* = -0.42$ V) (**34**), we nevertheless

observed formation of cycloadduct **2** in 67% yield and similar enantioselectivity (Fig. 3A).

Consistent with these results, attempts to replicate the [2 + 2] reaction by using $\text{Sc}(\text{OTf})_3$ in combination with a range of standard chemical one-electron reductants failed to produce any [2 + 2] products (Fig. 3B). Similar experiments using chemical one-electron oxidants also did not afford any photocycloadducts. However, if an energy transfer process is indeed relevant to this Lewis acid-catalyzed cycloaddition, it should be feasible to promote the reaction by using alternative triplet sensitizers. Indeed, when the cycloaddition of 2'-hydroxychalcone **2** and diene **3** was performed under 350 nm irradiation in the presence of benzil (**21**; $E_T = \sim 54$ kcal/mol) (**35**), we observed modest yields of the desired [2 + 2] cycloaddition product but comparable enantioselectivity to the $\text{Ru}(\text{bpy})_3(\text{PF}_6)_2$ -catalyzed reaction (Fig. 3C). Because of the high sensitivity of asymmetric catalysis to changes in mechanism (**36**), we interpret this result as strong corroborating evidence for Lewis acid-catalyzed triplet sensitization as the operative pathway.

Last, we investigated the hypothesis that the Lewis acid cocatalyst in this energy transfer process serves to lower the triplet energy of the hydroxychalcone substrate. The S_0-T_1 gap for free **2** was studied computationally [B3LYP/6-311+G(2d,p)]. These calculations gave a triplet energy of 51 kcal/mol (Fig. 4A), in reasonably good agreement with the reported experimental value of 54 kcal/mol (**27**). The analogous computation on the $\text{Sc}(\text{III})$ complex of **2**, however, suggested that the energy of the lowest optimized triplet state would be dramatically lowered to 32 kcal/mol (**37**). This bathochromic shift of 20 kcal/mol in triplet energy upon coordination to a Lewis acid would lie easily within a range where triplet energy transfer from $\text{Ru}^*(\text{bpy})_3^{2+}$ would be exergonic, in good accord with our design. The magnitude of the effect suggested by the calculation, however, was unexpectedly large. To validate these computational results, we next investigated the emissive properties of **2** at near-infrared (IR) wavelengths corresponding to the predicted triplet energy. In the absence of $\text{Sc}(\text{OTf})_3$, there was no observable emission signal at wavelengths longer than 800 nm. However, when the emission study was conducted in the presence of added $\text{Sc}(\text{OTf})_3$, we observed a feature at 876 nm, corresponding to an excited-state energy of 33 kcal/mol, in excellent agreement with the computational prediction (Fig. 4B). Moreover, the emission was partially quenched in the presence of oxygen, consistent with emission from a triplet state.

Collectively, these studies reveal a previously unrecognized effect of Lewis acid coordination on the excited states of organic substrates. We have found that complexation of 2'-hydroxychalcones with $\text{Sc}(\text{III})$ results in a dramatic decrease in the energy of the triplet state. Current work in our laboratory is aimed at investigating the applicability of this strategy to other Lewis basic organic substrates and other transformations, which we hope will enable a flexible and robust strategy

for catalytic enantiocontrol in a broad range of organic triplet state reactions.

REFERENCES AND NOTES

1. Y. Inoue, *Chem. Rev.* **92**, 741–770 (1992).
2. R. Brimiouille, D. Lenhart, M. M. Maturi, T. Bach, *Angew. Chem. Int. Ed. Engl.* **54**, 3872–3890 (2015).
3. N. Hoffmann, *Chem. Rev.* **108**, 1052–1103 (2008).
4. T. Bach, J. P. Hehn, *Angew. Chem. Int. Ed. Engl.* **50**, 1000–1045 (2011).
5. C. K. Prier, D. A. Rankic, D. W. C. MacMillan, *Chem. Rev.* **113**, 5322–5363 (2013).
6. J. Du, K. L. Skubi, D. M. Schultz, T. P. Yoon, *Science* **344**, 392–396 (2014).
7. L. J. Rono, H. G. Yayla, D. Y. Wang, M. F. Armstrong, R. R. Knowles, *J. Am. Chem. Soc.* **135**, 17735–17738 (2013).
8. D. Uraguchi, N. Kinoshita, T. Kizu, T. Ooi, *J. Am. Chem. Soc.* **137**, 13768–13771 (2015).
9. D. A. Nicewicz, D. W. C. MacMillan, *Science* **322**, 77–80 (2008).
10. D. A. DiRocco, T. Rovis, *J. Am. Chem. Soc.* **134**, 8094–8097 (2012).
11. A. Studer, D. P. Curran, *Angew. Chem. Int. Ed. Engl.* **55**, 58–102 (2016).
12. C. Müller, A. Bauer, T. Bach, *Angew. Chem. Int. Ed. Engl.* **48**, 6640–6642 (2009).
13. R. Alonso, T. Bach, *Angew. Chem. Int. Ed. Engl.* **53**, 4368–4371 (2014).
14. M. M. Maturi, T. Bach, *Angew. Chem. Int. Ed. Engl.* **53**, 7661–7664 (2014).
15. N. Vallavolu, S. Selvakumar, S. Jockusch, M. P. Sibi, J. Sivaguru, *Angew. Chem. Int. Ed. Engl.* **53**, 5604–5608 (2014).
16. A. Tröster, R. Alonso, A. Bauer, T. Bach, *J. Am. Chem. Soc.* **138**, 7808–7811 (2016).
17. H. Guo, E. Herdtweck, T. Bach, *Angew. Chem. Int. Ed. Engl.* **49**, 7782–7785 (2010).
18. R. Brimiouille, T. Bach, *Angew. Chem. Int. Ed. Engl.* **53**, 12921–12924 (2014).
19. R. Brimiouille, H. Guo, T. Bach, *Chemistry* **18**, 7552–7560 (2012).
20. R. Brimiouille, T. Bach, *Science* **342**, 840–843 (2013).
21. R. Brimiouille, A. Bauer, T. Bach, *J. Am. Chem. Soc.* **137**, 5170–5176 (2015).
22. H. Wang, X. Cao, X. Chen, W. Fang, M. Dolg, *Angew. Chem. Int. Ed. Engl.* **54**, 14295–14298 (2015).
23. F. D. Lewis, D. K. Howard, J. D. Oxman, *J. Am. Chem. Soc.* **105**, 3344–3345 (1983).
24. F. D. Lewis, S. V. Baranyuk, *J. Am. Chem. Soc.* **111**, 8653–8661 (1989).
25. L. Ruiz Espelt, I. S. McPherson, E. M. Wiensch, T. P. Yoon, *J. Am. Chem. Soc.* **137**, 2452–2455 (2015).
26. A. G. Amador, E. M. Sherbrook, T. P. Yoon, *J. Am. Chem. Soc.* **138**, 4722–4725 (2016).
27. Y. Norikane, H. Itoh, T. Arai, *J. Phys. Chem. A* **106**, 2766–2776 (2002).
28. K. Kalyanasundaram, *Coord. Chem. Rev.* **46**, 159–244 (1982).
29. Further details are provided in the supplementary materials.
30. The absolute configuration of the cycloadducts was determined by Riley oxidation of compound **9** to a crystalline derivative, which was unambiguously confirmed by single-crystal x-ray crystallography. Details are given in the supplementary materials.
31. The nature of this background process is poorly understood and is the subject of ongoing studies.
32. H. Cong, D. Ledbetter, G. T. Rowe, J. P. Caradonna, J. A. Porco Jr., *J. Am. Chem. Soc.* **130**, 9214–9215 (2008).
33. H. Cong, C. F. Becker, S. J. Elliott, M. W. Grinstaff, J. A. Porco Jr., *J. Am. Chem. Soc.* **132**, 7514–7518 (2010).
34. C. M. Elliott, R. A. Freitag, D. D. Blaney, *J. Am. Chem. Soc.* **107**, 4647–4655 (1985).
35. W. G. Herkstroeter, A. A. Lamola, G. S. Hammond, *J. Am. Chem. Soc.* **86**, 4537–4540 (1964).
36. E. N. Jacobsen, W. Zhang, M. L. Guler, *J. Am. Chem. Soc.* **113**, 6703–6704 (1991).

ACKNOWLEDGMENTS

We gratefully acknowledge experimental assistance from M. Arnold and M. Shea in obtaining near-IR luminescence spectra. We also

thank J. Schomaker and M. Ju for access to chiral HPLC instrumentation. Experimental details for all studies reported in this paper are described in the supplementary materials. Funding for this project was provided by the NIH (GM09888). The computational resources were supported in part by NSF (CHE-0840494). T.R.B. acknowledges support from a NIH Chemical Biology Interface Training grant (T32 GM008505). T.R.B. conceived the project, conducted the optimization studies described in the supplementary materials, and performed the mechanistic studies. Z.D.M. collected the data reported in Table 1 and Fig. 2 and conducted the cyclic voltammetry studies. D.M.B. and T.R.B. performed the computational studies. I.A.G. collected and analyzed x-ray crystallographic data, which are available free of charge from the Cambridge Crystallographic Data Centre under

accession number CCDC 1507886. All authors contributed to the writing and editing of the manuscript.

SUPPLEMENTARY MATERIALS

www.sciencemag.org/content/354/6318/1391/suppl/DC1
Materials and Methods
Supplementary Text
Figs. S1 to S7
Tables S1 to S18
References (37–51)
Spectral and Chromatographic Data

16 August 2016; accepted 18 November 2016
10.1126/science.aai8228

VOLCANOLOGY

Seismic constraints on caldera dynamics from the 2015 Axial Seamount eruption

William S. D. Wilcock,^{1*} Maya Tolstoy,² Felix Waldhauser,² Charles Garcia,¹ Yen Joe Tan,² DelWayne R. Bohnenstiehl,³ Jacqueline Caplan-Auerbach,⁴ Robert P. Dziak,⁵ Adrien F. Arnulf,⁶ M. Everett Mann³

Seismic observations in volcanically active calderas are challenging. A new cabled observatory atop Axial Seamount on the Juan de Fuca ridge allows unprecedented real-time monitoring of a submarine caldera. Beginning on 24 April 2015, the seismic network captured an eruption that culminated in explosive acoustic signals where lava erupted on the seafloor. Extensive seismic activity preceding the eruption shows that inflation is accommodated by the reactivation of an outward-dipping caldera ring fault, with strong tidal triggering indicating a critically stressed system. The ring fault accommodated deflation during the eruption and provided a pathway for a dike that propagated south and north beneath the caldera's east wall. Once north of the caldera, the eruption stepped westward, and a dike propagated along the extensional north rift.

On land, seismic monitoring is one of the most widely used tools for characterizing volcanic cycles (1). Seismic monitoring of submarine volcanoes, which account for ≥80% of Earth's volcanism (2), is far more difficult because of the challenges of sustaining long-term observations and recovering instruments after an eruption (3). However, the volcanoes that form mid-ocean ridges erupt frequently with a uniform basaltic composition while also having shallow magmatic systems that can be imaged seismically at high resolution. These features make mid-ocean ridge volcanoes good targets for studies of eruption dynamics.

Calderas are important and complex features of many volcanoes. Most high-resolution con-

straints on the internal structure of the ring faults forming calderas come from geological studies of partially eroded calderas, and these have led to a long-standing debate about their orientation and configuration at depth (4, 5). Earthquake observations at several locations support the existence of outward-dipping ring faults (6–9), but the only detailed seismic observation of the role of a ring fault in an eruption of a basaltic volcano comes from Bárðarbunga volcano, Iceland (10). There the lateral propagation of a dike sourced from a 12-km-deep magma chamber led to the collapse of a subglacial caldera with slip on a subvertical ring fault.

Axial Seamount is the most prominent volcanic feature on the Juan de Fuca mid-ocean ridge and is formed by the intersection of the ridge with the Cobb-Eickelberg hot spot. The summit at 1400-m depth below sea surface is characterized by a shallow caldera measuring 8.5 km by 3 km (Fig. 1A), which connects to rifts on the south and north flanks that form segments of the Juan de Fuca ridge. The caldera is underlain by a 14-km-long by 3-km-wide shallow magma and mush body with complex structure that is up to a kilometer thick, extends beyond both the northern and southern limits of the caldera, and

¹School of Oceanography, University of Washington, Seattle, WA 98195, USA. ²Lamont-Doherty Earth Observatory, Columbia University, Palisades, NY 10964, USA. ³Department of Marine, Earth, and Atmospheric Sciences, North Carolina State University, Raleigh, NC 27695, USA. ⁴Geology Department, Western Washington University, Bellingham, WA 98225, USA. ⁵National Oceanic and Atmospheric Administration (NOAA), Pacific Marine Environmental Laboratory, Newport, OR 97365, USA. ⁶Institute for Geophysics, Jackson School of Geosciences, University of Texas, Austin, TX 78758, USA.

*Corresponding author. Email: wilcock@uw.edu

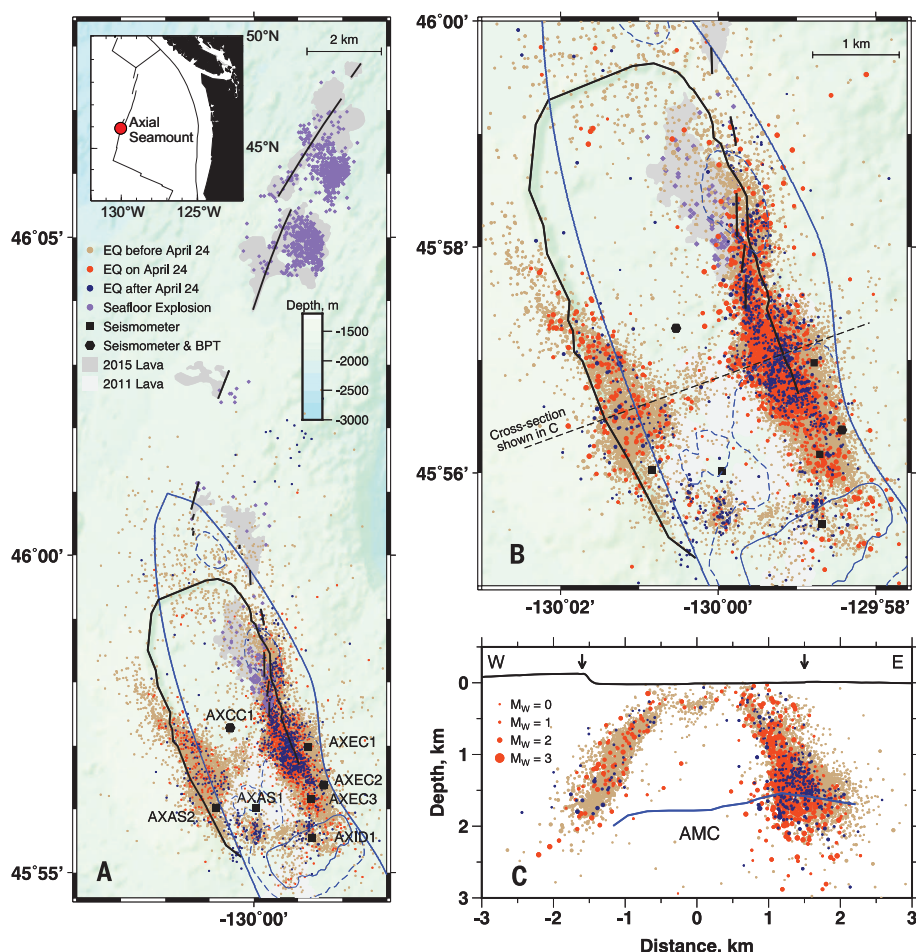


Fig. 1. Locations of earthquakes and seafloor explosions. (A) Bathymetric map showing the seismic network and colocated bottom-pressure and tilt (BPT) instruments, lava flows for the 2011 and 2015 eruptions (21), the distribution of 26,574 epicenters located with at least 12 arrival times by means of the double-difference technique, and seafloor explosions. The caldera rim (black line), eruptive fissures (black ticks), footprint of the magma chamber (blue solid line) (11), and depth contours for the magma chamber at depths of 1.25 km (faint blue line) and 1.5 km (dashed blue line) below the seafloor are also shown. The inset shows the location of Axial Seamount relative to plate boundaries (black lines) and land (black shading) in the northeast Pacific Ocean. (B) As in (A) but for the caldera region, with symbol sizes scaled by magnitude of earthquakes. (C) Vertical cross section across the caldera showing the projected locations of earthquakes within 0.5 km of the profile. Also shown is the roof of the axial magma chamber (AMC) (11). Arrows show the edges of the caldera.

is slightly offset to the east (11). Diking-eruptive events in the southeast caldera and south rift in 1998 and 2011 were documented with seafloor pressure sensors (12, 13) and hydrophones (14, 15). Although earthquake migration associated with dike propagation was observed for the 1998 eruption (14), earthquake depths could not be constrained for these eruptions. The expectation of future eruptions motivated the deployment in 2014 of a multidisciplinary real-time cabled observatory on Axial Seamount (16).

The cabled seismic network at the summit of Axial Seamount (Fig. 1) spans the southern half of the caldera, where the two prior recorded eruptions occurred, and comprises seven seismometers, two of which are colocated with hydrophones and bottom-pressure and tilt sensors (17). Seismic data are available starting in November

2014, with time-corrected data streaming from late January 2015. In the first year of operation, nearly 200,000 local earthquakes were detected, and they show a temporal distribution (Fig. 2) that is similar to prior seafloor eruptions (3, 15). Earthquake rates increase from <500 day $^{-1}$ to ~ 2000 day $^{-1}$ leading up to the onset of the eruption on 24 April 2015, then decrease rapidly following the seismic crisis, reaching a background level within a month of 20 day $^{-1}$.

Leading up to the eruption, the earthquakes are strongly correlated with tides (Fig. 2), with rates of seismicity about six times greater during the lowest tides than the highest tides (fig. S1A). This pattern can be attributed to the faults unclamping when the ocean loading is at a minimum (18). There is no evidence that the triggering signal strengthens over the 5 months leading up

to the eruption (fig. S2), but it weakens substantially after the eruption (supplementary text and fig. S1B), suggesting that it occurs primarily when the volcano is critically stressed (19).

In the 3 months prior to the eruption, $\sim 60,000$ earthquakes were located using double difference methods (20). Most are small with a median moment magnitude (M_w) of 0.1, and only 35 have $M_w \geq 2$. Earthquakes are concentrated beneath the east and west walls of the caldera (Fig. 1, fig. S3, and movie S1), with about five times as many beneath the east wall. In cross section (Fig. 1C), the earthquakes define outward-dipping fault zones extending from near the surface to ~ 2 -km depth. These zones dip at 60° to 70° , with the dip decreasing slightly at shallow depths. Many of the remaining epicenters are located near the southern and northern ends of the caldera and in a diffuse band of shallow seismicity that extends across the caldera just south of $45^\circ 57'N$ at a location that coincides with the southern boundary of the 2015 eruption (21) and a northward transition from a melt rich to crystal mush magma chamber, as it was imaged in 2002 (11). The epicenters, thus, define a figure eight, with the southern ring more clearly depicted as a result of the station coverage (Fig. 1B and fig. S3B).

For 6 hours preceding the start of the eruption, coincident with high tide, bursts of 7- to 10-Hz tremor are observed (Fig. 3 and fig. S4C) across the network, but are not coherent enough to locate. Tremor is not observed in the weeks before, or after, the eruption, and is thus inferred to indicate magma movement within the magma chamber before crustal rupture. At $\sim 04:20$ UTC on 24 April, as the tremor ends, the rate and magnitude of seismicity start to increase. Over about 2 hours, the earthquake rate reaches a saturation level of 500 to 600 hour $^{-1}$, and the median magnitude increases from 0.5 to nearly 2, likely indicating the initiation of diking. At $\sim 05:30$, tilt sensors start to detect slight deformation, with more rapid deformation at $\sim 06:15$ (17), including a flip in polarity as the seismicity suggests a dike propagation past the central caldera station (movie S2). Bottom-pressure signals, indicating the start of deflation, were observed at $\sim 06:00$ to $06:30$, with a notable increase in rate around $\sim 07:15$ (17) (movie S2). Seismic energy levels peak between 06:00 and 07:30 and then decrease progressively through the day (Fig. 3).

The cumulative distribution of hypocenters for the eruption is similar to that beforehand, with earthquakes concentrated near the east and west walls (Fig. 3). Of 31 earthquakes on 24 April with $M_w > 2.5$, all but one occurs on the eastern side, where the locations show a clear temporal pattern. Prior to 06:00 the seismicity along the east and west walls is north of $45^\circ 57'N$, with most of it, including all earthquakes with $M_w \geq 2.0$, north of $45^\circ 58'N$ (figs. S5 and S6). Over about 1.5 hours, from 06:15 to 07:45, the locus of seismicity on the east wall migrates 2.5 km south to $45^\circ 56.5'N$ (Fig. 3B, fig. S5, and movie S2), consistent with the southward propagation of a dike. Up until 07:00, the earthquakes align closely with the north-south

strike of southernmost eruptive fissures (21), suggesting that the fissure might be opening. After 07:00, they follow the strike of the east wall. Earthquakes for the remainder of the crisis occur beneath the whole east wall and on the west wall but are concentrated on the east wall south of the 2015 eruptive vents between $45^{\circ}56.5'N$ and $45^{\circ}57.5'N$, where they are presumably associated with deflation.

Starting at 08:01 on 24 April, the seismic network recorded ~37,000 impulsive events (fig. S4B) consistent with sound sources on the seafloor that propagate through the water column and are detected on the seismometers as a train of reverberations. Unlike the earthquakes, the times of explosions are not correlated with tides (fig. S7). These events are spatially closely associated with all the new lava flows (21) (Fig. 1A). The first impulsive event was observed within the caldera with events then commencing successively on the flows to the north.

Impulsive acoustic signals from the seafloor associated with active lava flows have been reported from several locations (22–25) and in deep-water locations have generally been attributed to the expansion of magmatic gases in Strombolian eruptions (24, 26). The presence of pyroclastic ash deposits associated with the 2015 Axial eruption (21), coupled with the high CO_2 contents of some lavas from prior eruptions (27), is consistent with the occurrence of similar explosions at Axial. However, the lava flows are also covered with numerous pits, which are interpreted as small steam explosions and may be the dominant source of explosive acoustic signals at this location (21).

Whatever the mechanisms, the explosive signals start soon after magma reaches the seafloor (25). The first detected explosion within the caldera occurred within an hour of the onset of rapid deflation, and earlier explosions may have been missed in the noise of the seismic crisis. The onset times on the north rift suggest that the dike propagated at a speed of 0.55 m/s (Fig. 3). This is at the upper end of speeds observed in Iceland, Afar, and the Gulf of Aden (28–30) and faster than the speed of 0.23 m/s observed well down rift for the 1998 eruption of Axial Seamount (14) and thus is consistent with the rapid deflation observed for this eruption (17). The summit network detected no earthquakes associated with dike propagation along the north rift, a result of a shadowing effect from the elongated magma chamber and high noise levels from nearby earthquakes. However, northward dike propagation is supported by observations on a single seismic station 20 km southeast of the caldera (fig. S8). We infer that the dike started northwards around 07:15 at the outset of rapid deflation, taking <2 hours to reach the site of the first explosion on the north rift at 09:04. Explosions near the northern end of the 2015 lava flows continued until 21 May (fig. S7), which coincides with the time the caldera started to reinflate (17), lending further support to a mechanism that links the explosions to fresh lava reaching the seafloor and showing that the plumbing system of the caldera links to the north rift dike.

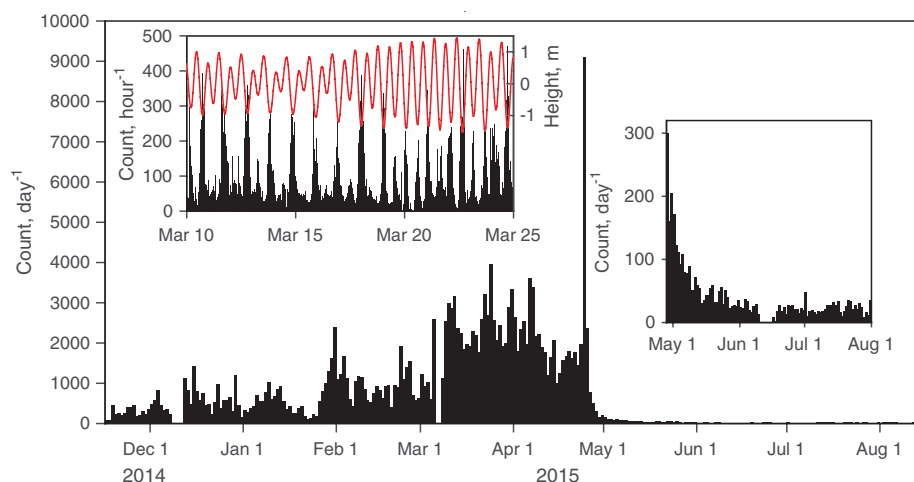


Fig. 2. Histogram of earthquake detections for 9 months spanning the 2015 eruption. (Right inset) Magnification of the period after the eruption. **(Left inset)** Histogram of hourly detections for 15 days in March with ocean tides superimposed. Gaps in the histogram in December, March, and June are intervals for which data are unavailable

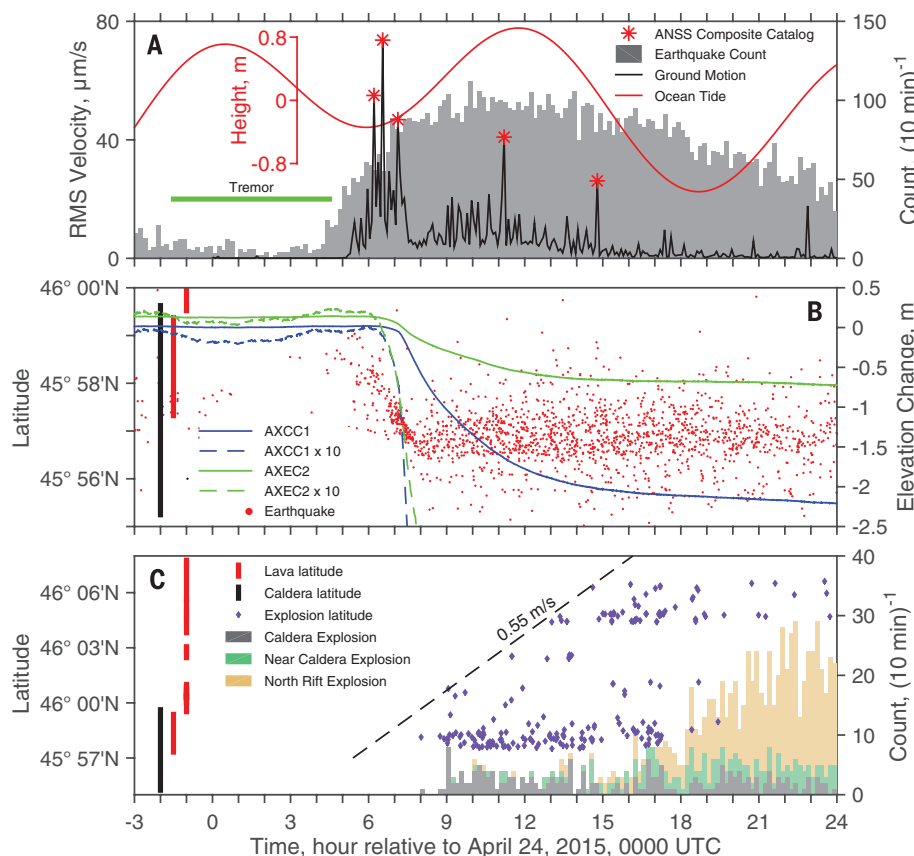


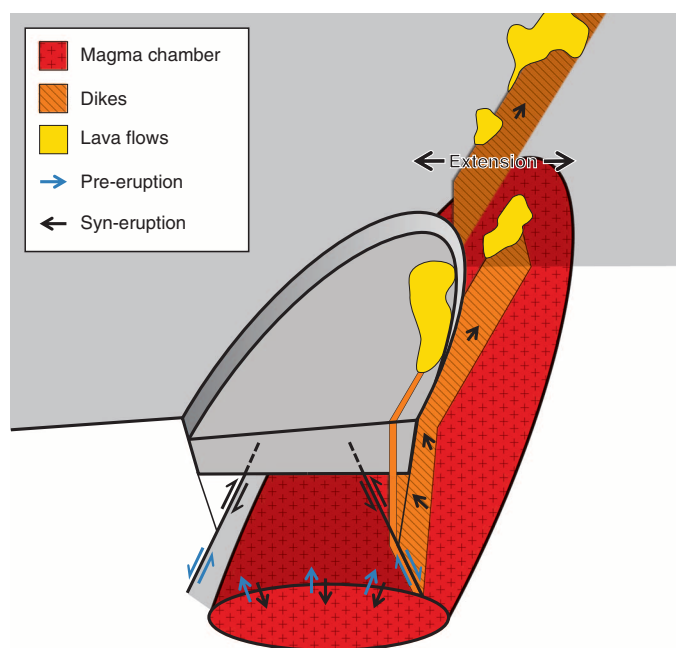
Fig. 3. Chronology for the 24 April 2015 eruption. (A) Histogram of earthquake counts, root mean square ground motion at station AXCC1 in the center of the caldera averaged over 5 min, times of earthquakes detected on land and included in the Advanced National Seismic System (ANSS) composite catalog, and ocean tide height. **(B)** Latitude of earthquakes beneath the east wall and the change in seafloor elevation recorded at stations AXCC1 and AXEC1 (17). **(C)** Histogram of explosions within the caldera and on the north rift and plot of latitudes for a subset of explosions.

The fault structure in the caldera is consistent with analog models obtained from sandbox simulations of caldera collapse due to underpressure

(31–33), which show that with sufficient subsidence, an outward-dipping ring fault forms first, followed by a peripheral inward-dipping

Fig. 4. Cartoon illustrating the dynamics of the caldera and emplacement of dikes.

Normal faulting on the outward-dipping ring fault accommodates magma chamber inflation (blue arrows). This fault motion reverses while dikes are emplaced and the magma chamber deflates (black arrows).



ring fault. At Axial Seamount, the outward-dipping normal fault zones were active both during inflation and syn-eruptive deflation and they project to the caldera floor ~0.75 km inward from walls (Fig. 1C). We infer that the caldera walls are formed by a second ring of inward-dipping normal faults, features that appear to be visible in seismic images (11), that either deformed aseismically during this volcanic cycle or were not reactivated. The analog models predict that the outward-dipping faults nucleate near the outer margins of the magma chamber. The separation of the fault zones that we observe is consistent with the 3- to 4-km width of the magma chamber (11), but the magma chamber is offset about 0.5 to 1 km east of the caldera. We speculate that the magma chamber may have migrated slightly eastward with the Cobb-Eickelberg hot spot melting anomaly since the caldera formed. Comparisons of natural calderas with analog models suggest that the formation of two sets of ring structures requires a ratio of caldera diameter to subsidence less than ~14 (34). For Axial Seamount, the maximum height of the walls (160 m) and short- and long-axis dimensions yield ratios of 20 and 50, respectively. However, the caldera may have undergone substantial magmatic infilling since its formation, implying that the ratios may have originally been lower.

The caldera substantially modulates the eruption. The north rift intersects the center of the north rim, but within the caldera and just to the north, the eruptive fissures are offset 2 km to the east (21). We infer that beneath the caldera, a dike exited the side of the pressurized magma chamber where extensional stresses are highest (35) and followed a path of weakness coinciding with the eastern ring fault zone (Fig. 4). The southward migration of earthquakes and change in the north-south tilt signal at the caldera center (17) (movie S2) are consistent with the propagation of

a dike that stalled upon reaching the northern limit of the 1998 and 2011 eruptions. Almost certainly at the same time, when the seismic noise levels were too high to detect earthquakes outside the network, the dike also propagated north, essentially extending the trend of the Axial south rift. Once north of the caldera, but still within the footprint of the Axial magma chamber, diking stepped westward into the extensional north rift, forming a second dike (Fig. 4). Although we cannot rule out that a single westward-stepping dike generated both the eruptions along the east wall of the caldera and the eruptions along the north rift (21), we prefer a model with two dikes tapping separate sections of the magma chamber. The eruption of north rift lavas with more evolved compositions (lower MgO) compared to the eastern caldera flows (21) is consistent with the dikes feeding these flows being sourced from different portions of the magma reservoir (Fig. 4), and the distribution of eruptive fissures and lava flows (Fig. 1A) are consistent with an overlapping spreading center. Injection of magma into the outward-dipping ring fault can be accommodated by the subsidence of the central block, but broadly distributed subsidence associated with deflation will increase horizontal compressive stresses above the caldera. This likely explains why the caldera eruption was limited in volume and most of the magma was injected along the rift (21).

At time scales on the order of a year, eruptions at Axial Seamount appear to be predictable based on a critical level of inflation (16). Similarly, it is clear from this study and prior work (3, 14, 19) that high and increasing microearthquake rates and strong tidal triggering also foreshadow eruptions on mid-ocean ridges. On shorter time scales of days to weeks, it is not clear if there are notable geophysical precursors. The 2015 Axial eruption was not preceded by a short-term increase in tidal triggering (fig. S2), and earthquake rates decreased

noticeably in the 2 weeks beforehand (Fig. 2). The only precursor appears to be tremor observed a few hours ahead of the seismic crisis (Fig. 3A). For future eruptions at Axial, the development of the hydrothermal portion of the cabled observatory (16) will provide additional tools to search for precursory signals originating near the magma-hydrothermal interface.

The 2015 eruption of Axial Seamount bears many similarities to diking events on both submarine (3, 14, 15, 25, 30) and subaerial (10, 28, 29) spreading centers, although in areas of thicker lithosphere, rifting episodes lead to larger earthquakes and often involve multiple dikes (28–30) because the magma chamber must refill multiple times to accommodate the spreading (36). On land, in Iceland and Afar, the combination of seismic and geodetic data shows that the propagation of dikes over tens of kilometers is accompanied by subsidence above a deflating crustal magma chamber (10, 28, 29) and at Bárðarbunga volcano by the collapse of a caldera (10). Because the Axial seismic network is compact and the ring faults are shallow, we are able to show that the outward-dipping inner ring fault also accommodates inflation prior to eruption. At Bárðarbunga volcano (10) and several other calderas (37), collapse occurs well after the onset of magma withdrawal, but at Axial, the onset of deflation and seismicity are coincident, supporting the inference that the dynamics of calderas are influenced by the depth of the magma chamber and the strength of preexisting ring faults (37).

REFERENCES AND NOTES

1. V. M. Zobin, *Introduction to Volcanic Seismology* (Elsevier, Waltham, MA, ed. 2, 2012).
2. J. A. Crisp, *J. Volcanol. Geotherm. Res.* **20**, 177–211 (1984).
3. M. Tolstoy et al., *Science* **314**, 1920–1922 (2006).
4. C. G. Newhall, D. Dzurisin, *U.S. Geol. Surv. Bull.* **1855** (1988).
5. A. Geyer, J. Marti, *Front. Earth Sci.* **2**, 1–13 (2014).
6. J. Mori, C. McKee, *Science* **235**, 193–195 (1987).
7. J. Mori et al., in *Fire and Mud: Eruptions and Lahars of Mount Pinatubo, Philippines*, C. G. Newhall, R. S. Punongbayan, Eds. (Univ. of Washington Press, Seattle, 1996), pp. 335–350.
8. G. Ekström, *Earth Planet. Sci. Lett.* **128**, 707–712 (1994).
9. S. Prejean, A. Stork, W. Ellsworth, D. Hill, B. Julian, *Geophys. Res. Lett.* **30**, 2247 (2003).
10. M. T. Gudmundsson et al., *Science* **353**, aaf8988 (2016).
11. A. F. Arnulf et al., *Geology* **42**, 655–658 (2014).
12. C. G. Fox, W. W. Chadwick Jr., R. W. Embley, *Nature* **412**, 727–729 (2001).
13. W. W. Chadwick Jr., S. L. Nooner, D. A. Butterfield, M. D. Lilley, *Nat. Geosci.* **5**, 474–477 (2012).
14. R. P. Dziak, C. G. Fox, *Geophys. Res. Lett.* **26**, 3429–3432 (1999).
15. R. P. Dziak et al., *Nat. Geosci.* **5**, 478–482 (2012).
16. D. S. Kelley, J. R. Delaney, S. K. Juniper, *Mar. Geol.* **352**, 426–450 (2014).
17. S. L. Nooner, W. W. Chadwick Jr., *Science* **354**, 1399–1403 (2016).
18. W. S. D. Wilcock, *Geophys. Res. Lett.* **28**, 3999–4002 (2001).
19. D. F. Stroup, D. R. Bohnenstiehl, M. Tolstoy, F. Waldhauser, R. T. Weekly, *Geophys. Res. Lett.* **34**, L15301 (2007).
20. F. Waldhauser, W. L. Ellsworth, *Bull. Seismol. Soc. Am.* **90**, 1353–1368 (2000).
21. W. W. Chadwick Jr. et al., *Geophys. Res. Lett.* **10**, 1002/2016GL071327 (2016).
22. J. Caplan-Auerbach, F. Duennel, *Geochim. Geophys. Geosyst.* **2**, 1024 (2001).
23. V. Schlindwein, C. Riedel, *Geochim. Geophys. Geosyst.* **11**, Q01002 (2010).

24. R. P. Dziak *et al.*, *Geophys. Res. Lett.* **42**, 1480–1487 (2015).
25. Y. J. Tan, M. Tolstoy, F. Waldhauser, W. S. D. Wilcock, *Nature* **10.1038/nature20116** (2016).
26. R. A. Sohn *et al.*, *Nature* **453**, 1236–1238 (2008).
27. C. Helo, M.-A. Longpré, N. Shimizu, D. A. Clague, J. Stix, *Nat. Geosci.* **4**, 260–263 (2011).
28. T. J. Wright *et al.*, *Nat. Geosci.* **5**, 242–250 (2012).
29. F. Sigmundsson *et al.*, *Nature* **517**, 191–195 (2015).
30. A. Ahmed *et al.*, *Geophys. J. Int.* **205**, 1244–1266 (2016).
31. O. Roche, O. T. H. Druitt, O. Merle, *J. Geophys. Res.* **105**, 395–416 (2000).
32. B. Kennedy, J. Stix, J. W. Vallance, Y. Lavalée, M.-A. Longpré, *Geol. Soc. Am. Bull.* **116**, 515–524 (2004).
33. S. Buchardt, T. R. Walter, *Bull. Volcanol.* **72**, 297–308 (2010).
34. V. Acocella, *Earth Sci. Rev.* **85**, 125–160 (2007).
35. A. Gudmundsson, L. B. Marinoni, J. Marti, *J. Volcanol. Geotherm. Res.* **88**, 1–13 (1999).
36. W. R. Buck, P. Einarsson, B. Brandsdóttir, *J. Geophys. Res.* **111**, B12404 (2006).
37. L. Michon, F. Massin, V. Famin, V. Ferrazzini, G. Roult, *J. Geophys. Res.* **116** (B3), B03209 (2011).

ACKNOWLEDGMENTS

The seismic data used for this study are archived at the Incorporated Research Institutions for Seismology Data Management System and the Ocean Observatories Initiative (OOI) Data Portal. The earthquake catalogs are archived in the Interdisciplinary Earth Data Alliance Marine Geoscience Data System (DOI: 10.1594/IEDA/323843). This work was supported by the National Science Foundation under awards

OCE-1536219, OCE-1536320, OCE-1635276, OCE-1357076, and DGE-1256082. The seismic network was installed and is operated by the OOI Cabled Array team, led by J. Delaney and D. Kelley. This paper is Pacific Marine Environmental Laboratory contribution no. 4522.

SUPPLEMENTARY MATERIALS

www.sciencemag.org/content/354/6318/1395/suppl/DC1
Materials and Methods
Figs. S1 to S11
Movies S1 and S2
References (38–40)

15 July 2016; accepted 28 October 2016
10.1126/science.aah5563

VOLCANOLOGY

Inflation-predictable behavior and co-eruption deformation at Axial Seamount

Scott L. Nooner^{1*} and William W. Chadwick Jr.²

Deformation of the ground surface at active volcanoes provides information about magma movements at depth. Improved seafloor deformation measurements between 2011 and 2015 documented a fourfold increase in magma supply and confirmed that Axial Seamount's eruptive behavior is inflation-predictable, probably triggered by a critical level of magmatic pressure. A 2015 eruption was successfully forecast on the basis of this deformation pattern and marked the first time that deflation and tilt were captured in real time by a new seafloor cabled observatory, revealing the timing, location, and volume of eruption-related magma movements. Improved modeling of the deformation suggests a steeply dipping prolate-spheroid pressure source beneath the eastern caldera that is consistent with the location of the zone of highest melt within the subcaldera magma reservoir determined from multichannel seismic results.

Successful volcanic eruption forecasting is traditionally based on short-term (minutes to hours) increases in seismicity, surface deformation, or both during the time that magma is already moving toward the surface (1, 2). Successful forecasts made days to weeks in advance are much rarer because the patterns of geophysical signals are generally not clear or repeatable enough. However, some notable successes at volcanoes such as Mount St. Helens and in Iceland have been documented (3, 4). Seven months in advance of an April 2015 eruption at Axial Seamount, we made a successful forecast that it would occur within a 15-month time window, on the basis of long-term deformation monitoring. The deformation measured during the 2015 eruption also provides important constraints on the location and depth of magma reservoirs and conduits.

Axial Seamount is a heavily instrumented submarine volcano that is part of the Ocean Observatories Initiative (OOI) Cabled Array (5, 6). Axial Seamount is distinguished from other submarine volcanoes in that it has a long-term volcano deformation time series that spans three eruptions. A combination of bottom pressure recorders (BPRs) and mobile pressure recorders (MPRs) (7–11) provided measurements of vertical deformation from 2000 to 2015. Both methods use changes in the overlying water pressure to detect vertical displacements of the seafloor with a resolution of ~1 cm. BPRs record continuously to capture sudden events (such as eruptions) over minutes to days, but these instruments are not ideal for longer-term measurements because of sensor drift. MPR campaign-style surveys require a remotely operated vehicle (ROV) to deploy the instrument at seafloor benchmarks (fig. S1) and, after correcting for sensor drift, can document gradual deformation over months to years (9, 10). MPR data can constrain BPR drift where the two are colocated. Autonomous, battery-powered BPRs have been used at Axial since the mid-1980s (12, 13) and, in September 2014, the OOI

Cabled Array began providing real-time data from three BPR-tilt instruments (5, 6). At the time of the 2015 eruption, three autonomous BPRs, three cabled BPRs, and 10 MPR benchmarks were deployed at Axial (Fig. 1 and fig. S2).

After the 2011 eruption at Axial Seamount (14), a time- or inflation-predictable model was proposed in which the volcano erupts at or near a threshold level of inflation (15, 16). The 2015 eruption provided a test for this model and its usefulness in forecasting. The average linear rate of inflation measured at the caldera center between 2000 and 2010 was 15 ± 0.2 cm/year (Fig. 2), with higher rates measured in the months after the 1998 eruption and before the eruption in 2011 (14). After 2011, we initially expected the next eruption to occur in 2018 if the pattern of deformation repeated itself (14). However, from continued monitoring we found that the rate of inflation increased substantially after the 2011 eruption. We observed that the average inflation rate at the caldera center was 61 ± 1.4 cm/year between August 2011 and September 2013 (Fig. 2). A marked increase in the magma supply may explain the fourfold increase over the 2000–2010 inter-eruption rate (11). Continuation of this higher rate of inflation during 2013–2014 was observed after a Monterey Bay Aquarium Research Institute autonomous underwater vehicle (AUV) collected repeat high-resolution bathymetry (17) and with data recovered from a prototype self-calibrating BPR (18) in August 2014. Thus, in September 2014, we revised our forecast that Axial would erupt sometime during 2015 (19, 20). The expected eruption began on 24 April 2015, detected in real time by the OOI Cabled Array (21).

This long-term forecast was unusually successful for any volcano (1, 2). The level of inflation as the 2015 eruption began was only 30 cm higher than in 2011 (Fig. 2). This observation supports the model of a pressure threshold in the shallow magma reservoir above which diking events are triggered, but it also suggests that the threshold may increase with time because of accumulating tectonic stress, as observed in Iceland and Ethiopia (22, 23). Nevertheless, the volcanic system at Axial may be unusually repeatable due to the continuous magma supply and the thin ocean crust in a mid-ocean ridge setting. The increase in magma supply rate documented by the inflation data led to a marked decrease in the eruption

¹University of North Carolina Wilmington, Wilmington, NC 28403, USA. ²Oregon State University/Cooperative Institute for Marine Resources Studies, Hatfield Marine Science Center, Newport, OR 97365, USA.

*Corresponding author. Email: nooners@uncw.edu

recurrence interval (1998–2011 versus 2011–2015), as well as a change in lava composition erupted at the summit (24).

Pre-eruption inflation changed abruptly to co-eruption deflation at ~06:00 on 24 April 2015 (all times GMT), more than an hour after seismicity began to increase (21), due to magma intruding out of the summit reservoir (fig. S4). The 2015 eruption extended >20 km from the northeastern edge of the caldera and along the north rift zone (24), in contrast to the last two eruptions, which were on the south rift (25, 26). The total subsidence at the caldera center was similar in 2015 and 2011 (–2.45 and –2.43 m, respectively), which suggests that roughly the same volume of magma was removed from the magma reservoir. However, the rate of deflation was noticeably higher in 2015 than in 2011. For example, the total subsidence in the first 24 hours amounted to –2.22 m in 2015 (91% of the total), compared with only –1.57 m in 2011 (65% of the total). In 2015, the rate of deflation decreased quasi-exponentially until 5 May and was followed by a transitional period of alternating minor inflation and deflation until 19 May, when rapid re-inflation resumed (fig. S5). Thus, the deflation lasted much longer in 2015: 25 days compared with only 6 days in 2011. Notably, this is similar to the duration of the impulsive seismoacoustic events detected on the north rift zone (21) that could be interpreted as steam explosions during lava flow emplacement (24).

We captured co-eruption deformation during the submarine dike intrusion and eruption with in situ tiltmeters at two sites on the OOI Cabled Array (11). The tilt signals can be closely related to the seismicity generated by the initial dike intrusion (21). Tilt magnitudes and directions began to change at 05:25 (Fig. 3), soon after the seismic crisis began. At this time, most of the earthquakes were located beneath the northeastern edge of the caldera (21), where the dike intrusion initiated and the southernmost eruptive fissures are located (24). Between 06:00 and 08:00, the earthquakes propagated 3 to 4 km southward along the eastern edge of the caldera. The tilt signals changed substantially (Fig. 3) during this time period in a way that is consistent with a dike intruding southward but not reaching the surface in this area (21).

We observed >100 microradians (μrad) of downward tilt toward the south in ~1 hour, which then abruptly reversed at 07:10 (Fig. 3A) in the central caldera tiltmeter [Axial caldera center (AXCC)] record. This behavior is consistent with modeling of lateral dike propagation past the instrument (27), because the tilt component parallel to the direction of dike propagation (north-south at Axial) is most sensitive to the lengthening of the dike. The initial tilt is in the direction of dike propagation, and the reversal in tilt direction occurs when the dike tip passes the tiltmeter. At the same time, the east-west component of the AXCC tiltmeter also reversed direction from slow eastward tilt (toward the dike axis) to a rapid westward tilt (away from the dike axis) (Fig. 3, A and B). Dike modeling (27) shows that the tilt

component perpendicular to the dike axis (east-west at Axial) is most sensitive to the depth to the top of the dike, and the initial tilt is downward toward the dike axis, which reverses to tilt away from the dike axis when the top of the dike nears the surface. This tilt record suggests that the dike propagated to the south for 3 to 4 km before

stalling out and continuing to the north along the north rift zone.

We observed several large and nearly instantaneous easterly jumps in tilt magnitude between 06:13 and 07:10 from the eastern caldera tiltmeter [Axial eastern caldera (AXEC)] located closer to the dike axis. By 07:10, the net tilt amounted to

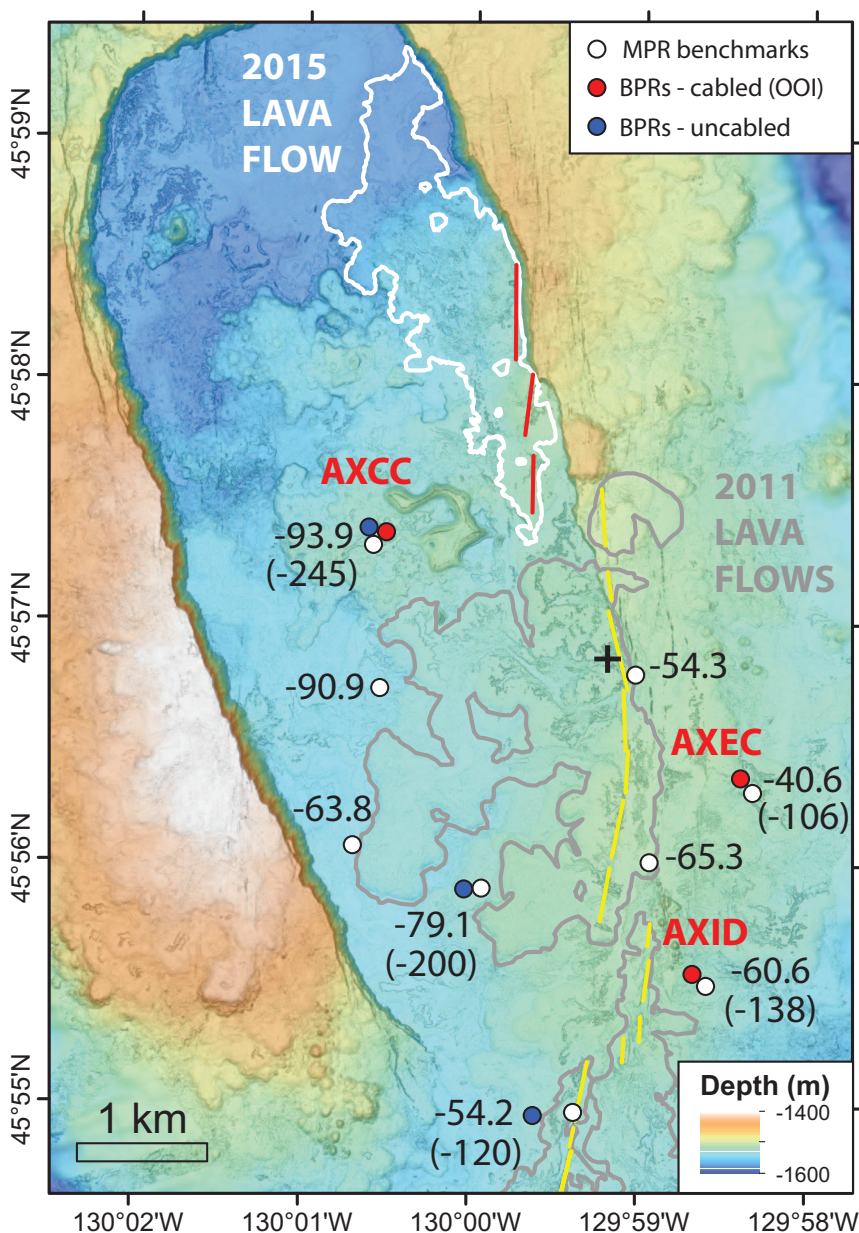


Fig. 1. Map of the summit caldera of Axial Seamount. Locations of MPR benchmarks (white circles) and BPR instruments (red and blue circles) are indicated. An additional benchmark located 10 km south of the caldera center is not visible. Numbers show vertical displacements in centimeters at each of the MPR benchmarks between 14 September 2013 and 25 August 2015, a period that included pre-eruption inflation, co-eruption deflation, and post-eruption inflation. Numbers in parentheses show subsidence in centimeters during deflation only, as measured by the BPRs. BPRs on the OOI Cabled Array (red dots) include tiltmeters (data shown in Fig. 3). The map also shows locations of 2015 lava flows and eruptive fissures [white outlines and red lines, respectively (24)] and 2011 lava flows and eruptive fissures [gray outlines and yellow lines, respectively (26)]. The + symbol denotes the centroid of the best-fit prolate-spheroid deformation model (Fig. 4). AXID, Axial International District.

>1000 μrad before it reversed and started gradually decreasing (Fig. 3, C and D). In contrast to the AXCC tiltmeter, which recorded smoothly varying tilt signals, we interpreted the large sudden offsets in the AXEC tilt record as either inelastic deformation (perhaps cracking or faulting near the dike axis) or slight movements of the instrument caused by earthquake shaking during the peak of the seismic swarm. This makes the AXEC tilt signals more difficult for us to interpret in the context of dike models. However, after 08:00, both tilt records were again smooth and became dominated by deformation due to the ongoing deflation rather than from the dike intrusion (fig. S6).

We used the MPR results from September 2013 to August 2015 for the net vertical displacement at seafloor benchmarks in and near the summit caldera to model the source of the inflation and deflation signals (Fig. 1). This time period includes some pre-eruption inflation, the co-eruption deflation, and some post-eruption re-inflation (Fig. 2). The 10 MPR stations in 2015, compared with only 6 in 2011, provided better constraints for ground deformation models. We fit the MPR data from all 10 MPR stations to a suite of models, including a point-source (28), a penny-shaped sill (29), and a prolate spheroid (30) (figs. S7 to S9 and table S1). The best-fitting source for the 2013–2015 time period ($\chi^2_{\text{reduced}} = 34.2$) is a prolate spheroid with the major axis dipping at 77° in the direction of 286° , with major and minor axes of 2.2 and 0.38 km, respectively, and a depth to center of 3.81 km (Fig. 4 and fig. S8). The fit of the observed data to this model is much better than the fit to previous sill or point-source models (9, 10, 14).

The best-fitting deformation source for the inter-eruption period between the previous MPR surveys (an inflation-only period with data from six stations from July 2011 to September 2013) is very similar, a steeply dipping prolate spheroid with the major axis dipping at 75° in the direction of 290° , major and minor axes of 2.2 and 0.33 km, and a depth of 3.77 km (fig. S7). We suggest that the source of the deformation is the same for time periods dominated by inflation or deflation. The location of the 2013–2015 source is east-southeast of the caldera center, but its steep dip to the west-northwest causes the maximum uplift or subsidence to be observed near the caldera center (Fig. 4). The prolate spheroid shape approximates a nearly vertical conduit, and the location of its top (at 1.6 km depth beneath the eastern edge of the caldera) is almost the same

as the shallowest part of the magma body imaged by multichannel seismic (MCS) surveys (31). The southern half of the caldera was also where the MCS data showed the highest percentage of melt, interpreted as the locus of magma supply from the underlying hot spot (31). The eastern edge of the caldera was the source area of the dikes that fed the 2015 eruption (21, 24), as well as the two previous eruptions (25, 26). The best-fitting deformation model does not necessarily show the geometry of the entire magma body, which is approximated by a horizontal ellipsoid underlying the caldera from MCS data. The deformation model instead shows where the greatest volume change occurred during inflation and deflation. Inflation and deflation at Axial Seamount appears to be concentrated in a nearly vertical conduit that feeds the high-melt core of the magma body

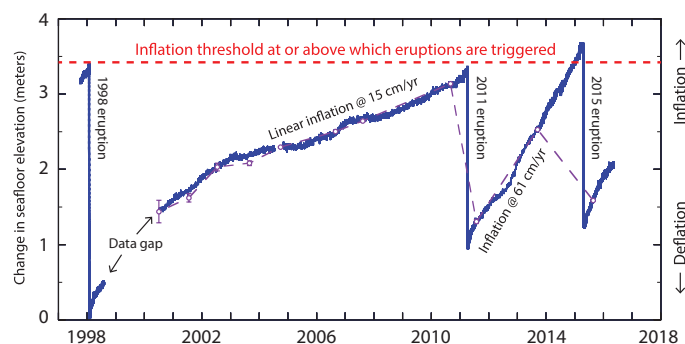


Fig. 2. Deformation time series at the caldera center. Long-term time series of inflation and deflation at the center of the caldera at Axial Seamount (to 19 May 2016). Purple dots represent MPR measurements (error bars indicate 1 SD); blue curves show BPR data (drift-corrected after 2000). The relative depth of data before and after the 1998–2000 gap in measurements is unknown.

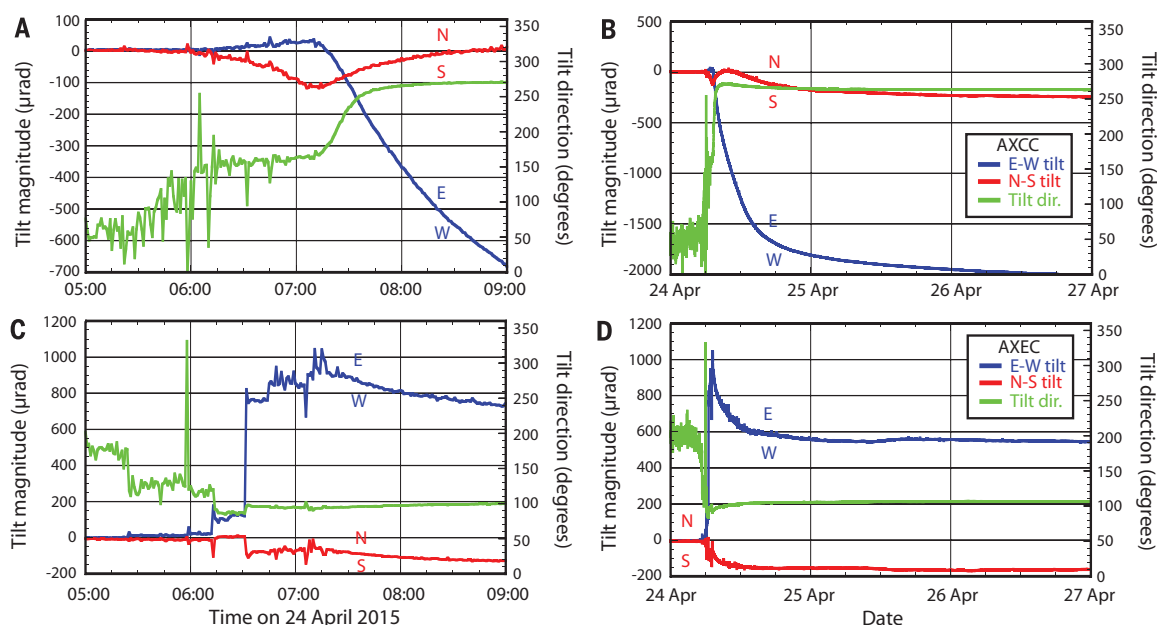


Fig. 3. Co-eruption tilt. Results show east-west (blue) and north-south (red) components and net tilt direction (green) from OOI Cabled Array instruments at stations AXCC (A and B) and AXEC (C and D), shown in Fig. 1. Tilts at station AXCC are consistent with north-to-south propagation of a dike along the eastern edge of the caldera, with the dike tip passing by the station at 07:10 on 24 April. Tilts on 25 to 27 April mainly reflect deflation during the eruption, which lasted until 19 May.

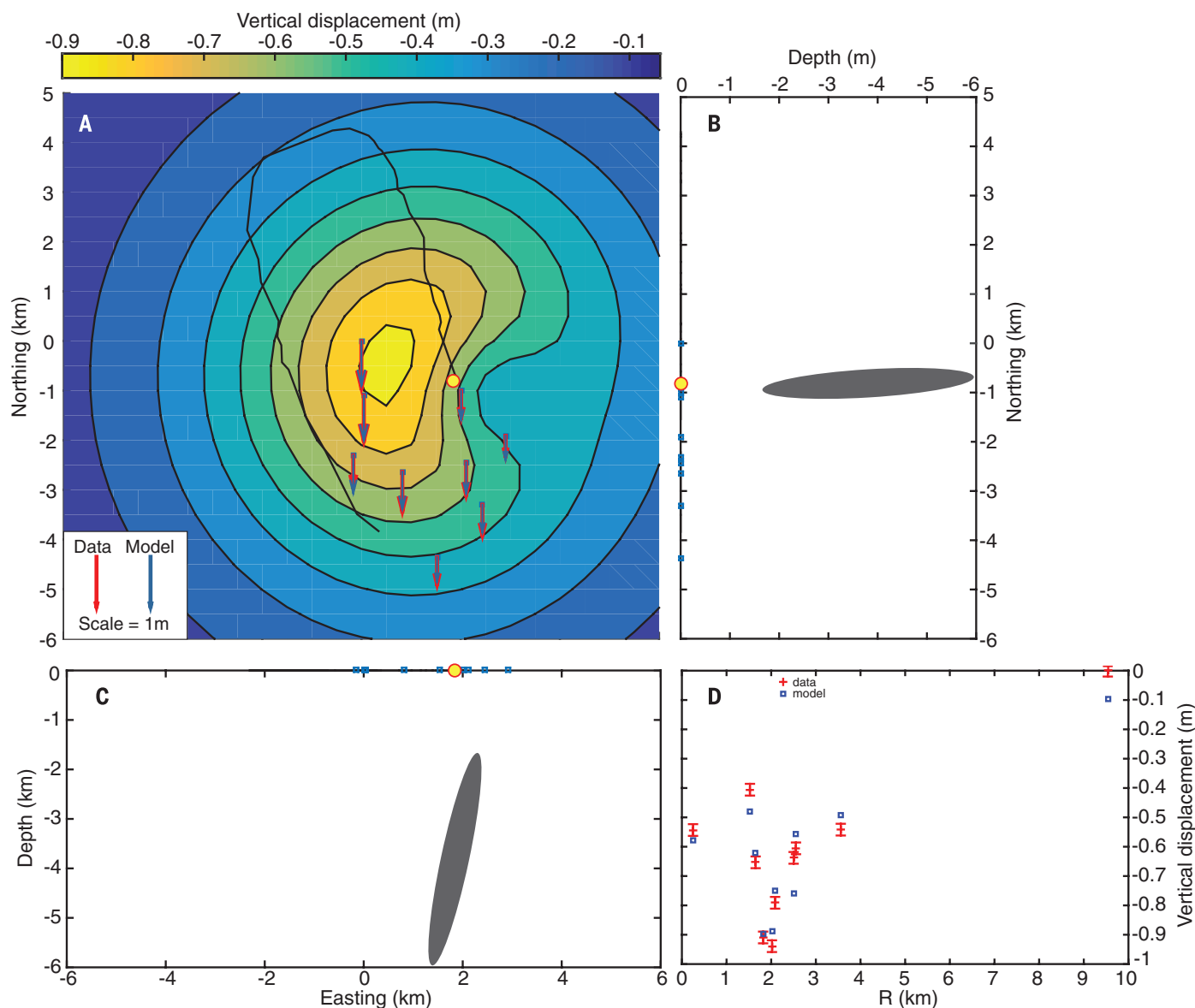


Fig. 4. Deformation modeling results. (A) Map view of vertical displacements expected from the best-fit prolate-spheroid model (color contours and blue vectors) and comparison with the 2013–2015 MPR data (red vectors). (B) North-south and (C) east-west depth profiles show orientation of the steeply dipping prolate-spheroid model. Yellow circles in (A) to (C) show the surface projection of the prolate-spheroid centroid. (D) Plot of vertical displacement versus radial distance (R) from the model centroid, comparing data (red crosses; data are mean \pm SD) and model calculations (blue squares).

imaged by Arnulf *et al.* (31), and the surrounding mush zones of the magma body have less of an influence on surface deformation.

To calculate the volume of magma removed from the subcaldera reservoir during the 2015 eruption, we used the prolate spheroid source parameters obtained from modeling the 2013–2015 MPR data to solve for the volume change due to the co-eruption subsidence only (11), as recorded by BPR instruments at five locations (fig. S9 and table S1). The volume change was $2.88 \times 10^8 \text{ m}^3$, which is 1.95 times the volume of lava erupted in 2015 (24). This implies that $1.40 \times 10^8 \text{ m}^3$ of magma was in the dike that intruded along the north rift zone. The length of the dike was $\sim 24 \text{ km}$ from seismicity and the location of 2015 eruption sites (21, 24), so with

an average dike height of 2 to 3 km, as was assumed for the previous eruptions at Axial (14), the required dike thickness would be 2 to 3 m to match the estimated dike volume. This is much greater than the 1-m dike thickness from similar calculations for the 1998 and 2011 eruptions. A thick dike could explain the high deflation rate and the longer duration in 2015 compared with 2011. Axial did not have an eruption on its north rift zone in decades or more, whereas at least the last three eruptions have been on the south rift zone (32). Larger accumulated extensional stress on the north rift may have resulted in the intrusion of a wider dike that accommodated a higher rate of magma transport from the summit reservoir and took longer to solidify (22, 33, 34). Inflation re-

sumed as soon as co-eruption deflation stopped (Fig. 1), with 33 cm of uplift at the caldera center from the 25 August 2015 MPR survey and another 80 cm as of 19 May 2016 from OOI data, indicating that more than one-third of the magma volume lost in 2015 was recovered in the first year (table S1).

We successfully forecast the 2015 eruption of Axial Seamount from seafloor deformation data and captured the eruption in real time from tilt and pressure instruments on the OOI Cabled Array. The tilt data showed that the dike initially propagated 3 to 4 km south before stalling out and continuing to the north, consistent with the seismic data (21). Improved modeling of the magma source for the eruption revealed a steeply dipping magma conduit beneath the eastern

caldera, in agreement with the location of a high-melt zone from recent seismic results (31). Uplift rates have gradually decreased with time since the 2015 eruption, so it is unclear whether the higher magma supply rate evident from 2011–2015 will continue. If reinflation continues at ~60 cm/year, the next dike intrusion could occur as early as 2019 but will occur later if the inflation rate slows or if higher tectonic stresses from previous dike intrusions need to be overcome (22). Variations in the magma supply rate complicate forecasts but may be at least partially explained by a deeper magma body hydraulically connected to the shallow magma reservoir (35). These complexities could be overcome using a generalized time-predictable model after several more eruption cycles have been observed (16). However, for the first time, we will be able to continuously update the next eruption and/or intrusion forecast for Axial Seamount with real-time data from the OOI Cabled Array.

REFERENCES AND NOTES

- R. S. J. Sparks, *Earth Planet. Sci. Lett.* **210**, 1–15 (2003).
- P. Segall, *Geol. Soc. Lond. Spec. Publ.* **380**, 85–106 (2013).
- D. A. Swanson et al., *J. Geodyn.* **3**, 397–423 (1985).
- E. Sturkell et al., *J. Volcanol. Geotherm. Res.* **150**, 14–34 (2006).
- D. S. Kelley, J. R. Delaney, S. K. Juniper, *Mar. Geol.* **352**, 426–450 (2014).
- NSF Ocean Observatories Initiative, Data Portal, Bottom Pressure Tilt (RS03CCAL-MJ03F-BOTPTA301, RS03ECAL-MJ03E-BOTPTA302, RS03INT2-MJ03D-BOTPTA303), data from 16 September 2014 to 20 May 2016; <http://ooinet.oceanobservatories.org>.
- C. G. Fox, *Geophys. Res. Lett.* **26**, 3437–3440 (1999).
- C. G. Fox, W. W. Chadwick Jr., R. W. Embley, *Nature* **412**, 727–729 (2001).
- W. W. Chadwick Jr., S. Nooner, M. Zumberge, R. W. Embley, C. G. Fox, *J. Volcanol. Geotherm. Res.* **150**, 313–327 (2006).
- S. L. Nooner, W. W. Chadwick Jr., *Geochem. Geophys. Geosyst.* **10**, Q02002 (2009).
- Methods, supplementary text, figures, and a table are available as supplementary materials on Science Online.
- W. W. Chadwick Jr., S. L. Nooner, Processed Bottom Pressure Recorder (BPR) data from uncabled instruments deployed at Axial Seamount on the Juan de Fuca Ridge (investigators William Chadwick and Scott Nooner), Integrated Earth Data Applications (IEDA) (2015); <http://get.iedadata.org/doi/322282>.
- C. G. Fox, Processed Bottom Pressure Recorder (BPR) data from uncabled instruments deployed at Axial Seamount on the Juan de Fuca Ridge (investigator Chris Fox), Integrated Earth Data Applications (IEDA) (2016); <http://get.iedadata.org/doi/322344>.
- W. W. Chadwick Jr., S. L. Nooner, D. A. Butterfield, M. D. Lilley, *Nat. Geosci.* **5**, 474–477 (2012).
- M. L. Burt, G. Wadge, W. A. Scott, *Bull. Volcanol.* **56**, 87–97 (1994).
- L. Sandri, W. Marzocchi, P. Gasperini, *Geophys. J. Int.* **163**, 1203–1218 (2005).
- D. W. Caress et al., "Vertical deformation of the Axial Seamount summit from repeated 1-m scale bathymetry surveys with AUVs," abstract presented at 2015 Annual GSA Meeting, Baltimore, MD, 1 to 4 November 2015 (GSA Abstracts with Programs vol. 47, 2015).
- G. S. Sasagawa, M. J. Cook, M. A. Zumberge, *Earth Space Sci.* **3**, 381–385 (2016).
- W. W. Chadwick Jr., S. L. Nooner, Online blog documenting successful forecast of the 2015 eruption at Axial Seamount (2015); www.pmel.noaa.gov/eoi/axial_blog.html.
- W. W. Chadwick Jr., S. L. Nooner, "Axial Inflation: Past, Present & Future," talk presented at NOVAE Workshop, Seattle, WA, 23 April 2015; http://novae.ocean.washington.edu/story/Axial_Inflation_Past_Present_and_Future.
- W. S. D. Wilcock et al., *Science* **354**, 1395–1399 (2016).
- W. R. Buck, P. Einarsson, B. Brandsdottir, *J. Geophys. Res.* **111**, B12404 (2006).
- I. J. Hamling, T. J. Wright, E. Calais, L. Bennati, E. Lewi, *Nat. Geosci.* **3**, 713–717 (2010).
- W. W. Chadwick Jr. et al., *Geophys. Res. Lett.* **10**, 1002/2016GL071327 (2016).
- W. W. Chadwick Jr. et al., *Geochem. Geophys. Geosyst.* **14**, 3939–3968 (2013).
- D. W. Caress et al., *Nat. Geosci.* **5**, 483–488 (2012).
- A. T. Okamura, J. J. Dvorak, R. Y. Koyanagi, W. R. Tanigawa, "Surface deformation during dike propagation, in The Puu Oo eruption of Kilauea volcano, Hawaii: Episodes 1 through 20, January 3, 1983, through June 8, 1984," E. W. Wolfe, Ed. (U.S. Geol. Surv. Prof. Pap. 1463, 1988), pp. 165–181.
- K. Mogi, *Bull. Earthquake Res. Inst. Univ. Tokyo* **36**, 99–134 (1958).
- Y. Fialko, Y. Khazan, M. Simons, *Geophys. J. Int.* **146**, 181–190 (2001).
- X. Yang, P. M. Davis, J. H. Dieterich, *J. Geophys. Res.* **93**, 4249–4257 (1988).
- A. F. Arnulf et al., *Geology* **42**, 655–658 (2014).
- D. A. Clague et al., *Geochem. Geophys. Geosyst.* **14**, 4403–4443 (2013).
- P. T. Delaney, D. D. Pollard, *Am. J. Sci.* **282**, 856–885 (1982).
- R. Qin, W. R. Buck, *Earth Planet. Sci. Lett.* **265**, 466–474 (2008).
- T. Reverso et al., *J. Geophys. Res.* **119**, 4666–4683 (2014).

ACKNOWLEDGMENTS

The BPR and tilt data presented here are archived at the Integrated Earth Data Applications Marine Geoscience Data System (12, 13) and at the OOI Data Portal (6). This work was supported by NSF awards OCE-1356216 and 1546616 and by the National Oceanic and Atmospheric Administration, Pacific Marine Environmental Laboratory (NOAA-PMEL), Earth-Ocean Interactions Program. We thank M. Fowler and the crews of R/V *Thomas G. Thompson*, ROV *Jason*, and AUV *Sentry* for logistical support at sea during expedition TN327. This work would not have been possible without the support of the NOAA-PMEL Engineering Division and the University of Washington OOI Cabled Array team, led by J. Delaney and D. Kelley. The paper benefited from helpful input from two anonymous reviewers. This is PMEL contribution number 4509.

SUPPLEMENTARY MATERIALS

www.sciencemag.org/content/354/6318/1399/suppl/DC1
Methods
Supplementary Text
Figs. S1 to S9
Table S1
References

30 June 2016; accepted 28 October 2016
10.1126/science.aah4666

GEOCHEMISTRY

Large gem diamonds from metallic liquid in Earth's deep mantle

Evan M. Smith,^{1*} Steven B. Shirey,² Fabrizio Nestola,³ Emma S. Bullock,⁴ Jianhua Wang,² Stephen H. Richardson,⁵ Wuyi Wang¹

The redox state of Earth's convecting mantle, masked by the lithospheric plates and basaltic magmatism of plate tectonics, is a key unknown in the evolutionary history of our planet. Here we report that large, exceptional gem diamonds like the Cullinan, Constellation, and Koh-i-Noor carry direct evidence of crystallization from a redox-sensitive metallic liquid phase in the deep mantle. These sublithospheric diamonds contain inclusions of solidified iron-nickel-carbon-sulfur melt, accompanied by a thin fluid layer of methane \pm hydrogen, and sometimes majoritic garnet or former calcium silicate perovskite. The metal-dominated mineral assemblages and reduced volatiles in large gem diamonds indicate formation under metal-saturated conditions. We verify previous predictions that Earth has highly reducing deep mantle regions capable of precipitating a metallic iron phase that contains dissolved carbon and hydrogen.

Earth has a metallic liquid outer core, and it has been predicted from theory and experiments that the deep mantle could precipitate iron alloys. The presence of such metallic iron phases, especially in high enough abundance, would have profound effects on the physical and chemical properties of Earth's deep mantle. However, the inaccessibility of the deep Earth makes it challenging to observe. Upwelling mantle regions melt adiabatically, pro-

ducing prolific basaltic volcanism and silicate mantle residues, both of which appear too oxidized to have originated from a deeper region of metal saturation. Thus, physical evidence for such reducing regions—essential for understanding mantle evolution—has been virtually absent.

We have identified a genetically distinct diamond population that samples these metal-saturated regions of Earth's mantle. These diamonds are typified by the 3106-carat (1 carat = 0.2 g) Cullinan diamond and are almost always classified as type II, referring to their minimal nitrogen content (<5 to 20 parts per million). More specifically, diamonds that are Cullinan-like tend to be large, inclusion-poor, relatively pure, irregularly shaped, and resorbed (1–3). Combining the traits into an acronym leads us to term them CLIPPIR diamonds to distinguish them from other populations of diamond, especially other

¹Gemological Institute of America, New York, NY 10036, USA. ²Department of Terrestrial Magnetism, Carnegie Institution for Science, Washington, DC 20015, USA. ³Department of Geosciences, University of Padova, Padova 35131, Italy. ⁴Geophysical Laboratory, Carnegie Institution for Science, Washington, DC 20015, USA. ⁵Department of Geological Sciences, University of Cape Town, Rondebosch 7701, South Africa.

*Corresponding author. Email: evan.smith@gia.edu

varieties of type II diamonds lacking these features (2, 4).

Examination of 53 CLIPPIR diamonds with inclusions shows that a magnetic, metallic inclusion is the most common trapped material (Fig. 1 and fig. S1), appearing as the only inclusion in 38 of the 53 diamonds. Similar inclusions have been mistakenly identified as graphite on the basis of appearance (1, 2) because they are camouflaged by prominent graphitic decompression cracks. Five metallic inclusions from the 38 diamonds were exposed by polishing for chemical microanalysis (Fig. 2). We found a multiphase assemblage composed primarily of cohenite [(Fe,Ni)₃C], an interstitial Fe-Ni alloy, iron sulfide (pyrrhotite) segregations, and some more minor accessory phases (Fe-phosphate, Cr-Fe-oxide, and Fe-oxide) (Fig. 2 and table S1). X-ray diffraction confirms the identification of the carbide as cohenite (5). Small amounts of graphite occur at the diamond-inclusion interface and the fractures radiating from inclusions. We detected a thin fluid jacket of CH₄ around most of the inclusions by Raman spectroscopy (5). In 13 samples, H₂ was also detected, accompanying intense CH₄ signals (Fig. 1). Taking these observations together, we interpret the inclusions as former Fe-Ni-C-S melt with minor dissolved H, P, Cr, and O, indicating a reducing environment.

The remaining 15 diamonds contain inclusions of silicate minerals from a high-pressure origin, such as Cr-poor majoritic garnet (5) and CaSi-perovskite (CaPv) inverted to lower pressure phases (figs. S2 and S3). Some of these silicates also have coexisting metal and CH₄ ± H₂ fluid trapped in the same inclusion (figs. S2, S3, and S4). We therefore infer that these silicate inclusion assemblages were trapped under similar reducing conditions as the metal-only population at minimum pressures of 12 GPa (360 km depth). The presence of garnet precludes a deeper origin than 750 km because of the maximum stability of the mineral in eclogite (6, 7). These constraints suggest that CLIPPIR diamonds may form within the mantle transition zone at 410 to 660 km depth.

The rare previous reports of various native Fe, Fe-Ni, and Fe-carbide inclusions in diamond were interpreted as unusual and isolated occurrences (8–10). Though such inclusions are indicative of reducing conditions, these reports have fallen short of establishing systematic genetic relationships. The physical characteristics of these previously studied diamonds, and the textures and mineral assemblages of their metallic inclusions, are distinctly different from those of CLIPPIR diamonds.

We did not observe wüstite or ferropericlasite—normal products of carbonate reduction reactions (11)—in the assemblage, which rules out previous models proposed for other sublithospheric diamonds (12). Instead, multiple lines of evidence support a model of diamond growth from metallic liquid. Previous experiments have demonstrated diamond growth from a Fe-Ni-C-S melt, which solidifies to a Fe-carbide, Fe-Ni alloy, sulfide, and graphite assemblage that mimics the natural Fe-Ni-C-S inclusions in CLIPPIR diamonds

(13). The preserved CH₄ and H₂ characteristic of CLIPPIR diamonds are likewise observed in synthetic diamonds grown in molten Fe-Ni alloy. Inclusions in synthetic diamonds are often carbides or other alloys with fluid CH₄ and H₂ from hydrogen inadvertently dissolved in the metallic liquid (14). In general, a metallic liquid is a favorable medium for growing large diamonds such as CLIPPIR diamonds, with few inclusions and little or no chemical zonation, because the carbon supply is well buffered and carbon diffuses rapidly (13).

The growth of large diamonds (>5 cm) in the mantle might be accommodated by a liquid pocket that provides the unobstructed space necessary at deep mantle pressure. The high temperature of the sublithospheric mantle could enhance dislocation mobility, allowing formation of the dislocation networks commonly seen in CLIPPIR diamonds (5). The characteristically low nitrogen content in CLIPPIR diamonds might also be explained by N partitioning into the metal (4) or high-pressure mantle nitride phases (15).

The mantle likely becomes more reducing with depth, and thus capable of Fe-Ni precipitation (16). This hypothesis is supported by multiple lines of theoretical and experimental evidence suggesting Fe-Ni metal saturation below 250 ± 30 km (17–21). The increasing stability of Fe³⁺ in subcalcic pyroxene, majoritic garnet, and eventually (Fe,Mg)SiO₃ (bridgmanite) with pressure causes progressive disproportionation by the reaction 3Fe²⁺ → 2Fe³⁺ + Fe⁰. Whereas Fe³⁺ is maintained within the silicates, Fe⁰ exsolves as a stable metallic phase. The reduction of the liquidus temperature from the dissolution of C and S into the metallic phase allows it to be fluid at mantle conditions (21).

We suggest that the Fe-Ni-C-S melt inclusions reported here are samples of this metallic liquid. The metallic inclusions may be direct evidence of charge disproportionation and the resulting limited activity of oxygen in the transition zone. These redox conditions may be widespread and persistent through time, given that CLIPPIR diamonds are found in kimberlites from different continents with emplacement ages spanning at least 1 billion years. For example, the Cullinan diamond was recovered from the 1.18-billion-year-old Premier kimberlite in South Africa (22), whereas several of our specimens come from the 90-million-year-old Letseng kimberlite in Lesotho (1).

Dissolved carbon must reach supersaturation to crystallize diamond from a metallic liquid at compositions in which diamond is the liquidus phase. In a purely Fe-C system, the increase in liquidus temperature with increasing pressure outpaces mantle geotherms and suggests that a C-rich metallic melt may intersect the liquidus and begin crystallizing diamond if it is transported downward (23). An alternative mechanism that could trigger C crystallization is a change in the melt composition, such as an increase in S concentration (24) or a decrease in Fe content. Direct assimilation of introduced C and other minor components such as H and O, perhaps

during subduction, could also drive diamond crystallization at deeper levels in the mantle. As diamond growth proceeds within the metallic liquid, occasional droplets of the Fe-Ni-C-S melt are included, as shown by the CLIPPIR metallic inclusions.

Other aspects of the CLIPPIR suite of diamonds and their metallic inclusions potentially constrain the host rock for the metallic liquid, suggest a storage capacity for other volatiles, and lend insight into carbon subduction. The modest Ni/Fe ratios of the metal, though also a function of oxygen fugacity, suggest either a lower mantle origin or an association with subducted eclogite, because they are too low to be derived from more Ni-rich upper mantle peridotite (21). The abundance of CaPv, sometimes with a CaTiO₃ component, and the presence of Cr-poor majoritic garnets support an association with subducted eclogite at the depth of the transition zone or uppermost lower mantle (Fig. 3).

Variably light carbon isotopic compositions measured in seven of the CLIPPIR diamonds range in δ¹³C from −26.9 to −3.8 per mil (table S2), consistent with the similarly large range of values observed in eclogitic diamonds and one previous study of type II diamonds (25). Such isotopically light compositions are thought to result from the recycling of crustal carbon. Intuitively, one might consider eclogite to be too oxidized to permit the precipitation of an iron liquid, but at depth, subducting eclogite can be comparable to or better than peridotite at generating metallic iron (5, 26, 27). In an eclogite host, mantle metals should remain in small, isolated intergranular pockets (21), but localized rock deformation associated with convection can encourage metal segregation (28) that could further localize strain. Interconnectivity and agglomeration of the metallic liquid may be essential for efficient C scavenging and, ultimately,

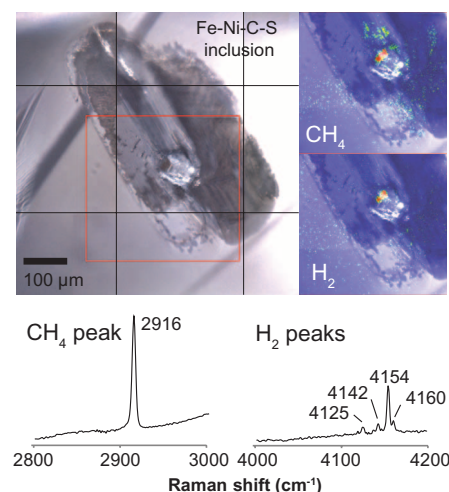


Fig. 1. Representative Fe-Ni-C-S melt inclusion. Raman maps show CH₄ and H₂ concentrated at the inclusion nucleus, with warmer colors representing higher intensities (sample 100517599181). Equal vertical scaling is applied to both the CH₄ and H₂ spectra. The vertical axis is intensity in arbitrary units.

Fig. 2. Scanning electron microscopy x-ray maps of Fe-Ni-C-S melt inclusions.

(A and B) Cohenite $[(\text{Fe,Ni})_3\text{C}]$ (green) is surrounded by interstitial Fe-Ni alloy (pink) and segregations of Fe-rich sulfide (teal), likely pyrrhotite. Detailed Ni, Fe, and C maps for the dashed area in (B) show that the cohenite is relatively Ni-poor but Fe- and C-rich. (C) Fe-phosphate bleb within sulfide and a large cohenite grain (no Fe-Ni alloy intersected). The samples shown are Letseng_889, inclusion E (A); Letseng_890, inclusion A (B); and OC2, inclusion D (C).

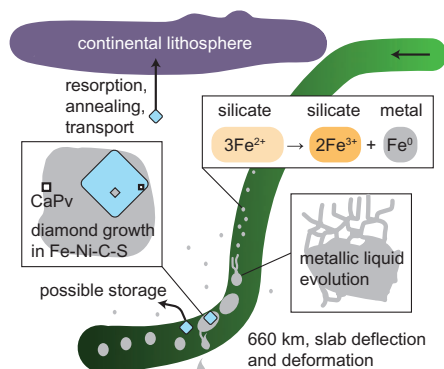
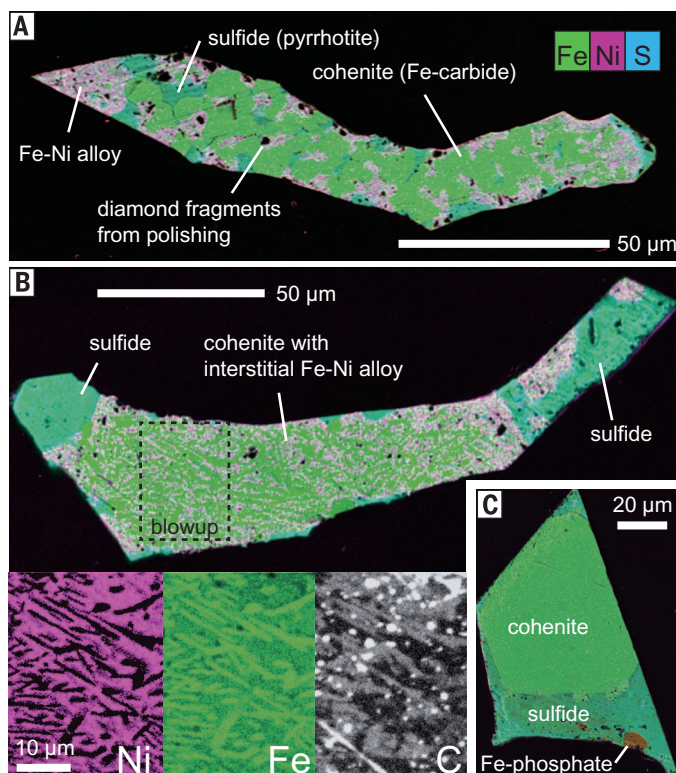


Fig. 3. Model of CLIPPIR diamond formation.

Formation of metallic iron proceeds in subducting eclogite by disproportionation. Metal segregation may be aided by deformation of the subducting slab in the transition zone. The liquid metal composition evolves to Fe-Ni-C-S, also dissolving P and H. Diamond crystallization occurs within metallic liquid pockets, likely in the pressure range of 12 to 25 GPa. Pocket walls become a site of CaSi-perovskite (CaPv) crystallization, where it can be included in diamond. Carbon saturation is achieved by increasing pressure, assimilating further C, or another mechanism such as increasing S content. After growth, diamonds are physically separated from the growth environment and may be transported and entrained by a kimberlite eruption.

diamond growth. Partitioning of Ni, C, S, P, H, and other elements from the eclogite into the metal would accompany the creation of a liquid metallic iron alloy (24).

The common occurrence of cohenite in these inclusions shows that Fe-Ni metal can dissolve substantial C, supporting a role of Fe-Ni metal in reduced portions of the mantle in the deep carbon cycle (24, 29). Furthermore, the growth of CLIPPIR diamonds themselves indicates that the metal can facilitate extreme local excesses of pure C in the transition zone or deeper mantle. A high solubility of H in the high-pressure liquid metal is confirmed by hydrogen in the Fe-Ni-C-S inclusions, which suggests that metallic Fe-Ni may also contribute to the deep Earth hydrogen budget. In this regard, the storage and cycling of any element that is soluble in the metallic liquid merit consideration. Furthermore, if present in high enough concentrations in mantle rocks, Fe-Ni metallic liquid could affect mantle rheology. It might act as a weak phase, like ferropericlase in the lower mantle, that accommodates more strain than neighboring strong phases and leads to shear localization (30).

Our observations verify and further constrain the prediction that the mantle has regions that are reducing enough to precipitate iron alloys. We know that there must be large variations in the redox conditions of the mantle, given the contrast between Earth's Fe-Ni core and the oxidized silicate lithosphere. These direct, diamond-based observations of regionally metal-saturated conditions in the upper mantle imply similar reducing conditions elsewhere in the mantle. Previous experiments and theory suggest comparably reducing conditions in the D'' layer, within large low shear-wave velocity provinces, at higher levels in the lower mantle, and in the transition zone (16, 17, 19–21, 27, 29, 31). The presence of metal has

implications for the seismic velocity, thermal and electrical conductivity, rheology, and volatile element cycling in Earth's deep mantle (16, 29, 32).

REFERENCES AND NOTES

1. D. C. Bowen, R. D. Ferraris, C. E. Palmer, J. D. Ward, *Lithos* **112**, 767–774 (2009).
2. A. E. Moore, S. Afr. J. Geol. **117**, 219–236 (2014).
3. A. E. Moore, S. Afr. J. Geol. **112**, 23–38 (2009).
4. E. M. Smith, M. G. Kopylova, W. Peck, *Can. J. Earth Sci.* **51**, 510–516 (2014).
5. Materials and methods are available as supplementary materials on Science Online.
6. B. Harte, N. C. F. Hudson, in *Proceedings of 10th International Kimberlite Conference: Volume One*, D. G. Pearson et al., Eds. (Springer India, 2013), pp. 235–253.
7. C. H. Wijbrans, A. Rohrbach, S. Klemme, *Contrib. Mineral. Petrol.* **171**, 50 (2016).
8. F. V. Kaminsky, R. Wirth, *Can. Mineral.* **49**, 555–572 (2011).
9. D. E. Jacob, A. Kronz, K. S. Viljoen, *Contrib. Mineral. Petrol.* **146**, 566–576 (2004).
10. S. Mikhail et al., *Geochim. Geophys. Geosyst.* **15**, 855–866 (2014).
11. Y. N. Palyanov et al., *Proc. Natl. Acad. Sci. U.S.A.* **110**, 20408–20413 (2013).
12. A. R. Thomson, M. J. Walter, S. C. Kohn, R. A. Brooker, *Nature* **529**, 76–79 (2016).
13. E. I. Zhmulev et al., *Geochem. Int.* **50**, 205–216 (2012).
14. E. M. Smith, W. Wang, *Diamond Relat. Mater.* **68**, 10–12 (2016).
15. L. F. Dobrzynetska et al., *Proc. Natl. Acad. Sci. U.S.A.* **106**, 19233–19238 (2009).
16. D. J. Frost, C. A. McCammon, *Annu. Rev. Earth Planet. Sci.* **36**, 389–420 (2008).
17. D. J. Frost et al., *Nature* **428**, 409–412 (2004).
18. C. Ballhaus, *Earth Planet. Sci. Lett.* **132**, 75–86 (1995).
19. A. Rohrbach, C. Ballhaus, P. Ulmer, U. Golla-Schindler, D. Schönbohm, *J. Petrol.* **52**, 717–731 (2011).
20. A. Rohrbach et al., *Nature* **449**, 456–458 (2007).
21. A. Rohrbach, S. Ghosh, M. W. Schmidt, C. H. Wijbrans, S. Klemme, *Earth Planet. Sci. Lett.* **388**, 211–221 (2014).
22. C. B. Smith, thesis, University of the Witwatersrand (1983).
23. O. T. Lord, M. J. Walter, R. Dasgupta, D. Walker, S. M. Clark, *Earth Planet. Sci. Lett.* **284**, 157–167 (2009).
24. K. Tsuno, R. Dasgupta, *Earth Planet. Sci. Lett.* **412**, 132–142 (2015).
25. H. J. Millard et al., *Nature* **303**, 791–792 (1983).
26. P. Bell, H. Mao, R. Weeks, A. Valkenburg, *Carnegie Inst. Washington Yearbook* **75**, 515–520 (1976).
27. J. Liu, J. Li, R. Hrubak, J. S. Smith, *Proc. Natl. Acad. Sci. U.S.A.* **113**, 5547–5551 (2016).
28. J. W. Hustoft, D. L. Kohlstedt, *Geochim. Geophys. Geosyst.* **7**, Q02001 (2006).
29. A. Rohrbach, M. W. Schmidt, *Nature* **472**, 209–212 (2011).
30. J. Girard, G. Amulele, R. Farla, A. Mohiuddin, S. Karato, *Science* **351**, 144–147 (2016).
31. Z. Zhang et al., *Geophys. Res. Lett.* **43**, 3693–3699 (2016).
32. R. Dasgupta, M. M. Hirschmann, *Earth Planet. Sci. Lett.* **298**, 1–13 (2010).

ACKNOWLEDGMENTS

Sincere thanks go to C. Locke, K. S. Moe, U. D'Haenens-Johansson, P. Johnson, and T. Moses for help with sample selection; A. Chan and J. Lai for help with sample preparation; J. Liao for photography; and K. Smit, L. Loudin, A. Balter, A. Shahar, and D. G. Pearson for valuable discussion and feedback. J. Butler is thanked for donating a sample to this study. Carbon standards were generously lent by C. Jackson and Z. Du. Anonymous reviewers are thanked for their constructive comments. The Deep Carbon Observatory is acknowledged for support to S.B.S. and F.N., the National Science Foundation for support to S.B.S. and J.W. (grant no. EAR1049992), and the European Research Council for support to F.N. (INDIMEDEA, grant no. 307322). Data files with a sample catalog, microprobe analyses, Raman spectra, and x-ray diffraction analyses are available in the supplementary materials.

SUPPLEMENTARY MATERIALS

www.sciencemag.org/content/354/6318/1403/suppl/DC1
Materials and Methods
Supplementary Text
Figs. S1 to S4
Tables S1 to S2
References (33–40)
Data S1 to S4

30 September 2016; accepted 15 November 2016
10.1126/science.aal1303

INDUCED SEISMICITY

Fault activation by hydraulic fracturing in western Canada

Xuwei Bao and David W. Eaton*

Hydraulic fracturing has been inferred to trigger the majority of injection-induced earthquakes in western Canada, in contrast to the Midwestern United States, where massive saltwater disposal is the dominant triggering mechanism. A template-based earthquake catalog from a seismically active Canadian shale play, combined with comprehensive injection data during a 4-month interval, shows that earthquakes are tightly clustered in space and time near hydraulic fracturing sites. The largest event [moment magnitude (M_W) 3.9] occurred several weeks after injection along a fault that appears to extend from the injection zone into crystalline basement. Patterns of seismicity indicate that stress changes during operations can activate fault slip to an offset distance of >1 km, whereas pressurization by hydraulic fracturing into a fault yields episodic seismicity that can persist for months.

The rate of earthquakes induced by fluid injection from oil and gas operations in parts of North America has surged in recent years (1, 2). In many areas, this increase is primarily associated with high-rate injection of large volumes of saltwater into porous rock formations (3–5). However, the United States, United Kingdom, and Canada each have well-documented earthquakes induced by hydraulic fracturing of low-permeability shale formations, with reported moment magnitudes (M_W) ranging from 2.0 to 4.6 (6–9). Seismicity triggered by hydraulic fracturing appears to be strongly localized. In western Canada, for example, induced seismicity of $M_W \geq 3$ is associated with only ~0.3% of hydraulically fractured wells (2).

Although we understand the basic principles of injection-induced seismicity (10, 11), critical details remain incomplete concerning activation of rupture on a fluid-pressurized fault. For massive saltwater injection into a permeable layer, we believe the primary triggering mechanism is an increase in pore pressure within an expanding subsurface volume, which tends to destabilize pre-existing faults by shifting stress conditions into the shear-failure regime (1, 10). The fault-activation process is less clear in the case of hydraulic fracturing, where injection usually occurs within a highly impermeable layer, inhibiting diffusive transport of injected fluids and/or pore pressure (2). Moreover, earthquake nucleation requires unstable slip conditions on a fault, as resistance to sliding must diminish faster than elastic unloading during fault slip. Yet current rate-and-state constitutive laws for rock friction favor aseismic slip in response to increasing pore-fluid pressure (12, 13). Resolving these apparent inconsistencies and developing valid predictive models for earthquakes induced by hydraulic fracturing remain important challenges.

Intermittent sequences of induced earthquakes began in December 2013 within a region of previous seismic quiescence west of Fox Creek, Alberta (Fig. 1). These earthquake sequences exhibit clear spatial and temporal correlation with hydraulic fracturing of the upper Devonian Duvernay Formation (9), a prolific hydrocarbon source rock that consists of organic-rich mudstone, interfingered with impermeable limestone (14). In response to increased levels of seismicity, real-time seismographic monitoring in this area has been enhanced by the installation of a network of broadband sta-

tions (15). In the present study, this network is supplemented by data from four broadband seismograph stations installed by an oil and gas operator within the most seismically active part of this region (Fig. 2). The application of algorithms for template-based matched filtering (16) and double-difference relocation (17) has yielded improved magnitude detection threshold and better focal-depth resolution than has heretofore been achieved using regional observations.

In order to undertake a comprehensive comparison between seismicity and injection parameters, we compiled injection data for all wells that were completed in the Duvernay zone from December 2014 to March 2015 (18). At six drilling locations (well pads), hydraulic fracturing was performed in multiple stages within horizontal wellbores. Virtually all of the induced seismicity occurred in spatial clusters concentrated within a lateral distance of ~2 km from hydraulically fractured wells (Fig. 2), with sparse detectable earthquake activity in the intervening areas between clusters. Although no template events were available with which to detect small earthquakes between clusters, even without such template events, we can confidently exclude intercluster seismicity of magnitude greater than M_W 2.0 on the basis of detection characteristics of the local array. As argued by previous authors on the basis of temporal and spatial correlation (2, 9), it is highly unlikely that seismicity in this area has been primarily induced by saltwater injection. For example, to the end of the time interval for this study, there was only one saltwater disposal well operating in

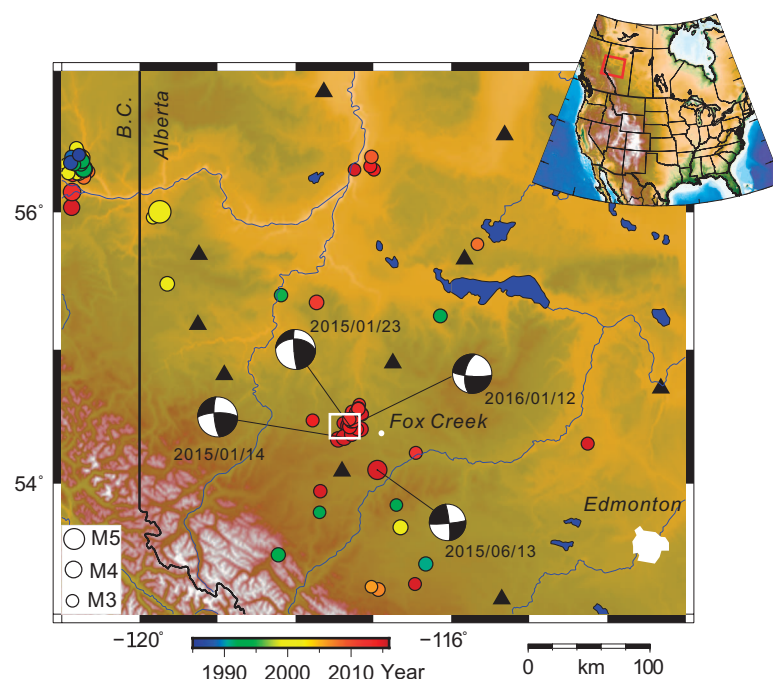


Fig. 1. Seismicity of northwestern Alberta, Canada, for the period 1985–2016. Symbol size indicates magnitude, and color denotes date of occurrence. B.C., British Columbia. Seismicity west of Fox Creek commenced in December 2013 and correlates in space and time with local hydraulic-fracturing operations (9). Focal mechanisms of the largest earthquakes, from (32–34), are labeled by year/month/date of occurrence. White rectangle outlines the area in Fig. 2.

Department of Geoscience, University of Calgary, Calgary, Alberta T2N 1N4, Canada.

*Corresponding author. Email: eatond@ucalgary.ca

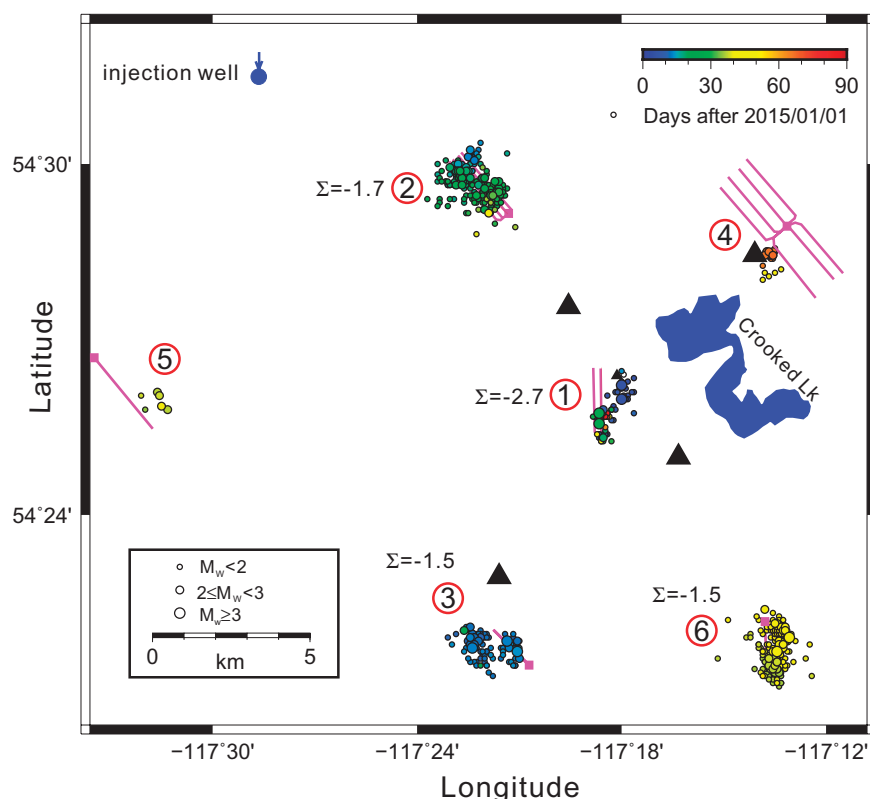


Fig. 2. Details of seismicity induced by hydraulic fracturing at six well pads from December 2014 to March 2015. Black triangles show local broadband seismograph stations; small black triangle near well pad 1 shows a station that was deployed for a short time after the M_w 3.9 event. Event symbols are colored by date of occurrence and are scaled on the basis of magnitude. Well pads are numbered sequentially by initiation of hydraulic-fracturing operations.

this area (Fig. 2), injecting into a layer that is higher in the stratigraphic succession (Mississippian Debolt Formation). After 3 years of operation to the end of March 2015, the cumulative injected volume at the disposal well was only $9.94 \times 10^4 \text{ m}^3$, a small volume compared with that in other regions where induced seismicity from saltwater disposal has been documented (19).

For the most part, observed induced seismicity exhibits a clear temporal correlation with hydraulic-fracturing activities. As evident from graphs of daily average injection pressure and cumulative injected volume (Fig. 3), most of the induced seismicity occurred during hydraulic-fracturing operations at proximal well pads. Cluster 1 is an exception to this behavior and was seismically active from early January to late March. Persistent but intermittent seismicity within this cluster lacks any clear indication of Omori-type decay in seismicity rate, which is generally characteristic of earthquake aftershock sequences; instead, it is characterized by three distinct posttreatment event sequences (S1 to S3), each defined by a pattern of increasing and/or decreasing event magnitudes followed by a brief hiatus. The largest induced earthquake (M_w 3.9) took place on 23 January 2015 during sequence S1, 2 weeks after completion of hydraulic fracturing at pad 1. This event occurred during flowback, a postinjection process

during which fracturing fluid is partially recovered in a controlled manner (20). This timing invites speculation that the earthquake was triggered by fluid withdrawal; however, only ~7% of the injected fluids at well 1 flowed back to the well-head, an unusually low recovery level compared with typical values of ~50% in other parts of western Canada (27). This limited recovery of flowback fluids is indicative of fluid retention within a subsurface region that is in hydrological contact with the primary or secondary network of induced hydraulic fractures (22).

The combined availability of a relatively complete earthquake catalog and comprehensive injection data enables accurate determination of several important parameters. For example, an often-cited relationship postulates that maximum seismic moment for injection-induced earthquakes is limited to the product of the net volume of injected fluid and the effective modulus of rigidity that describes the fault zone (19). This model assumes that the stimulated rock-mass is fully saturated, proximal faults are critically stressed, brittle failure occurs within a volume that is weakened by anthropogenic pore pressure increase, and induced earthquakes follow a Gutenberg-Richter magnitude distribution with a b -value near unity. On the basis of the cumulative injected volume for each well pad, we used this relation to calculate a

time-dependent upper limit for moment magnitude. The calculated envelope is in general agreement with our observations (Fig. 3). Similarly, the seismogenic index (Σ), defined as $\log_{10} N_{\geq M}(t) - \log_{10} V_f(t) + bM$, provides a measure of site-specific seismotectonic characteristics that expresses the (time-independent) potential for induced seismicity per unit of injected fluid volume (23). For a given location, calculation of Σ requires observations of the earthquake magnitude-frequency distribution (where N is the number of events having a magnitude $\geq M$), the b parameter of the Gutenberg-Richter scaling law, and the net injected fluid volume, V_f . The calculated seismogenic index for our study area ranges between -2.7 and -1.5. These values of Σ exceed values obtained elsewhere for hydraulic fracturing (-9.4 to -4.4) but fall within a previously documented range (23) for geothermal reservoirs (-3.2 to 0.4). These findings suggest that seismic hazard in the Fox Creek area may be more typical of that for geothermal projects than for other shale plays.

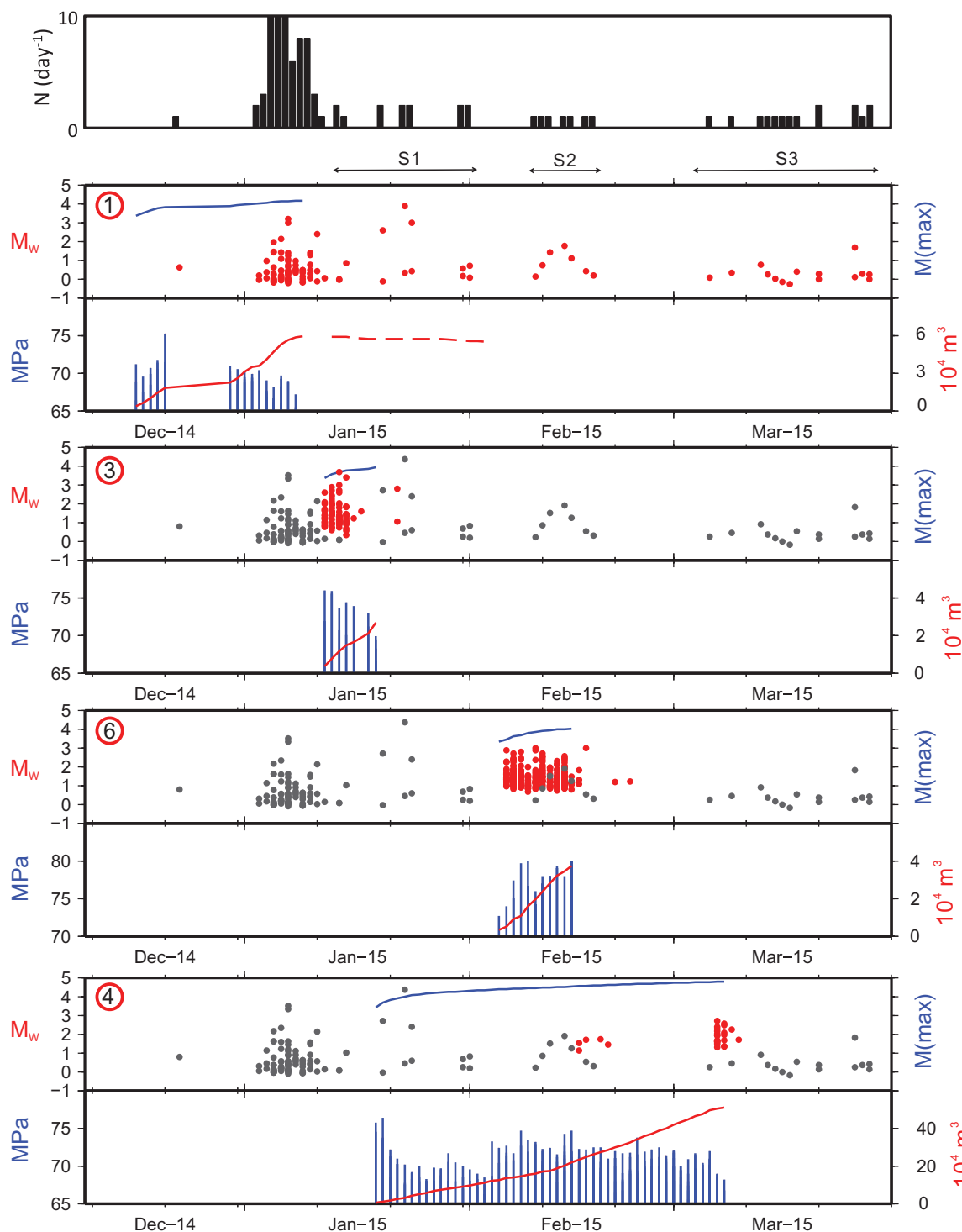
An east-west cross section through cluster 1, where the station geometry is most optimal for determination of precise focal hypocenter locations, reveals two distinct, steeply dipping bands of seismicity extending from the injection zone within the Duvernay Formation into the upper part of crystalline basement (Fig. 4). These bands of seismicity are interpreted as en echelon fault strands within a roughly north-south trending strike-slip fault system, a scenario consistent with nodal planes evident from regional focal mechanisms (Fig. 1). Independent support for the existence of such a fault system is provided by statistical analysis of seismicity patterns (24), coupled with geochemical models for widespread dolomitization of the underlying Swan Hills carbonate platform (25) that invoke basement faults as migration pathways for large volumes of dolomitizing fluids. The bulk of seismicity within the east fault strand is located >1 km from the nearest injection well and, similar to the other five clusters, this strand was mainly active during hydraulic-fracturing operations.

In contrast, the more proximal west fault strand was repeatedly activated for several months after completion of the treatment program. The hypocenter distribution suggests that the fault zone intersects the Duvernay Formation between the two injection wells. Hydraulic fracturing was performed in these wells using a so-called zipper frac technique, which involves staggered injection stages between two wells (26). Considering that ~93% of injected hydraulic fracturing fluids at well pad 1 were not recovered during flowback, it is likely that sustained pressurization of the fault zone occurred. Induced seismicity sequences appear to have occurred in a retrograde fashion, with the hypocenter of the largest event (sequence S1) located at the deepest level within the upper part of Precambrian crystalline basement, followed by migration of subsequent sequences (S2 and S3) to shallower levels, closer to the injection zone.

A recent analytical study that considered poroelastic coupling of stress and pore pressure in a homogeneous medium shows that, at large

Fig. 3. Comparison of seismicity and injection schedules for selected clusters.

For each cluster (numbered as in Fig. 2), the top shows seismicity (red dots) and calculated maximum magnitude (blue curve) (19); the bottom shows average daily treatment pressure (blue bars) and cumulative injected volume (red curve). Cluster 1 seismicity is repeated as gray dots in other graphs, for timing comparison. Black bar graph at top shows number of events per day for cluster 1, which lacks a typical Omori decay. At well 1, flowback (dashed curve) indicates recovery of only 7% of injected fluid. S1 to S3 indicate time windows for interpreted sequences. A complete set of graphs for all clusters is shown in the supplementary materials (fig. S9).



distances from a fluid injection site, stresses ultimately dominate over pore-pressure increase (27). Similarly, a numerical analysis, also based on poroelasticity theory, suggests that a 2013–2014 episode of seismicity induced by hydraulic fracturing in the Fox Creek area is best explained by the elastic response of the solid matrix, rather than fluid diffusion (28). In our study, the east and west strands of cluster 1 appear to delineate faults with similar orientations but contrasting activation sig-

natures. As shown in fig. S10 of the supplementary materials, when the elastic response of the surrounding medium to hydraulic fracturing at well pad 1 is considered, seismicity within the east strand largely falls within a positive Coulomb stress-change regime (up to ~ 0.1 MPa), consistent with previous findings (28). On the other hand, hypocenters for the west strand fall largely within a regime wherein elastic stresses induced by hydraulic fracturing are predicted to inhibit

fault slip, implying that a different triggering mechanism is required.

According to a model for nucleation and arrest of dynamic rupture on a pressured fault (29), the existence of a permeable and aerially extensive fault that is imperfectly aligned with the optimal orientation within the regional stress field enables pressurization to occur over a large fault patch before nucleation of rupture. As shown in fig. S11 of the supplementary materials, postinjection

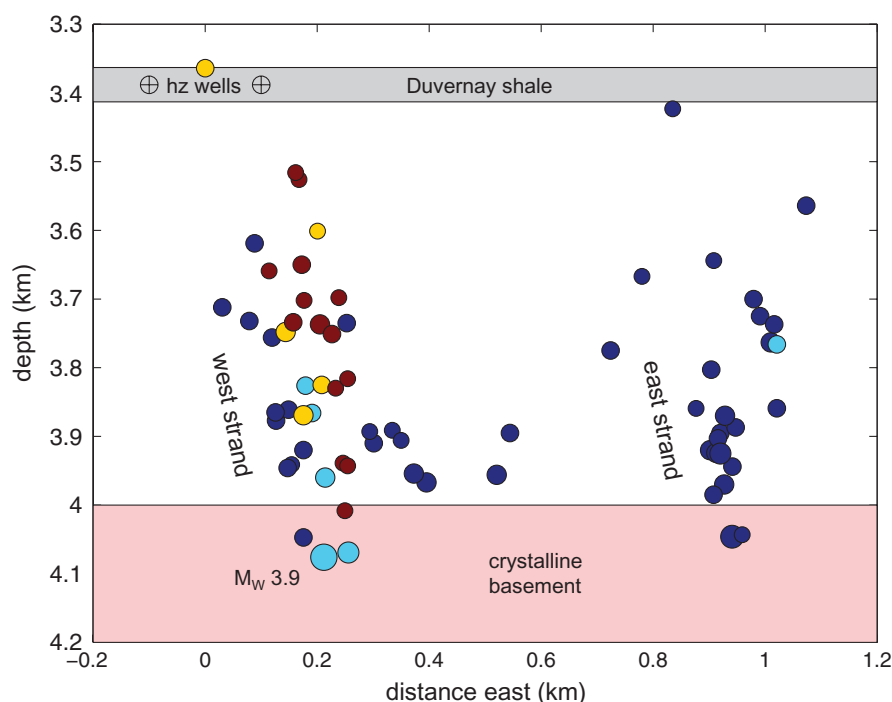


Fig. 4. Cross section through cluster 1, showing east and west fault strands inferred from double-difference event locations. Dark blue symbols show events that occurred during hydraulic fracturing in two horizontal (hz) wells. Light blue, yellow, and red symbols show subsequent events during sequences S1, S2, and S3, respectively.

activation of the M_W 3.9 earthquake is consistent with pore-pressure diffusion along the west fault strand. Taken together, our observations suggest that (i) a ~2-week delay in occurrence of the largest event after completion of hydraulic fracturing corresponds with relatively aseismic pressure diffusion on the west fault strand; (ii) earthquake nucleation occurred within the uppermost crystalline basement and was triggered by an estimated pore-pressure change of ~0.12 MPa; and (iii) the slip regime within the weakened, fluid-pressurized fault segment above the initial rupture during sequence S1 was subject to renucleation during sequences S2 and S3, months after elastic stresses from the hydraulic fracturing operations had subsided, on the basis of lack of seismicity within the east fault strand.

The occurrence of the M_W 3.9 earthquake on 23 January 2015 prompted, shortly thereafter, the introduction of new regulations applicable to this region that include a “traffic-light protocol” that mandates immediate shutdown in hydraulic fracturing operations following an earthquake of M_L (local magnitude) 4.0 or greater within 5 km of an affected well (30). Similar magnitude-based traffic-light protocols have been established in other jurisdictions (31). As seen in many studies of injection-induced seismicity from massive salt-water disposal, in this study, a reactivated fault zone is imaged by well-located hypocenters. Our results indicate that fault activation during and after hydraulic fracturing can be triggered by different mechanisms, including stress changes due to the elastic response of the rock-mass to

hydraulic fracturing or pore-pressure changes due to fluid diffusion along a permeable fault zone. Although stress-related triggering appears to diminish shortly after operations, a fluid-pressurized fault may be susceptible to persistent seismicity for a period of at least several months. This suggests that increased sensitivity of a fluid-pressurized fault should be considered in ongoing development of mitigation strategies for seismicity induced by hydraulic fracturing.

REFERENCES AND NOTES

- W. L. Ellsworth, *Science* **341**, 1225942 (2013).
- G. M. Atkinson *et al.*, *Seismol. Res. Lett.* **87**, 631–647 (2016).
- C. Frohlich, *Proc. Natl. Acad. Sci. U.S.A.* **109**, 13934–13938 (2012).
- K. M. Keranen, M. Weingarten, G. A. Abers, B. A. Bekins, S. Ge, *Science* **345**, 448–451 (2014).
- M. Weingarten, S. Ge, J. W. Godt, B. A. Bekins, J. L. Rubinstein, *Science* **348**, 1336–1340 (2015).
- A. Holland, *Bull. Seismol. Soc. Am.* **103**, 1784–1792 (2013).
- H. Clarke, L. Eisner, P. Styles, P. Turner, *Geophys. Res. Lett.* **41**, 8308–8314 (2014).
- R. Skoumal, M. Brudzinski, B. Currie, *Bull. Seismol. Soc. Am.* **105**, 189–197 (2015).
- R. Schultz, V. Stern, M. Novakovic, G. Atkinson, Y. Gu, *Geophys. Res. Lett.* **42**, 2750–2758 (2015).
- M. K. Hubbert, W. W. Rubey, *Geol. Soc. Am. Bull.* **70**, 115–166 (1959).
- C. B. Raleigh, J. H. Healy, J. D. Bredehoeft, *Science* **191**, 1230–1237 (1976).
- Y. Guglielmi, F. Cappa, J. P. Avouac, P. Henry, D. Elsworth, *Science* **348**, 1224–1226 (2015).
- M. M. Scuderi, C. Collettini, *Sci. Rep.* **6**, 24852 (2016).
- S. Creaney *et al.*, in *Geological Atlas of the Western Canada Sedimentary Basin*, G. D. Mossop and I. Shetsen (comp.)

- (Canadian Society of Petroleum Geologists and Alberta Research Council, Calgary, Alberta, 1994), chap. 31.
- R. Schultz, V. Stern, Y. J. Gu, D. Eaton, *Seismol. Res. Lett.* **86** (2A), 385–397 (2015).
- E. Caffagni, D. W. Eaton, J. P. Jones, M. van der Baan, *Geophys. J. Int.* **206**, 644–658 (2016).
- F. Waldhauser, W. Ellsworth, *Bull. Seismol. Soc. Am.* **90**, 1353–1368 (2000).
- Materials and methods are available as supplementary materials on Science Online.
- A. McGarr, *J. Geophys. Res.* **119**, 1008–1019 (2014).
- K. B. Gregory, R. D. Vidic, D. A. Dzombak, *Elements* **7**, 181–186 (2011).
- BC Oil and Gas Commission, “Investigation of observed seismicity in the Montney Trend.” (BC Oil and Gas Commission, Fort St John, British Columbia, 2014).
- M. M. Sharma, R. Manchanda, in *SPE Annual Technical Conference and Exhibition*, 28–30 September 2014, Houston, TX (SPE-174946-MS, Society of Petroleum Engineers, Richardson, TX, 2015).
- C. Dinske, S. A. Shapiro, *J. Seismol.* **17**, 13–25 (2013).
- R. Schultz *et al.*, *Geophys. Res. Lett.* **43**, 2534–2542 (2016).
- D. Green, E. Mountjoy, *Bull. Can. Pet. Geol.* **53** (2), 101–129 (2005).
- M. Rafiee, M. Y. Soliman, E. Pirayesh, in *SPE Annual Technical Conference and Exhibition*, 8–10 October, San Antonio, TX (SPE-159786-MS, Society of Petroleum Engineers, Richardson, TX, 2012).
- P. Segall, S. Lu, *J. Geophys. Res. Solid Earth* **120**, 5082–5103 (2015).
- K. Deng, Y. Liu, R. M. Harrington, *Geophys. Res. Lett.* **43**, 8482–8491 (2016).
- D. I. Garagash, L. N. Germanovich, *J. Geophys. Res.* **117** (B10), B10310 (2012).
- Alberta Energy Regulator, Subsurface order no. 2, 19 February 2015.
- R. J. Walters, M. D. Zoback, J. W. Baker, G. C. Beroza, *Seismol. Res. Lett.* **86**, 1110–1118 (2015).
- H. Zhang, D. W. Eaton, G. Li, Y. Liu, R. M. Harrington, *J. Geophys. Res. Solid Earth* **121**, 972–993 (2016).
- R. Wang, Y. J. Gu, R. Schultz, A. Kim, G. M. Atkinson, *Geophys. Res. Lett.* **43**, 564–573 (2016).
- Trans-Alta catalog of Nanometrics, Inc.

ACKNOWLEDGMENTS

Funding for this study was provided by the Natural Sciences and Engineering Research Council of Canada (grant IRCSA 485691); Chevron Canada Resources, Ltd.; and the University of Calgary. Telemetered data from the Regional Alberta Observatory for Earthquake Studies Network (RAVEN) operated by the Alberta Geological Survey were used in this study. Facilities of Incorporated Research Institutions for Seismology (IRIS) Data Services were used to access waveforms from the RAVEN network. Seismographic data from four additional broadband stations, as well as flowback data for well pad 1, were provided by Repsol Canada. These four stations were installed and operated by Nanometrics, Inc. Injection pressures and volumes were accessed under license from the Well Completions and Frac Database, owned and licensed by Canadian Discovery, Ltd. The injection data can also be accessed online through the Alberta Energy Regulator at <http://aer.ca/>; using the well identification numbers listed in the supplementary material. Generic Mapping Tools (GMT) was used to prepare several figures. Calculated earthquake magnitudes, hypocenter locations, and injection data are provided as supplementary materials. X.B. and D.W.E. both warrant that they have no conflict of interest in this work.

SUPPLEMENTARY MATERIALS

www.sciencemag.org/content/354/6318/1406/suppl/DC1
Materials and Methods
Figs. S1 to S11
Tables S1 to S7
References (35–47)

31 May 2016; resubmitted 20 June 2016
Accepted 21 October 2016
Published online 17 November 2016
10.1126/science.aag2583

ELECTROCATALYSIS

Biaxially strained PtPb/Pt core/shell nanoplate boosts oxygen reduction catalysis

Lingzheng Bu,¹ Nan Zhang,¹ Shaojun Guo,^{2,3,4*} Xu Zhang,⁵ Jing Li,⁶ Jianlin Yao,¹ Tao Wu,¹ Gang Lu,⁵ Jing-Yuan Ma,⁷ Dong Su,^{6*} Xiaoqing Huang^{1*}

Compressive surface strains have been necessary to boost oxygen reduction reaction (ORR) activity in core/shell M/platinum (Pt) catalysts (where M can be nickel, cobalt, or iron). We report on a class of platinum-lead/platinum (PtPb/Pt) core/shell nanoplate catalysts that exhibit large biaxial strains. The stable Pt (110) facets of the nanoplates have high ORR specific and mass activities that reach 7.8 milliamperes (mA) per centimeter squared and 4.3 ampere per milligram of platinum at 0.9 volts versus the reversible hydrogen electrode (RHE), respectively. Density functional theory calculations reveal that the edge-Pt and top (bottom)-Pt (110) facets undergo large tensile strains that help optimize the Pt-O bond strength. The intermetallic core and uniform four layers of Pt shell of the PtPb/Pt nanoplates appear to underlie the high endurance of these catalysts, which can undergo 50,000 voltage cycles with negligible activity decay and no apparent structure and composition changes.

Nanostructured platinum (Pt) is an efficient catalyst for fuel cells as well as various industrial chemical reactions (1–4), but its high cost impedes its large-scale commercialization (5–7). The most successful catalysts for boosting the activity of catalysts for the oxygen reduction reaction (ORR) on a per-Pt-atom basis have been PtM alloy nanoparticles (NPs) (where M has been Ni, Co, or Fe, among other metals) with a Pt-skin surface (core-shell structure). However, the formation of either a disordered PtM core or nonuniform Pt-skin layer (8–14) usually results in poor electrocatalytic stability after long-term voltage cycling.

In general, tuning or optimizing the oxygen adsorption energy through adjusting the compressive strain of the Pt surface is believed to be an effective approach to improve the ORR activity (15, 16). Ordered intermetallic phases with high transition metal content can be used to provide better control over the compressive strain effect for optimized catalysis (17). The optimal compressive strain to Pt (111) facet in PtM/Pt core/shell NPs is particularly necessary for boosting ORR catalysis. The tensile strain on the Pt (111)

facet is usually believed to be undesirable because such surface strain will result in overly strong binding of the oxygen species to the surfaces during the catalysis process. Although the activity enhancement has been demonstrated in the core/shell electrocatalyst with a Pt monolayer shell (causing limited durability) and an intermetallic PtPb core (18), the control over the stable and active facets of Pt shell onto PtPb core, and the investigation of strong tensile strain for ORR enhancement have not been explored.

We report on a class of highly uniform PtPb/Pt core/shell nanoplates with large biaxial tensile strain for boosting ORR. Rather than use compressive strain to optimize the oxygen adsorption energy, we show that at a very high tensile strain, the Pt (110) plane located outside the nanoplates can exhibit the superior electrocatalytic activity for ORR (19, 20). By integrating the strong tensile strain of PtPb to Pt (110) facet along [100] direction with thin two-dimensional (2D) morphology and intermetallic phase (ensuring high chemical stability), the as-prepared nanoplate can deliver specific and mass activities for ORR that are 33.9 and 26.9 times greater than those of the commercial Pt/C catalyst (8, 21, 22). The PtPb nanoplates show negligible activity decay and no obvious structure and composition changes after a 50,000-cycle electrochemical accelerated durability test (ADT). They are also extremely active and stable for anodic oxidation reactions, largely outperforming those based on the PtPb NPs and the commercial Pt/C in both methanol oxidation reaction (MOR) and ethanol oxidation reaction (EOR).

We synthesized PtPb/Pt core/shell hexagonal nanoplates in nonaqueous conditions using platinum (II) acetylacetonate [Pt(acac)₂] and lead (II) acetylacetonate [Pb(acac)₂] as the metal precursors, oleylamine (OAm)/octadecene (ODE) mixture as solvents and surfactants, and ascorbic

acid (AA) as the reducing agent [details in the supplementary materials (23)]. The structure of nanoplates was characterized by transmission electron microscopy (TEM) and high-angle annular dark-field scanning TEM (HAADF-STEM). The as-prepared hexagonal nanoplates were the dominant product, with monodisperse edge length of ~16 nm and the synthetic yield approaching 100% (Fig. 1, A and B). The thickness of PtPb nanoplates was determined to be 4.5 ± 0.6 nm by analyzing the nanoplates vertical on the TEM grid (fig. S1). The overall Pt/Pb composition, measured by inductively coupled plasma atomic emission spectroscopy (ICP-AES), was 55.9/44.1 (Pt/Pb), consistent with the TEM energy-dispersive x-ray spectroscopy (TEM-EDX) result (Fig. 1C).

Powder x-ray diffraction (PXRD) pattern of the PtPb nanoplates showed that they were highly crystalline with intermetallic PtPb phase [Joint Committee on Powder Diffraction Standards (JCPDS) no. 06-0374] (Fig. 1D and fig. S2). The selected-area electron diffraction (SAED) of a single PtPb nanoplate showed its single crystalline and was consistent with the diffraction pattern from the [001] zone axis of PtPb (P63/mmc) hexagonal phase (Fig. 1E). However, a high-resolution TEM (HRTEM) image of the same nanoplate (Fig. 1F) revealed that the edge has a different crystalline structure with the interior. A few edge dislocations were also observed between the edge layer and the interior around the corners, which help to relax the misfit strain between the edge phases. The fast Fourier transform (FFT) patterns indicate a cubic phase at the edge layer and a hexagonal phase of the interior (see the insets of Fig. 1F).

The elemental distribution of Pt and Pb at the nanoplates was characterized using STEM-electron energy-loss spectroscopy (EELS) mapping (Fig. 1G), where the Pt (green), Pb (red), and combined (green versus red) images indeed confirmed the presence of a Pt edge layer around the PtPb core (Fig. 1G). Considering the SAED, HRTEM, and STEM-EELS mapping results together, we can conclude that a Pt shell layer with a cubic phase (Fm-3m) formed at the edge, and the diffraction pattern of Fig. 1E can be interpreted as the overlapped diffraction patterns from the <110> zone axis of strained Pt phase and [001] zone axis of PtPb phase. The Pt shell thickness was determined to be about 0.8 to 1.2 nm (four to six atomic layers).

The aberration-corrected HAADF-STEM imaging technique was further used to characterize the facets and interfaces of the PtPb nanoplates. The nanoplates were imaged from both the plate view and the side view (Fig. 2A). Figure 2B is a HAADF-STEM image along the PtPb [100] zone axis (side view), whereas Fig. 2C is a HAADF-STEM image from the [001] PtPb zone axis (plate view). Figure 2, D to F, are atomic-resolution STEM-HAADF images taken at higher magnifications from the areas indicated by the yellow rectangles. The Pt and PtPb phases can be identified from their different stacking sequences. Image simulation with a multisliced method, as well as the projection of atoms, was overlapped on Fig. 2, D to F. The results confirmed the PtPb(hexagonal)/Pt(cubic) core/shell structure: In addition to the

¹College of Chemistry, Chemical Engineering and Materials Science, Soochow University, Jiangsu 215123, China.

²Department of Materials Science and Engineering, and Department of Energy and Resources Engineering, College of Engineering, Peking University, Beijing 100871, China. ³The Beijing Innovation Center for Engineering Science and Advanced Technology (BIC-ESAT), College of Engineering, Peking University, Beijing 100871, China. ⁴Key Laboratory of Theory and Technology of Advanced Batteries Materials, College of Engineering, Peking University, Beijing 100871, China. ⁵Department of Physics and Astronomy, California State University, Northridge, CA 91330, USA. ⁶Center for Functional Nanomaterials, Brookhaven National Laboratory, Upton, NY 11973, USA. ⁷Shanghai Synchrotron Radiation Facility, Shanghai Institute of Applied Physics, Chinese Academy of Sciences, Shanghai 201204, China.

*Corresponding author. Email: guosj@pku.edu.cn (S.G.); dsu@bnu.gov (D.S.); hxq006@suda.edu.cn (X.H.)

Fig. 1. Morphology and structure characterization of PtPb hexagonal nanoplates.

Representative (A) HAADF-STEM image, (B) TEM image, (C) TEM-EDX, and (D) PXRD pattern of PtPb hexagonal nanoplates. (E) SAED and (F) HRTEM of one single hexagonal nanoplate. Insets of Fig. 1F are the FFT patterns from the white squares at the edge of and inside the nanoplate, respectively. (G) STEM-EELS elemental mapping of PtPb hexagonal nanoplates: HAADF-STEM image, Pt mapping in green, Pb mapping in red, and integrated mapping of Pt and Pb are shown. The compositional ratio between Pt/Pb is 55.9/44.1, as revealed by ICP-AES.

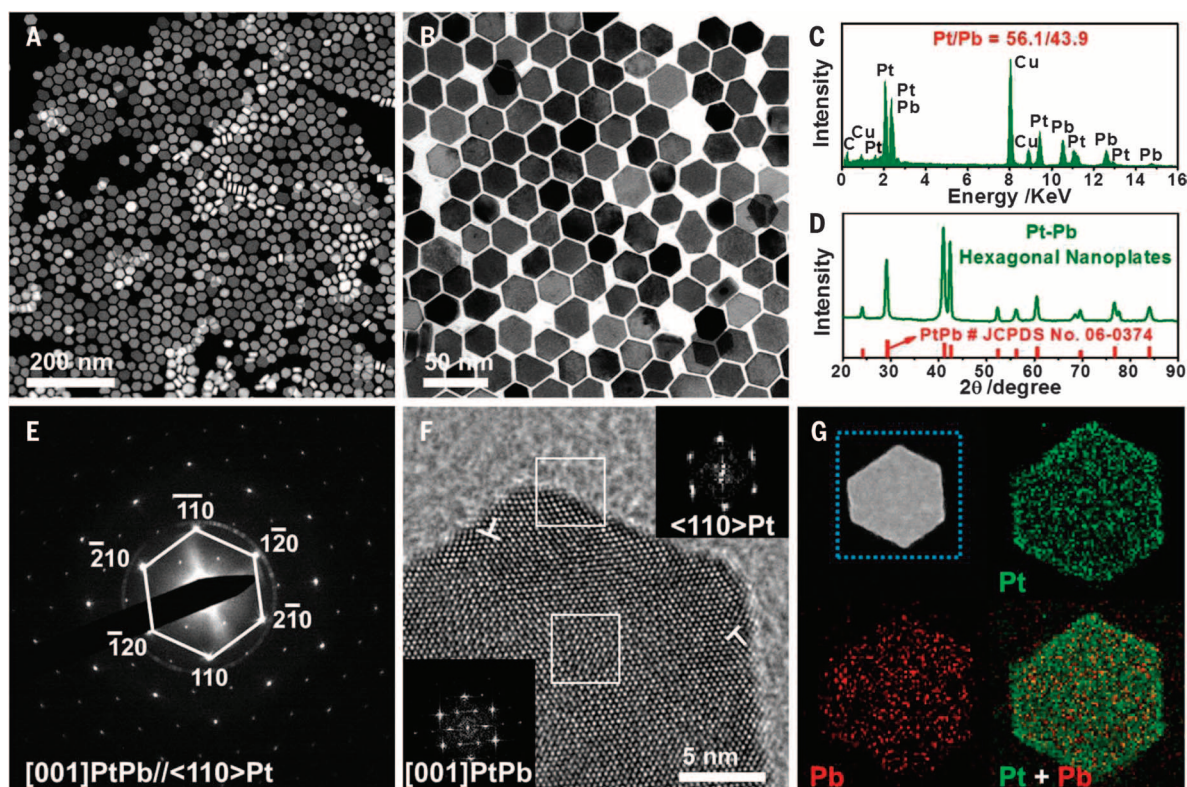
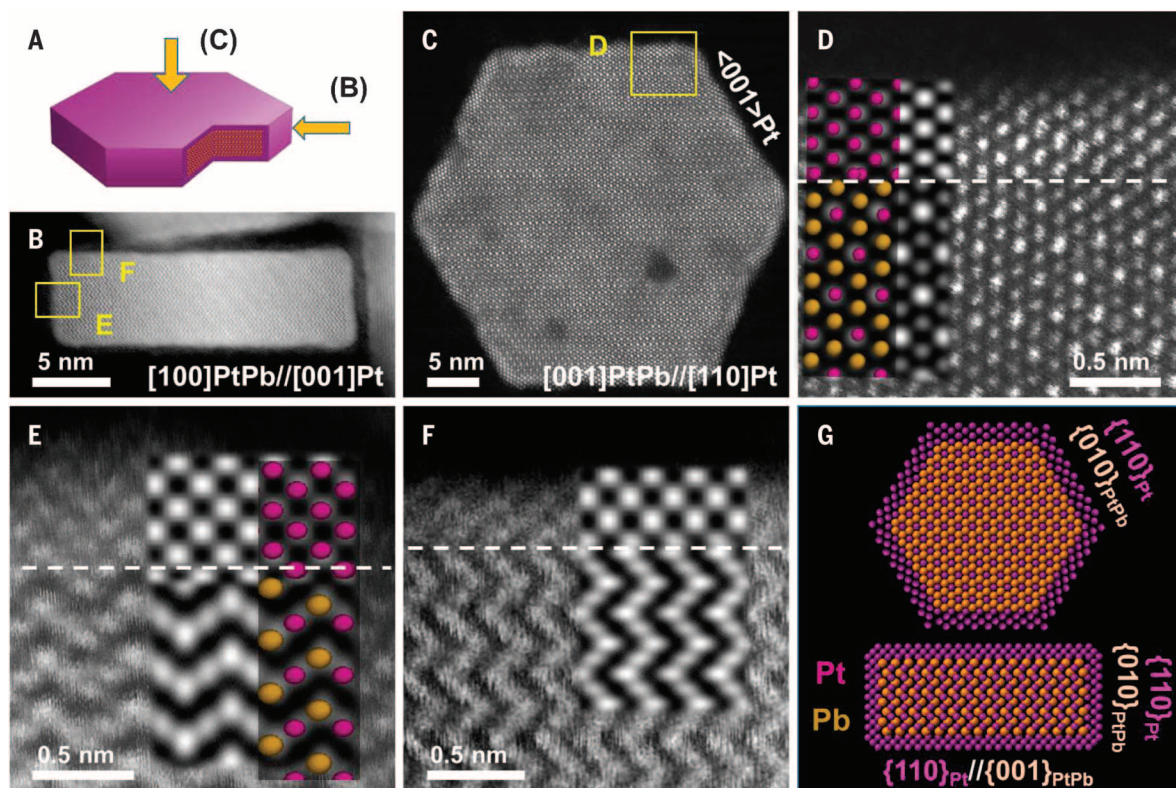


Fig. 2. Structure analysis of PtPb nanoplates.

(A) A model of one single hexagonal nanoplate, (B) HAADF-STEM image from in-plate view, (C) HAADF-STEM image from out-of-plate view. (D to F) (D) is a high-resolution HAADF image from the selected area in (C). (E) and (F) are high-resolution HAADF images from the selected areas in (B). Simulated HAADF images as well as the atomic models are superimposed on the experimental images. (G) The schematic atom models of the nanoplate showing the top interface $[(110)\text{Pt}]/[(100)\text{PtPb}]$ and the side interface $[(110)\text{Pt}]/[(001)\text{PtPb}]$.



Pt edge layers, there were top (bottom)-Pt layers on the plane surfaces of nanoplates, forming the “perfect” core/shell structure. Thus, two types of interfacial planes formed in PtPb nanoplates: $\{010\}$ PtPb// $\{110\}$ Pt between the PtPb and the edge-Pt layer, and $\{001\}$ PtPb// $\{110\}$ Pt between PtPb and top (bottom)-Pt layer (atomic schematic model of Fig. 2G and figs. S3 to S6). Herein, the unique Pt $\{110\}$ surface would be beneficial for ORR activity enhancement because Pt $\{110\}$ facet has been demonstrated to be intrinsically more active than Pt $\{111\}$ facet for the ORR in perchloric acid (24, 25). The SAED, HRTEM, and selected-area FFT analysis (figs. S4 to S6) further revealed that the top-Pt layers were fully coherent to the PtPb core, with an 11% compressive strain along the $[01-1]_{\text{Pt}}$ and a 7.5% tensile strain along $[100]_{\text{Pt}}$, whereas in the edge-Pt layer, the $[001]$ direction of Pt was fully confined within PtPb, resulting in a 7.5% tensile strain and little compressive strain (1.0%) along $[110]_{\text{Pt}}$ (fig. S3).

The synthesis of 2D pure metal nanoplates is challenging because of the intrinsically isotropic growth behavior of metals (26–28). Time-dependent composition and structure changes revealed that making intermetallic PtPb/Pt core/shell hexagonal nanoplates involved the initial formation of $\text{Pb}_3(\text{CO}_3)_2(\text{OH})_2$, the transformation of $\text{Pb}_3(\text{CO}_3)_2(\text{OH})_2$, the reduction of Pt species, and hereafter the interdiffusion to form structurally ordered intermetallic PtPb nanoplates (figs. S7 and S8). The use of AA as reductant is the key for the formation of well-organized Pt atomic layers because during the synthetic process, AA can work as a weak acid for removing the Pb, allowing the Pt atoms to diffuse and rearrange at higher temperatures.

We performed a set of control experiments using a variety of synthetic parameters, such as precursor, surfactant, and reducing agent, to investigate how the different synthetic reagents affect the growth of the well-defined PtPb hexagonal nanoplates. The synthesis of well-defined PtPb/Pt nanoplates depended highly on the concentration of Pt and Pb precursors, the combined use of OAm to ODE, and the use of proper reducing agents (figs. S9 to S15). The concentration of AA also had to stay within a critical range to obtain a high yield of PtPb/Pt core/shell nanoplates (fig. S14), and PtPb hexagonal nanoplates could not be made by replacing AA with other reducing agents, such as glucose and citric acid (fig. S15).

The electrochemical properties of the PtPb nanoplates as well as PtPb nanoparticles that we synthesized (figs. S16 and S17) were studied and further benchmarked against the commercial Pt/C from Johnson Matthey (JM) (Pt/C, 20 weight % Pt on Vulcan XC72R carbon, Pt particle size 2 to 5 nm) (fig. S18, A and B). Before the electrochemical measurement, the PtPb nanostructures were uniformly deposited on a commercial carbon (C, Vulcan) support (figs. S19 and S20, named as PtPb nanoplates/C and PtPb nanoparticles/C) via the sonication of PtPb nanostructures and C solution. The products were further treated with the mixture of ethanol/acetic acid to remove the surfactant (29). The inset of

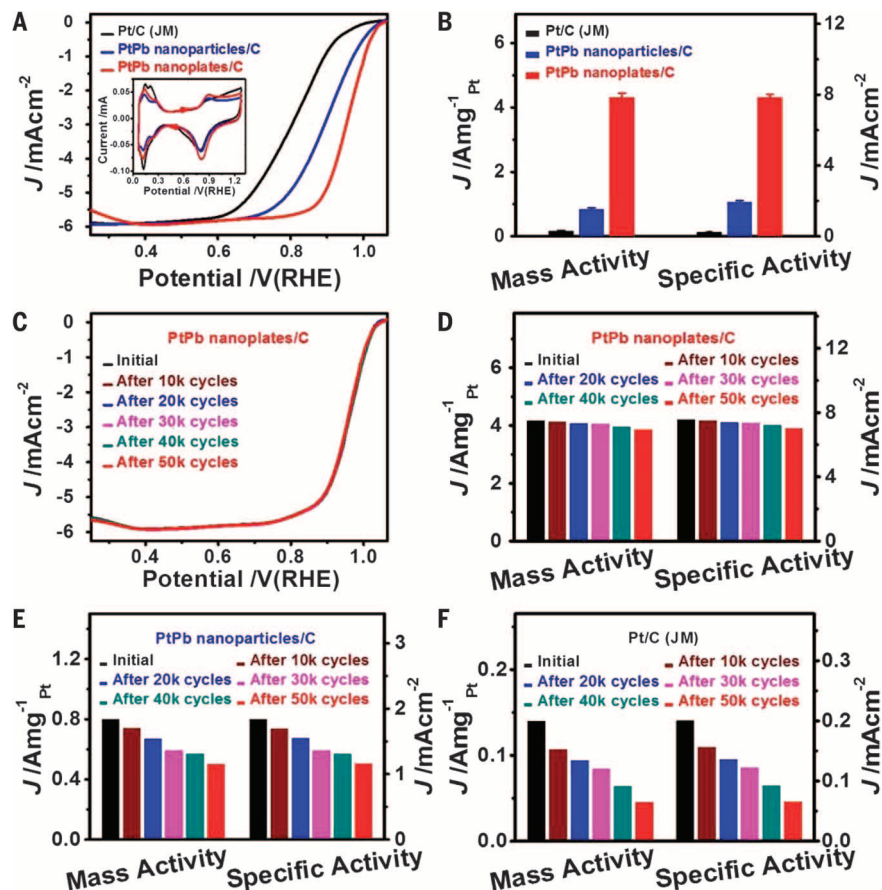


Fig. 3. Electrochemical performance of PtPb nanoplates/C, PtPb nanoparticles/C, and commercial Pt/C catalysts for ORR. (A) ORR polarization curves and (B) specific and mass activities of different catalysts. Inset in (A) is the CVs of different catalysts in 0.1 M HClO_4 solution at a sweep rate of 50 mV/s. The ORR polarization curves were recorded at room temperature in an O_2 -saturated 0.1 M HClO_4 aqueous solution. The activities were calculated based on five parallel measurements after Ohmic drop correction. (C) ORR polarization curves of the PtPb nanoplates/C catalyst before and after different potential cycles between 0.6 and 1.1 V versus RHE. (D) The changes on specific and mass activities of the PtPb nanoplates/C catalyst before and after different potential cycles. (E) The changes on specific and mass activities of the PtPb nanoparticles/C catalyst before and after different potential cycles. (F) The changes on specific and mass activities of the commercial Pt/C catalyst before and after different potential cycles.

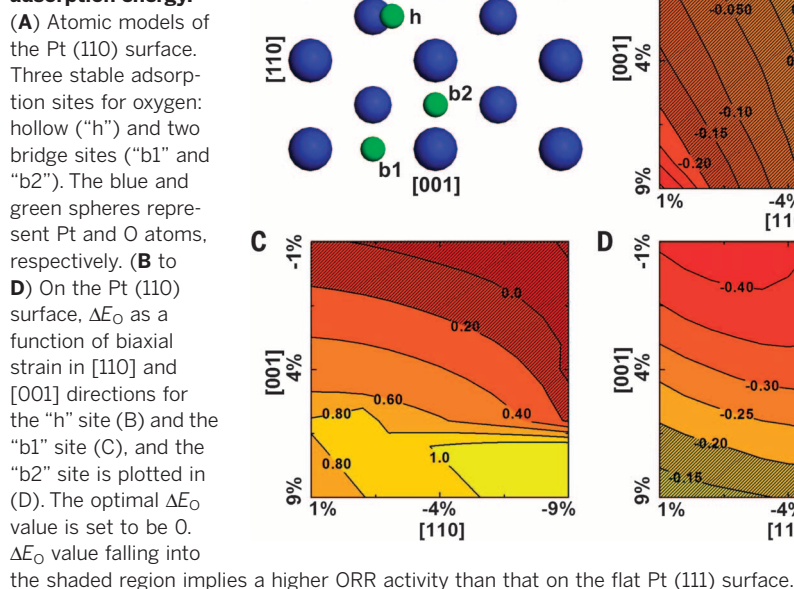
Fig. 3A shows cyclic voltammograms (CVs) of PtPb nanoplates/C, PtPb nanoparticles/C, and commercial Pt/C catalysts in N_2 -purged 0.1 M HClO_4 solution at a sweep rate of 50 mV/s. The PtPb nanoplates showed greater electrochemical active surface area (ECSA) of 55.0 m^2/g than PtPb nanoparticles (43.4 m^2/g) because of their thinness and even comparable ECSA to that of the commercial Pt/C (68.9 m^2/g).

To evaluate the electrocatalytic activities toward ORR, the ORR polarization curves of PtPb nanoplates/C, PtPb nanoparticles/C and commercial Pt/C were measured in an O_2 -saturated 0.1 M HClO_4 solution under Ohmic drop correction (Fig. 3A). As shown in Fig. 3B and table S1, the specific activity (SA) of PtPb nanoplates/C could reach 7.8 mA/cm^2 at 0.9 V versus reversible hydrogen electrode (RHE), 4.1 and 33.9 times greater than those of PtPb nanoparticles/C (1.9 mA/cm^2) and commercial Pt/C (0.23 mA/cm^2). The mass activity (MA) of PtPb nanoplates/C is 4.3 $\text{A}/\text{mg}_{\text{Pt}}$ at 0.9 V

versus RHE, which is ~ 9.8 times that of the 2020 U.S. Department of Energy target (30), and places them among the most efficient bimetallic catalysts reported for ORR (8, 21, 22).

The electrochemical durability of the PtPb/Pt core/shell nanoplates was evaluated at the potential between 0.6 and 1.1 V versus RHE in 0.1 M HClO_4 solution. Figure 3C shows the ORR polarization curves of the PtPb nanoplates/C before and after 10,000, 20,000, 30,000, 40,000, and 50,000 potential cycles. After 50,000 sweeping cycles, there was almost no shift in ORR polarization curves and only 7.7% loss of mass activity for the PtPb nanoplates (Fig. 3D). However, under the same condition, the PtPb nanoparticles/C showed a large negative shift in ORR polarization curves (fig. S21A) and 37.0% loss of mass activity (Fig. 3E). The commercial Pt/C showed a much larger negative shift in ORR polarization curves (fig. S21B) with 66.7% loss of mass activity (Fig. 3F). The structures of the catalysts before and after

Fig. 4. DFT calculations of oxygen adsorption energy.



the durability tests were characterized by TEM, SEM-EDX, HRTEM, elemental mappings, and extended x-ray absorption fine structure (EXAFS) (figs. S19, S22, and S23), showing that there was negligible change on the morphology and composition of the PtPb nanoplates (figs. S19, G to I, and S22, D to F) and Pt-Pt atomic distance (fig. S23) after long-term cycles. Under the same condition, the PtPb nanoparticles show noticeable morphology and composition changes (fig. S20, C and D), and the commercial Pt/C catalyst exhibited large size changes and substantial aggregation after 50,000 cycles (fig. S18, C and D). We think that the high catalytic stability of PtPb/Pt core/shell nanoplates originates from their special structure, in which the well-defined Pt shell can hinder the loss of interior transition metal through the place-exchange mechanism during electrochemical condition and thus improve their ORR durability, which is hardly afforded by the previously reported PtPb/Pt core/shell structures suffering from the typical electrocatalytic activity loss possibly due to their too thin Pt shell (18, 31).

To understand the exceptional ORR performance of the core/shell PtPb/Pt nanoplates, we performed density functional theory (DFT) calculations for the oxygen adsorption energy (E_O) on the PtPb nanoplates. The ORR activity reaches the maximum at some optimal value of E_O (32, 33). For convenience, we shifted the optimal E_O value to 0 eV and use ΔE_O to represent the difference of a given E_O value relative to this optimal reference. In general, both surface strain and ligand effect can influence the catalytic activity of a core-shell nanostructure, and they can be tuned by the variation of alloy composition in the core. We ignored the ligand effect because it is often negligible for a shell thickness >0.6 nm (34). The HRTEM images revealed that the Pt skin thick-

ness of PtPb/Pt nanoplates is between 0.8 and 1.2 nm. Therefore, herein we focus entirely on surface strain.

The SAED and HRTEM results revealed a large tensile strain along [001] and a compressive strain along [110] on both the top-Pt and edge-Pt surfaces of the nanoplates. Thus, we calculated ΔE_O on the Pt (110) surface as a function of strain in the [001] and [110] directions. Specifically, the strain applied in [001] direction ranged from -1% (compressive) to 9% (tensile), and the strain applied in [110] direction varied from 1% to -9%. Under each biaxial strain, three types of the most stable oxygen adsorption sites on the (110) surface were examined (Fig. 4A): the face-center cubic (fcc) hollow sites ("h"), the bridge sites in [001] direction ("b1"), and the bridge sites in [110] direction ("b2"). Both "b1" and "b2" sites consist of the low-coordinated surface atoms. We also calculated ΔE_O on the flat (111) surface of Pt. The results of ΔE_O calculations are reported in Fig. 4, B to D.

The ΔE_O values on the "h" sites were nearly optimal for a wide range of biaxial strains. The adsorbed oxygen atom was metastable when the tensile strain in [001] direction was relatively small or the compressive strain in [110] direction was relatively large. In both cases, the Pt-O binding was much weaker on the "h" sites than their adjacent "b2" sites (Fig. 4, B and D) and the diffusion barrier was <0.05 eV from an "h" site to a "b2" site. Thus, the "h" sites under such biaxial strains did not contribute meaningfully to the overall ORR. However, under large tensile strain of 7.5% in [001] direction or a small compressive strain of 1% in [110] direction, the "h" sites became catalytically active and their ΔE_O values were comparable to those on the "b2" sites. Thus, the "h" sites on the edge-Pt surface of the nanoplates were stable and active for ORR. The

"b1" sites were not active for large tensile strains in [001] direction and were not responsible for the ORR performance of the nanoplates (Fig. 4C). On the "b2" sites, the Pt-O bond was usually strong and could poison the catalyst. However, the strong Pt-O binding could be weakened by tensile strains in [001] direction (Fig. 4D) and the "b2" sites became catalytically active under a large tensile strain of 7.5% in [001] direction. Because ΔE_O values were insensitive to the strain in [110] direction, the "b2" sites were active for ORR at both the top-Pt and edge-Pt surfaces. We attribute the high ORR activity of the PtPb/Pt core/shell nanoplates to the active "h" and "b2" sites under the appropriate large biaxial strains. It is generally believed that in M/Pt core/shell catalyst, the compressive strain can weaken the Pt-O binding on Pt (111) surface and increase the ORR activity (34–36), and low-coordinated surface atoms have stronger Pt-O binding, lowering the ORR activity (37, 38). However, our DFT calculations show that the tensile strains on Pt (110) facet can also increase the ORR activity and that the low-coordinated surface atoms ("b2") can be activated by large tensile strains.

The PtPb/Pt core/shell nanoplates reported herein also show high electrocatalytic activity and stability toward anodic fuel cell reactions such as methanol oxidation reaction (MOR) and ethanol oxidation reaction (EOR). As shown in figs. S24 to S26 and table S2, the PtPb nanoplates/C exhibit the MOR mass activity of 1.5 A/mgPt, 2.4 times and 7.9 times higher than those of PtPb nanoparticles and Pt catalysts, respectively, as well as higher stability. For EOR, it displays the specific activity of 2.5 mA/cm² and mass activity of 1.4 A/mg Pt, 1.9 and 2.5 times greater than those of PtPb nanoparticles/C, and 10.4 times and 8.8 times higher than those of the commercial Pt/C (fig. S24 and table S3), as well as greater stability (figs. S24 to S26).

REFERENCES AND NOTES

1. M. Winter, R. J. Brodd, *Chem. Rev.* **104**, 4245–4270 (2004).
2. A. Chen, P. Holt-Hindle, *Chem. Rev.* **110**, 3767–3804 (2010).
3. M. S. Dresselhaus, I. L. Thomas, *Nature* **414**, 332–337 (2001).
4. P. Strasser, *Science* **349**, 379–380 (2015).
5. H. A. Gasteiger, S. S. Kocha, B. Sompalli, F. T. Wagner, *Appl. Catal. B* **56**, 9–35 (2005).
6. H. A. Gasteiger, N. M. Marković, *Science* **324**, 48–49 (2009).
7. J. K. Nørskov, T. Bligaard, J. Rossmeisl, C. H. Christensen, *Nat. Chem.* **1**, 37–46 (2009).
8. S. I. Choi et al., *Nano Lett.* **13**, 3420–3425 (2013).
9. F. Saleem et al., *J. Am. Chem. Soc.* **135**, 18304–18307 (2013).
10. X. Xu et al., *Angew. Chem. Int. Ed.* **53**, 12522–12527 (2014).
11. T. Bian et al., *Nano Lett.* **15**, 7808–7815 (2015).
12. L. Zhang et al., *Science* **349**, 412–416 (2015).
13. C. Wang et al., *J. Am. Chem. Soc.* **133**, 14396–14403 (2011).
14. H. Zhu, S. Zhang, S. Guo, D. Su, S. Sun, *J. Am. Chem. Soc.* **135**, 7130–7133 (2013).
15. J. Zhang, H. Yang, J. Fang, S. Zou, *Nano Lett.* **10**, 638–644 (2010).
16. H. Yang, J. Zhang, K. Sun, S. Zou, J. Fang, *Angew. Chem. Int. Ed.* **49**, 6848–6851 (2010).
17. D. Wang et al., *Nat. Mater.* **12**, 81–87 (2013).
18. T. Ghosh, M. B. Vukmirovic, F. J. DiSalvo, R. R. Adzic, *J. Am. Chem. Soc.* **132**, 906–907 (2010).
19. J. Greeley et al., *Nat. Chem.* **1**, 552–556 (2009).
20. M. F. Francis, W. A. Curtin, *Nat. Commun.* **6**, 6261 (2015).
21. C. Chen et al., *Science* **343**, 1339–1343 (2014).
22. X. Q. Huang et al., *Science* **348**, 1230–1234 (2015).

23. See the supplementary materials on Science Online.
24. N. M. Marković, R. R. Adžić, B. D. Cahan, E. B. Yeager, *J. Electroanal. Chem.* **377**, 249–259 (1994).
25. M. D. Maciá, J. M. Campiña, E. Herrero, J. M. Feliu, *J. Electroanal. Chem.* **564**, 141–150 (2004).
26. X. Huang et al., *Nat. Nanotechnol.* **6**, 28–32 (2011).
27. X. Xia, J. Zeng, Q. Zhang, C. H. Moran, Y. Xia, *J. Phys. Chem. C* **116**, 21647–21656 (2012).
28. L. Chen et al., *Nano Lett.* **14**, 7201–7206 (2014).
29. V. Mazumder, S. Sun, *J. Am. Chem. Soc.* **131**, 4588–4589 (2009).
30. U.S. Department of Energy, Technical Plan: Fuel Cells (2016); www.energy.gov/sites/prod/files/2016/06/f32/fcto_myrrdd_fuel_cells_0.pdf.
31. C. Roychowdhury et al., *Chem. Mater.* **18**, 3365–3372 (2006).
32. J. K. Nørskov et al., *J. Phys. Chem. B* **108**, 17886–17892 (2004).

33. V. Stamenkovic et al., *Angew. Chem. Int. Ed.* **45**, 2897–2901 (2006).
34. X. Zhang, G. Lu, *J. Phys. Chem. Lett.* **5**, 292–297 (2014).
35. M. Mavrikakis, B. Hammer, J. K. Nørskov, *Phys. Rev. Lett.* **81**, 2819–2822 (1998).
36. P. Strasser et al., *Nat. Chem.* **2**, 454–460 (2010).
37. L. Li et al., *J. Phys. Chem. Lett.* **4**, 222–226 (2013).
38. D. F. van der Vliet et al., *Nat. Mater.* **11**, 1051–1058 (2012).

ACKNOWLEDGMENTS

This work was financially supported by the National Key Research and Development Program of China (2016YFB0100201), the National Natural Science Foundation of China (21571135 and 51671003), the Ministry of Science and Technology (2016YFA0204100), the start-up funding from Soochow University and Peking University, Young Thousand Talented Program, and the Priority Academic Program Development of Jiangsu Higher Education Institutions (PAPD). Part of

the electron microscopy work was performed at the Center for Functional Nanomaterials, Brookhaven National Laboratory, which is supported by the U.S. Department of Energy (DOE), Office of Basic Energy Science, under contract DE-SC0012704. The work at California State University Northridge was supported by the U.S. Army Research Office via the MURI grant W911NF-11-1-0353. We thank S. Cheng for his help in the simulation of STEM imaging. All data are reported in the main text and supplementary materials.

SUPPLEMENTARY MATERIALS

www.sciencemag.org/content/354/6318/1410/suppl/DC1
Materials and Methods
Figs. S1 to S28
Tables S1 to S3
References (39–84)

21 July 2016; accepted 2 November 2016
10.1126/science.aah6133

ELECTROCATALYSIS

Ultrafine jagged platinum nanowires enable ultrahigh mass activity for the oxygen reduction reaction

Mufan Li,¹ Zipeng Zhao,² Tao Cheng,³ Alessandro Fortunelli,^{3,4} Chih-Yen Chen,² Rong Yu,⁵ Qinghua Zhang,⁶ Lin Gu,⁶ Boris V. Merinov,³ Zhaoyang Lin,¹ Enbo Zhu,² Ted Yu,^{3,7} Qingying Jia,⁸ Jinghua Guo,⁹ Liang Zhang,⁹ William A. Goddard III,^{3*} Yu Huang,^{2,10*} Xiangfeng Duan^{1,10*}

Improving the platinum (Pt) mass activity for the oxygen reduction reaction (ORR) requires optimization of both the specific activity and the electrochemically active surface area (ECSA). We found that solution-synthesized Pt/NiO core/shell nanowires can be converted into PtNi alloy nanowires through a thermal annealing process and then transformed into jagged Pt nanowires via electrochemical dealloying. The jagged nanowires exhibit an ECSA of 118 square meters per gram of Pt and a specific activity of 11.5 milliamperes per square centimeter for ORR (at 0.9 volts versus reversible hydrogen electrode), yielding a mass activity of 13.6 amperes per milligram of Pt, nearly double previously reported best values. Reactive molecular dynamics simulations suggest that highly stressed, undercoordinated rhombus-rich surface configurations of the jagged nanowires enhance ORR activity versus more relaxed surfaces.

Platinum (Pt) represents the essential element for catalyzing the oxygen reduction reaction (ORR) (1–3). However, the high cost of Pt is the primary limiting factor preventing the widespread adoption of fuel cells that critically depend on ORR (4, 5). Therefore, higher Pt mass activity—the catalytic activity per given mass of Pt—must be achieved to reduce the required platinum usage. The Pt mass activity is determined by the specific activity (normalized by surface area) and the electrochemically active surface area (ECSA, normalized by mass). The specific activity can be optimized by tuning the chemical environment, including chemical composition (6–9), exposed catalytic surface (1, 10–12), and Pt coordination environment (13–16). To date, the highest specific activities have generally been achieved on single-crystal surfaces or well-defined nanoparticles (NPs) with specifically engineered facet structure and alloy

compositions. For example, the Pt₃Ni (111) single-crystal facet (1) and Pt₃Ni octahedral NPs have been shown to exhibit ORR-favorable surface structure for greatly enhanced activity (17–19), but such alloys typically suffer from insufficient stability because of electrochemical leaching of Ni during electrochemical cycling, as well as decreased ECSA because of agglomeration of the NPs. Introduction of Mo surface dopants can mitigate such leaching processes and help maintain the ORR-favorable Pt₃Ni (111) surface for enhanced activity and stability (19). On the other hand, ECSA may be improved by tailoring the geometrical factors through the creation of ultrafine nanostructures (20, 21) or core/shell nanostructures with an ultrathin Pt skin (22–24) that exposes most Pt atoms on the surface. Although high surface areas have been achieved on these structures, the reported ECSA values for these optimized structures are typically limited to ~70 m²/g_{Pt}.

To boost Pt mass activity and Pt utilization efficiency, an ideal catalyst should have an ORR-favorable chemical environment for high specific activity, optimized geometric factors for high ECSA (20–24), and a mechanism to maintain these high values for long periods of operation. We report the preparation of ultrafine jagged Pt nanowires (J-PtNWs) with rich ORR-favorable rhombic configurations that lead to a specific activity of 11.5 mA/cm² [at 0.9 V versus RHE (reversible hydrogen electrode)] and an ECSA of 118 m²/g_{Pt}. Together, these J-PtNWs deliver a mass activity of 13.6 A/mg_{Pt} (at 0.9 V versus RHE), which is ~50 times that of the state-of-the-art commercial Pt/C catalyst and nearly double the highest previously reported mass activity values of 6.98 A/mg_{Pt} (19) and 5.7 A/mg_{Pt} (23).

We prepared Pt/NiO core/shell nanowires by reducing platinum (II) acetylacetonate [Pt(acac)₃] and nickel(II) acetylacetonate [Ni(acac)₃] in a mixture solvent of 1-octadecene and oleylamine (25). Transmission electron microscopy (TEM) showed that the as-synthesized nanowires exhibit an apparent core/shell structure with a contrast of darker core and lighter shell. The nanowires have a typical overall diameter of ~5 nm or less, and a length of ~250 to 300 nm (Fig. 1A and fig. S1A). High-resolution TEM (HRTEM) confirmed the core/shell structure with a typical core diameter of 2.0 ± 0.2 nm (Fig. 1D). The shell shows well-resolved lattice fringes with a spacing of 0.24 nm,

¹Department of Chemistry and Biochemistry, University of California, Los Angeles, CA 90095, USA. ²Department of Materials Science and Engineering, University of California, Los Angeles, CA 90095, USA. ³Materials and Process Simulation Center, California Institute of Technology, Pasadena, CA 91125, USA. ⁴CNR-ICCOM, Consiglio Nazionale delle Ricerche, 56124 Pisa, Italy. ⁵National Center for Electron Microscopy in Beijing, School of Materials Science and Engineering, Tsinghua University, Beijing 100084, P. R. China. ⁶Institute of Physics, Chinese Academy of Sciences, Beijing 100190, P. R. China. ⁷Department of Chemical Engineering, California State University, Long Beach, CA 90840, USA. ⁸Department of Chemistry and Chemical Biology, Northeastern University, Boston, MA 02115, USA. ⁹Advanced Light Source, Lawrence Berkeley National Laboratory, Berkeley, CA 94720, USA. ¹⁰California NanoSystems Institute, University of California, Los Angeles, CA 90095, USA.

*Corresponding author. Email: wag@wag.caltech.edu (W.A.G.); yhuang@seas.ucla.edu (Y.H.); xduan@chem.ucla.edu (X.D.)

corresponding to the (111) interplanar distance of face-centered cubic (fcc) NiO (Fig. 1D), and the core displays a primary lattice spacing of 0.23 nm, corresponding to Pt (111) planes (Fig. 1D).

These Pt/NiO nanowires were then loaded onto carbon black and annealed in an argon/hydrogen mixture (Ar/H₂: 97/3) at 450°C to produce PtNi alloy nanowires. The overall morphology of the nanowire was maintained without obvious change in length or diameter, but the apparent core/shell contrast disappeared (Fig. 1B), suggesting the formation of uniform PtNi alloy nanowires. The HRTEM image of the annealed nanowire confirms a uniform contrast with a well-resolved lattice spacing of 0.21 nm throughout the entire nanowire diameter (Fig. 1E), consistent with the (111) lattice spacing of the PtNi alloy. This evolution, from the initial core/shell nanowires before annealing to uniform alloy nanowires after annealing, was also confirmed by high-angle annular dark-field scanning transmission electron microscope (HAADF-STEM) studies (fig. S1, C and D).

Our energy-dispersive x-ray (EDX) spectroscopy elemental analysis shows that the overall Pt/Ni ratio remained essentially the same (Pt/Ni: 15/85) before and after annealing (fig. S3, A and B). The EDX spectroscopy line scan profile of the as-prepared nanowires also confirms the core/shell structure with a Pt core (Fig. 1G) that diffuses homogeneously throughout the entire nanowire after annealing (Fig. 1H). X-ray diffraction (XRD) studies also confirm the evolution of the initial Pt/NiO core/shell configurations into a fully alloyed PtNi nanowire structure (fig. S4). Furthermore, x-ray photoelectron spectroscopy (XPS) studies demonstrate that the nickel valence state changed from Ni²⁺ in the Pt/NiO core/shell nanowires to mostly Ni⁰ after annealing, consistent with the formation of PtNi alloy (fig. S5).

We believe that the nanowire geometry is essential for ensuring the thermal stability of these ultrafine nanowires under high-temperature annealing. For example, a similar thermal annealing process applied to ultrafine PtNi NPs led to substantial aggregation of the NPs (a size increase from ~7 nm to aggregates of 10 to 30 nm) (fig. S2), which could be partly attributed to the movement and fusion of NPs. In contrast, nanowires supported on carbon black have multiple anchoring points and their mobility is much lower than that of NPs with a single point contact on a carbon support.

We used an electrochemical dealloying (leaching) process to gradually remove Ni atoms from the PtNi alloy nanowires, which allowed the rearrangement of Pt atoms on the surface to form the J-PtNWs. We performed cyclic voltammetry (CV) in N₂-saturated 0.1 M HClO₄ solution (0.05 V to 1.1 V versus RHE) with a sweep rate of 100 mV s⁻¹ (Fig. 2A). With the CV curves, the ECSA_{H_{upd}} was derived from the H_{upd} adsorption/desorption peak areas (0.05 V < E < 0.35 V) normalized by the total mass of the loaded Pt. The PtNi alloy nanowires initially showed an essentially negligible ECSA_{H_{upd}} during the first CV cycle. The ECSA_{H_{upd}} increased steadily with the increasing number of

CV cycles (Fig. 2B). The nanowires were fully activated in ~160 CV cycles to reach a stable ECSA_{H_{upd}} up to 118 m²/g_{Pt}, whereas the previous highest reported values were ~70 m²/g_{Pt} (Table 1).

Structural and elemental studies were performed to characterize the fully activated nanowires after CV cycles. Low-resolution TEM images show that the overall nanowire structure was well maintained

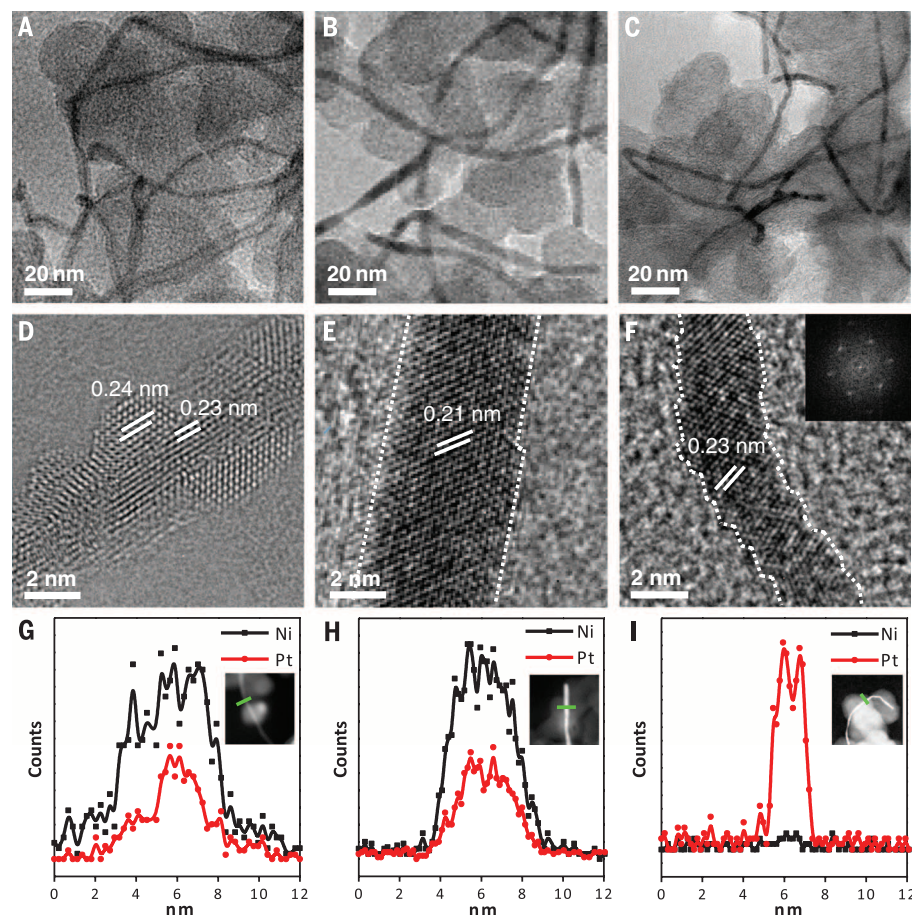


Fig. 1. Structure and composition characterization of different stages of the J-PtNW evolution process. (A to F) Representative TEM images (A to C) and HRTEM images (D to F) of the Pt/NiO core/shell nanowires, the PtNi alloy nanowires, and the J-PtNWs supported on carbon, respectively. The inset in (F) shows the corresponding FFT image. The dashed lines in (E) and (F) show the outline of the nanowires, highlighting the rough surface of the J-PtNWs. (G to I) EDX spectroscopy line-scan profiles of the corresponding nanowires show clearly the evolution from the Pt/NiO core/shell to PtNi alloy and then to pure PtNWs.

Table 1. Electrochemically active surface area (ECSA), specific activity, half-wave potential, and mass activity of J-PtNWs/C, R-PtNWs/C, and Pt/C catalysts, in comparison to those in several representative recent studies. NA, not applicable.

	ECSA (m ² /g _{Pt})	Specific activity (mA/cm ²) at 0.90 V	Half-wave potential (V)	Mass activity at 0.90 V	(A/mg _{Pt}) at 0.935 V
J-PtNWs/C (this work)	118	11.5	0.935	13.6	2.87
R-PtNWs/C (this work)	110	1.59	0.899	1.76	0.5
Pt/C (this work)	74	0.35	0.860	0.26	0.06
Octahedron Pt _{2.5} Ni/C (17)	21	NA	NA	3.3	NA
Nanoframe Pt ₃ Ni/C (23)	67.2	NA	NA	5.7	NA
Mo-Pt ₃ Ni/C (19)	67.7	10.3	NA	6.98	NA
DOE 2017 target	NA	NA	NA	0.44	NA

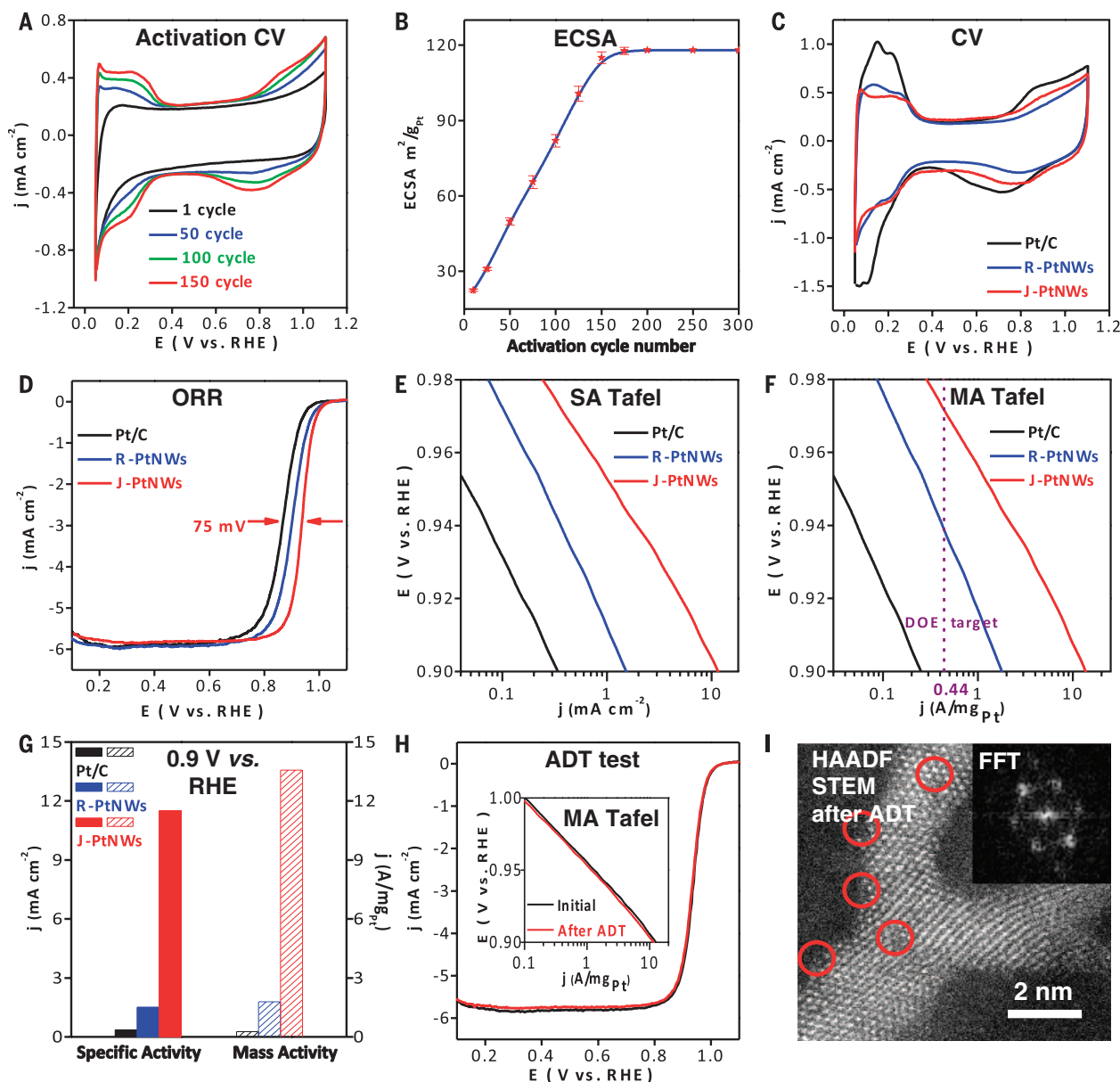


Fig. 2. Electrochemical performance of the jagged PtNWs (J-PtNWs) versus regular synthetic PtNWs (R-PtNWs) and commercial Pt/C catalyst.

(A) Cyclic voltammetry (CV) curves corresponding to different activation cycles of the dealloying process, clearly indicating the increasing surface area with increasing number of CV cycles. (B) The evolution of ECSA with increasing number of CV cycles, showing that 160 cycles are sufficient to construct the J-PtNW and reach a stable ECSA. (C and D) CV and ORR polarization curves for the J-PtNWs, R-PtNWs, and Pt/C catalyst, respectively. (E and F) Specific activity (SA) and mass activity (MA) Tafel plot for the J-PtNWs, R-PtNWs, and Pt/C catalyst, respectively. The purple dashed line indicates the 2017 mass

activity target (at 0.90 V versus RHE) set by DOE. (G) Comparison of specific activities and mass activities of the J-PtNWs, R-PtNWs, and Pt/C catalyst at 0.9 V versus RHE, showing that the J-PtNWs deliver 33 times the specific activity or 52 times the mass activity of the Pt/C catalyst. (H) ORR polarization curves and mass activity Tafel plot (inset) for the J-PtNWs before and after 6000 CV cycles between 0.6 and 1.0 V versus RHE, showing little loss in activity. The scan rate for the accelerated durability test (ADT) is 100 mV s⁻¹. (I) High-resolution HAADF-STEM image of the J-PtNWs after ADT. The circled areas indicate defective regions with missing atoms. The inset shows the corresponding FFT image.

after the electrochemical dealloying process (Fig. 1C). The HRTEM images show that the overall diameter of the nanowire shrank from ~5.0 nm to ~2.2 nm after the CV cycles, with well-resolved lattice spacing of 0.23 nm, again consistent with Pt (111) (Fig. 1F). The EDX spectroscopy line scan showed that Pt was the only dominant element in the resulting nanowires (Fig. 1I), further confirming complete Ni leaching. In addition, the

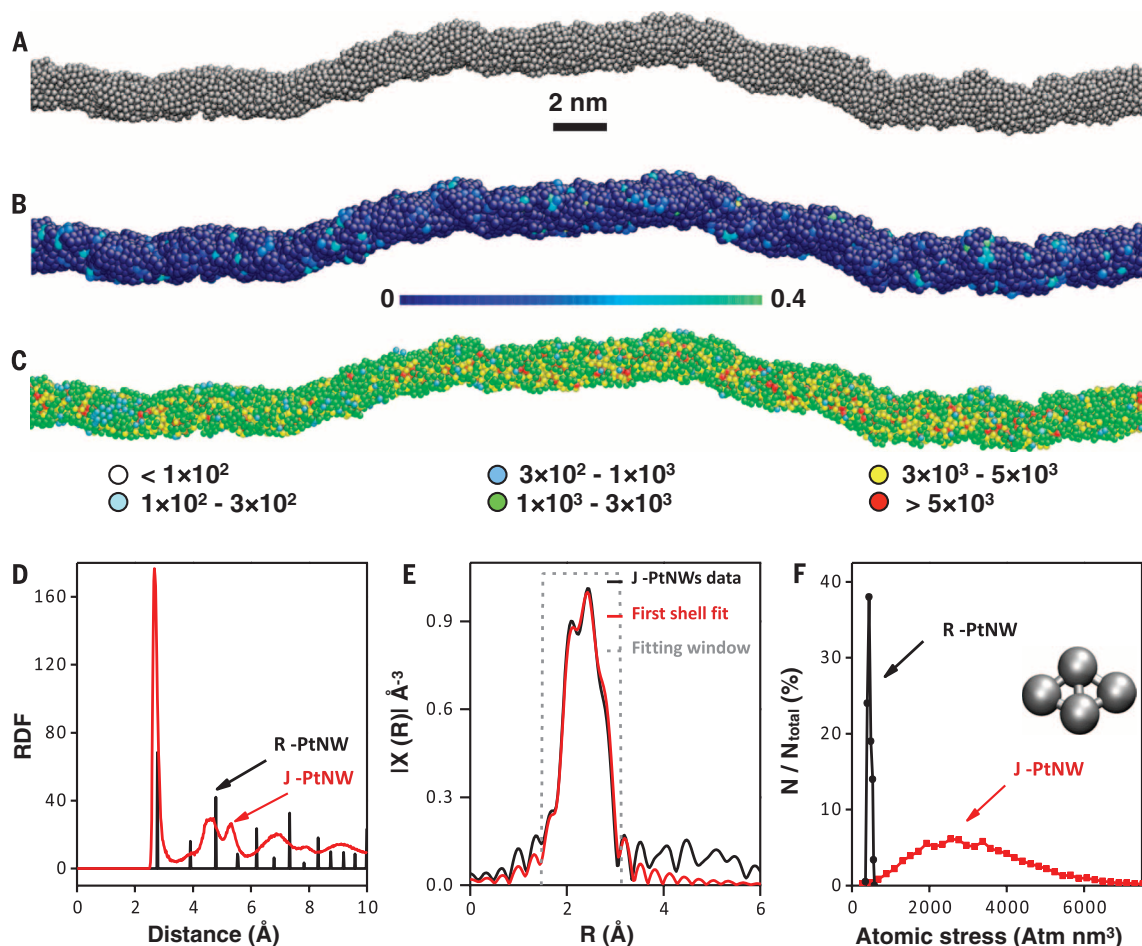
CV scan of the fully activated nanowires (after 160 CV cycles) in 0.1 M KOH showed an absence of typical Ni²⁺/Ni³⁺ redox signatures, in contrast to the partially activated (150 cycles) PtNi alloy nanowires in which the Ni²⁺/Ni³⁺ redox peaks were prominent (fig. S6). We also conducted a CO-stripping experiment to determine the ECSA_{CO} of J-PtNWs (fig. S7). The resulting ratio of ECSA_{H₂O}:ECSA_{CO} is 1.00:1.05, which is in agreement with that

of typical pure Pt material (10). Furthermore, TEM studies of the dealloyed nanowires also showed a highly jagged surface (Fig. 1, C and F) with rich atomic steps, in contrast to the relatively smooth surface observed in typical synthetic PtNWs (fig. S1B). On the basis of these observations, we denote the resulting nanowires as J-PtNWs.

The electrocatalytic performance of the resulting nanowires was compared with a commercial

Fig. 3. Structural analysis of the J-PtNWs obtained from ReaxFF reactive molecular dynamics and x-ray absorption spectroscopy.

(A) Pictorial illustrations of the final structure of a J-PtNW generated by reactive molecular dynamics simulations, with an average diameter of ~ 2.2 nm and length of ~ 46 nm. **(B)** J-PtNW with colored atoms to show the five-fold index. **(C)** J-PtNW with colored atoms to show distribution of atomic stress (in $\text{atm}\cdot\text{nm}^3$). **(D)** Pt-Pt radial distribution function (RDF) of the SMA-predicted J-PtNW (red) compared with the peaks of the RDF for the regular PtNW (black). **(E)** Pt L_3 edge FT-EXAFS spectrum (black) collected ex situ and the corresponding first-shell least-squares fit (red) for the J-PtNWs. **(F)** Distribution of the absolute values of the average atomic stress on surface rhombi for the R-PtNWs (black) and the J-PtNWs (red). A rhombus is an ensemble of four atoms arranged as two equilateral triangles sharing one edge, as shown in the inset.



Pt/C catalyst (10% mass loading of ~ 3 - to 5-nm Pt NPs on carbon support) and directly synthesized regular PtNWs (R-PtNWs, diameter ~ 1.8 nm; fig. S1B) with a relatively smooth surface (25). To assess ORR activity, we loaded all catalysts onto glassy carbon electrodes (Pt mass loading: $2.2 \mu\text{g}/\text{cm}^2$ for J-PtNWs, $2.55 \mu\text{g}/\text{cm}^2$ for R-PtNWs, and $7.65 \mu\text{g}/\text{cm}^2$ for Pt/C catalyst). We used CV to measure the ECSA (Fig. 2C). Overall, the J-PtNWs, R-PtNWs, and Pt/C catalyst showed ECSA values of 118, 110, and $74 \text{ m}^2/\text{g}_{\text{Pt}}$, respectively (Table 1). The synthetic R-PtNWs also exhibited a rather high ECSA that may be related to their ultrasmall diameters (~ 1.8 nm).

Figure 2D shows the ORR polarization curves normalized by glassy carbon electrode geometric area (0.196 cm^2). The half-wave potential for the J-PtNWs was 0.935 V , which is considerably higher than those of the commercial Pt/C catalyst (0.86 V) and the R-PtNWs (0.90 V), suggesting excellent ORR activity of the J-PtNWs. The Koutecky-Levich equation was used to calculate the kinetic current by considering the mass-transport correction. The specific and mass activities were normalized by the ECSA or the total mass of the loaded Pt, respectively. Overall, the J-PtNWs showed a specific activity of $11.5 \text{ mA}/\text{cm}^2$ at 0.90 V versus RHE, far higher than $0.35 \text{ mA}/\text{cm}^2$ for the Pt/C catalyst or

$1.59 \text{ mA}/\text{cm}^2$ for the R-PtNWs tested under the same conditions (Table 1). Together with their ultrahigh specific surface area, the J-PtNWs deliver a high mass activity of $13.6 \text{ A}/\text{mg}_{\text{Pt}}$ at 0.9 V versus RHE, which is 52 times that of the 10 weight percent Pt/C ($0.26 \text{ A}/\text{mg}_{\text{Pt}}$) and more than 7 times that of the R-PtNWs ($1.76 \text{ A}/\text{mg}_{\text{Pt}}$) (Fig. 2G and Table 1). The mass activity achieved in the J-PtNWs is nearly double the highest previously reported mass activity value of $6.98 \text{ A}/\text{mg}_{\text{Pt}}$ (19) and $5.7 \text{ A}/\text{mg}_{\text{Pt}}$ (23). This observed mass activity was highly reproducible and was between 10.8 and $13.8 \text{ A}/\text{mg}_{\text{Pt}}$ in >15 independently tested J-PtNW electrodes.

Because the current at 0.90 V is already near the diffusion-limited current in the ORR polarization curve, we also compared mass activity at half-wave potential of the J-PtNWs (0.935 V) in Table 1. Our analysis shows that the J-PtNWs still exhibited a mass activity 48 times that of the Pt/C catalyst. The Tafel plots of specific activity (Fig. 2E) exhibit slopes of 51, 72, and $74 \text{ mV}/\text{decade}^{-1}$ for the J-PtNWs, R-PtNWs, and Pt/C catalyst, respectively. A considerably smaller slope achieved in the J-PtNWs suggests significantly improved kinetics for ORR. Remarkably, the mass activity Tafel plot (Fig. 2F) shows that the J-PtNWs deliver mass activity 30 times the 2017 target set by

the U.S. Department of Energy (DOE) ($0.44 \text{ A}/\text{mg}_{\text{Pt}}$ at 0.90 V for MEA, highlighted by purple dashed line in Fig. 2F). The J-PtNWs can deliver the DOE targeted mass activity at 0.975 V (RHE), thus reducing the overpotential by 0.075 V .

We evaluated the durability of the J-PtNWs using accelerated deterioration tests (ADT) under a sweep rate of 100 mV s^{-1} between 0.6 V and 1.0 V in O_2 saturated 0.1 M HClO_4 . After 6000 cycles, the ECSA dropped by only $\sim 7\%$, the specific activity dropped by only $\sim 5.5\%$, and together the mass activity dropped by only 12% (Fig. 2H). The retention of high ECSA in J-PtNWs during ADT is in stark contrast to that of the Pt/C catalyst, which showed a much larger loss ($\sim 30\%$) in ECSA during similar ADTs. Ultrafine nanostructures (e.g., $\sim 2 \text{ nm}$) have shown severely worse stability relative to their bulk counterpart (26, 27) due to movement, aggregation, and Ostwald ripening processes. The unique one-dimensional geometry of nanowires and the multipoint contacts with the carbon support might reduce such movement and aggregation, and might also deter the Ostwald ripening process usually observed in spherical NPs (fig. S8), thereby contributing to the excellent durability. Indeed, our TEM studies before and after ADT showed little change in the

overall morphology or size of the J-PtNWs on the carbon support (fig. S9). High-resolution STEM studies showed that the jagged surface (with defective sites) was largely preserved after 6000 cycles (Fig. 2I).

The above results demonstrate that the J-PtNWs exhibit ultrahigh specific surface area and specific activity, together delivering a record-high mass activity for ORR. Notably, the J-PtNWs exhibit considerably higher specific activity and mass activity (11.5 mA/cm^2 or $13.6 \text{ A/mg}_{\text{Pt}}$ at 0.9 V) than those of R-PtNWs (1.59 mA/cm^2 or $1.76 \text{ A/mg}_{\text{Pt}}$ at 0.9 V), despite similar ECSA values ($118 \text{ m}^2/\text{g}_{\text{Pt}}$ for 2.2-nm J-PtNWs, $110 \text{ m}^2/\text{g}_{\text{Pt}}$ for 1.8-nm R-PtNWs). Relative to the Pt/C catalyst, the J-PtNWs show a factor of 33 increase in specific activity at 0.90 V versus RHE, which suggests that the activation energy for the rate-determining step of ORR on the J-PtNWs is reduced by 0.090 eV from that of the Pt/C catalyst [$\Delta E_{\text{act}} = k_B T \ln(SA_{\text{J-PtNW}}/SA_{\text{Pt/C}})$, where ΔE_{act} is the difference in activation energy, k_B is Boltzmann's constant, T is temperature, $SA_{\text{J-PtNW}}$ is the specific activity of J-PtNWs, and $SA_{\text{Pt/C}}$ is the specific activity of the Pt/C catalyst]. This decrease is plausible according to our various ORR computations (16).

To gain further insight on how the J-PtNWs could deliver substantially higher ORR activity, we conducted reactive molecular dynamics (RMD) studies using the reactive force field (ReaxFF) (28) to simulate the formation of J-PtNWs by leaching Ni atoms from initially $\text{Pt}_{15}\text{Ni}_{85}$ alloy nanowires (16), as well as a second moment approximation (SMA) tight-binding potential (29) for final local optimization and prediction of Pt-Pt distances (25). The RMD simulation resulted in a pure PtNW containing 7165 Pt atoms (in a length of $\sim 46 \text{ nm}$) with a diameter of $\sim 2.2 \text{ nm}$ and a highly jagged surface (Fig. 3A). Notably, the overall morphology of the predicted J-PtNWs resembles closely the experimentally obtained J-PtNWs as shown in TEM images in Fig. 1, both of which show modulating thread-like segments $\sim 2.2 \text{ nm}$ in diameter containing striction regions, bending points, and jagged surfaces.

The predicted radial distribution function for the J-PtNW exhibits a well-defined first-neighbor peak at about 2.70 \AA (Fig. 3D), which is ~ 2.2 to 2.5% shorter than the Pt-Pt first-neighbor distance predicted for the R-PtNWs (2.76 \AA) and the bulk Pt crystal (2.77 \AA), whereas the peaks associated with the second and farther neighbors are much broader and more blurred, similar to those reported in nanoporous NPs (16). These predicted Pt-Pt first-neighbor distances are well confirmed by the EXAFS analysis (Fig. 3E, fig. S10, and table S1), which reveals that the first-shell Pt-Pt bond length in the J-PtNWs (2.71 \AA) is $\sim 1.8\%$ shorter than that of the Pt foil (2.76 \AA).

Nanowires with small diameters ($\sim 2.2 \text{ nm}$ in this case) inherently have ultrahigh surface area that can be further enhanced by the surface roughness of a jagged morphology. We calculated the van der Waals surface area of the simulated J-PtNWs to be $\sim 110 \text{ m}^2/\text{g}_{\text{Pt}}$ (table S2), which agrees well with our experimental value derived from the ECSA ($118 \text{ m}^2/\text{g}_{\text{Pt}}$). However, the enhancement

of surface area alone cannot fully account for the observed ORR mass activity. Stressed and undercoordinated crystalline-like surface rhombi can markedly decrease the reaction barrier of the rate-determining steps of ORR, thus improving specific ORR activity (16). Surface rhombi are ensembles of four atoms arranged as two equilateral triangles sharing one edge (see the inset in Fig. 3F) and resembling the triangular tessellation of an fcc (111) surface, which we find to be superior to a square tessellation for ORR activity in the same way that the fcc (111) surface is more ORR-active than other compact fcc surfaces such as fcc (100) (1, 30). Moreover, rhombi that are stressed and undercoordinated but still crystalline-like exhibit smaller overall energy barriers for ORR than those encountered on the rhombi of the fcc (111) surface, as predicted via density functional theory calculations (16).

Several factors could contribute to the greatly enhanced ORR activity in the J-PtNWs:

(i) Our analysis shows that the coordination number of surface atoms in the J-PtNWs ranges mostly between 6 and 8 (fig. S11A), indicating that these surface atoms are undercoordinated relative to typical crystal surfaces [with coordination numbers of 8 or 9 for (100) or (111) facets, respectively]. Despite the low coordination number and jagged features, the crystalline-like character of surface atoms in J-PtNWs is confirmed from common neighbor analysis (CNA) (31–33), which shows that the ratio of CNA [5, 5, 5] triplets (a marker of icosahedral structure) (29, 34) to the total number of CNA triplets is rather low (84% of the atoms have a ratio below 0.0065) (Fig. 3B). Because the bonded pairs of type [5, 5, 5] are characteristic of icosahedral order, this low [5, 5, 5] ratio indicates a more crystalline-like feature (32) for our established model, which is also a crucial factor for enhancing ORR activity (16). Indeed, such crystalline-like character in our simulation model is consistent with the experimental fast Fourier transform (FFT) images (insets in Fig. 1F and Fig. 2I) showing that the J-PtNWs remain fcc-like after CV activation and repeated cycling. Additionally, the distribution of rhombus dihedral angles (fig. S11B) shows that most of the dihedral angles formed between the two triangles of the rhombus are in the range of 156° to 180° . Given the 180° dihedral angle for typical crystalline Pt (111) facets, this statistical analysis further confirms the high-crystallinity nature of the J-PtNWs, which is favorable for increased reactivity (16).

(ii) The surface atoms in the J-PtNWs exhibit rather high values of Cauchy atomic stress times atomic volume, about 10 times that for regular (100) or (111) facets (Fig. 3, C and F), as also confirmed by simulated and EXAFS-derived Pt-Pt distances (Fig. 3, D and E). Moreover, the ReaxFF surface energy of the J-PtNW is 2.7 J/m^2 , which exceeds the value for the Pt(111) surface (1.7 J/m^2); this latter ReaxFF value is in very good agreement with quantum mechanics and experimental values. This mechanical strain can decrease the binding energy of adsorbents on close-packed surfaces, which can make the surfaces more active (32, 35, 36), further contributing to the activity enhancement.

(iii) We found that the J-PtNWs possess a large ECSA (table S2) and also exhibit an unusually high number of the ORR-favorable rhombic structures on the surface. There are 76% rhombi per surface atom in the J-PtNW surface (table S2), considerably higher than the 57% previously reported for the nanoporous Pt-NPs (16).

Because Ni is sacrificial in the process of forming pure J-PtNWs, other sacrificial elements may also be selectively removed from their alloys through electrochemical, chemical, or thermal dealloying processes to result in jagged surfaces with improved catalytic activity. We also prepared similar J-PtNWs by electrochemical dealloying PtCo nanowires and achieved an ORR activity of $8.1 \text{ A/mg}_{\text{Pt}}$ (figs. S12 and S13), which exceeds the highest number reported previously ($6.98 \text{ A/mg}_{\text{Pt}}$). We attribute the lower mass activity relative to PtNi-derived J-PtNWs to the slightly larger diameter of the resulting nanowires (~ 2.5 versus $\sim 2.2 \text{ nm}$), leading to a smaller ECSA ($92 \text{ m}^2/\text{g}_{\text{Pt}}$ versus $118 \text{ m}^2/\text{g}_{\text{Pt}}$) and possibly to differences in the dealloying mechanism of Co with respect to Ni. These studies further demonstrate the validity and generality of our approach to deriving highly ORR-active J-PtNWs from alloy nanowires.

REFERENCES AND NOTES

1. V. R. Stamenkovic et al., *Science* **315**, 493–497 (2007).
2. N. S. Porter, H. Wu, Z. Quan, J. Fang, *Acc. Chem. Res.* **46**, 1867–1877 (2013).
3. J. Wu, H. Yang, *Acc. Chem. Res.* **46**, 1848–1857 (2013).
4. Y. J. Wang et al., *Chem. Rev.* **115**, 3433–3467 (2015).
5. Z. Peng, H. Yang, *Nano Today* **4**, 143–164 (2009).
6. D. Wang et al., *Nat. Mater.* **12**, 81–87 (2013).
7. C. Wang et al., *Adv. Funct. Mater.* **21**, 147–152 (2011).
8. D. F. van der Vliet et al., *Nat. Mater.* **11**, 1051–1058 (2012).
9. V. R. Stamenkovic et al., *Nat. Mater.* **6**, 241–247 (2007).
10. D. F. van der Vliet et al., *Angew. Chem. Int. Ed.* **51**, 3139–3142 (2012).
11. C. Cui, L. Gan, M. Heggen, S. Rudi, P. Strasser, *Nat. Mater.* **12**, 765–771 (2013).
12. V. R. Stamenkovic, B. S. Mun, K. J. J. Mayrhofer, P. N. Ross, N. M. Marković, *J. Am. Chem. Soc.* **128**, 8813–8819 (2006).
13. F. Calle-Vallejo, J. I. Martínez, J. M. García-Lastra, P. Sautet, D. Loffreda, *Angew. Chem. Int. Ed.* **53**, 8316–8319 (2014).
14. F. Calle-Vallejo et al., *Science* **350**, 185–189 (2015).
15. M. Escudero-Escribano et al., *Science* **352**, 73–76 (2016).
16. A. Fortunelli et al., *Chem. Sci.* **6**, 3915–3925 (2015).
17. S. Choi et al., *Nano Lett.* **13**, 3420–3425 (2013).
18. X. Huang et al., *Energy Environ. Sci.* **7**, 2957–2962 (2014).
19. X. Huang et al., *Science* **348**, 1230–1234 (2015).
20. H. Zhu, S. Zhang, S. Guo, D. Su, S. Sun, *J. Am. Chem. Soc.* **135**, 7130–7133 (2013).
21. S. Guo et al., *Angew. Chem. Int. Ed.* **52**, 3465–3468 (2013).
22. L. Zhang et al., *Science* **349**, 412–416 (2015).
23. C. Chen et al., *Science* **343**, 1339–1343 (2014).
24. S. Zhang et al., *J. Am. Chem. Soc.* **136**, 15921–15924 (2014).
25. See supplementary materials on Science Online.
26. L. Tang et al., *J. Am. Chem. Soc.* **132**, 596–600 (2010).
27. L. Tang, X. Li, R. C. Cammarata, C. Friesen, K. Sieradzki, *J. Am. Chem. Soc.* **132**, 11722–11726 (2010).
28. C. F. Sanz-Navarro et al., *J. Phys. Chem. A* **112**, 1392–1402 (2008).
29. F. Cleri, V. Rosato, *Phys. Rev. B* **48**, 22–33 (1993).
30. Y. Sha, T. H. Yu, B. V. Merinov, P. Shirvanian, W. A. Goddard III, *J. Phys. Chem. Lett.* **2**, 572–576 (2011).
31. D. Faken, H. Jonsson, *Comput. Mater. Sci.* **2**, 279–286 (1994).
32. S. Schnur, A. Groß, *Phys. Rev. B* **81**, 033402 (2010).
33. J. D. Honeycutt, H. C. Andersen, *J. Phys. Chem.* **91**, 4950–4963 (1987).

34. A. Stukowski, *Model. Simul. Mater. Sci. Eng.* **20**, 045021 (2012).
 35. M. F. Francis, W. A. Curtin, *Nat. Commun.* **6**, 6261 (2015).
 36. S. Zhang et al., *J. Am. Chem. Soc.* **136**, 7734–7739 (2014).

ACKNOWLEDGMENTS

Supported by DOE Office of Basic Energy Sciences, Division of Materials Science and Engineering, award DE-SC0008055 (X.D., M.L., and Z.L. for materials synthesis and characterizations); NSF grant CHE-1508692 (Y.H., Z.Z., and E.Z. for electrochemical studies); NSF grant CBET-

1512759 (W.A.G., A.F., B.V.M., and T.C. for theoretical computations); and National Natural Science Foundation of China project numbers 51525102, 51390475, and 51371102 (R.Y. for STEM studies). The Advanced Light Source is supported by the Office of Science, Office of Basic Energy Sciences, of DOE under contract DE-AC02-05CH11231. We thank M. A. Marcus for support during the acquisition of XAS data and C. Wu for help with EXAFS data analysis. The aberration-corrected TEM results were achieved (in part) using Titan 80-300 and JEM-ARM 200F. In this work we used the resources of the National Center for Electron Microscopy in Beijing. A patent application on this subject has been filed [UC case no. 2017-108-1-LA (102352-0512)].

SUPPLEMENTARY MATERIALS

www.sciencemag.org/content/354/6318/1414/suppl/DC1
 Materials and Methods
 Figs. S1 to S13
 Tables S1 and S2
 References (37–39)

18 April 2016; resubmitted 25 August 2016
 Accepted 26 October 2016
 Published online 17 November 2016
 10.1126/science.aaf9050

TORNADOES

More tornadoes in the most extreme U.S. tornado outbreaks

Michael K. Tippett,^{1,2*} Chiara Lepore,³ Joel E. Cohen^{4,5,6}

Tornadoes and severe thunderstorms kill people and damage property every year. Estimated U.S. insured losses due to severe thunderstorms in the first half of 2016 were \$8.5 billion (US). The largest U.S. effects of tornadoes result from tornado outbreaks, which are sequences of tornadoes that occur in close succession. Here, using extreme value analysis, we find that the frequency of U.S. outbreaks with many tornadoes is increasing and that it is increasing faster for more extreme outbreaks. We model this behavior by extreme value distributions with parameters that are linear functions of time or of some indicators of multidecadal climatic variability. Extreme meteorological environments associated with severe thunderstorms show consistent upward trends, but the trends do not resemble those currently expected to result from global warming.

In the United States, tornado outbreaks have substantial effects on human lives and property. Tornado outbreaks are sequences of six or more tornadoes that are rated F1 and greater on the Fujita scale or rated EF1 and greater on the Enhanced Fujita scale and that occur in close succession (1, 2). About 79% of tornado fatalities during the period 1972 to 2010

occurred in outbreaks (1), and 35 people died in U.S. tornado outbreaks in 2015. No significant trends have been found in either the annual number of reliably reported tornadoes (3) or of outbreaks (1). However, recent studies indicate increased variability in large normalized economic and insured losses from U.S. thunderstorms (4), increases in the annual number of

days on which many tornadoes occur (3, 5), and increases in the annual mean and variance of the number of tornadoes per outbreak (6). Here, using extreme value analysis, we find that the frequency of U.S. outbreaks with many tornadoes is increasing and that it is increasing faster for more extreme outbreaks. We model this behavior by extreme value distributions with parameters that are linear functions of time or of some indicators of multidecadal climatic variability. Extreme meteorological environments associated with severe thunderstorms show consistent upward trends, but the trends do not resemble those currently expected to result from global warming.

Linear trends in the percentiles of the number of tornadoes per outbreak (Fig. 1A) are positive, statistically significant, and increase exponentially faster with percentile probability (Fig. 1B). This behavior is consistent with the positive trends in

¹Department of Applied Physics and Applied Mathematics, Columbia University, New York, NY, USA. ²Center of Excellence for Climate Change Research, Department of Meteorology, King Abdulaziz University, Jeddah, Saudi Arabia. ³Lamont Doherty Earth Observatory, Columbia University, Palisades, NY 10964, USA. ⁴Laboratory of Populations, Rockefeller University, New York, NY 10065, USA. ⁵The Earth Institute and Department of Statistics, Columbia University, New York, NY 10027, USA. ⁶Department of Statistics, University of Chicago, Chicago, IL 60637, USA.
 *Corresponding author. Email: mkt14@columbia.edu

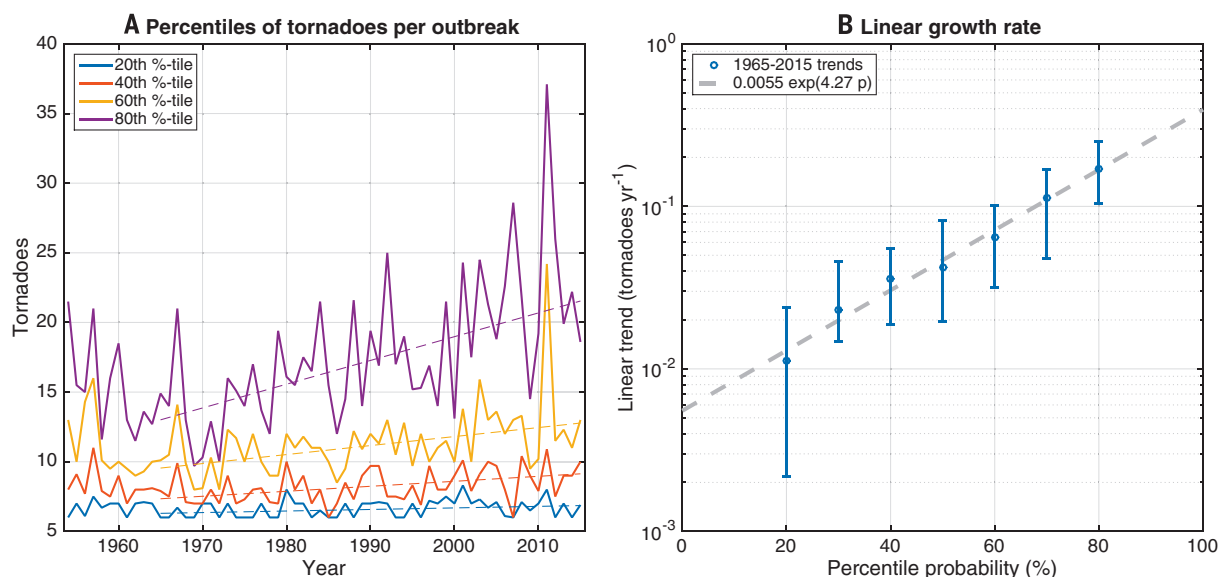


Fig. 1. Numbers of tornadoes per outbreak. (A) Annual 20th, 40th, 60th, and 80th percentiles of the number of E/F1+ tornadoes per outbreak (6 or more E/F1+ tornadoes), 1954 to 2015 (solid lines), and quantile regression fits to 1965 to 2015, assuming linear growth in time (dashed lines). (B) Linear growth rates as a function of percentile probability. Error bars are 95% bootstrap confidence intervals and indicate linear trends that are statistically significantly different from zero.

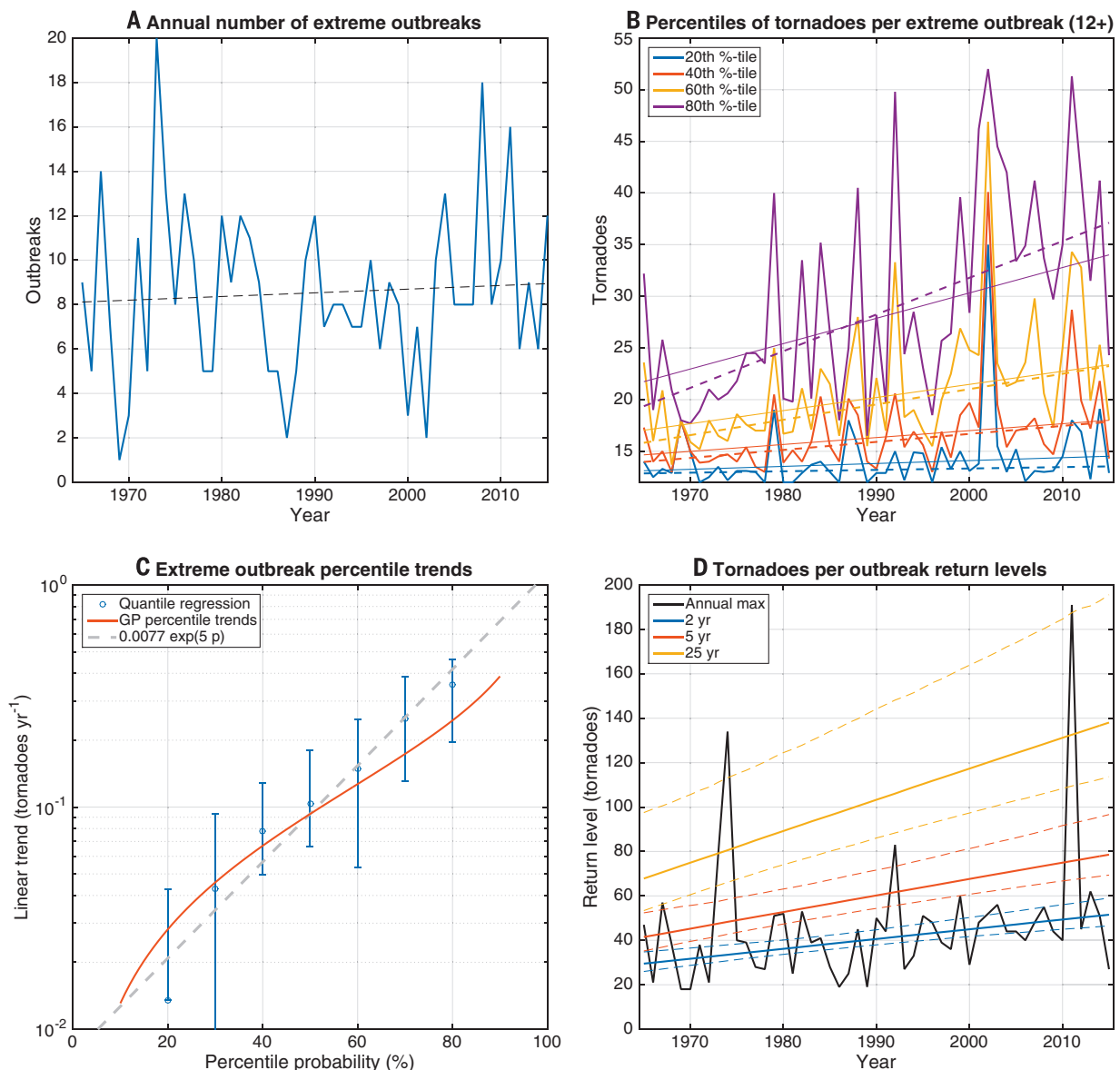


Fig. 2. Extreme outbreaks. (A) Annual number of extreme outbreaks (12 or more E/F1+ tornadoes). (B) Annual 20th, 40th, 60th, and 80th percentiles of the number of E/F1+ tornadoes per extreme outbreak, 1965 to 2015 (jagged solid lines), along with quantile regression lines (dashed lines) and percentiles of the GP distribution with a linear trend in the scale parameter (solid lines). (C) Quantile regression linear growth rates (slopes), along with 95% confidence intervals (blue) and corresponding growth rates of a GP distribution with linear trend in the scale parameter as functions of percentile probability (solid red line). (D) Annual maxima (black line), along with GP return levels as functions of year for return periods of 2, 5, and 25 years (solid colored lines), and 90% bootstrap confidence intervals (dashed lines).

mean and variance (6), which suggested that the distribution of the number of tornadoes per outbreak is shifting to the right (increasing mean) and that higher percentiles of the distribution are shifting faster than the mean (increasing variance). The increase of percentile trends with percentile probability is consistent with trends in the frequency of tornado days with many tornadoes increasing with threshold (5).

Nonstationary generalized extreme value (GEV) distributions with trends in their parameters do not reproduce the observed upward trend in the slopes of percentiles as a function of percentile probability (supplementary materials and fig. S1). Therefore, we use the Generalized Pareto (GP)

approach with a threshold of 12 E/F1+ tornadoes [(2) and fig. S2]. We refer to outbreaks with 12 or more E/F1+ tornadoes as “extreme outbreaks” (2). There were 435 extreme outbreaks from 1965 through 2015, no statistically significant trends in the annual number of extreme outbreaks ($P = 0.66$) (Fig. 2A), and no statistically significant autocorrelation in the numbers of tornadoes per extreme outbreak (fig. S2C). The GP distributions found here have shape parameter around 0.3 (finite mean and variance) and are lighter-tailed distributions than was found considering tornadoes per day (rather than outbreaks) and a threshold of one (Pareto shape parameter of 0.61, infinite mean and variance) (7).

The percentiles of the number of tornadoes per extreme outbreak (Fig. 2B) also have upward trends that are statistically significant (above the 30th percentile) and depend approximately exponentially on the percentile probability (Fig. 2C). Allowing a trend as a function of time in the GP threshold u would give percentile trends (slopes) that are the same for all percentiles, contrary to observation. Permitting a linear trend as a function of time in the scale $\tilde{\sigma}$ improves the fit to the data statistically significantly. According to this model, the scale parameter and the percentiles increase linearly with time (Table 1), and higher percentiles increase faster. The standardized quantile-quantile plot in fig. S3 shows

Table 1. Generalized Pareto distribution parameters. Distributions are fitted to the number of E/F1+ tornadoes per outbreak for outbreaks with 12 or more E/F1+ tornadoes. The negative log likelihood (NLL), maximum likelihood estimates, and their standard errors are indicated for each model. The likelihood ratio (LR) test *P* value compares nonstationary models with the stationary distribution.

	$\hat{\sigma}_0$	$\hat{\sigma}_1$	$\hat{\xi}_0$	$\hat{\xi}_1$
Stationary (NLL = 1449)				
Maximum likelihood estimates	7.6	–	0.3	–
Standard error estimates	0.621	–	0.067	–
$\hat{\sigma} = \hat{\sigma}_0 + \hat{\sigma}_1 t$ (NLL = 1440)				
LR <i>P</i> value = 2×10^{-5}				
Maximum likelihood estimates	4.73	0.12	0.26	–
Standard error estimates	0.736	0.029	0.062	–
$\hat{\xi} = \hat{\xi}_0 + \hat{\xi}_1 t$ (NLL = 1447)				
LR <i>P</i> value = 0.04				
Maximum likelihood estimates	7.48	–0.13	0.0066	–
Standard error estimates	0.61	–	0.088	0.0031
$\hat{\sigma} = \hat{\sigma}_0 + \hat{\sigma}_1 \times \text{AMO}$ (NLL = 1442)				
LR <i>P</i> value = 2×10^{-4}				
Maximum likelihood estimates	8.18	8.48	0.28	–
Standard error estimates	0.6531	2.2009	0.0626	–
$\hat{\sigma} = \hat{\sigma}_0 + \hat{\sigma}_1 \times \text{PDO}$ (NLL = 1449)				
LR <i>P</i> value = 0.3				
Maximum likelihood estimates	7.71	–0.52	0.29	–
Standard error estimates	0.63	0.54	0.067	–
$\hat{\sigma} = \hat{\sigma}_0 + \hat{\sigma}_1 \times \text{CONUS temperature}$ (NLL = 1444)				
LR <i>P</i> value = 0.001				
Maximum likelihood estimates	8.31	1.62	0.28	–
Standard error estimates	0.70	0.52	0.065	–

fairly good agreement between the data and the GP distribution, with a linear trend in its scale parameter as a function of time. Data quantiles exceed those of the model at high percentiles (standardized model quantile values of 3 to 4 in fig. S3), meaning that the model predicts that outbreaks with many tornadoes would occur more often than is observed. The difference between model and data quantiles falls within the range expected from sampling variability (fig. S3). We cannot reject the model on this basis.

The slopes of the percentiles of the GP distribution with a linear trend in its scale parameter are approximately exponential in the percentile probability and match well those estimated by quantile regression (Fig. 2C). The trends from quantile regression and from the nonstationary GP distribution deviate from exponential dependence on the percentile probability near the end points of 0% and 100% probability. Adding a trend to the scale parameter ξ results in a marginally statistically significant ($P = 0.04$) (Table 1) upward trend that is statistically insignificant when the largest value (in 2011) is withheld ($P = 0.1$) (table S2). The scale trends change little when

the outbreak value from 2011 is withheld (table S2). Return levels for 2-, 5-, and 25-year return periods are shown in Fig. 2D along with 90% bootstrap confidence intervals (5000 bootstrap samples with bias correction and acceleration). The estimated number of tornadoes in the 5-year most extreme outbreak roughly doubles from 40 in 1965 to nearly 80 in 2015.

The outbreak trends in the tornado report database may reflect changes in reporting rather than real properties of tornadoes (8). The environments associated with tornadoes and severe thunderstorms provide valuable evidence that is independent of report data for assessing the variability of severe convective storms (4, 9–13). We use a two-part environmental proxy for the number of tornadoes per outbreak (2, 6). Here, we define extreme environments as those with values of the outbreak proxy greater than 12, matching the extreme outbreak definition. The proxy is computed using reanalysis data (2) and depends on two factors, convective available potential energy (CAPE) and a measure of vertical wind shear, storm relative helicity (SRH). Modeling studies project that CAPE will increase in future

warmer climates (14, 15), and Elsner *et al.* (5) hypothesized that climate change and increases in CAPE could already be leading to more active areas of severe convection on days with tornadoes.

However, we find no statistically significant trends in the percentiles of CAPE conditional on extreme environments (Fig. 3A) nor in the percentiles of CAPE conditional on CAPE > 1 J kg^{–1} (not shown). On the other hand, there are statistically significant upward trends in the percentiles of SRH conditional on extreme environments (Fig. 3B), and these trends are the source of the trends in the percentiles of the outbreak number proxy (Fig. 3C). The linear growth rates (slopes) of the proxy for the number of tornadoes per extreme outbreak are approximately exponential in the percentile probabilities, like those for the number of tornadoes in extreme outbreaks, and have roughly the same range of values. Percentiles of environments (not extreme) conditional on the environmental occurrence proxy show the same qualitative behavior (fig. S5). Therefore, we cannot at present associate previously identified features of a warmer climate with the observed changes in our environmental proxy and, by extension, with the changes in tornado outbreak statistics.

The observed trends in the statistics of outbreaks and extreme environments may be related to low-frequency climate variability other than climate change. Multidecadal variability in U.S. tornado activity has been compared with sea surface temperature (SST)-forced variability (16). We explore the connection between multidecadal climate signals and outbreak statistics using a nonstationary GP distribution whose scale parameter is a linear function of the climate signal rather than time.

The Atlantic Multidecadal Oscillation (AMO) (17) affects North American climate, is characterized by variations in North Atlantic SST, and can be explained as an oceanic response to mid-latitude atmospheric forcing (18). The AMO shows multidecadal variability, increasing from about 1970 through the mid-2000s (fig. S4A). The GP distribution whose scale parameter is a linear function of the AMO index fits the data significantly better than the stationary GP distribution but not better than a linear time trend (Table 1).

Another important pattern of climate variability is the Pacific Decadal Oscillation (PDO) (19) (fig. S4B). The GP distribution whose scale parameter is a linear function of the PDO index does not fit the data significantly better than the stationary GP distribution (Table 1).

Contiguous U.S. (CONUS) annual average temperature is increasing, and that change has prompted investigations of changes in the U.S. tornado climatology (20). Taking the GP scale parameter to depend linearly on CONUS temperature gives a significantly better fit to the data than does the stationary GP distribution but not a better fit than the GP distribution with a scale parameter that depends linearly on either time or the AMO index (Table 1).

Many changes in U.S. tornado report statistics have been ascribed to changes in reporting practices, technology, and other nonmeteorological

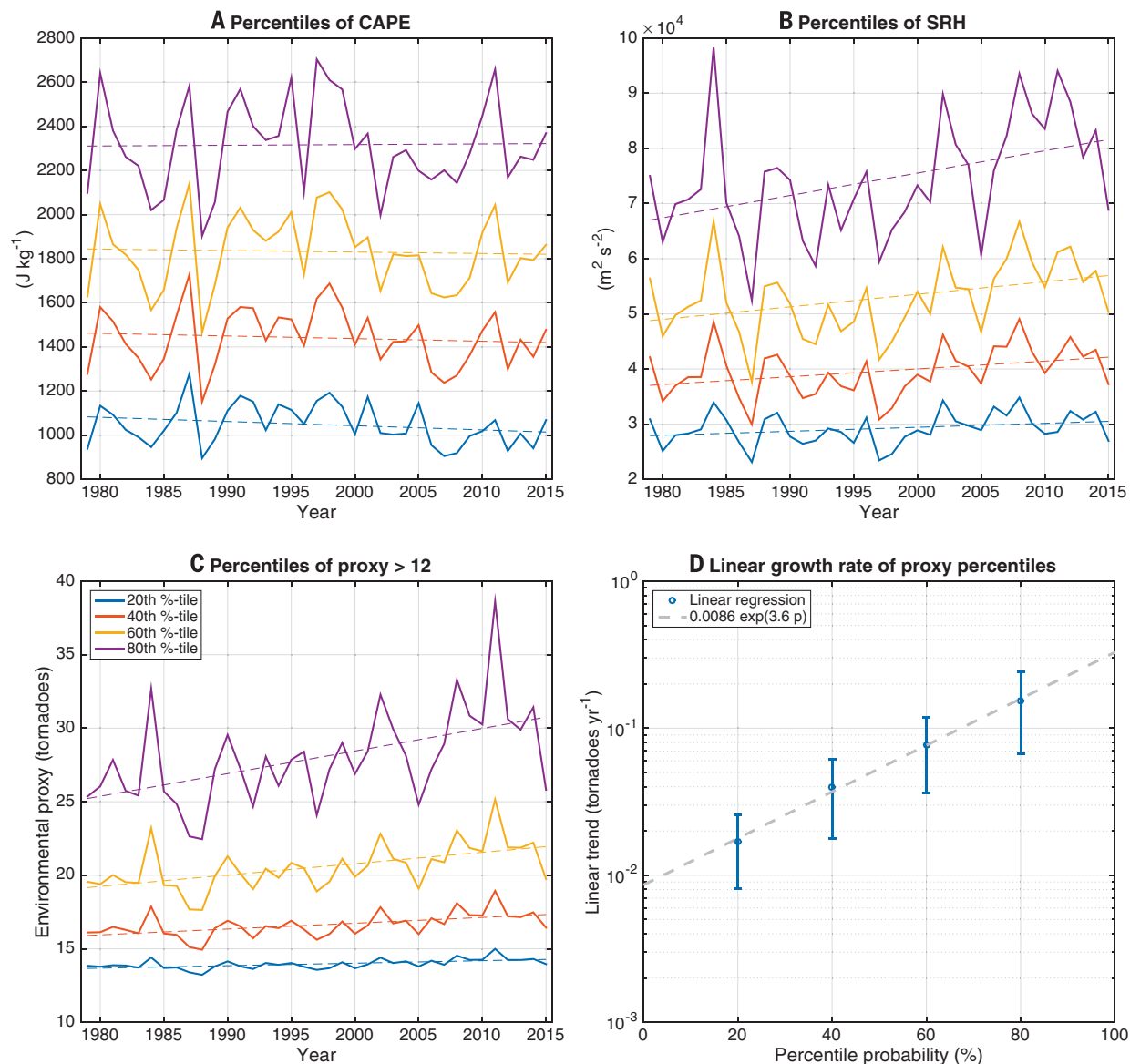


Fig. 3. Extreme environments. Percentiles of (A) CAPE and (B) SRH conditional on the proxy for the number of E/F1+ tornadoes per outbreak (see methods for definition) exceeding 12. (C) Percentiles of the proxy for the number of tornadoes per extreme outbreak. (D) Linear growth rate (ordinary least-squares estimates of slope and 95% confidence intervals) of the extreme outbreak proxy percentiles as a function of percentile.

factors (8). However, recent findings point to increases in the number of tornadoes per event, whether events are defined as days when tornadoes occur (3, 5) or as tornado outbreaks (6). Here, we found statistically significant upward trends in the higher percentiles of the number of tornadoes per outbreak. We modeled these trends using extreme value distributions with a time-varying scale parameter. Similar behavior in an environmental proxy suggested that the behavior of the tornado reports is not due simply to changes in reporting practice or technology.

Climate change has been proposed as contributing to changes in tornado statistics (5, 20). Climate model projections indicate that CAPE, one of the factors in our environmental proxy, will increase in a warmer climate, leading to more frequent environments favorable to severe thun-

derstorms in the United States (14, 15). However, the proxy trends here are not due to increasing CAPE but instead due to trends in SRH, a quantity related to vertical wind shear that was previously identified as a factor in increased year-to-year variability of U.S. tornado numbers (17). Therefore, we cannot at present associate the observed changes in our environmental proxy and, by extension, the changes in tornado outbreak statistics, with previously identified features of a warmer climate. This conclusion is, of course, subject to revision by the discovery of other implications of a warmer climate for severe thunderstorm environments.

The question of which climatic factors have driven the observed changes in tornado activity has important implications for the future. If global warming is changing tornado activity, then we might expect to see either continued increases in

the number of tornadoes per outbreak or at least no return to earlier levels. On the other hand, if multidecadal variability, anthropogenic or natural, is responsible, then a return toward earlier levels might be possible in the future. Further clouding the future, many of the outbreak measures (annual maximum and higher percentiles of the number of tornadoes per outbreak) reached their lowest values in more than a decade in 2015. As a final caveat, inferring tornadic activity solely from the environment has considerable uncertainty even in the current climate and at least as much in projected climates (21).

REFERENCES AND NOTES

1. C. M. Fuhrmann et al., *Weather Forecast.* **29**, 684–701 (2014).
2. Materials and methods are available as supplementary materials on Science Online.

3. H. E. Brooks, G. W. Carbin, P. T. Marsh, *Science* **346**, 349–352 (2014).
4. J. Sander, J. F. Eichner, E. Faust, M. Steuer, *Weather Clim. Soc.* **5**, 317–331 (2013).
5. J. B. Elsner, S. C. Elsner, T. H. Jagger, *Clim. Dyn.* **45**, 651–659 (2015).
6. M. K. Tippett, J. E. Cohen, *Nat. Commun.* **7**, 10668 (2016).
7. J. B. Elsner, T. H. Jagger, H. M. Widen, D. R. Chavas, *Environ. Res. Lett.* **9**, 024018 (2014).
8. S. M. Verbout, H. E. Brooks, L. M. Leslie, D. M. Schultz, *Weather Forecast.* **21**, 86–93 (2006).
9. H. E. Brooks, N. Dotzek, in *Climate Extremes and Society*, H. F. Diaz, R. Murnane, Eds. (Cambridge Univ. Press, New York, 2007), pp. 35–54.
10. E. D. Robinson, R. J. Trapp, M. E. Baldwin, *J. Appl. Meteorol. Climatol.* **52**, 2147–2161 (2013).
11. M. K. Tippett, *Geophys. Res. Lett.* **41**, 6956–6961 (2014).
12. J. T. Allen, M. K. Tippett, A. H. Sobel, *Nat. Geosci.* **8**, 278–283 (2015).
13. M. Lu, M. K. Tippett, U. Lall, *Geophys. Res. Lett.* **42**, 4224–4231 (2015).
14. R. J. Trapp, N. S. Diffenbaugh, A. Gluhovsky, *Geophys. Res. Lett.* **36**, L01703 (2009).
15. N. S. Diffenbaugh, M. Scherer, R. J. Trapp, *Proc. Natl. Acad. Sci. U.S.A.* **110**, 16361–16366 (2013).
16. S. J. Weaver, S. Baxter, A. Kumar, *J. Clim.* **25**, 6666–6683 (2012).
17. D. B. Enfield, A. M. Mestas-Núñez, P. J. Trimble, *Geophys. Res. Lett.* **28**, 2077–2080 (2001).
18. A. Clement *et al.*, *Science* **350**, 320–324 (2015).
19. N. J. Mantua, S. R. Hare, Y. Zhang, J. M. Wallace, R. C. Francis, *Bull. Am. Meteorol. Soc.* **78**, 1069–1079 (1997).
20. E. Agee, J. Larson, S. Childs, A. Marmo, *J. Appl. Meteorol. Climatol.* **55**, 1681–1697 (2016).
21. R. J. Trapp, K. A. Hoogewind, *J. Clim.* **29**, 5251–5265 (2016).

ACKNOWLEDGMENTS

The authors thank A. Rhimes and K. McKinnon for suggestions on the use of quantile regression with count data. We thank two reviewers who provided constructive and helpful comments. M.K.T. and C.L. were partially supported by a Columbia University Research Initiatives for Science and Engineering (RISE) award; Office of Naval Research awards N00014-12-1-0911 and N00014-16-1-2073; NOAA's Climate Program Office's Modeling, Analysis, Predictions, and Projections program award NA14OAR4310185; and the Willis Research Network. J.E.C. was partially supported by U.S. National Science Foundation grant DMS-1225529 and thanks P. K. Rogerson for assistance during this work. The views expressed herein are those of the authors and do not necessarily reflect the views of any of the sponsoring agencies. The study was led by M.K.T.; calculations were carried out and the manuscript was drafted by M.K.T. C.L. prepared the environmental data. All authors were involved with designing the research, analyzing the results, and revising and editing the manuscript. All the authors declare no competing interests. Correspondence and material requests should be addressed to M.K.T. U.S. tornado report data come from NOAA's Storm Prediction Center www.spc.noaa.gov/wcm. North American Regional Reanalysis data are provided by the NOAA/Office of Oceanic and Atmospheric Research/Earth System Research Laboratory Physical Sciences Division, Boulder, Colorado, USA, from their website at www.esrl.noaa.gov/psd and the Data Support Section of the Computational and Information Systems Laboratory at the National Center for Atmospheric Research (NCAR). NCAR is supported by grants from the National Science Foundation.

SUPPLEMENTARY MATERIALS

www.sciencemag.org/content/354/6318/1419/suppl/DC1
Materials and Methods
Figs. S1 to S5
Tables S1 and S2
References (22–29)

4 August 2016; accepted 17 November 2016
Published online 1 December 2016
10.1126/science.aah7393

CONSERVATION

A global map of roadless areas and their conservation status

Pierre L. Ibisch,^{1,2*} Monika T. Hoffmann,¹ Stefan Kreft,^{1,2} Guy Pe'er,^{2,3,4}
Vassiliki Kati,^{2,5} Lisa Biber-Freudenberger,^{1,6} Dominick A. DellaSala,^{7,8}
Mariana M. Vale,^{9,10} Peter R. Hobson,^{1,2,11} Nuria Selva^{12*}

Roads fragment landscapes and trigger human colonization and degradation of ecosystems, to the detriment of biodiversity and ecosystem functions. The planet's remaining large and ecologically important tracts of roadless areas sustain key refugia for biodiversity and provide globally relevant ecosystem services. Applying a 1-kilometer buffer to all roads, we present a global map of roadless areas and an assessment of their status, quality, and extent of coverage by protected areas. About 80% of Earth's terrestrial surface remains roadless, but this area is fragmented into ~600,000 patches, more than half of which are <1 square kilometer and only 7% of which are larger than 100 square kilometers. Global protection of ecologically valuable roadless areas is inadequate. International recognition and protection of roadless areas is urgently needed to halt their continued loss.

The impact of roads on the surrounding landscape extends far beyond the roads themselves. Direct and indirect environmental impacts include deforestation and fragmentation, chemical pollution, noise disturbance, increased wildlife mortality due to car collisions, changes in population gene flow, and facilitation of biological invasions (1–4). In addition, roads facilitate “contagious development,” in that they provide access to previously remote areas, thus opening them up for more roads, land-use changes, associated resource extraction, and human-caused disturbances of biodiversity (3, 4). With the length of roads projected to increase by >60% globally from 2010 to 2050 (5), there is an urgent need for the development of a comprehensive global strategy for road development if continued biodiversity loss is to be abated (6). To help mitigate the detrimental effects of roads, their construction should be concentrated as much as possible in areas of relatively low “environmental values” (7). Likewise, prioritizing the protection of remaining roadless areas that are regarded as important for biodiversity and ecosystem functionality requires an assessment of their extent, distribution, and ecological quality.

Such global assessments have been constrained by deficient spatial data on global road networks. Importantly, recent publicly available and rapidly improving data sets have been generated by crowd-sourcing and citizen science. We demonstrate their potential through OpenStreetMap, a project with an open-access, grassroots approach to mapping and updating free global geographic data, with a focus on roads. The available global road data sets, OpenStreetMap and gROADS, vary in length, location, and type of roads; the former is the data set with the largest length of roads (36 million km in 2013) that is not restricted to specific road types (table S1). OpenStreetMap is more complete than gROADS, which has been used for other global assessments (7), but in certain regions, it contains fewer roads than sub-

global or local road data sets [see the example of Center for International Forestry Research data for Sabah, Malaysia (8); table S1]. Given the pace of road construction and data limitations, our results overestimate the actual extent of global roadless areas.

The spatial extent of road impacts is specific to the impact in question and to each particular road and its traffic volume, as well as to taxa, habitat, landscape, and terrain features. Moreover, for a given road impact, its area of ecological influence is asymmetrical along the road and can vary among seasons, between night and day, according to weather conditions, and over longer time periods. We conducted a comprehensive literature review of 282 publications dealing with “road-effects zones” or including the distance to roads as a covariate, of which 58 assessed the spatial influence of the road (table S2). All investigated road impacts were documented within a distance of

¹Centre for Economics and Ecosystem Management, Eberswalde University for Sustainable Development, Alfred-Moeller-Straße 1, 16225 Eberswalde, Germany. ²Society for Conservation Biology–Europe Section, 1133 15th Street Northwest, Suite 300, Washington, DC 20005, USA. ³Department of Conservation Biology, UFZ–Centre for Environmental Research, Permoserstraße 15, 04318 Leipzig, Germany. ⁴German Centre for Integrative Biodiversity Research (iDiv) Halle-Jena-Leipzig, Deutscher Platz 5e, 04103 Leipzig, Germany. ⁵Department of Environmental and Natural Resources Management, University of Patras, Seferi 2, 30100 Agrinio, Greece. ⁶Department of Ecology and Natural Resources Management, Center for Development Research, University of Bonn, Walter-Flex-Straße 3, 53113 Bonn, Germany. ⁷Geos Institute, 84 4th Street, Ashland, OR 97520, USA. ⁸Society for Conservation Biology–North America Section, 1133 15th Street Northwest, Suite 300, Washington, DC 20005, USA. ⁹Department of Ecology, Federal University of Rio de Janeiro, Av. Brg. Trompowski s/n, 21044-020 Rio de Janeiro, Brazil. ¹⁰Society for Conservation Biology–Latin America and Caribbean Section, 1133 15th Street Northwest, Suite 300, Washington, DC 20005, USA. ¹¹Writtle College, Lordship Road, Writtle, Chelmsford, Essex CM1 3RR, 01245 42420, UK. ¹²Institute of Nature Conservation, Polish Academy of Sciences, Mickiewicza 33, 31-120 Kraków, Poland.
*Corresponding author. Email: pierre.ibisch@hnee.de (P.L.I.); nuriselva@gmail.com (N.S.)

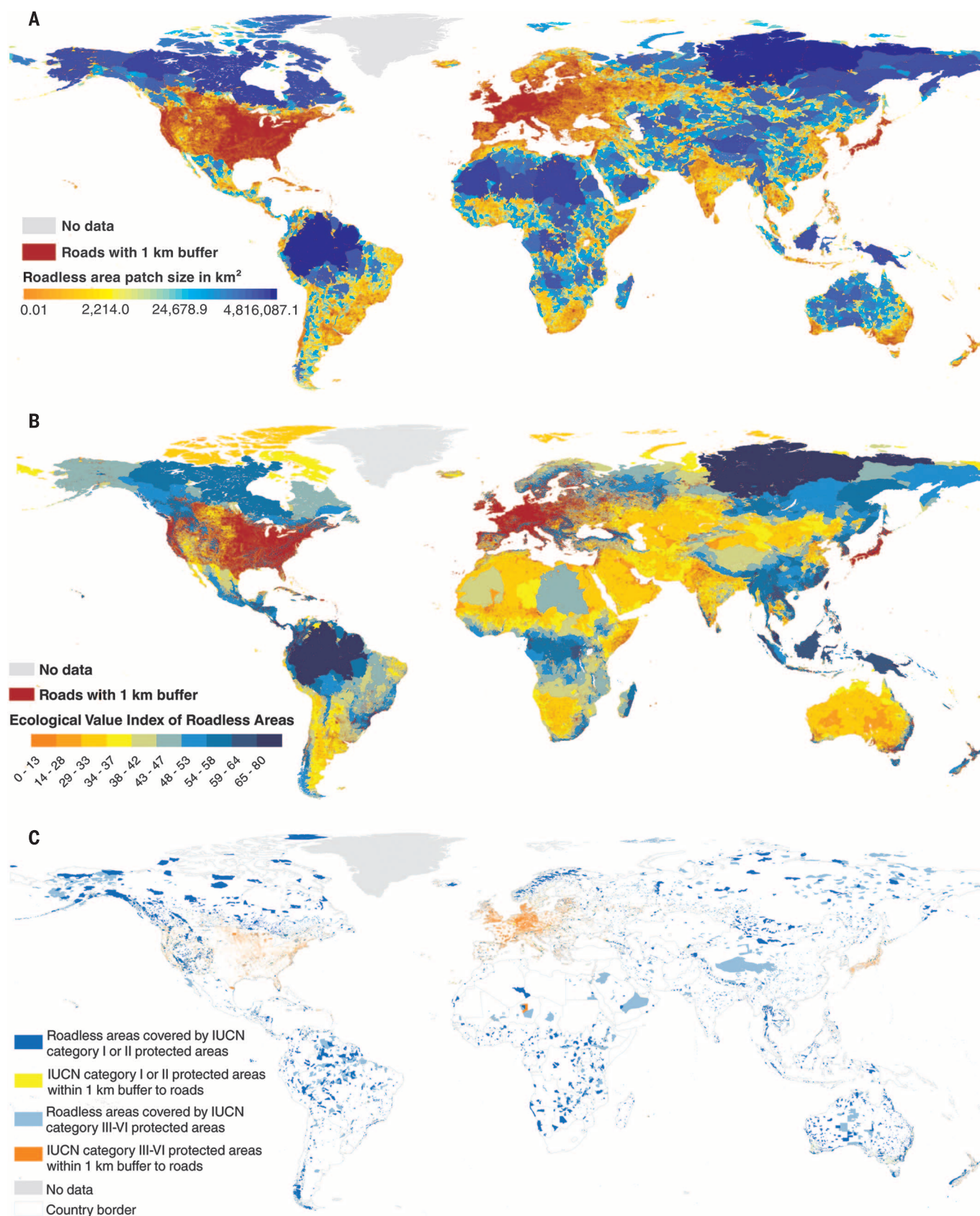


Fig. 1. The global distribution of roadless areas, based on a 1-km buffer around all roads. The distribution is depicted according to (A) size classes, (B) the ecological value index of roadless areas (EVIRA; based on patch size, connectivity, and ecosystem functionality), and (C) representation in protected areas (8).

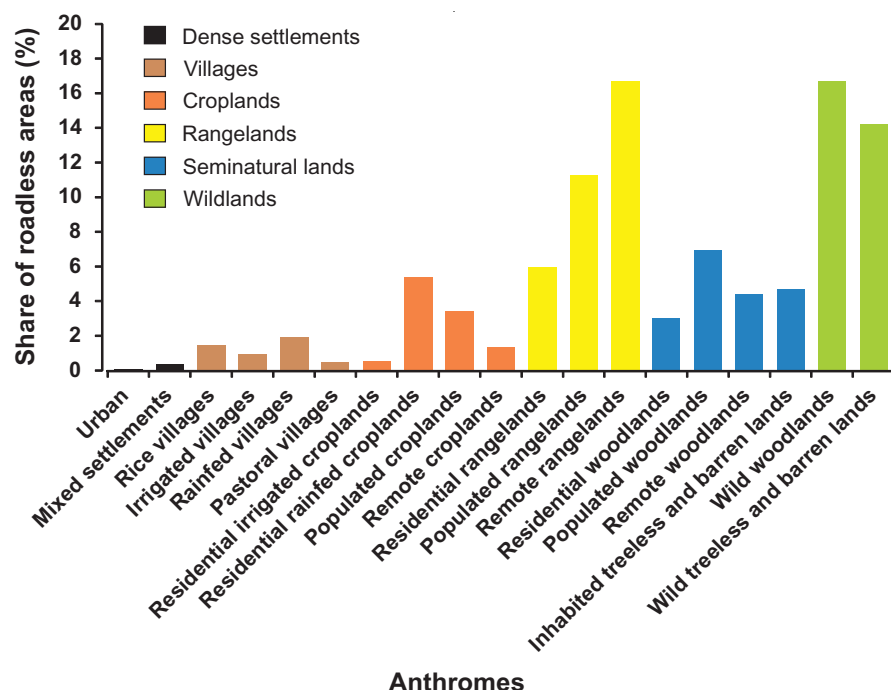


Fig. 2. Extent of roadless areas (1-km buffer) across anthromes. The majority of the world's roadless areas are in remote and unmodified landscapes, but they also occur in anthropogenically modified landscapes. The so-called anthromes were mapped according to (10).

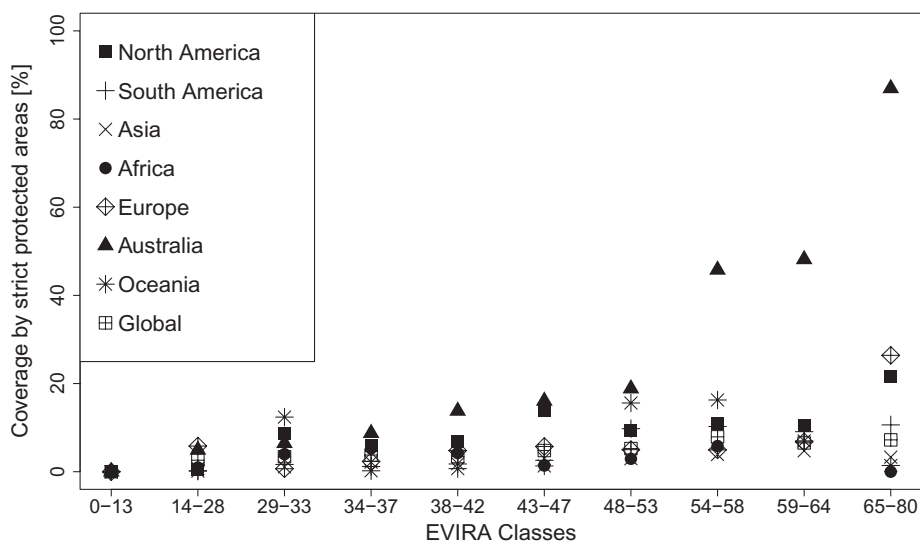


Fig. 3. Coverage of roadless areas by strictly protected areas (IUCN categories I and II) compared with global and continental EVIRA values. If priority were given to protecting roadless areas with high ecological functionality, we should see a positive correlation, with higher coverage associated with higher EVIRA values.

1 km from the road, 39% reached out to 2 km from the road, and only 14% extended out to 5 km from the road (fig. S1). Because the 1-km buffer along each side of the road represents the zone with the highest level and variety of road impacts, we defined roadless areas as those land units that are at least 1 km away from all roads and, therefore, less influenced by road effects. We com-

pared results from using this criterion with the outcomes from using an alternative 5-km buffer (see fig. S2 and table S3). We excluded all large water bodies, as well as Greenland and Antarctica, which are mostly covered by ice, from the analyses.

Roadless areas with a 1-km buffer to the nearest road cover about 80% of Earth's terrestrial surface (~105 million km²). However, these roadless areas

are dissected into almost 600,000 patches. More than half of the patches are <1 km²; 80% are <5 km²; and only 7% are >100 km² (table S4 and fig. S3). If the buffer is extended to 5 km, there is a substantial reduction in roadless areas to about 57% of the world's terrestrial surface (~75 million km²), dissected into 50,000 patches (fig. S2 and table S3). The occurrence, distribution, and size of roadless areas differ considerably among continents (Fig. 1A and fig. S4). For instance, the mean size of roadless patches (1-km buffer) is 48 km² in Europe, compared with >500 km² in Africa. Because of comparatively large gaps in available spatial data on roads in many segments of the tropics, the number and size of roadless areas are overestimated and should be treated with caution (e.g., Borneo; table S1).

All identified roadless areas were assessed for a set of ecological properties that were selected to reflect their relative importance to biodiversity, ecological functions, and ecosystem resilience: patch size, connectivity, and ecosystem functionality (9) (table S5). We normalized these three indicators to between 0 and 100 to calculate an additive and unitless index of the ecological value of each roadless area identified (termed the ecological value index of roadless areas, or EVIRA) [Fig. 1B and fig. S5; the specific rationale and technicalities of the chosen indicators are described in table S5 (8)]. The EVIRA values range from 0 to 80. A sensitivity analysis shows that ecosystem functionality and patch size are the best single indicators for the final index values (table S6 and figs. S6 to S8). Areas with relatively high index values tend to have a lower coefficient of variation (fig. S9).

We used the International Union for Conservation of Nature (IUCN) and UN Environment Programme-World Conservation Monitoring Centre data set of global protected areas to determine the extent of roadless areas that are protected (8) (Fig. 1C). The roadless areas distribution across human-dominated landscapes was determined following the classification of so-called anthromes, defined as biomes shaped by human land use and infrastructure (10) (Fig. 2 and table S7).

When examining the density of roads within different biomes, large discrepancies in distribution are apparent. The tundra and rock and ice-covered biomes are nearly entirely roadless, whereas temperate broadleaf and mixed forests have the lowest share of roadless areas (41%; figs. S9 and S10). Boreal forests of North America and Eurasia still retain large tracts of roadless areas (figs. S10 and S11). In the tropics, large roadless landscapes (>1000 km²) remain in Africa, South America, and Southeast Asia, with the Amazon having the single largest roadless segment. In relation to the anthromes (10), about two-thirds of the world's roadless areas can be described as remote and unmodified landscapes [26% uninhabited or sparsely inhabited treeless and barren lands; 21% natural and remote seminatural woodlands, with 17% wild woodlands therein (8); Fig. 2 and table S7]. The remaining one-third consists of rangelands, indicating that roadless areas can also occur in anthropogenically modified landscapes.

Fig. 4. Synergies and conflicts between conservation of roadless areas and the United Nations' Sustainable Development Goals. Scores <-0.5 (blue bars) indicate that conflicts with the goal prevail; scores between -0.5 and 0.5 (yellow) indicate a mixture of synergies and conflicts with the goal; and scores >0.5 (green) indicate prevailing synergies with the goal [for details, see table S11 (8)]. The scores reflect substantial imminent conflicts between various Sustainable Development Goals and conservation of roadless areas (table S11).



About one-third of the world's roadless areas have low EVIRA values. Patches with relatively low EVIRA values (ranging from 0 to 37; namely, $<50\%$ of the maximum value) account for 35% of the overall roadless area distribution, because most are small, fragmented, isolated, or otherwise heavily disturbed by humans. Some large tracts of roadless areas,

such as arid lands in northern Africa or central Asia, occur in areas of sparse vegetation and low biodiversity and, thus, have low index values for ecosystem functionality (9) (Fig. 1B). High EVIRA values occur both in tropical and boreal forests. The relative conservation value of roadless areas is context-dependent. Comparatively small or

moderately disturbed roadless areas have higher conservation importance in heavily roaded environments, such as most of Europe, the conterminous United States, and southern Canada.

Although the world's protected areas cover 14.2% of the terrestrial surface, only 9.3% of the overall expanse of roadless areas is within protected areas (all IUCN categories; Fig. 1C and table S8). There is no major difference in the coverage of roadless areas by strictly protected areas (IUCN categories I and II) versus the coverage of the overall landscape by strictly protected areas (3.8% roadless versus 4.2% overall). Only in North America, Australia, and Oceania are more than 6% of roadless areas under strict protection (table S8). If conservation efforts were to prioritize functional, ecologically important roadless areas, we would find a positive relation between strict protection coverage and EVIRA values of roadless areas. However, with the exception of Australia, this is not the case (Fig. 3 and table S9). Asia and Africa have particularly low protection coverage for roadless areas with high EVIRA values. For instance, we found gaps in the Asian tropical southeast, as well as in boreal biomes.

The recent Global Biodiversity Outlook (11) gives a bleak account of the progress made toward reaching the United Nations' biodiversity agenda as specified in the 20 Aichi Targets of the Convention on Biological Diversity (12). Governments have failed on several accounts to keep their use of natural resources well within safe ecological limits (target 4); to halt or at least halve the rate of habitat loss and substantially reduce the degradation and fragmentation of natural habitats (target 5); and to appropriately protect areas of particular importance for biodiversity and ecosystem services (target 11). To achieve global biodiversity targets, policies must explicitly acknowledge the factors underlying prior failures (13). Despite increasing scientific evidence for the negative impacts of roads on ecosystems, the current global conservation policy framework has largely ignored road impacts and road expansion. Furthermore, key policies on road infrastructure and development, such as the Cohesion Policy of the European Union, fail to take into account biodiversity.

In the much wider context of the United Nations' Sustainable Development Goals, conflicting interests can be seen between goals intended to safeguard biodiversity and those promoting economic development (14). We analyzed how roadless areas relate to the global conservation and sustainability agendas. As a transparent synthesis, we calculated simple scores of conflicts versus synergies of Sustainable Development Goals and Aichi Targets with the conservation of roadless areas (tables S10 and S11). Roads are explicitly mentioned in the Sustainable Development Goals only for their contribution to economic growth (goal 8), promoting further expansion into remote rural areas, and consideration is given neither to the environmental nor the social costs of road development. The resulting scores reflect substantial imminent conflicts (Fig. 4 and table S10); only in five Sustainable Development Goals do synergies with conservation of roadless

areas prevail, and four Sustainable Development Goals are predominantly in conflict with conservation of roadless areas. Maybe even more surprisingly, several of the Aichi Targets are ambivalent with respect to conserving roadless areas, rather than being in synergy entirely [six conflicting versus 11 synergistic targets (8); table S11].

There is an urgent need for a global strategy for the effective conservation, restoration, and monitoring of roadless areas and the ecosystems that they encompass. Governments should be encouraged to incorporate the protection of extensive roadless areas into relevant policies and other legal mechanisms, reexamine where road development conflicts with the protection of roadless areas, and avoid unnecessary and ecologically disastrous roads entirely. In addition, governments should consider road closure where doing so can promote the restoration of wildlife habitats and ecosystem functionality (4). Our global map of roadless areas represents a first step in this direction. During planning and evaluation of road projects, financial institutions, transport agencies, environmental nongovernmental organizations, and the engaged public should consider the identified roadless areas.

The conservation of roadless areas can be a key element in accomplishing the United Nations' Sustainable Development Goals. The extent and protection status of valuable roadless areas can serve as effective indicators to address several Sustainable Development Goals, particularly goal 15 ("Protect, restore and promote sustainable use of terrestrial ecosystems, sustainably manage forests, combat desertification, and halt and reverse land degradation and halt biodiversity loss") and goal 9 ("Build resilient infrastructure, promote inclusive and sustainable industrialization and foster innovation"). Enshrined in the protection of roadless areas should be the objective to seek and develop alternative socioeconomic models that do not rely so heavily on road infrastructure. Similarly, governments should consider how roadless areas can support the Aichi Targets (see tables S10 and S11). For instance, the target of expanding protected areas to cover 17% of the world's terrestrial surface could include a representative proportion of roadless areas.

Although we acknowledge that access to transportation is a fundamental element of human well-being, impacts of road infrastructure require a fully integrated environmental and social cost-benefits approach (15). Still, under current conditions and policies, limiting road expansion into roadless areas may prove to be the most cost-effective and straightforward way of achieving strategically important global biodiversity and sustainability goals.

REFERENCES AND NOTES

1. S. C. Trombulak, C. A. Frissell, *Conserv. Biol.* **14**, 18–30 (2000).
2. N. Selva et al., *Environ. Manage.* **48**, 865–877 (2011).
3. W. F. Laurance, A. Balmford, *Nature* **495**, 308–309 (2013).
4. N. Selva, A. Switalski, S. Kreft, P. L. Ibsch, in *Handbook of Road Ecology*, R. van der Ree, D. J. Smith, C. Grilo, Eds. (Wiley Chichester, 2015), pp. 16–26.

5. J. Dulac, "Global land transport infrastructure requirements. Estimating road and railway infrastructure capacity and costs to 2050" (International Energy Agency, 2013).
6. W. F. Laurance et al., *Curr. Biol.* **25**, R259–R262 (2015).
7. W. F. Laurance et al., *Nature* **513**, 229–232 (2014).
8. Materials and methods are available as supplementary materials on Science Online.
9. L. Freudenberger, P. R. Hobson, M. Schluck, P. L. Ibsch, *Ecol. Complex.* **12**, 13–22 (2012).
10. E. C. Ellis, K. Klein Goldewijk, S. Siebert, D. Lightman, N. Ramankutty, *Glob. Ecol. Biogeogr.* **19**, 589–606 (2010).
11. P. W. Leadley, et al., "Progress towards the Aichi Biodiversity Targets: An assessment of biodiversity trends, policy scenarios and key actions, Global Biodiversity Outlook 4 (GBO-4)" (Technical Report, Secretariat of the Convention on Biological Diversity, 2013); www.cbd.int/doc/publications/cbd-ts-78-en.pdf.
12. Convention on Biological Diversity, "Decision adopted by the Conference of the Parties to the Convention on Biological Diversity at its Tenth Meeting, X/2. The Strategic Plan for Biodiversity 2011–2020 and the Aichi Biodiversity Targets" (UN Environment Programme/Conference on Biological Diversity/Conference of the Parties, 2010); www.cbd.int/decision/cop/?id=12268.
13. D. P. Tittensor et al., *Science* **346**, 241–244 (2014).
14. United Nations, "Transforming our world: The 2030 Agenda for Sustainable Development. Resolution adopted by the General Assembly (A/70/L.1)" (2015); www.un.org/ga/search/view_doc.asp?symbol=A/RES/70/L.1&Lang=E.
15. L. Mandle et al., *Conserv. Lett.* **9**, 221–227 (2015).

ACKNOWLEDGMENTS

The data set is available through www.roadless.online and Dryad at <http://dx.doi.org/10.5061/dryad.q4975>. The study was funded by the Centre for Ecomics and Ecosystem Management at Eberswalde University for Sustainable Development, Germany; the Academy of Sciences and Literature, Mainz, Germany

("Biodiversity in Change," Nees Institute, Bonn University); and the Institute of Nature Conservation, Polish Academy of Sciences. Special thanks go to W. Barthlott for continued inspiration and support. The authors declare that they have no competing interests. P.L.I. acknowledges the research professorships "Biodiversity and natural resource management under global change" (2009–2015) and "Ecosystem-based sustainable development" (2015 onward) awarded by Eberswalde University for Sustainable Development. G.P. acknowledges funding from the European Union Framework Programme 7 project EU BON (ref. 308454). N.S. acknowledges funding from the National Science Center (DEC-2013/08/M/NZ9/00469) and the National Centre for Research and Development in Poland (Norway grants, POLNOR/198352/85/2013). P.L.I., N.S., and V.K. conceived the study. M.T.H. collected and analyzed all data, with assistance from P.L.I., L.B.-F., and G.P. P.L.I. wrote a first draft of the text and moderated its critical revision with important contributions by M.T.H., S.K., N.S., and D.A.D. All authors contributed to the interpretation of the data and critical revision of further versions. N.S., M.T.H., M.M.V., V.K., S.K., L.B.-F., and P.L.I. elaborated the supplementary materials. We appreciate the extraordinary contribution of D. Biber, who adapted Insensa-GIS to our needs. We acknowledge J. Sauermann's contributions to data processing. J.-P. Mund suggested exploring the OpenStreetMap data set. This study is part of the Roadless Areas Initiative of the Society for Conservation Biology, led by the Policy Committee of the Europe Section.

SUPPLEMENTARY MATERIALS

www.sciencemag.org/content/354/6318/1423/suppl/DC1
Materials and Methods
Figs. S1 to S11
Tables S1 to S11
Data Sources
References (16–180)

18 March 2016; accepted 16 November 2016
10.1126/science.aaf7166

PLANT PATHOLOGY

Regulation of sugar transporter activity for antibacterial defense in *Arabidopsis*

Kohji Yamada,^{1,2*} Yusuke Saijo,^{3,4} Hirofumi Nakagami,^{5†} Yoshitaka Takano^{1*}

Microbial pathogens strategically acquire metabolites from their hosts during infection. Here we show that the host can intervene to prevent such metabolite loss to pathogens. Phosphorylation-dependent regulation of sugar transport protein 13 (STP13) is required for antibacterial defense in the plant *Arabidopsis thaliana*. STP13 physically associates with the flagellin receptor flagellin-sensitive 2 (FLS2) and its co-receptor BRASSINOSTEROID INSENSITIVE 1-associated receptor kinase 1 (BAK1). BAK1 phosphorylates STP13 at threonine 485, which enhances its monosaccharide uptake activity to compete with bacteria for extracellular sugars. Limiting the availability of extracellular sugar deprives bacteria of an energy source and restricts virulence factor delivery. Our results reveal that control of sugar uptake, managed by regulation of a host sugar transporter, is a defense strategy deployed against microbial infection. Competition for sugar thus shapes host-pathogen interactions.

Plants assimilate carbon into sugar by photosynthesis, and a broad spectrum of plant-interacting microbes exploit these host sugars (1, 2). In *Arabidopsis*, pathogenic bacterial infection causes the leakage of sugars to the extracellular spaces (the apoplast) (3), a major site of colonization by plant-infecting bacteria.

Although leakage may be a consequence of membrane disintegration during pathogen infection, some bacterial pathogens promote sugar efflux to the apoplast by manipulating host plant sugar transporters (4, 5). Interference with sugar absorption by bacterial and fungal pathogens reduces their virulence, highlighting a general

importance of sugar acquisition for microbial infection (4–7).

Plants control apoplastic sugar levels by sugar transporters and glycoside hydrolases. For example, sucrose exported to the apoplast is hydrolyzed to glucose and fructose by cell-wall invertases (cwINVs), which are then transported to the cytoplasm by sugar transport proteins (STPs) (8). Of the 14 *Arabidopsis* STP transporters, STP1 and STP13 largely govern the uptake of monosaccharides (9). In plant defense, STP13 contributes to resistance against the gray mold fungus *Botrytis cinerea* in *Arabidopsis* (10). On the contrary, the *Lr67res* mutation, which results in impaired transporter activity of LR67 (an STP13 ortholog), enhances resistance against both rust and powdery mildew fungal pathogens in wheat, although the process remains undetermined (11).

To investigate whether sugar uptake by STP1 and STP13 contributes to antibacterial defense in *Arabidopsis*, we spray-inoculated the phytopathogenic bacterium *Pseudomonas syringae* pv. *tomato* (*Pst*) DC3000 (12) onto *stp1 stp13* double-mutant plants. The plants showed increased susceptibility to *Pst* DC3000 (Fig. 1A, left) but exhibited a wild-type (WT)-like stomatal closure

response (13) to the flg22 peptide of bacterial flagellin (fig. S1). Thus, the elevated susceptibility of *stp1 stp13* plants seems to reflect defects in their postinvasion defenses. Indeed, growth of syringe-infiltrated *Pst* DC3000 Δ *hrcC*, a less virulent strain lacking the type III secretion system (T3SS) that delivers virulence factors called effectors into plant cells, was also elevated in *stp1 stp13* plants (Fig. 1A, right). Our results suggest that STP1 and STP13 restrict bacterial proliferation in the apoplast by retrieving sugars.

To determine whether apoplastic monosaccharide levels fluctuate during antibacterial defense, we measured apoplastic glucose levels after exposure to flg22. Apoplastic glucose levels in the leaves of *stp1 stp13* plants were significantly higher than in WT plants but were indistinguishable from WT amounts in nonelicited plants (fig. S2A). Moreover, cwINV activity was comparably induced in WT and *stp1 stp13* plants in response to flg22 (fig. S2B). Together, these data indicate that STP1 and/or STP13 absorb cwINV-generated monosaccharides in the apoplast during antibacterial defense and thus perhaps significantly reduce apoplastic sugar content during bacterial challenge.

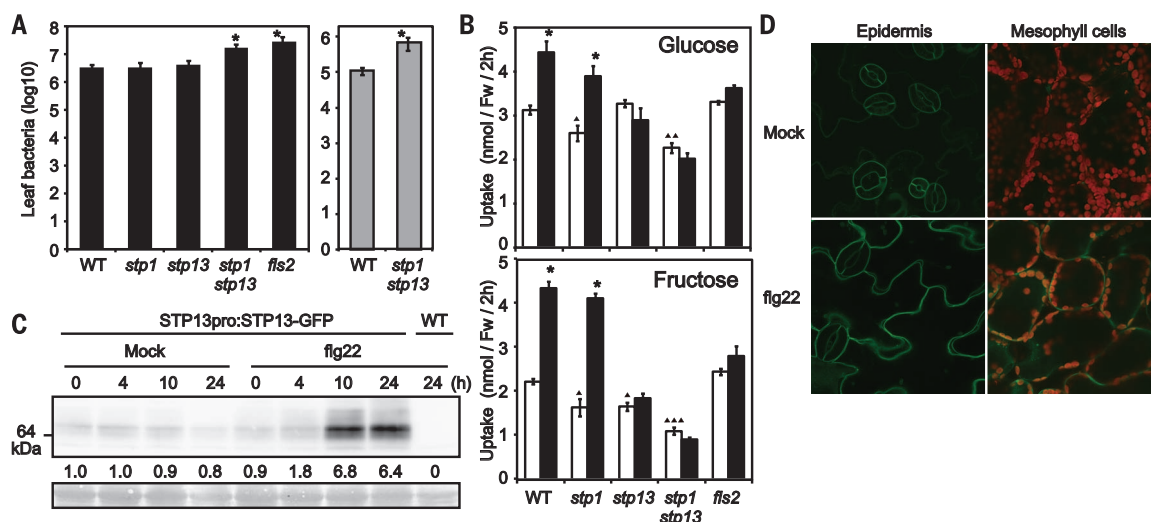
We also found that monosaccharide uptake activity in *Arabidopsis* seedlings increased after flg22 application, but not in the absence of the leucine-rich repeat receptor kinase (LRR-RK) flagellin-sensitive 2 (FLS2), the flg22 receptor in *Arabidopsis* (Fig. 1B), further suggesting that plants actively absorb sugars during antibacterial defense. Because the contribution of STP1 and STP13 to antibacterial defense implies their roles in flg22-induced monosaccharide uptake activity in *Arabidopsis* plants, we measured monosaccharide uptake in *stp1* and *stp13* plants upon mock

and flg22 application. *stp1* plants retained an increase in monosaccharide uptake in response to flg22, whereas the basal activity of mock-treated plants was reduced (Fig. 1B). By contrast, *stp13* plants failed to show enhanced activity after flg22 application (Fig. 1B). This demonstrated that STP1 and STP13 contribute to basal and flg22-induced monosaccharide uptake activity, respectively. Consistent with this role of STP13, the introduction of functional STP13–green fluorescent protein (STP13-GFP) (9) expressed by native *STP13* regulatory DNA sequences eliminated the elevated apoplastic glucose levels of *stp1 stp13* plants in response to flg22 (fig. S2C). Nevertheless, STP1 and STP13 seem to work redundantly in antibacterial defense, given the enhanced susceptibility of *stp1 stp13* double mutants, but not *stp13* single mutants, to *Pst* DC3000 (Fig. 1A, left). STP1-mediated activity may compensate for the absence of STP13 by absorbing monosaccharide beyond the threshold required for bacterial suppression. Indeed, simultaneous loss of STP1 and STP13 caused significantly lowered monosaccharide uptake with or without flg22 application (Fig. 1B), which probably led to the enhanced susceptibility of *stp1 stp13* plants.

The STP13 dependence of flg22-induced monosaccharide uptake prompted us to explore the molecular mechanisms for regulation of STP13 activity during antibacterial defense. We found that *STP13*, but not *STP1*, expression was induced in response to flg22 (fig. S3). The abundance of STP13-GFP also rose in seedlings and mature leaves after flg22 application (Fig. 1C and fig. S4). STP13-GFP fluorescence spread at the plasma membranes of epidermal and mesophyll cells after flg22 application but was detected mainly

¹Graduate School of Agriculture, Kyoto University, Kyoto, Japan. ²Graduate School of Bioscience and Bioindustry, Tokushima University, Tokushima, Japan. ³Graduate School of Biological Sciences, Nara Institute of Science and Technology, Ikoma, Japan. ⁴Japan Science and Technology Agency (JST), Precursory Research for Embryonic Science and Technology (PRESTO), Kawaguchi, Japan. ⁵RIKEN Center for Sustainable Resource Science, Yokohama, Japan. *Corresponding author. Email: kohjiyamada226@gmail.com (K.Y.); ytkano@kais.kyoto-u.ac.jp (Y.T.) †Present address: Max Planck Institute for Plant Breeding Research, Cologne, Germany.

Fig. 1. Sugar transporters STP1 and STP13 contribute to antibacterial defense, and STP13 activity is induced in response to flg22. (A) Growth of spray-inoculated *Pst* DC3000 (black) or syringe-inoculated *Pst* DC3000 Δ *hrcC* (gray) in *Arabidopsis* leaves. Results are means \pm SE, $n = 5$ biological replicates (*, $P < 0.05$ compared to the corresponding values of WT plants in two-tailed t tests). (B) ¹⁴C-labeled monosaccharide uptake activity in *Arabidopsis* seedlings 24 hours after water (mock, white) or 4 μ M flg22 (black) application. Results are means \pm SE, $n = 3$ (*, $P < 0.05$ compared to the corresponding values of each mock treatment; Δ , $P < 0.05$, $\Delta\Delta$, $P < 0.005$, $\Delta\Delta\Delta$, $P < 0.0005$ compared to the corresponding values of mock-treated WT plants; two-tailed t tests). Fw, fresh weight of seedlings. (C) Anti-GFP immunoblot analysis for STP13-GFP in



Arabidopsis seedlings exposed to water (mock) or 0.5 μ M flg22. Numbers below the immunoblot represent relative intensities of STP13-GFP bands, normalized to backgrounds in Ponceau S-stained loading controls (bottom) and with the 0-hours mock treatment value set as 1.0. (D) GFP fluorescence of STP13-GFP in *Arabidopsis* seedlings exposed to water (mock) or 0.5 μ M flg22 for 10 hours. Red fluorescence indicates autofluorescence of chloroplasts.

to guard cells upon mock treatment (Fig. 1D). Thus, *STP13* was transcriptionally activated during antibacterial defense.

Posttranslational modifications, including phosphorylation, can also modulate transporter activity (14), and to investigate such modification of *STP13* during antibacterial defense, we first identified *STP13*-interacting proteins. The initiation of plant immunity occurs when exogenous or endogenous immune elicitors are perceived by pattern-recognition receptors (PRRs) at the plasma membrane (15), where *STP13* is also localized. We tested whether *STP13* associates with PRRs by coimmunoprecipitation (co-IP) analysis, using a transient expression system in *Nicotiana benthamiana*. *STP13*-FLAG coimmunoprecipitated with GFP fusions of FLS2 and two other PRRs, elongation factor-Tu receptor (EFR) and Pep receptor 1 (PEPR1), which recognize the elf18 peptide of bacterial elongation factor-Tu and the endogenous elicitor-active Pep peptides, respectively (15, 16) (fig. S5), but did not coimmunoprecipitate with the GFP fusion of the plasma membrane marker protein low-temperature-inducible 6b (LTI6b) (fig. S5), indicating the specificity of *STP13* interactions with these PRRs at the plasma membrane. Upon ligand perception, these PRRs associate with another LRR-RK, BRASSINOSTEROID INSENSITIVE 1-associated receptor kinase 1 (BAK1), which triggers the activation of downstream factors including the receptor-like cytoplasmic kinase botrytis-induced kinase 1 (BIK1) through trans-phosphorylation events (15). We found that BAK1-hemagglutinin epitope (BAK1-HA), as well as FLS2-HA, associated with *STP13*-FLAG in *Arabidopsis* protoplasts, whereas BIK1-HA did not (Fig. 2A). Moreover, *STP13*-GFP associated with FLS2 and BAK1 in mock-treated and 10-hour flg22-treated stable transgenic plants (Fig. 2B and fig. S6); an FLS2-BAK1 association was also detectable 10 hours after flg22 application (fig. S7). From these interaction data, we infer that *STP13* exists in complexes with FLS2 and/or BAK1, irrespective of their ligand-

dependent activation states. The results suggest that *STP13* participates in various PRR complexes, each of which may directly regulate *STP13* activity during antibacterial defense.

We next asked whether *STP13* is phosphorylated by PRR complexes in vitro. In multipass transmembrane proteins such as transporters, the longer cytoplasmic regions tend to be phosphorylated (17). We tested whether two *STP13* fragments, the middle loop (ML, located between the sixth and seventh transmembrane domains) and the C-terminal tail (CT), expressed as glutathione *S*-transferase (GST) fusions in *Escherichia coli*, could be phosphorylated (fig. S8, A and B). A maltose-binding protein (MBP) fusion to BAK1 cytoplasmic kinase domain (CD) phosphorylated GST-*STP13* CT but not GST-*STP13* ML. Neither MBP-PEPR1 CD nor MBP-BIK1 phosphorylated *STP13* fragments in vitro (fig. S8C). We used PEPR1 CD for this assay because FLS2 CD shows weak in vitro kinase activity (18). Several serine and threonine residues occur in the *STP13* CT fragment (Fig. 2C, top), including the previously reported serine (S) phosphorylation site S513 (17). Although we substituted S513 with a non-phosphorylatable alanine (A) residue, MBP-BAK1 CD still phosphorylated GST-*STP13* CT (S513A) (Fig. 2C, left). By contrast, BAK1-mediated *STP13* phosphorylation was reduced by alanine substitution at threonine 485 (T485) but unaffected by alanine substitutions at S517, S523, and T524 (Fig. 2C). We concluded that BAK1 phosphorylates *STP13* at T485. The corresponding residue was conserved in *STP13* orthologs of other plant species (fig. S9A), but rarely among *Arabidopsis* STP homologs (fig. S9B), implying that critical and specific regulation of *STP13* occurs through T485 phosphorylation in plants.

To examine whether T485 phosphorylation affects the transporter activity of *STP13*, we tested the function of *STP13* (T485D)-GFP, in which T485 was substituted with a phosphomimic aspartic acid (D) residue. When introduced to a yeast strain deficient in multiple

monosaccharide transporters, *STP13* (T485D)-GFP promoted yeast growth on 10 mM glucose, more so than did *STP13*-GFP, although this enhancement became less clear at lower glucose concentrations (fig. S10, A and B). In addition, *STP13* (T485D)-GFP yeast cells absorbed more ^{14}C -labeled monosaccharides than did *STP13*-GFP cells (Fig. 3A and fig. S10C). On the other hand, the T485A substitution did not affect monosaccharide uptake activity (Fig. 3A), indicating that basal sugar transport activity of *STP13* is insensitive to the T485A substitution. Protein accumulation and intracellular localization of *STP13* were unaffected by the T485D substitution (fig. S10, D and 0E), which suggests that the T485D substitution affects *STP13* transporter activity per se. We observed a low affinity [Michaelis constant (K_m), $121.3 \pm 6.3 \mu\text{M}$] and high capacity (V_{\max} value, $8.5 \pm 0.6 \text{ nmol/10 min}$) of *STP13* (T485D)-GFP cells for glucose, compared with a K_m of $71.7 \pm 3.6 \mu\text{M}$ and a V_{\max} of $3.3 \pm 0.3 \text{ nmol/10 min}$ of *STP13* (T485A)-GFP cells (fig. S10F).

To test whether T485 phosphorylation also affects *STP13* activity in planta, we measured flg22-induced glucose uptake in *STP13*-GFP and *STP13* (T485A)-GFP plants in the *stp1 stp13* background. Although the T485A substitution did not affect *STP13* activity in yeast cells or in nonelicited plants (Fig. 3, A and B), it reduced flg22-induced glucose uptake activity in plants (Fig. 3B). Protein accumulation in *STP13*-GFP and *STP13* (T485A)-GFP plants was comparable (fig. S11). We concluded that *STP13* underwent phosphorylation at T485 in response to flg22, which enhanced its sugar transport capacity. Glucose uptake in response to flg22 also increased somewhat in *STP13* (T485A)-GFP plants (Fig. 3B), probably via transcriptional induction. Thus, *STP13* activity is regulated at transcriptional and posttranslational levels during antibacterial defense.

We investigated the contribution of *STP13* T485 phosphorylation to antibacterial defense.

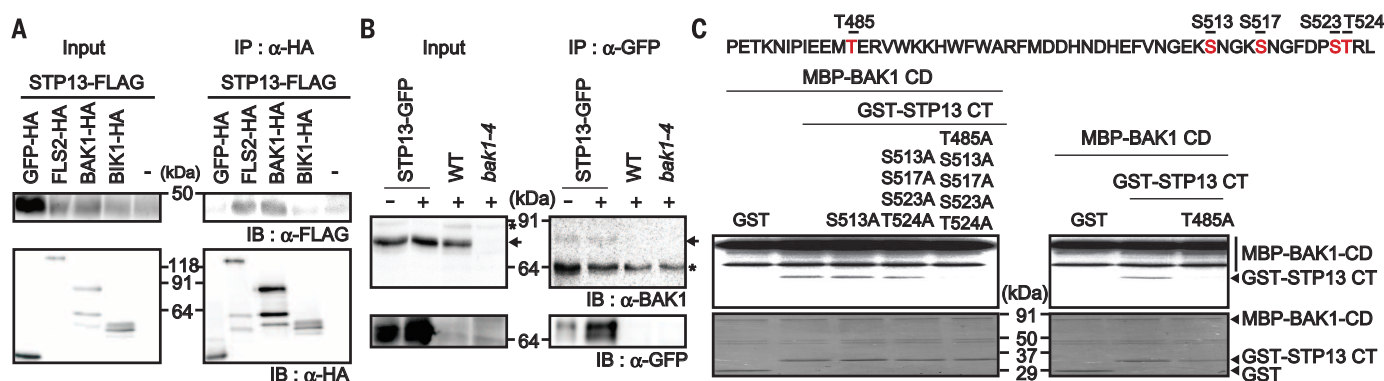
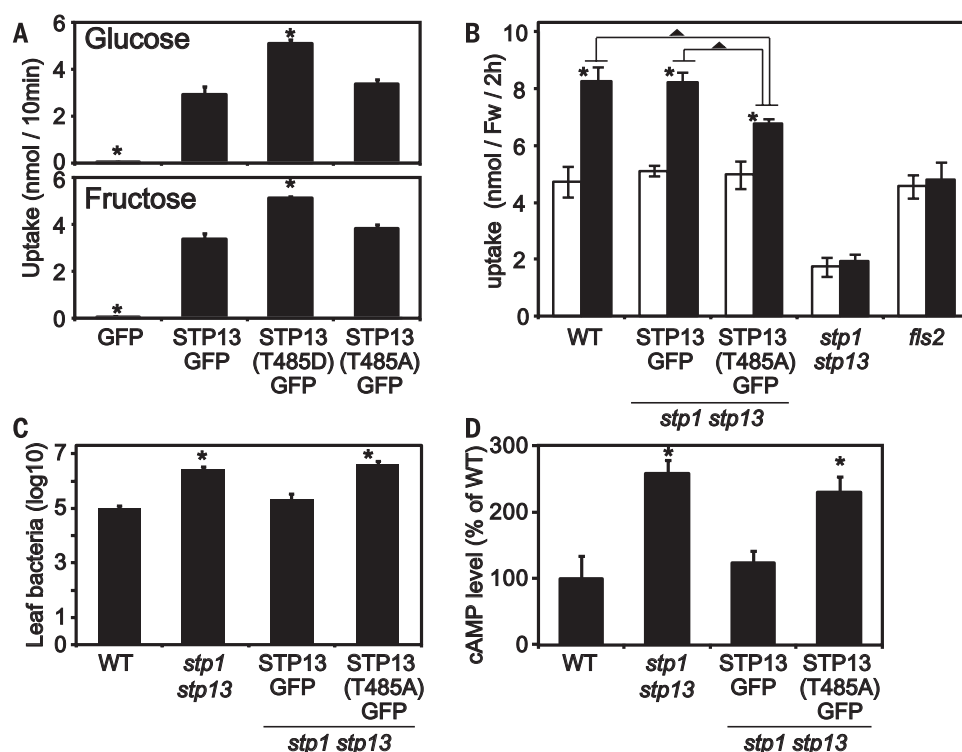


Fig. 2. *STP13* participates in FLS2 complexes and is phosphorylated by BAK1. (A and B) Coimmunoprecipitation analysis between *STP13* and known FLS2 complex components in *Arabidopsis* protoplasts (A) and transgenic *Arabidopsis* plants (B). + and – indicate 0.5 μM flg22 and mock treatment, respectively, for 10 hours. IP and IB denote immunoprecipitation and immunoblotting with the indicated antibodies. BAK1 (arrows) and cross-reactive bands (asterisks) are indicated. (C) Autoradiograph of an in vitro kinase assay. Serine and threonine residues in the *STP13*-CT fragment (top) are highlighted in red. Coomassie brilliant blue–stained controls are shown below.

Fig. 3. Regulation of STP13 activity by T485 phosphorylation is required to suppress bacterial proliferation, partly by limiting virulence factor delivery.

(A) ^{14}C -labeled monosaccharide uptake assay in yeast cells. Results are means \pm SE, $n = 3$ (*, $P < 0.05$ in two-tailed t tests compared to the corresponding values of STP13-GFP cells). (B) Glucose uptake activity in *Arabidopsis* seedlings 24 hours after water (mock, white) or 4 μM flg22 (black) application. Results are means \pm SE, $n = 3$ (*, $P < 0.05$, compared to the corresponding values of each mock treatment; \blacktriangle , $P < 0.05$, compared between indicated values; two-tailed t tests). (C) Growth of spray-inoculated *Pst* DC3000 in *Arabidopsis* leaves. Results are means \pm SE, $n = 5$ (*, $P < 0.05$ compared to the values of WT plants using two-tailed t tests). (D) cAMP amounts in *Arabidopsis* leaves at 10 hours after spray inoculation with *Pst* DC3000 (avrPto-Cya). Results are means \pm SE, $n = 4$ (*, $P < 0.05$ compared to the corresponding values of WT plants using a two-tailed t test).



Complementation of *stp1 stp13* mutant plants with STP13-GFP restored resistance to bacterial infection to WT levels (Fig. 3C), whereas the alanine-substituted version, STP13 (T485A)-GFP, was ineffective. Thus, regulation of STP13 activity through T485 phosphorylation is required for the plant to suppress bacterial proliferation.

Pathogens coordinate virulence factor expression in response to localized environments in their hosts. In the case of phytopathogenic bacteria such as *Pst* DC3000, T3SS regulatory cascades are activated via recognition of external sugars (19, 20). We speculated that reduced sugar uptake activity in *stp1 stp13* plants might therefore augment bacterial effector delivery into plant cells. To test this hypothesis, we inoculated plants with bacteria expressing the T3SS effector avrPto fused to adenylate cyclase (Cya) (21), which produces cyclic adenosine 3',5'-monophosphate (cAMP) only when delivered into eukaryotic cells. We observed higher cAMP levels in *stp1 stp13* plants than in WT plants, without increased bacterial growth (Fig. 3D and fig. S12), indicating elevated effector delivery in *stp1 stp13* plants. Introduction of STP13-GFP, but not STP13 (T485A)-GFP, reversed this trend (Fig. 3D). We conclude that phosphorylation-dependent regulation of STP13 activity suppresses bacterial effector delivery. The likely mechanism is that STP13 reduces sugar content in the apoplast, resulting in limited bacterial T3SS activation.

Our findings illuminate a critical role for sugar transporter regulation during bacterial challenge (fig. S13). Stimulation of STP13 activity suppresses bacterial effector delivery (Fig. 3D), thereby reducing bacterial virulence. Moreover,

the elevated growth of $\Delta hrcC$ strain, which is defective in T3SS effector delivery, in the apoplast of *stp1 stp13* plants (Fig. 1A, right) suggests that apoplastic sugars represent an energy source for bacterial proliferation. Phytopathogenic bacteria exploit various host-derived metabolites, in addition to sugars, as energy sources or signaling molecules (22, 23). Regulation of metabolite uptake upon recognition of microbial molecules may thus emerge as a key host defense strategy to restrict pathogen proliferation.

REFERENCES AND NOTES

- R. T. Voegelé, K. W. Mendgen, *Euphytica* **179**, 41–55 (2011).
- J. Doidy et al., *Trends Plant Sci.* **17**, 413–422 (2012).
- K. Wang, M. Senthil-Kumar, C. M. Ryu, L. Kang, K. S. Mysore, *Plant Physiol.* **158**, 1789–1802 (2012).
- L. Q. Chen et al., *Nature* **468**, 527–532 (2010).
- M. Cohn et al., *Mol. Plant Microbe Interact.* **27**, 1186–1198 (2014).
- R. Wahl, K. Wippel, S. Goos, J. Kämper, N. Sauer, *PLOS Biol.* **8**, e1000303 (2010).
- T. Li, B. Liu, M. H. Spalding, D. P. Weeks, B. Yang, *Nat. Biotechnol.* **30**, 390–392 (2012).
- J. S. Eom et al., *Curr. Opin. Plant Biol.* **25**, 53–62 (2015).
- K. Yamada et al., *J. Biol. Chem.* **286**, 43577–43586 (2011).
- P. Lemonnier et al., *Plant Mol. Biol.* **85**, 473–484 (2014).
- J. W. Moore et al., *Nat. Genet.* **47**, 1494–1498 (2015).
- X. F. Xin, S. Y. He, *Annu. Rev. Phytopathol.* **51**, 473–498 (2013).
- W. Zeng, S. Y. He, *Plant Physiol.* **153**, 1188–1198 (2010).
- K. H. Liu, Y. F. Tsay, *EMBO J.* **22**, 1005–1013 (2003).

- D. Couto, C. Zipfel, *Nat. Rev. Immunol.* **16**, 537–552 (2016).
- K. Yamada et al., *EMBO J.* **35**, 46–61 (2016).
- T. S. Nühse, A. Stensballe, O. N. Jensen, S. C. Peck, *Plant Cell* **16**, 2394–2405 (2004).
- B. Schwesinger et al., *PLOS Genet.* **7**, e1002046 (2011).
- T. V. Huynh, D. Dahlbeck, B. J. Staskawicz, *Science* **245**, 1374–1377 (1989).
- J. L. Stauber, E. Loginicheva, L. M. Schechter, *Res. Microbiol.* **163**, 531–539 (2012).
- L. M. Schechter, K. A. Roberts, Y. Jamir, J. R. Alfano, A. Collmer, *J. Bacteriol.* **186**, 543–555 (2004).
- A. Rico, G. M. Preston, *Mol. Plant Microbe Interact.* **21**, 269–282 (2008).
- J. C. Anderson et al., *Proc. Natl. Acad. Sci. U.S.A.* **111**, 6846–6851 (2014).

ACKNOWLEDGMENTS

We thank S. Singkaravanti-Ogawa and T. Hirase for technical support and I. Smith for critical reading. We thank K. Yamaguchi-Shinozaki, S. Tsuge, J. M. Ward, A. Reinders, and J. Mogami for published materials. This work was supported by Japan Society for the Promotion of Science KAKENHI grants (14J04880 and 16K18656, K.Y.; 15H01247, H.N.; 15H04457 and 15H05780, Y.T.), by JST PRESTO (Y.S.), and by the Asahi Glass Foundation (Y.T.). K.Y. and Y.T. conceived this study. K.Y. performed all experiments and data analyses. H.N. provided technical assistance. K.Y., Y.S., and Y.T. designed experiments and wrote the manuscript. The supplementary materials contain additional data.

SUPPLEMENTARY MATERIALS

www.sciencemag.org/content/354/6318/1427/suppl/DC1
Materials and Methods
Figs. S1 to S13
Table S1
References (24–33)

15 July 2016; accepted 11 November 2016
Published online 24 November 2016
10.1126/science.aah5692

RIBOSOMES

The cryo-EM structure of a ribosome-Ski2-Ski3-Ski8 helicase complex

Christian Schmidt,¹ Eva Kowalinski,² Vivekanandan Shanmuganathan,¹ Quentin Defenouillère,^{3,4} Katharina Braunger,¹ André Heuer,¹ Markus Pech,¹ Abdelkader Namane,³ Otto Berninghausen,¹ Micheline Fromont-Racine,³ Alain Jacquier,³ Elena Conti,^{2*} Thomas Becker,^{1*} Roland Beckmann^{1*}

Ski2-Ski3-Ski8 (Ski) is a helicase complex functioning with the RNA-degrading exosome to mediate the 3'-5' messenger RNA (mRNA) decay in turnover and quality-control pathways. We report that the Ski complex directly associates with 80S ribosomes presenting a short mRNA 3' overhang. We determined the structure of an endogenous ribosome-Ski complex using cryo-electron microscopy (EM) with a local resolution of the Ski complex ranging from 4 angstroms (Å) in the core to about 10 Å for intrinsically flexible regions. Ribosome binding displaces the autoinhibitory domain of the Ski2 helicase, positioning it in an open conformation near the ribosomal mRNA entry tunnel. We observe that the mRNA 3' overhang is threaded directly from the small ribosomal subunit to the helicase channel of Ski2, primed for ongoing exosome-mediated 3'-5' degradation.

The translation and decay of eukaryotic mRNAs are mutually interdependent processes in the life cycle of a transcript. Beyond the general observations that translational efficiency inversely correlates with decay rates, there is increasing evidence of close links between the ribosome and ribonuclease complexes (1). The best-characterized example is the translation-dependent degradation of defective transcripts in mRNA surveillance pathways (2). A hallmark of these pathways is the intermittent pausing or stalling of ribosomes at faulty features in the message, such as the presence of a premature stop codon in nonsense-mediated mRNA decay (NMD), a sequence that inhibits translation elongation in no-go decay (NGD) or an unnatural end in nonstop decay (NSD) (2). Another hallmark of surveillance pathways is that decay is often initiated by an endonucleolytic cleavage of ribosome-associated mRNAs (2, 3), followed by rapid degradation in the 3'-5' direction by the exosome or in the 5'-3' direction by Xrn1 (4). In contrast, mRNA turnover generally starts with the shortening of the poly(A)-tail before proceeding with the exosome or with Xrn1 after removal of the 5' cap structure (4). Recent studies in *Saccharomyces cerevisiae* (5-7) and *Drosophila melanogaster* (8) have shown that decapping and 5'-3' degradation of the bulk of mRNAs can also

occur on polysomes. However, direct physical links between the translation and degradation machineries are currently unknown.

In the 3'-5' decay pathways, the exosome functions together with the Ski2-Ski3-Ski8 (Ski) complex (4). The Ski complex is built around a helicase with 3'-5' RNA unwinding activity (Ski2) that is thought to feed the unwound RNA 3' end to the exosome (9). The Ski and exosome complexes are evolutionarily conserved from yeast to humans. In *S. cerevisiae*, their interaction is mediated by a bridging factor, Ski7 (10). Ski7 also contains a guanosine triphosphate (GTP) binding domain with a specific function in NSD (11, 12) and with striking similarity to Hbs1 (13, 14), a translational guanosine triphosphatase (GTPase) that together with Dom34 and ABCE1 triggers dissociation of stalled ribosomes in NSD and NGD (2). These observations have led to a model in which Ski7 binds ribosomes undergoing NSD and recruits the Ski-exosome complex to degrade the associated mRNAs (11, 12, 15). This model, however, still lacks direct experimental evidence.

We set out to investigate whether and how the Ski proteins associate with ribosomes. We analyzed polysome gradients from yeast strains expressing tandem-affinity-purification (TAP)-tagged versions of Ski7 and of the scaffolding subunit of the Ski complex, Ski3 (table S1), which were tested for activity in a nonstop reporter decay assay (fig. S1A). Surprisingly, Ski7 accumulated in the low-molecular-weight fractions of the gradient and did not comigrate with ribosomes (Fig. 1A). In contrast, Ski3 was distributed across the gradient, with a prominent peak at the 80S ribosome fractions. Upon ribonuclease (RNase) treatment, the polysome profile collapsed into a single monosome peak where essentially all Ski3 cosedimented (Fig. 1A). This indicated that the Ski complex interacts directly with ribosomes, and we speculate that 80S ribosomes with short mRNA

overhangs as generated by our RNase treatment serve as preferred substrates for the Ski complex.

Next, we used a nonstop reporter gene with an N-terminal Protein A tag (Fig. 1B) (16) to allow purification of the ribosome nascent chain complex (RNC) and expressed it in yeast strains lacking *SKI7* and either *HBS1* or *DOM34* (table S1) to stabilize the mRNA and to prevent stalled ribosomes from being dissociated (3, 11, 12). Estimating the relative abundance of proteins by label-free mass spectrometry, we found that all three subunits of the Ski complex were enriched in the 80S ribosome fractions as compared to the total eluate (Fig. 1C and fig. S1B). We conclude that yeast ribosomes that are stalled on nonstop mRNAs associate with the subunits of the Ski complex in the absence of Ski7 and Dom34 or Hbs1.

We purified endogenous ribosome-Ski complexes from wild-type yeast strains with TAP-tagged Ski3 (fig. S1C and table S1) and collected cryo-electron microscopy (cryo-EM) data. After thorough three-dimensional classification (fig. S2), we obtained a stable class that could be reconstructed to an average overall resolution of 3.8 Å (Fig. 2, A and B, and fig. S3A). Local resolution of the Ski complex ranged from 4 Å in the core part to ~10 Å for intrinsically flexible regions (fig. S3B). We assembled a near-complete atomic model for the ribosome and the Ski complex (fig. S3, C to E, and table S2), based on known high-resolution crystal structures (9, 17, 18) that were particularly useful in the peripheral low-resolution regions (fig. S3B). The refined model (fig. S3D and table S3) also includes 34 nucleotides of mRNA, A- and P-site tRNAs, and eIF-5A in the ribosomal E-site (19).

The Ski complex specifically recognizes the small ribosomal subunit (40S) (Fig. 2, A to C). It binds near the entry of the mRNA tunnel and bridges the 40S head with the body and beak regions (Fig. 2C and fig. S4). The overall structure of the Ski complex is similar to that previously described (9). It binds the ribosome via the Ski2 helicase, the N-terminal arm of the tetratricopeptide repeat (TPR) protein Ski3, and one copy of the WD40 protein Ski8 (Ski8_{OUT}), whereas the second copy of Ski8 (Ski8_{IN}) and most of the C-terminal part of Ski3 face the solvent. Ski8_{OUT} is sandwiched between Ski3 and the 40S platform proteins uS2, uS5, and eS21 (Fig. 2D and fig. S4A). The DEXH helicase core of Ski2 uses the RecA2 domain to bind the 40S between the shoulder at ribosomal RNA (rRNA) helix h16 (fig. S4B) and the head at the uS3 and eS10 proteins (Fig. 2E), while the RecA1 and helical domains remain engaged with the rest of the Ski complex (Fig. 2C). Finally, the so-called arch or insertion domain of Ski2 that protrudes from the helicase core (17) interacts with the head of the 40S at uS3, uS10, and rRNA helix h41 (Fig. 2F and fig. S4C). In a similar way, the closely related nuclear helicase Mtr4 is recruited to preribosomal targets by the interaction of its arch domain with specific adaptor proteins for exosome-mediated rRNA processing (20).

Both the ribosome and Ski complex undergo conformational changes upon binding (fig. S5). In the 40S, rRNA helix h16 adopts an unusually

¹Gene Center and Center for Integrated Protein Science Munich, Department of Biochemistry, Feodor-Lynen-Strasse 25, University of Munich, 81377 Munich, Germany. ²Max Planck Institute of Biochemistry, Department of Structural Cell Biology, Am Klopferspitz 18, 82152 Martinsried, Munich, Germany.

³Institut Pasteur, Génétique des Interactions Macromoléculaires, Centre National de la Recherche Scientifique, Unité Mixte de Recherche 3525, Rue du Docteur Roux 25-28, 75724 Paris, France. ⁴Sorbonne Universités, UPMC Paris 6, Complexité du Vivant, 75252 Paris Cedex 05, France.

*Corresponding author. Email: beckmann@genzentrum.lmu.de (R.B.); becker@genzentrum.lmu.de (T.B.); conti@biochem.mpg.de (E.C.)

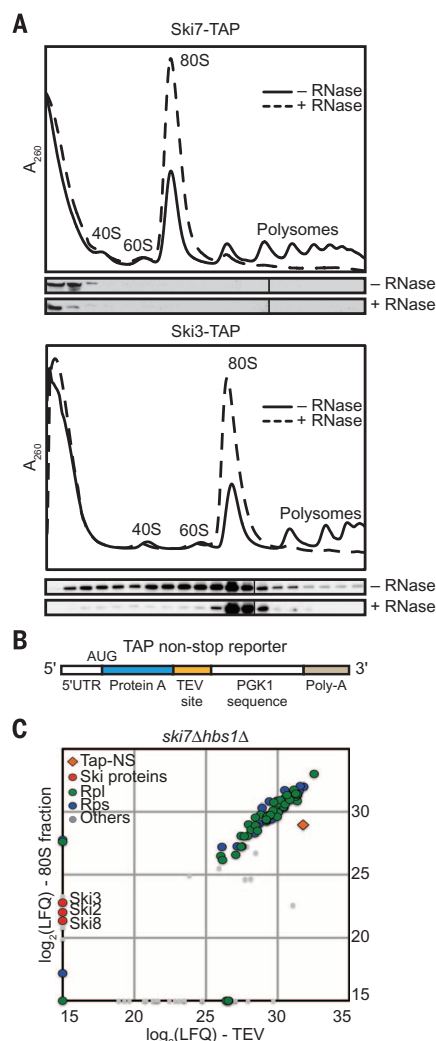


Fig. 1. Association of *S. cerevisiae* Ski complex to 80S ribosomes. (A) Polysome profiles from cells expressing TAP-tagged Ski7 or Ski3 with and without RNase treatment. Fractions were analyzed by immunoblotting using an α -Protein A antibody. (B) Schematic representation of the TAP nonstop reporter gene used for the purification of nonstop ribosomal complexes. (C) Label-free quantification (LFQ) by liquid chromatography–tandem mass spectrometry (LC-MS/MS) of the proteins associated with the nonstop ribosomal complexes in a *Δski7/Δhbs1Δ* mutant strain. The intensity of each protein was compared with that in the eluate after Tobacco etch virus protease (TEV) cleavage (x axis, TEV eluate; y axis, 80S fraction).

bent conformation (fig. S5A). Compared with previous crystal structures (9, 17), the N-terminal arm of Ski3 moves about 30 Å (fig. S5B) into a more open conformation as it approaches the beak protein eS12 (fig. S4D). The arch domain of Ski2 flexes about 30° [60° compared with Mtr4 (21)] as it moves away from the RNA helicase channel entry (fig. S5C). Thus, ribosome binding changes the conformation of the two structural elements previously shown to autoinhibit the RNA-dependent adenosine triphosphatase (ATPase) activity of the Ski complex (9). The cryo-EM reconstruction shows density for an mRNA molecule binding in the

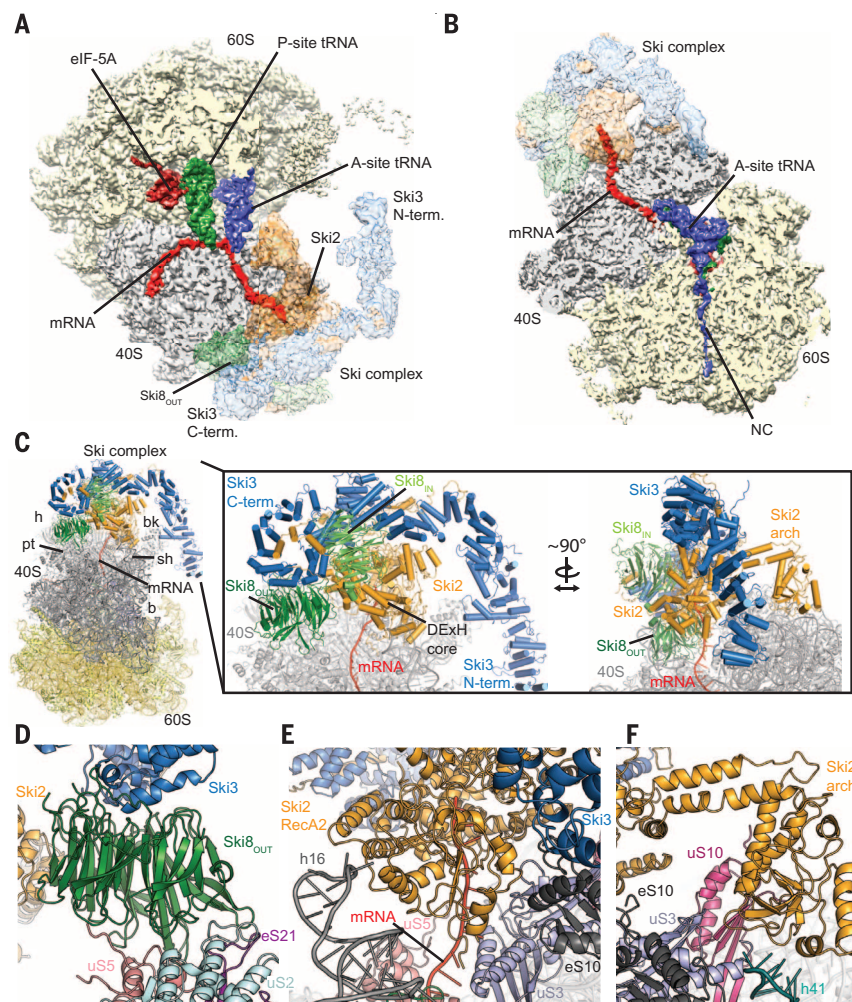


Fig. 2. Cryo-EM structure of the yeast ribosome–Ski assembly. (A and B) Top and side view of the ribosome–Ski complex showing densities low-pass filtered according to local resolution for the Ski subunits, A-site tRNA, P-site tRNA, eIF-5A, mRNA, and the nascent polypeptide chain (NC). (C) Overall structure of the Ski complex bound to the 80S. The mRNA is shown in red. The zoom-in panels show two orthogonal views of the interaction of the Ski complex with the head of the 40S. General structural features of the Ski complex and the 40S subunit (h, head; b, body; bk, beak; pt, platform; sh, shoulder) are indicated. (D to F) Close-up views of the interactions centered at Ski8_{OUT}, at the DEXH core of Ski2, and at the arch domain of Ski2.

canonical path of the 40S. The mRNA exits the ribosome through a constriction formed by uS3, uS5, and eS30 (Fig. 3A and fig. S6A); crosses a narrow crevice about 15 Å in length; and contacts a basic loop protruding from the RecA2 domain of Ski2 (residues 545 to 606) (Fig. 3B and fig. S6A). After this flexible segment, the mRNA threads through an opening formed between the helical and RecA2 domains of Ski2 (Fig. 3B). Here, at the so-called unwinding β -hairpin (17, 21), the ribonucleotide chain bends as it enters the helicase channel (Fig. 3B and fig. S6, B and C). In the Ski2 channel, four nucleotides follow the same path previously observed in Mtr4 (fig. S6C) (21).

The structural analysis indicates that the 3' overhang of the ribosome-associated mRNA provides additional intermolecular contacts and has the appropriate geometry for channeling the RNA 3' end into the Ski complex. We tested this model in RNase protection assays in vitro using different Ski2 mutants (RecA2 basic loop deleted or mutated)

(fig. S7, A and B). The accumulation of protected 9- to 10-nucleotide-long fragments characteristic of the wild-type complex (9) decreased with the Ski2 mutants, suggesting that the RecA2 loop contributes to RNA binding even in the absence of ribosomes. Furthermore, we prepared stalled RNCs with 3' mRNA overhangs of different length (0, 10, 20, or 50 nucleotides) (fig. S7C) and performed binding assays. Consistent with our polysome gradients after RNase treatment and with the structural data, binding of the Ski complex was increased when using RNCs with overhangs of 10 to 20 nucleotides (fig. S7D). Additionally, ribosome footprint analysis of the endogenous ribosome–Ski complexes (table S1) revealed a length distribution of protected mRNA fragments with not only the 28- to 30-nucleotide (nt) peak for ribosomes alone (22) but also a second peak with extended fragment length between 35 and 42 nt (Fig. 3C), consistent with the expected additional protection by the Ski complex (9). We

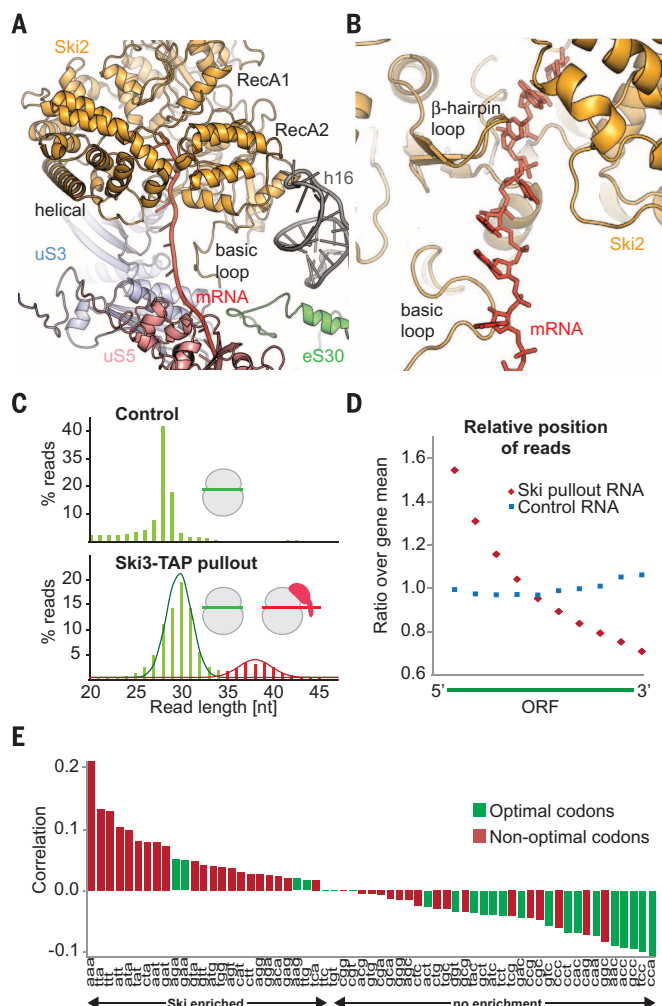


Fig. 3. Structural and biochemical features of the Ski-ribosome interactions with the mRNA 3' end. (A) Path of the mRNA 3' overhang that extends from the ribosome entry site to the DExH core of the Ski2 helicase. (B) Close-up view of the opening formed between the Ski2 RecA2 domain (including the basic loop) and the helical domains (including the β -hairpin loop). (C) Length distribution of ribosome-protected footprints (RPFs) from native 80S ribosomes and the Ski3-TAP pullout samples. (D) Relative positional distribution of RNA reads from 5' to 3' over the ORFs in the respective mRNA of the Ski pullout compared with that of control mRNA. (E) Codon correlation plot ranked by Ski enrichment (stop codons were removed). Spearman correlation values were calculated between the footprint ratio (Ski3-TAP pullout against control) and codon occurrence across the genome for all codons.

further analyzed the associated mRNAs of the endogenous ribosome-Ski complexes by targeted ribosomal profiling (fig. S8). When assessing the positions of the mRNA reads along the open reading frames (ORFs), we found a significant decrease in fragment numbers toward the 3' end as compared with the even distribution observed in the control samples (Fig. 3D). When assessing the codon frequency of the ORFs, we found an enrichment in nonoptimal (destabilizing) codons (Fig. 3E), which are generally connected to shorter half-lives and faster decay of transcripts (23). These data argue in favor of the ribosome-Ski complexes being engaged in ongoing 3'-5' mRNA degradation, consistent with the idea of the Ski complex channeling RNAs directly to the exosome for 3'-5' degradation.

Our study suggests a model whereby a stalled ribosome-Ski complex recruits a preassembled

exosome-Ski7 complex (15) to degrade its associated mRNA (fig. S9). Because there are fewer Ski complexes than ribosomes in the cell (24), it is tempting to speculate that appropriate targeting of the Ski and exosome complexes might involve a short 3' mRNA overhang on the ribosome. Such targets would be expected, for example, in co-translational quality-control pathways characterized by an endonucleolytic cleavage in the vicinity of the ribosome (2). For 3'-5' degradation, the mRNA has to be extracted and, eventually, the ribosome needs to be recycled. Our ribosome-Ski complex is likely a transient intermediate whereby the mRNA has not been extracted from the ribosome due to the lack of adenosine triphosphate (ATP) (required for Ski2 helicase activity) or the lack of other factors (such as the exosome). Although the exact series of events remains to be established, we note that the ribosome surfaces

used to interact with translational GTPases such as Hbs1 or the ribosome recycling ATPase ABCE1 (2) are accessible in the Ski-bound ribosome. Finally, an early study showed evidence that the human ortholog of Ski2 colocalizes with 40S subunits and 80S ribosomes in HeLa cells (25), suggesting that analogous ribosome-Ski complexes are likely to exist in higher eukaryotes. Thus, the direct link between the translation and 3'-5' degradation machineries that we identified in *S. cerevisiae* might operate broadly in different mRNA decay pathways and in different species.

REFERENCES AND NOTES

1. B. Roy, A. Jacobson, *Trends Genet.* **29**, 691–699 (2013).
2. C. J. Shoemaker, R. Green, *Nat. Struct. Mol. Biol.* **19**, 594–601 (2012).
3. M. K. Doma, R. Parker, *Nature* **440**, 561–564 (2006).
4. R. Parker, *Genetics* **191**, 671–702 (2012).
5. W. Hu, T. J. Sweet, S. Chammongpol, K. E. Baker, J. Collier, *Nature* **461**, 225–229 (2009).
6. W. Hu, C. Petzold, J. Collier, K. E. Baker, *Nat. Struct. Mol. Biol.* **17**, 244–247 (2010).
7. V. Pelechano, W. Wei, L. M. Steinmetz, *Cell* **161**, 1400–1412 (2015).
8. S. Antic, M. T. Wolfinger, A. Skucha, S. Hosiner, S. Dörner, *Mol. Cell Biol.* **35**, 2309–2320 (2015).
9. F. Halbach, P. Reichelt, M. Rode, E. Conti, *Cell* **154**, 814–826 (2013).
10. Y. Araki et al., *EMBO J.* **20**, 4684–4693 (2001).
11. A. van Hoof, P. A. Frischmeyer, H. C. Dietz, R. Parker, *Science* **295**, 2262–2264 (2002).
12. P. A. Frischmeyer et al., *Science* **295**, 2258–2261 (2002).
13. G. C. Atkinson, S. L. Baldauf, V. Hauryliuk, *BMC Evol. Biol.* **8**, 290 (2008).
14. E. Kowalinski, A. Schuller, R. Green, E. Conti, *Structure* **23**, 1336–1343 (2015).
15. E. Kowalinski et al., *Mol. Cell* **63**, 125–134 (2016).
16. Q. Defenouillere et al., *Proc. Natl. Acad. Sci. U.S.A.* **110**, 5046–5051 (2013).
17. F. Halbach, M. Rode, E. Conti, *RNA* **18**, 124–134 (2012).
18. A. Ben-Shem et al., *Science* **334**, 1524–1529 (2011).
19. C. Schmidt et al., *Nucleic Acids Res.* **44**, 1944–1951 (2016).
20. M. Thoms et al., *Cell* **162**, 1029–1038 (2015).
21. J. R. Weir, F. Bonneau, J. Hentschel, E. Conti, *Proc. Natl. Acad. Sci. U.S.A.* **107**, 12139–12144 (2010).
22. N. T. Ingolia, S. Ghaemmaghami, J. R. S. Newman, J. S. Weissman, *Science* **324**, 218–223 (2009).
23. V. Presnyak et al., *Cell* **160**, 1111–1124 (2015).
24. S. Ghaemmaghami et al., *Nature* **425**, 737–741 (2003).
25. X. Qu et al., *Nucleic Acids Res.* **26**, 4068–4077 (1998).

ACKNOWLEDGMENTS

The cryo-EM map for the ribosome-Ski complex and the respective atomic coordinates have been deposited in the EMDatBank and ProteinDataBank with accession codes EMD-3461 and 5MC6, respectively. Sequencing data are available at Gene Expressing Omnibus (GEO) with the accession number GSE70259. The authors declare no competing financial interests. We thank the Leibniz-Rechenzentrum Munich (LRZ) for providing computational services and support. This work was supported by the German Research Council (SFB646 to R.B., T.B., and E.C.; GRK1721 to R.B. and E.C.; FOR1805 to R.B. and SFB1035 to E.C.), by the Max Planck Gesellschaft (E.C.), and by the Agence Nationale de la Recherche (2011-BSV6-011-02 and ANR-14-CE-10-0014-01 to Q.D., A.J., and M.F.-R.). R.B. and E.C. acknowledge support by the Center for Integrated Protein Science Munich (CIPS-M), the Graduate School of Quantitative Biosciences Munich (QBM), and the European Research Council (Advanced Grants CRYOTRANSLATION and DEAD2THEEND). We also acknowledge the support of Ph.D. and postdoctoral fellowships from Boehringer Ingelheim Fonds (to C.S. and K.B.); from QBM (to V.S.); from the Ministère de l'Enseignement Supérieur et de la Recherche and from the Fondation ARC pour la Recherche sur le Cancer (to Q.D.); and from EMBO, Marie Curie, and the Daimler und Benz Stiftung (to E.K.).

SUPPLEMENTARY MATERIALS

www.sciencemag.org/content/354/6318/1431/suppl/DC1
Materials and Methods
Supplementary Text
Figs. S1 to S9
Tables S1 to S3
References (26–47)

24 March 2016; resubmitted 26 September 2016
Accepted 21 November 2016
10.1126/science.aaf7520

STRUCTURAL BIOLOGY

The structure and flexibility of conical HIV-1 capsids determined within intact virions

Simone Mattei,^{1,2} Bärbel Glass,³ Wim J. H. Hagen,¹
Hans-Georg Kräusslich,^{2,3} John A. G. Briggs^{1,2*}

HIV-1 contains a cone-shaped capsid encasing the viral genome. This capsid is thought to follow fullerene geometry—a curved hexameric lattice of the capsid protein, CA, closed by incorporating 12 CA pentamers. Current models for core structure are based on crystallography of hexameric and cross-linked pentameric CA, electron microscopy of tubular CA arrays, and simulations. Here, we report subnanometer-resolution cryo-electron tomography structures of hexameric and pentameric CA within intact HIV-1 particles. Whereas the hexamer structure is compatible with crystallography studies, the pentamer forms using different interfaces. Determining multiple structures revealed how CA flexes to form the variably curved core shell. We show that HIV-1 CA assembles both aberrant and perfect fullerene cones, supporting models in which conical cores assemble *de novo* after maturation.

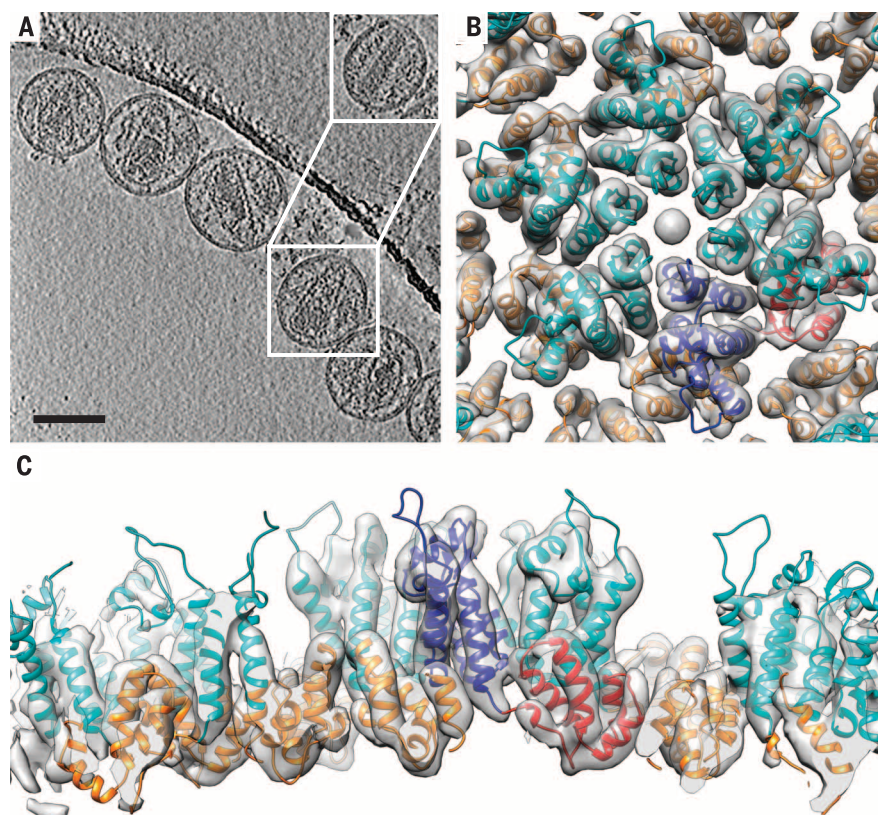
HIV-1 is initially produced as an immature, noninfectious particle with the main structural protein Gag forming a membrane-associated protein layer. Cleavage of Gag separates individual domains, leading to morphological conversion into the mature, infectious virion. The cleaved CA protein, consisting of two α -helical domains connected by a flexible

linker, assembles into a conical core encasing the viral genome (1–4). The core has been suggested to constitute a fullerene cone: a lattice of CA hexamers that flexes to accommodate different local curvatures on the conical surface, and which is closed by insertion of five pentamers toward the narrow end of the cone and seven toward the broad end (5). The different core mor-

phologies seen in a minority of HIV-1 particles and in other retroviruses can be modeled as fullerene structures in which different distributions of the pentamers determine the overall shape (5, 6).

The structure of the mature hexameric assembly of CA has been studied by using recombinant CA assembled into tubular arrays for cryo-electron microscopy (cryo-EM) (7, 8) and by x-ray crystallography of mutant, cross-linked CA (9) or wild-type CA in a hexameric lattice (10). The 10-nm hexamer-hexamer spacing in these arrays matches that detected in cores purified from intact viruses (11). The mature CA hexamer consists of a central ring formed by the N-terminal domains of CA (NTD), and an external ring formed by the C-terminal domains of CA (CTD) that links hexamers together. The x-ray structure of a CA pentamer, stabilized by targeted insertion of cysteine residues, was found to be quasi-equivalent to the hexamer (12). Models for the core have been generated by arranging hexamers and pentamers into cones resembling those seen *in vivo* and subjecting these arrangements to coarse-grained (13) and all-atom molecular dynamics (MD) simulations (8). Thus, currently available structural information about hexamers, pentamers, and cores derives

Fig. 1. The structure of the CA hexamer. (A) Computational slice through a representative tomographic reconstruction of HIV-1 virions. Scale bar, 100 nm. Inset shows a computational slice through the top of the core in the boxed virion, indicating that individual hexamers can be resolved. (B) Cryo-ET reconstruction of the mature CA hexameric lattice (gray isosurface) viewed from outside the core. The final structural model of the hexamer is shown, with the NTD in cyan and the CTD in orange. One monomer is highlighted in blue (NTD) and red (CTD). (C) As in (B), viewed perpendicular to the lattice. See also movie S1.



¹Structural and Computational Biology Unit, European Molecular Biology Laboratory, Meyerhofstrasse 1, 69117 Heidelberg, Germany. ²Molecular Medicine Partnership Unit, European Molecular Biology Laboratory–Universitätsklinikum Heidelberg, Heidelberg, Germany. ³Department of Infectious Diseases, Virology, Universitätsklinikum Heidelberg, Im Neuenheimer Feld 324, 69120 Heidelberg, Germany.

*Corresponding author. Email: john.briggs@embl.de

from the analysis of crystals, in vitro assemblies, and in silico simulations.

Here, we applied cryo-electron tomography (cryo-ET) and subtomogram averaging to determine the structure, arrangement, and flexibility of CA within intact, wild-type HIV-1. Purified and inactivated HIV-1 was vitrified and imaged by using a dose-symmetric tilt scheme (14) (table S1 and Fig. 1A). From reconstructed tomograms of 539 particles, 552 cores were identified and subtomograms were extracted along the surface of the cores. The subtomograms were subjected to a reference-free, iterative alignment and averaging procedure (15). From the aligned, motion-corrected, dose-filtered, and contrast-transfer function-corrected subtomograms, we generated a final, sixfold symmetric structure of the hexameric CA lattice within the virion core at 6.8 Å resolution (Fig. 1, B and C, movie S1, and fig. S1).

We compared our reconstruction to the available crystal structures of hexameric CA (9, 10, 16) and found the fully hydrated wild-type hexameric crystal structure [Protein Data Bank (PDB) 4XFX] (10) to be the closest representation of the hexameric CA lattice in intact HIV-1. CA monomers taken from PDB 4XFX were flexibly fitted into each of the CA densities in the EM map (Fig. 1, B and C). The fitted structure preserves the tertiary domain structures seen in the crystal, whereas the relative positions of the domains have undergone a slight rotation around the linker connecting NTD and CTD to adapt from the flat crystal lattice to the curved in-virus lattice (fig. S2A). The presence of additional density within the pore formed by the NTDs suggests that the recently proposed binding site for deoxynucleoside triphosphates (17) is occupied in the assembled core (fig. S2, B and C).

To assemble a fullerene cone, the CA lattice must bend to adopt different local curvatures—more tightly curved at the tip than at the base of the cone, and curved in one direction, but not in the other, on the side of the cone. CA has previously been suggested to achieve this by modulating the relative orientation of its two domains (9, 10), by motion around the CTD dimer interface (8), or by variability in the trimeric interface formed by the CTD (18). To determine how CA flexes in the viral cone, we calculated the tilt and the twist between all pairs of neighboring hexamers in our data set (Fig. 2A). We then classified the pairs of hexamers according to the measured angles (fig. S3) and determined the structure of each class. In this way, we determined the structures, at subnanometer resolution, of 18 different conformations with different tilt and twist angles (table S2, fig. S3, and movies S2 and S3). Into each EM map, we rigid-body fitted the NTDs and CTDs that had resulted from the flexible fit into the symmetrized hexamer. We found that tilt and twist are accommodated by movements of the NTD relative to the CTD around the flexible linker (Fig. 2B), as well as by relative rotations around the CTD dimer and trimer interfaces (Fig. 2, C and D). In all cases, the main range of these movements was considerably smaller than previously suggested (8, 10, 18) (fig. S4). We con-

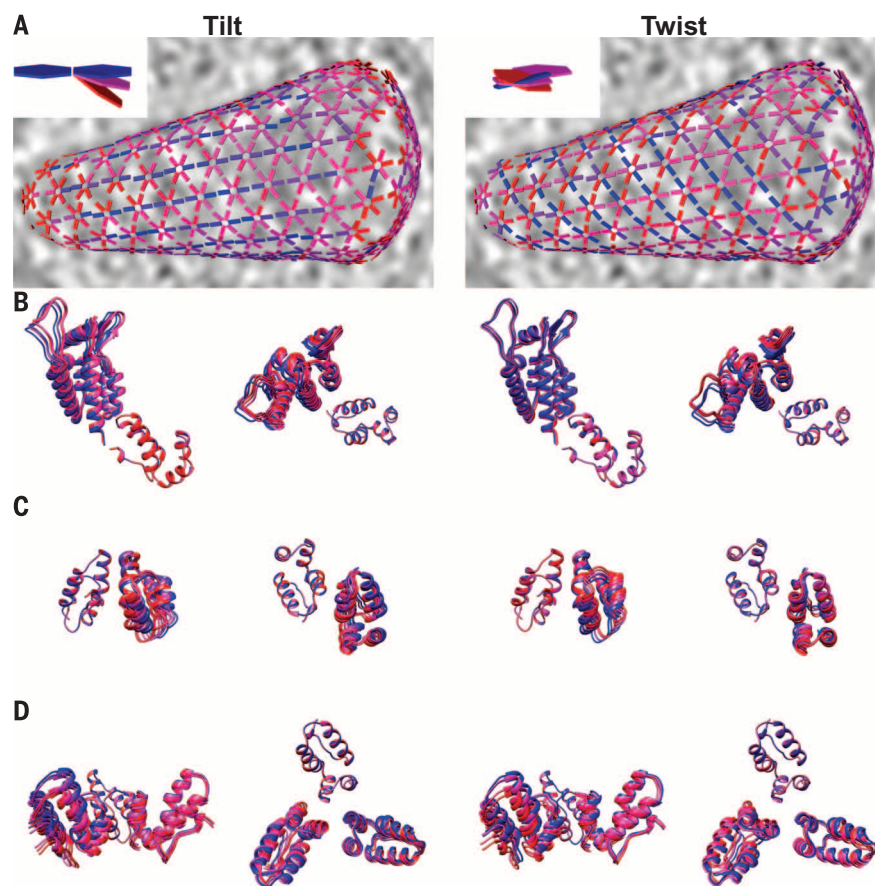


Fig. 2. Structural flexibility in the CA hexameric lattice. (A) The distribution of tilt (left column) and twist (right column) angles between hexamers within a single core. The tilt/twist angle is indicated by the color of the connecting lines between hexamer positions from blue (low/negative values) to red (high/positive values). Insets show a schematic illustration of tilt and twist angles. (B to D) The flexibility in the CA lattice that accommodates different tilts and twists is illustrated by superimposing the CA domains from structures determined with tilt angles from $-1 \pm 3^\circ$ to $29 \pm 3^\circ$, and twist angles from $-12 \pm 3^\circ$ to $12 \pm 3^\circ$, color-coded as in (A), for (B) the monomer, (C) the CTD dimeric interface, and (D) the trimeric CTD trimeric interface. See also movies S2 and S3.

clude that variable curvature is achieved by small structural movements in CA that are distributed over multiple CA-CA interfaces.

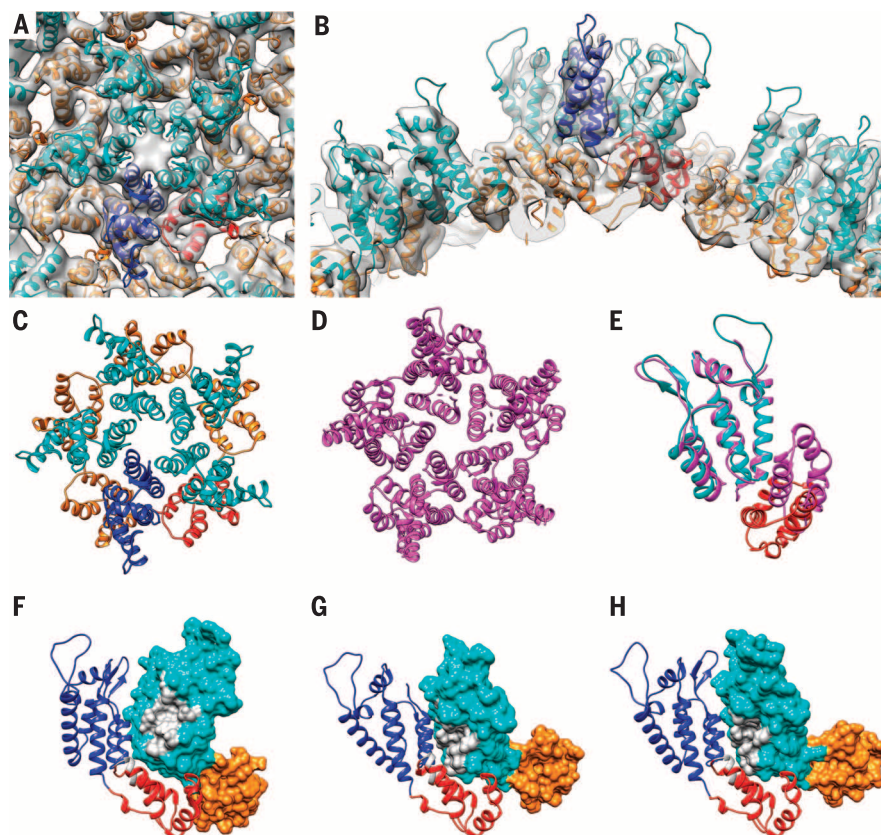
Forming a fullerene cone requires that the capsid incorporates 12 pentamers or pentameric defects. We analyzed the positions and arrangements of hexamers to identify the position and the orientation of pentamerically coordinated positions in the lattice. We extracted subtomograms at these positions and averaged them directly to generate a low-resolution structure in which a CA pentamer was clearly visible (fig. S5A), demonstrating that pentameric CA is present in the HIV-1 core. After further iterative alignment and averaging, we obtained a structure of the pentamer within HIV-1 at 8.8 Å resolution (Fig. 3, A and B, movie S4, and fig. S1). We placed CA monomers from our final hexameric CA structure into the pentameric EM map and flexibly fit them into the map to produce a structural model for the pentamer (Fig. 3, A to C).

Notably, the structure differs appreciably from the available crystal structure of in vitro cross-

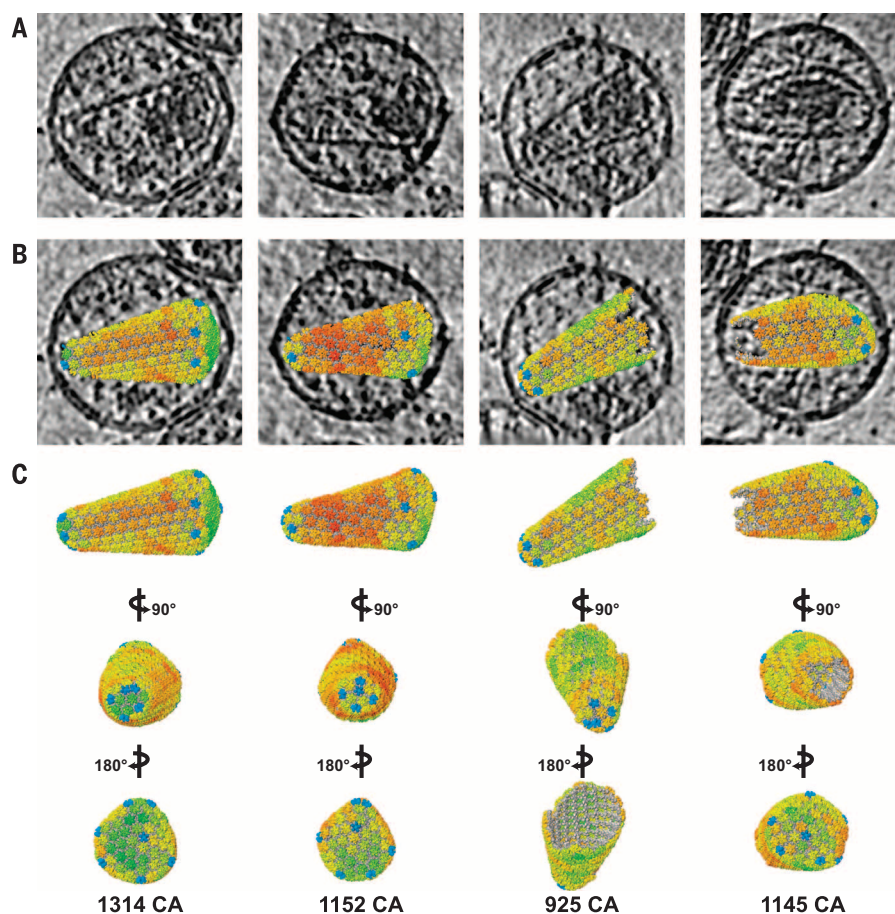
linked pentameric CA (12). The NTDs, organized around the fivefold axis, have undergone a rotation of $\sim 19^\circ$ relative to the hexameric conformation that excludes helix 3 from the interprotomer interface, resulting in a central 10-helix bundle where helix 1 interacts with helix 2 in the neighboring protomer (Fig. 3, C and D). Despite this difference, as in the crystal structure, the five arginine 18 residues are in close proximity in the center of the bundle, consistent with a proposed role for the charge state of arginine 18 in regulating the hexamer to pentamer transition (12). The relative positions of the CA domains have also changed, leading to a different NTD-CTD interface in the in-virus pentamer than in the cross-linked pentameric CA and the in-virus hexamer (Fig. 3E and movie S5). In the in-virus pentamer, the loop between helices 3 and 4 sits above helix 8 of the neighboring CTD, whereas the C-terminal part of helix 7 and a few residues from the NTD-CTD linker interact with helix 11 of the neighboring CTD. As a result, the pocket that exists in the hexamer between the two CA domains

Fig. 3. The structure of the CA pentamer.

(A) Cryo-ET reconstruction of the CA pentamer (gray isosurface) viewed from outside the core. The final structural model of the core pentamer is shown with the NTD in cyan and the CTD in orange. One monomer is highlighted in blue (NTD) and red (CTD). (B) As in (A), viewed perpendicular to the lattice. See also movie S4. (C) Our structural model of the pentamer, for comparison to (D) the crystal structure of the pentamer (PDB 3P05). (E) Comparison of the NTD-CTD interface in the pentamer (cyan/red), and in the pentamer crystal structure (magenta). (F) Two adjacent monomers within our in-virus pentamer, with one shown as a surface view. To illustrate how the NTD-CTD interface is opened up in the pentamer compared to the hexamer, the residues involved in the CPSF6 binding interface are colored in gray. (G) As in (F) for the two adjacent monomers in the cross-linked pentameric crystal structure. (H) As in (F) for two adjacent monomers in our hexamer. See also movie S5.

**Fig. 4. The arrangement of hexamers and pentamers in cores.**

(A) Computational slices through the tomographic reconstructions of four HIV-1 particles, two with complete conical cores (left columns), and two with incomplete cores (right columns). Other cores are illustrated in fig. S7. (B) As in (A), superimposed with the position and orientation of each aligned hexameric and pentameric unit, revealing the fullerene structure. The CTDs are colored gray; the NTDs of the hexameric units are colored according to the quality of their alignment from red (for low cross-correlation values) to green (for high cross-correlation values); the NTDs of the pentameric units are depicted in blue. (C) Three views of the cores. The number of copies of CA making up each of the illustrated cores is shown. See also movie S6.



and that is the binding site for cellular host factors is opened out, and the NTD face of the pocket is exposed (Fig. 3, F to H).

By solving the pentameric structure, we also visualized the interactions between the pentamer and the neighboring hexamers. We found that the pentamer-hexamer CA-CTD dimer interface is similar to that in the interhexamer interface, but that to accommodate the higher local curvature, the three helices (helix 10) around the threefold interface move closer together than in any of the hexamer-hexamer interfaces (fig. S4F).

For a subset of 107 cores, we analyzed the overall distribution of hexamers and pentamers identified during subtomogram averaging and applied a further multireference alignment step to minimize the number of false-negatives (Fig. 4 and figs. S6 and S7). The cores were mostly conical, but as expected, other morphologies were present, including tubular, polyhedral, and triangular shapes. Most of the cores showed one or more local regions where the CA lattice was disrupted or absent. These imperfections did not have characteristic shape, size, or location and were observed at the tip, side, and base of the core (Fig. 4 and fig. S7). We did not observe a recurrent seam along the longitudinal axis of the cores (19). The observed imperfections may represent assembly defects, or may result from damage during virus purification. In six cores, we observed complete, hexameric lattices closed by the insertion of 12 pentamers—they were perfect fullerene structures (Fig. 4, movie S6, and fig. S7) containing between 1122 and 1314 copies of CA. As predicted, the shape of the cores varied according to the distribution of pentamers. HIV CA is therefore able to assemble perfect, closed fullerene cones within virus particles. Although it is currently unclear whether imperfect cores can retain infectivity, we consider it reasonable to assume that correct CA assembly results in closed structures.

A recent report suggests that the core is formed by rewinding of the immature lattice in a non-diffusional manner, leading to pseudo-fullerene structures with strain defects such as seams (20). Our observations are inconsistent with this model. In most models for core assembly, the immature lattice disassembles upon maturation and the mature lattice assembles de novo from individual CA molecules or small multimers (21–25). Our observations are consistent with de novo polymerization of CA in a reversible manner that allows relaxation of the local structure during assembly (13). This would permit formation of perfect fullerene cones with only small, distributed changes in CA hexamer structure as observed here. We found that at sites of high curvature, pentamers are incorporated. These are stabilized by different CA-CA interaction interfaces than those in the hexamer. When perfect, the resulting core is tightly closed, preventing access of cellular components to the genetic material. On the outside of the core, pentamer and hexamer expose different parts of the CA protein surface to the cytoplasm during infection, which would allow them to interact differently and specifically with host cell factors.

REFERENCES AND NOTES

- W. I. Sundquist, H. G. Kräusslich, *Cold Spring Harb. Perspect. Med.* **2**, a006924 (2012).
- N. M. Bell, A. M. Lever, *Trends Microbiol.* **21**, 136–144 (2013).
- E. O. Freed, *Nat. Rev. Microbiol.* **13**, 484–496 (2015).
- S. Mattei, F. K. M. Schur, J. A. G. Briggs, *Curr. Opin. Virol.* **18**, 27–35 (2016).
- B. K. Ganser, S. Li, V. Y. Klishko, J. T. Finch, W. I. Sundquist, *Science* **283**, 80–83 (1999).
- B. K. Ganser-Pornillos, U. K. von Schwedler, K. M. Stray, C. Aiken, W. I. Sundquist, *J. Virol.* **78**, 2545–2552 (2004).
- S. Li, C. P. Hill, W. I. Sundquist, J. T. Finch, *Nature* **407**, 409–413 (2000).
- G. Zhao et al., *Nature* **497**, 643–646 (2013).
- O. Pornillos et al., *Cell* **137**, 1282–1292 (2009).
- A. T. Gres et al., *Science* **349**, 99–103 (2015).
- J. A. Briggs, T. Wilk, R. Welker, H. G. Kräusslich, S. D. Fuller, *EMBO J.* **22**, 1707–1715 (2003).
- O. Pornillos, B. K. Ganser-Pornillos, M. Yeager, *Nature* **469**, 424–427 (2011).
- J. M. A. Grime et al., *Nat. Commun.* **7**, 11568 (2016).
- W. J. H. Hagen, W. Wan, J. A. G. Briggs, *J. Struct. Biol.* **S1047-8477(16)30113-7** (2016).
- Materials and methods are available as supplementary materials on Science Online.
- O. Pornillos, B. K. Ganser-Pornillos, S. Banumathi, Y. Hua, M. Yeager, *J. Mol. Biol.* **401**, 985–995 (2010).
- D. A. Jacques et al., *Nature* **536**, 349–353 (2016).
- G. Obal et al., *Science* **349**, 95–98 (2015).
- Z. Yu et al., *J. Mol. Biol.* **425**, 112–123 (2013).
- G. A. Frank et al., *Nat. Commun.* **6**, 5854 (2015).
- J. Benjamin, B. K. Ganser-Pornillos, W. F. Tivol, W. I. Sundquist, G. J. Jensen, *J. Mol. Biol.* **346**, 577–588 (2005).
- J. A. Briggs et al., *Structure* **14**, 15–20 (2006).
- P. W. Keller et al., *J. Virol.* **87**, 13655–13664 (2013).
- C. L. Woodward, S. N. Cheng, G. J. Jensen, *J. Virol.* **89**, 1267–1277 (2015).
- A. Levandovsky, R. Zandi, *Phys. Rev. Lett.* **102**, 198102 (2009).

ACKNOWLEDGMENTS

We thank S. Dodonova, K. Qu, F. Schur, and W. Wan for technical assistance and discussion. This study was supported by Deutsche Forschungsgemeinschaft grants BR 3635/2-1 (to J.A.G.B.) and KR 906/7-1 (to H.-G.K.). The Briggs laboratory acknowledges financial support from the European Molecular Biology Laboratory and from the Chica und Heinz Schaller Stiftung. This study was technically supported by the European Molecular Biology Laboratory IT services unit. A representative tomogram, the EM structures, and the fitted models have been deposited in the Electron Microscopy Data Bank and the PDB. The database accession numbers are listed in table S3. S.M., H.-G.K., and J.A.G.B. designed the experiments. B.G. and S.M. prepared samples. W.H.J.H. implemented tomography acquisition schemes. S.M. acquired the data. S.M. performed image processing. S.M. and J.A.G.B. analyzed the data. S.M. and J.A.G.B. wrote the manuscript with support from all authors.

SUPPLEMENTARY MATERIALS

www.sciencemag.org/content/354/6318/1434/suppl/DC1
Materials and Methods

Figs. S1 to S7

Tables S1 to S3

Movies S1 to S6

References (26–39)

6 July 2016; accepted 18 November 2016

10.1126/science.aah4972

STRUCTURAL BIOLOGY

Translational termination without a stop codon

Nathan R. James, Alan Brown, Yuliya Gordiyenko, V. Ramakrishnan*

Ribosomes stall when they encounter the end of messenger RNA (mRNA) without an in-frame stop codon. In bacteria, these “nonstop” complexes can be rescued by alternative ribosome-rescue factor A (ArfA). We used electron cryomicroscopy to determine structures of ArfA bound to the ribosome with 3'-truncated mRNA, at resolutions ranging from 3.0 to 3.4 angstroms. ArfA binds within the ribosomal mRNA channel and substitutes for the absent stop codon in the A site by specifically recruiting release factor 2 (RF2), initially in a compact preaccommodated state. A similar conformation of RF2 may occur on stop codons, suggesting a general mechanism for release-factor-mediated translational termination in which a conformational switch leads to peptide release only when the appropriate signal is present in the A site.

In bacteria, 2 to 4% of mRNA transcripts lack an in-frame stop codon as a result of faulty transcription or nucleolytic cleavage (1). When translated, the inability to recruit release factors causes ribosomes to stall at the 3' end of these “nonstop” transcripts. Translating ribosomes also stall at the 3' end of intact transcripts when a stop codon is either read through or bypassed by translational frameshifting (2, 3). Because the accumulation of stalled ribosomes is potentially lethal (4), bacteria have evolved various

mechanisms to rescue these complexes (2, 3). Trans-translation is the primary rescue mechanism, present in nearly all sequenced bacterial species, and redirects ribosomes to resume translation on transfer-messenger RNA (tmRNA). The reading frame of tmRNA encodes a degradation signal with a stop codon, which results in both recycling of the stalled ribosome and proteolysis of the aberrant polypeptide. Trans-translation is a promising target for antibiotic development (4); however, any therapeutic approach would need to circumvent the backup mechanisms of alternative ribosome-rescue factors A (ArfA) and B (ArfB), which can allow some species of bacteria to survive in the absence of a functional trans-translation system (2, 3).

Medical Research Council (MRC) Laboratory of Molecular Biology, Francis Crick Avenue, Cambridge, CB2 0QH, UK.
*Corresponding author. Email: ramak@mrc-lmb.cam.ac.uk

ArfA, in particular, acts as a fail-safe for trans-translation in many bacterial species (5). In *Escherichia coli*, ArfA can support continued growth in the absence of trans-translation with few phenotypic consequences (5, 6). Under normal conditions, the *arfA* transcript is cleaved by ribonuclease (RNase) III to produce a nonstop mRNA substrate for trans-translation, resulting in the truncated ArfA protein being tagged for degradation (7–9), although a small constitutively expressed population of full-length ArfA may result from the translation of uncleaved *arfA* transcripts (7). When trans-translation is impaired or overwhelmed, full-length ArfA may rescue the synthesis of its truncated form. ArfA relieves stalled ribosomes through a mechanism that requires peptidyl-tRNA hydrolysis by release factor 2 (RF2) but not the paralogous release factor 1 (RF1) (10, 11). This is in contrast to ArfB, which shares homology with the catalytic domains of these release factors and is able to directly hydrolyze peptidyl tRNA within stalled ribosomes (12).

To understand how RF2 functions with ArfA instead of a stop codon, we solved the structure of the *E. coli* ribosome programmed with a 3'-truncated mRNA (figs. S1 and S2 and table S1), and in complex with ArfA and RF2 (Fig. 1A) or ArfA(A18T) and RF2 (Fig. 1B), by electron cryo-microscopy to resolutions between 3.0 and 3.4 Å. The amino acid substitution A18T (Ala¹⁸→Thr¹⁸) abolishes the ability of ArfA to support peptidyl-tRNA hydrolysis (5), although the mutant can still bind and recruit RF2 to stalled ribosomes (5, 11). The structures reveal two distinct conformations of RF2 on the ribosome and explain how ArfA specifically recognizes nonstop complexes.

In both structures, ArfA interacts with the decoding-center nucleotides G530 and A1492 of the 16S ribosomal RNA (rRNA) (Fig. 2). A1492 is stacked within helix 44, interacting with ArfA via the rRNA backbone, whereas A1493 is flipped out and disordered. These nucleotides are unchanged from their positions in an unoccupied A site (Fig. 2A), suggesting that ArfA specifically recognizes a vacant decoding center. ArfA does not induce the remodeling of the decoding center, in particular the flipping-out of A1492, which occurs during stop-codon recognition (Fig. 2D).

The C terminus of ArfA protrudes into the otherwise-unoccupied mRNA channel downstream of the decoding center and, in agreement with hydroxyl radical probing data (13), contacts the rRNA that lines it (Fig. 3A). The conserved KKGKS motif (fig. S3A, residues 34 to 37) forms an expansive helical turn within the channel that may help to anchor ArfA to the ribosome (Fig. 3B). Below the turn, ArfA binds first to helix 1 of the 16S rRNA and then to helix 18 on the opposite wall of the mRNA channel (Fig. 3B). The C terminus beyond Gly⁴⁶ exits through the channel entrance and makes few contacts with the ribosome. This is consistent with the last ~18 residues being truncated as a result of RNase III cleavage and dispensable for ribosome rescue (8).

The positioning of the C-terminal tail suggests that ArfA may discriminate against translating ribosomes by recognizing vacant mRNA channels. A similar hypothesis has been proposed for small protein B (SmpB), which is delivered to the ribosome with tmRNA (14), and ArfB (12). SmpB and ArfB both have C termini that insert into the mRNA channel, although these tails and their interactions with the ribosome are distinct from that of ArfA (fig. S4). A discriminatory role for the ArfA C terminus is consistent with the marked decline of ArfA-dependent peptide release as the 3' length of mRNA increases (11, 15). However, recent data have shown that ArfA can bind ribosomes, and even recruit RF2, regardless of the presence of mRNA in the channel (13). This suggests that simultaneous occupancy of the channel may be possible, but only in the absence of mRNA can ArfA position RF2 in a productive conformation for peptidyl-tRNA hydrolysis.

The basis for RF2 recruitment is provided by ArfA residues 25 to 30, which form a β -addition motif with the $\beta 5$ strand of RF2 domain 2 (Fig. 3C). Phe²⁵ of ArfA protrudes into a conserved hydrophobic pocket of RF2 formed by Val¹⁹⁸ from the $\beta 4$ strand and Phe²¹⁷ from the $\beta 5$ strand (Fig. 3C). This pocket is absent in RF1 from all known ArfA-containing species (fig. S3, B and C), likely explaining the exclusivity of ArfA for RF2 (10, 11). The RF2 recognition loop between the $\beta 4$ and $\beta 5$ strands that confers stop-codon speci-

ficity (16) faces the solvent and does not interact with ArfA.

With wild-type (WT) ArfA, RF2 adopts an extended conformation that resembles the crystal structures of release factors bound to stop codons (16–20) (Fig. 1A). Consistent with a shared mechanism of catalysis for canonical and ArfA-mediated termination, the catalytic GGQ motif of domain 3 is accommodated within the peptidyl-transferase center (PTC) (Fig. 1A, inset). By contrast, RF2 adopts a compact conformation with ArfA(A18T) that resembles the crystal structures of isolated release factors (21–23), the only difference being the position of domain 1. In this preaccommodated conformation, domain 3 lies across an eight-stranded β sheet formed by domains 2 and 4, with the GGQ motif facing the anticodon arm of the P-site tRNA approximately 60 Å from the PTC (Fig. 1B).

A preaccommodated conformation of release factors on ribosomes has previously been proposed as an initial codon-sampling state during stop-codon recognition (17, 18). This hypothesized state rationalizes the compact release-factor form seen in three different crystal structures (21–23) and in solution by small-angle x-ray scattering (SAXS) (23), although another SAXS study observed only the extended conformation (24). Further support for a physiological role of the compact form comes from hydroxyl radical probing (25) and fluorescence resonance energy transfer (26) experiments that show discrete release-factor

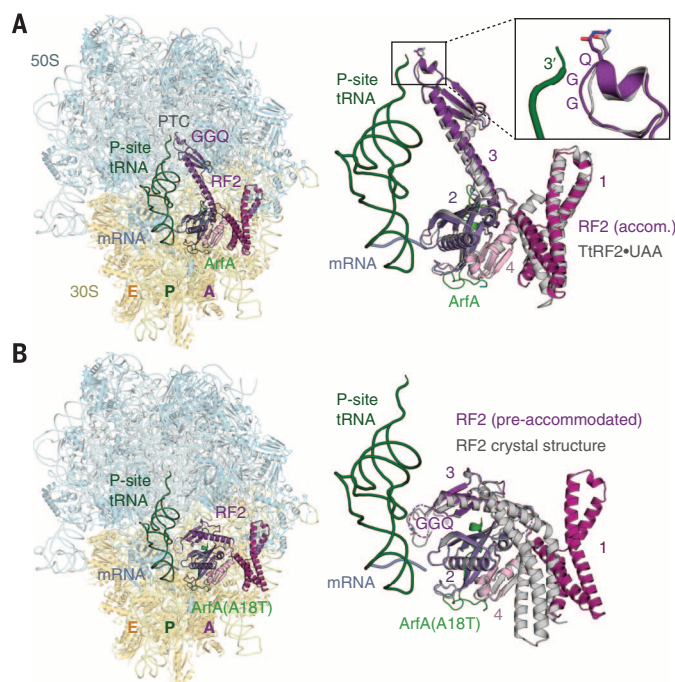


Fig. 1. Structures of nonstop complexes recognized by ArfA and ArfA(A18T). (A) Overview of the bacterial ribosome with a 3'-truncated mRNA in complex with ArfA and RF2 (left). ArfA and RF2 occupy the A site, with a nonhydrolyzable aminoacyl tRNA in the P site. RF2 adopts a similar conformation on the ribosome with ArfA as with a UAA stop codon (right). The catalytic GGQ motif of RF2 domain 3 is accommodated within the peptidyl-transferase center (PTC) (inset). (B) Overview of a nonstop complex recognized by ArfA(A18T) (left). Preaccommodated RF2 resembles the isolated RF2 crystal structure (Protein Data Bank ID 1GQE) (right). The GGQ motif faces the P-site tRNA. Movement of domain 1 results from contacts with the L7/L12 stalk base.

conformations on the ribosome, depending on the identity of the A-site codon. However, due to its presumably transient nature, structural data for a codon-sampling state are lacking.

Here, the preaccommodated conformation results from the A18T substitution, which prevents the interdependent folding of the ArfA N terminus with the switch loop of RF2. The switch loop connects the $\alpha 7$ helix of domain 3 with the $\beta 9$ strand of domain 4 and has been proposed to mediate accommodation during canonical termination by undergoing a disorder-to-order transition (19). In the mutant structure,

the RF2 switch loop and the first 14 residues of ArfA are disordered. A18T is located within the α helix of ArfA that packs against the central β sheet of RF2 but faces away from the interface (Fig. 4A). However, the ordered N terminus of WT ArfA turns tightly to run antiparallel to this α helix (Fig. 4B). Compared with alanine, a polar threonine residue would be unable to pack against Ile¹¹ in this conformation (Fig. 4B). By contrast, a hydrophobic A18C (Ala¹⁸→Cys¹⁸) substitution has little effect on ArfA activity (13).

The ordered N terminus of WT ArfA induces conformational changes in the RF2 switch loop.

As also occurs in stop-codon recognition (16, 19), the switch loop becomes partially α -helical, extending the $\alpha 7$ helix (Fig. 4B). This is followed by a $\sim 100^\circ$ kink as the conserved Trp³¹⁹ residue interacts with ArfA at the RF2-specific hydrophobic pocket (Fig. 3C). An additional α -helical turn leads into the $\beta 9$ strand. Compression of the switch loop draws the $\alpha 7$ helix, together with the rest of domain 3, from its interface with domain 2 such that the GGQ motif rises and accommodates into the PTC (Fig. 4C).

Upon accommodation, there is also a $\sim 10^\circ$ rotation of RF2 domains 2 and 4 (Fig. 4C), which increases the interface with the ribosome by 25%. Together with a movement of the ArfA α helix, these changes result in a tighter fit between ArfA, RF2, and the decoding center. The decoding nucleotide A1492 of the 16S rRNA switches from a syn to an anti configuration within helix 44 (Fig. 2C) and stacks with A1913 at the apex of helix 69 of the 23S rRNA. This may help to reposition helix 69, allowing C1914 to coordinate the turn adopted by ArfA residues 11 to 14 (Fig. 4B). The movement of domain 2 appears to pull domain 1, together with the L7/L12 stalk base, into closer contact with the small subunit, possibly stabilizing RF2 in its accommodated state (fig. S5A).

To further explore the interaction between ArfA and the switch loop, we examined the compatibility of WT ArfA from *E. coli* with *Thermus thermophilus* RF2 (TtRF2), which has a distinct switch-loop composition (Fig. 4D). The structure shows that, although TtRF2 is recruited to stalled ribosomes through the conserved hydrophobic pocket with ArfA, it adopts a compact conformation similar to that of *E. coli* RF2 recruited by ArfA (A18T) (Fig. 4D), and the N terminus of ArfA remains disordered. The inability to accommodate

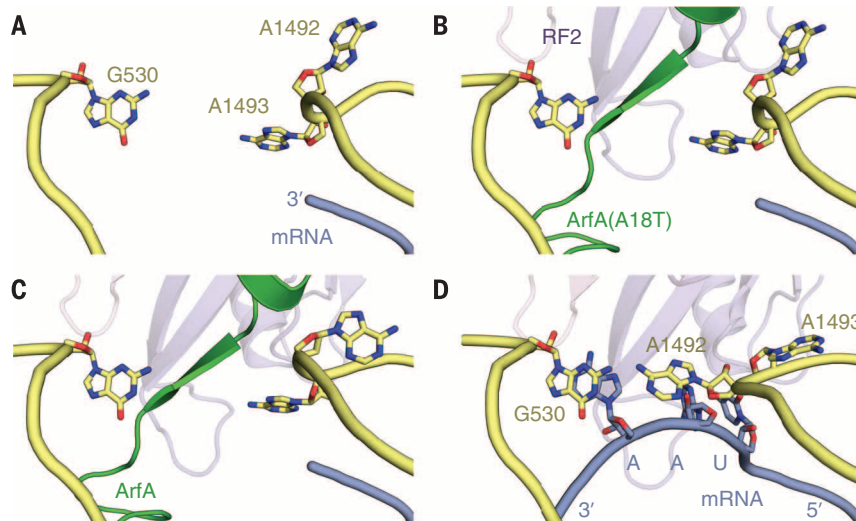


Fig. 2. Conformations of the decoding nucleotides. (A) Conformation of the decoding center with an unoccupied A site. A1493 is disordered in this and all ArfA-containing structures. (B) ArfA(A18T) recognizes a vacant A site and does not remodel the decoding center. (C) Closer contacts between WT ArfA, RF2, and the ribosome cause A1492 to switch from a syn to an anti configuration. (D) Canonical termination on a UAA stop codon involves remodeling of the decoding center that does not occur with ArfA.

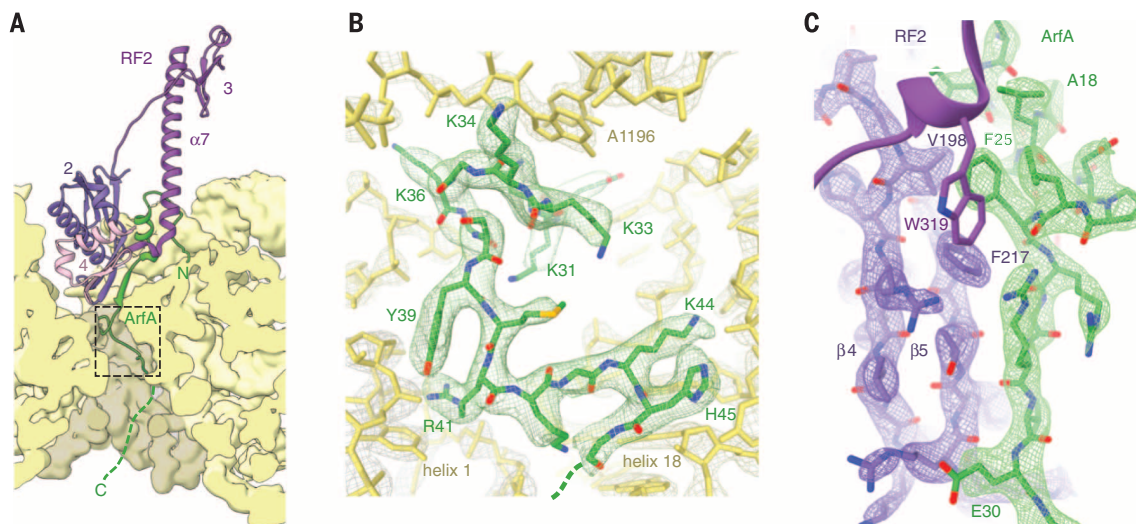


Fig. 3. Interactions between ArfA, RF2, and the ribosome. (A) The N-terminal half of ArfA binds RF2 while the C-terminal tail occupies the mRNA channel. The path of ArfA as it emerges from the channel entrance, which can be traced in unfiltered maps, is indicated with a green dashed line. The boxed area indicates the region of ArfA shown in (B). (B) Interactions between ArfA and the rRNA lining the mRNA channel for the region highlighted in (A), as viewed from the channel entrance. (C) Both WT ArfA and

ArfA(A18T) form an antiparallel β sheet with domain 2 of RF2. F25 packs against an RF2-specific hydrophobic pocket formed by V198 and F217. With WT ArfA, this pocket is also recognized by W319 from the switch loop of accommodated RF2. Single-letter abbreviations for the amino acid residues are as follows: A, Ala; C, Cys; D, Asp; E, Glu; F, Phe; G, Gly; H, His; I, Ile; K, Lys; L, Leu; M, Met; N, Asn; P, Pro; Q, Gln; R, Arg; S, Ser; T, Thr; V, Val; W, Trp; and Y, Tyr.

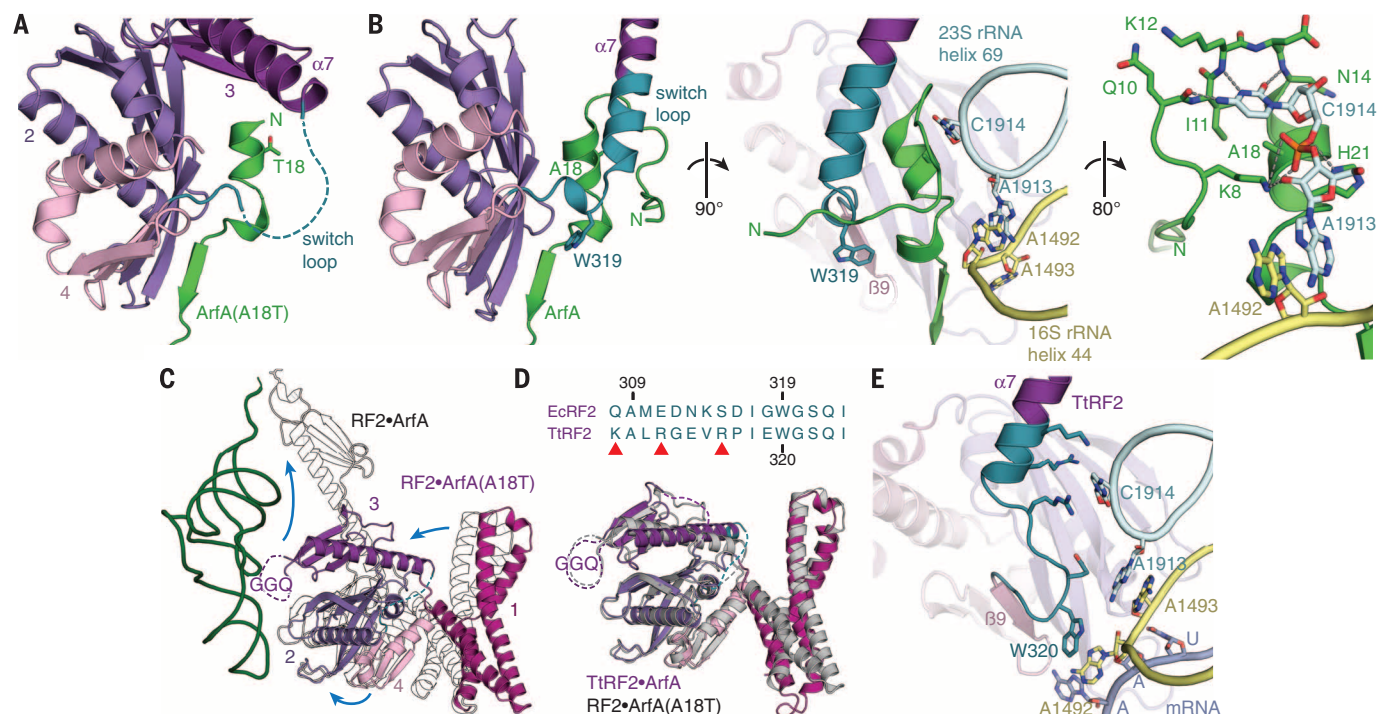


Fig. 4. Switch-loop stabilization and RF2 accommodation. (A) In the structure of the nonstop complex recognized by ArfA(A18T), the first 14 residues of ArfA(A18T) and the switch loop between domains 3 and 4 of RF2 are disordered. (B) In the structure with WT ArfA, the ordered N terminus of ArfA helps to stabilize the switch loop of RF2, which extends the $\alpha 7$ helix. A1913 from helix 69 of the 23S rRNA stacks with A1492 from helix 44 of the 16S rRNA, while C1914 from helix 69 stabilizes residues 10 to 14 of ArfA. (C) RF2 recruited by ArfA(A18T) adopts a compact conformation with the GGQ loop disordered

and facing the P-site tRNA. Superposition with accommodated RF2 (outlined) reveals that all four domains move during accommodation. (D) TtRF2 has a switch-loop composition (top) incompatible with ArfA and adopts a pre-accommodated conformation on the ribosome (bottom), similar to *E. coli* RF2 recruited by ArfA(A18T). Red arrowheads denote residues of TtRF2 with long side chains that would clash with ArfA. (E) During stop-codon recognition, the switch loop of TtRF2 is stabilized by interactions that are dependent on the stop-codon-induced remodeling of the decoding center.

presumably results from clashes between ArfA and the longer side chains of the TtRF2 switch loop. Taken together, our structures demonstrate that accommodation of RF2 is dependent on switch-loop stabilization by the ArfA N terminus.

These switch-loop interactions appear to emulate the interactions between RF2 and the ribosome that result from stop-codon-dependent rearrangement of the decoding center (Fig. 4E). During canonical termination, the conserved tryptophan of the switch loop stacks with flipped-out A1492 while the $\alpha 7$ -helix extension interacts directly with helix 69, which adopts a different conformation when A1492 is flipped out (16, 20).

The delivery of RF2 in a preaccommodated state, followed by a conformational switch that depends on specific changes in the decoding center, shares many parallels with the universal elongation (27) and eukaryotic termination pathways (28) (fig. S5, B and C). Both aminoacyl tRNAs and the structurally unrelated eukaryotic release factor 1 (eRF1) adopt preaccommodated conformations during codon sampling that prevent premature engagement of reactive groups with the PTC before accommodating into the PTC upon codon recognition. A similar pathway for bacterial release factors is consistent with a 4000-fold difference in dissociation rates between stop and sense codons, despite similar association rates (29), and may explain the accuracy of termination in bacteria ($\sim 10^{-5}$), which

is comparable to the fidelity of aminoacyl-tRNA selection (30).

In summary, our structures reveal the mechanism of ArfA-mediated ribosome rescue on 3'-truncated mRNA and provide insights into how a conserved conformational switch might maintain the accuracy of translational termination in bacteria.

REFERENCES AND NOTES

1. K. Ito et al., *PLOS ONE* **6**, e28413 (2011).
2. K. C. Keiler, *Nat. Rev. Microbiol.* **13**, 285–297 (2015).
3. E. Giudice, R. Gillet, *Trends Biochem. Sci.* **38**, 403–411 (2013).
4. N. S. Ramadoss et al., *Proc. Natl. Acad. Sci. U.S.A.* **110**, 10282–10287 (2013).
5. Y. Chadani et al., *Mol. Microbiol.* **78**, 796–808 (2010).
6. Y. Komine, M. Kitabatake, T. Yokogawa, K. Nishikawa, H. Inokuchi, *Proc. Natl. Acad. Sci. U.S.A.* **91**, 9223–9227 (1994).
7. Y. Chadani et al., *Genes Genet. Syst.* **86**, 151–163 (2011).
8. F. Garza-Sánchez, R. E. Schaub, B. D. Janssen, C. S. Hayes, *Mol. Microbiol.* **80**, 1204–1219 (2011).
9. R. E. Schaub, S. J. Poole, F. Garza-Sánchez, S. Benbow, C. S. Hayes, *J. Biol. Chem.* **287**, 29765–29775 (2012).
10. Y. Chadani, K. Ito, K. Kutsukake, T. Abo, *Mol. Microbiol.* **86**, 37–50 (2012).
11. Y. Shimizu, *J. Mol. Biol.* **423**, 624–631 (2012).
12. M. G. Gagnon, S. V. Seetharaman, D. Bulkley, T. A. Steitz, *Science* **335**, 1370–1372 (2012).
13. D. Kurita, Y. Chadani, A. Muto, T. Abo, H. Himeno, *Nucleic Acids Res.* **42**, 13339–13352 (2014).
14. C. Neubauer, R. Gillet, A. C. Kelley, V. Ramakrishnan, *Science* **335**, 1366–1369 (2012).
15. F. Zeng, H. Jin, *RNA* **22**, 49–60 (2016).
16. A. Weixlbaumer et al., *Science* **322**, 953–956 (2008).
17. U. B. S. Rawat et al., *Nature* **421**, 87–90 (2003).
18. B. P. Klaholz et al., *Nature* **421**, 90–94 (2003).
19. M. Laurberg et al., *Nature* **454**, 852–857 (2008).

20. A. Korostelev et al., *Proc. Natl. Acad. Sci. U.S.A.* **105**, 19684–19689 (2008).
21. B. Vestergaard et al., *Mol. Cell* **8**, 1375–1382 (2001).
22. D. H. Shin et al., *J. Mol. Biol.* **341**, 227–239 (2004).
23. G. Zöldák et al., *Nucleic Acids Res.* **35**, 1343–1353 (2007).
24. B. Vestergaard et al., *Mol. Cell* **20**, 929–938 (2005).
25. S. L. He, R. Green, *Nat. Struct. Mol. Biol.* **17**, 465–470 (2010).
26. K. Trapp, S. Joseph, *J. Mol. Biol.* **428**, 1333–1344 (2016).
27. R. M. Voorhees, V. Ramakrishnan, *Annu. Rev. Biochem.* **82**, 203–236 (2013).
28. S. Shao et al., *Cell* **167**, 1229–1240 (2016).
29. B. Hetrick, K. Lee, S. Joseph, *Biochemistry* **48**, 11178–11184 (2009).
30. D. V. Freistuffer, M. Kwiatkowski, R. H. Buckingham, M. Ehrenberg, *Proc. Natl. Acad. Sci. U.S.A.* **97**, 2046–2051 (2000).

ACKNOWLEDGMENTS

We thank Y. Shimizu for providing the arfA clone, A. C. Kelley for providing tRNA, R. S. Hegde for providing *E. coli* RF2, S. H. W. Scheres for help with RELION-2.0, J. Grimmett and T. Darling for computing support, and C. D. Rae and S. Shao for comments. The work was supported by grants to V.R. from the UK MRC (MC_U105184332), the Wellcome Trust (WT096570), the Agouron Institute, and the Louis-Jeantet Foundation. The maps have been deposited with the Electron Microscopy Data Bank under the accession codes EMD-3489, EMD-3490, EMD-3492, and EMD-3493. Atomic coordinates have been deposited with the Protein Data Bank under IDs 5MDV, 5MDW, 5MDY, and 5MDZ.

SUPPLEMENTARY MATERIALS

www.sciencemag.org/content/354/6318/1437/suppl/DC1
Materials and Methods
Figs. S1 to S5
Table S1
References (31–50)

30 August 2016; accepted 17 November 2016
Published online 1 December 2016
10.1126/science.aai9127

PROTEIN ENGINEERING

Engineering extrinsic disorder to control protein activity in living cells

Onur Dagliyan,^{1,2,3} Mirosław Tarnawski,⁴ Pei-Hsuan Chu,³ David Shirvanyants,² Ilme Schlichting,⁴ Nikolay V. Dokholyan,^{1,2*} Klaus M. Hahn^{3*}

Optogenetic and chemogenetic control of proteins has revealed otherwise inaccessible facets of signaling dynamics. Here, we use light- or ligand-sensitive domains to modulate the structural disorder of diverse proteins, thereby generating robust allosteric switches. Sensory domains were inserted into nonconserved, surface-exposed loops that were tight and identified computationally as allosterically coupled to active sites. Allosteric switches introduced into motility signaling proteins (kinases, guanosine triphosphatases, and guanine exchange factors) controlled conversion between conformations closely resembling natural active and inactive states, as well as modulated the morphodynamics of living cells. Our results illustrate a broadly applicable approach to design physiological protein switches.

Proteins have been engineered to respond to light or small molecules in living cells through a number of mechanisms, including oligomerization (1–4), control of targeting sequences (1, 5, 6), split proteins (2), sterically blocking the active site (1, 7, 8), and engineered allosteric control (9–13). Engineering allostery has the potential to be especially versatile and valuable, as sensory domains can be inserted where they do not interfere with normal protein interactions, more readily producing fully functional analogs to replace endogenous protein. Allosteric sites have been identified by using both screening approaches (10, 14) and rational analysis of sequence conservation (10, 11). A number of domains, including the light-sensitive LOV2 domain (11) and drug-responsive uniRapR domain (12, 13) used here, have been applied. Nonetheless, it remains challenging to identify allosteric sites by rational analysis and to produce reversible, robust allosteric switches that have on and off states that replicate natural levels of protein activity. Here, we present a generalizable approach to identify surface loops where the disorder of the attached domain can be effectively transferred to the active site in a controlled fashion (harnessing extrinsic disorder) (9, 10, 12–15), to produce on and off states that mimic naturally occurring protein states.

In previous work, we identified an allosteric site in kinases where insertion of an engineered domain (uniRapR) conferred rapamycin-induced kinase activation (12, 13). Insertion of the uniRapR domain rendered kinases catalytically inactive until the domain bound rapamycin (12, 13, 16). Molecular

dynamics simulations indicated that the protein loop containing the insertion site was mechanically coupled to the adenosine triphosphate-binding site (13). We hypothesized that insertion of a light-responsive domain at the same site could lead to optogenetic control of kinases (Fig. 1A). We chose the LOV2 domain because the 10 Å spacing between its N and C termini enabled us to insert the domain with minimal perturbation into a loop (Fig. 1B) that connects parts of a tightly folded structural unit (two interacting antiparallel β -strands). The spacing between LOV2's termini becomes much more flexible upon irradiation, because of disordering of terminal helices (17, 18); this could perturb the conformation of the loop and the β -strands. Introducing disorder into the loop would cause protein inhibition, rather than the activation caused by rapamycin-induced folding of the uniRapR domain (fig. S1). The light-induced conformational changes in LOV2 (3.8 kcal/mol of free energy) (19) should be more than sufficient to disorder portions of host proteins (fig. S2), whose overall stabilities are on the order of 5 to 15 kcal/mol (20).

We focused on Src kinase because of evidence that its activity is controlled by spatiotemporal dynamics in vivo (16, 21). The LOV2 domain was inserted at Gly²⁹⁶ (G296) of a constitutively active Src mutant (Phe⁵³⁵ replaces Tyr⁵³⁵, YF). We named the new Src analog PI-Src, for photo-inhibitable Src. In vitro kinase activity assays revealed that this LOV2-Src fusion was indeed strongly inhibited upon exposure to blue light (Fig. 1C). Light had no effect on the activity of kinase dead (KD) or constitutively active (YF) Src. Inhibition was not sensitive to small variations in linker length (fig. S3). To test PI-Src in living cells, we generated SYF cells (cells lacking the Src family members Src, Yes, and Fyn) expressing PI-Src(YF). Phosphotyrosine blots of cell lysates showed that irradiation inhibited phosphorylation of multiple Src substrates (Fig. 1C and fig. S4). Consistent with Src's reported roles in motility (13, 16, 21), irradiation reduced migration rates and caused reversible collapse of

lamellipodia (fig. S5 and movie S1). Similar effects were produced by the Src inhibitor PP2 (fig. S5 and movie S2).

To investigate how distortion of the insertion loop led to a reduction in kinase activity, we built a structural model of PI-Src, and examined its light-induced conformational changes using discrete molecular dynamics (22, 23). Although we expected to observe randomly distorted conformations of PI-Src in the lit state, we saw instead that the active and inactive states of PI-Src were strikingly similar to the crystal structures of active and inactive wild-type (WT) Src (correlation coefficient = 0.82) (Fig. 1D). This suggested that irradiation shifts PI-Src from its physiological active state to a conformation strongly resembling Src's native inactive state (fig. S6).

The physiologically relevant conformations of PI-Src raised the possibility of examining how Src controls the motility of living cells. We generated SYF cells expressing PI-Src(WT). In the dark, PI-Src(WT) showed the perinuclear distribution (Fig. 1E) typical of endogenous, inactive Src (16). Upon irradiation, the PI-Src translocated to focal adhesions at the cell periphery and induced changes in cell morphodynamics (increased protrusion and retraction, polarization, and polarized movement in some cases) (movie S3). Returning the cells to the dark reversed focal adhesion localization (Fig. 1E) but not effects on cell morphodynamics (fig. S7). It is thought that Src localization to focal adhesions is mediated by Src SH2-SH3 domains and is not dependent on kinase activity (24, 25). The light-induced distortion of the catalytic domain that inhibits the kinase may also perturb autoinhibitory interactions, exposing the SH2 and SH3 domains; this likely generated the reversible focal adhesion localization we observed and suggested that focal adhesion localization was sufficient to affect cell morphodynamics even without catalytic activity. In support of this hypothesis, we found that PI-Src(KD) also translocated reversibly to adhesions and induced changes in morphodynamics upon irradiation and that elimination of the SH2 and SH3 domains from PI-Src (KD) prevented both focal adhesion localization and effects on cell morphodynamics (fig. S7). Movement away from focal adhesions, which occurred 30 to 40 s after irradiation was halted, indicated that the conformational change of PI-Src was reversible in cells (fig. S7) and was consistent with LOV2's rate of return to the dark conformation ($t_{1/2}$ = 18.5 s at 37°C in cells) (26). In contrast, effects on cell morphodynamics were retained for >20 min after irradiation was halted, potentially because of feedback kinetics and/or inactivation pathways not involving Src.

Controlling protein activity via LOV2 insertion would be much more valuable if it could be readily applied to multiple-protein families. We tested a more generalizable approach by identifying an allosteric site for LOV2 insertion in the Rho family guanosine triphosphatase (GTPase) Rac1. We focused on surface-exposed and evolutionarily nonconserved loops to avoid possible structural perturbations and asked whether these loops were mechanically coupled to the active site. For the

¹Program in Molecular and Cellular Biophysics, University of North Carolina at Chapel Hill, Chapel Hill, NC 27599, USA.

²Department of Biochemistry and Biophysics, University of North Carolina at Chapel Hill, Chapel Hill, NC 27599, USA.

³Department of Pharmacology and Lineberger Comprehensive Cancer Center, University of North Carolina at Chapel Hill, Chapel Hill, NC 27599, USA. ⁴Department of Biomolecular Mechanisms, Max Planck Institute for Medical Research, Jahnstrasse 29, 69120 Heidelberg, Germany.

*Corresponding author. Email: khahn@med.unc.edu (K.M.H.); dokh@email.unc.edu (N.V.D.)

Fig. 1. Design concept and PI-Src. (A) Domains conferring either photoinhibition (LOV2), or activation induced by small molecules (uniRapR), function at the same allosteric site. (B) The termini of LOV2 and uniRapR domains are closely spaced for insertion. (C) Paxillin phosphorylation assays show that PI-Src's catalytic activity is inhibited upon irradiation. SYF cells expressing PI-Src(YF) show reduced phosphorylation of cell lysates blotted with antibody against phosphorylated Tyr (anti-pTyr). Blue denotes irradiation. Error bars show SEM ($n = 3$). (D) (Left) Inactive (blue) and active (gray) conformations of WT Src. The red circle (L) is the insertion site. Conformational changes were quantified by displaying the pairwise distance changes (Δd) between all residues as a heat map. (Right) The top left triangle shows distances for WT Src, computed from published crystal structures. The bottom triangle shows distances for PI-Src, determined using molecular dynamics simulations of the dark and lit states. Decreased distance (blue); increased distance (red). (E) In SYF cells, irradiation causes PI-Src(WT) to translocate to focal adhesions (FA, red arrows), edge movements to increase, and cells to polarize and translocate. When cells are returned to the dark, FA translocation is reversed but effects on morphodynamics persist. [Irradiation (blue); $n = 18$ cells; quantification in fig. S7.]

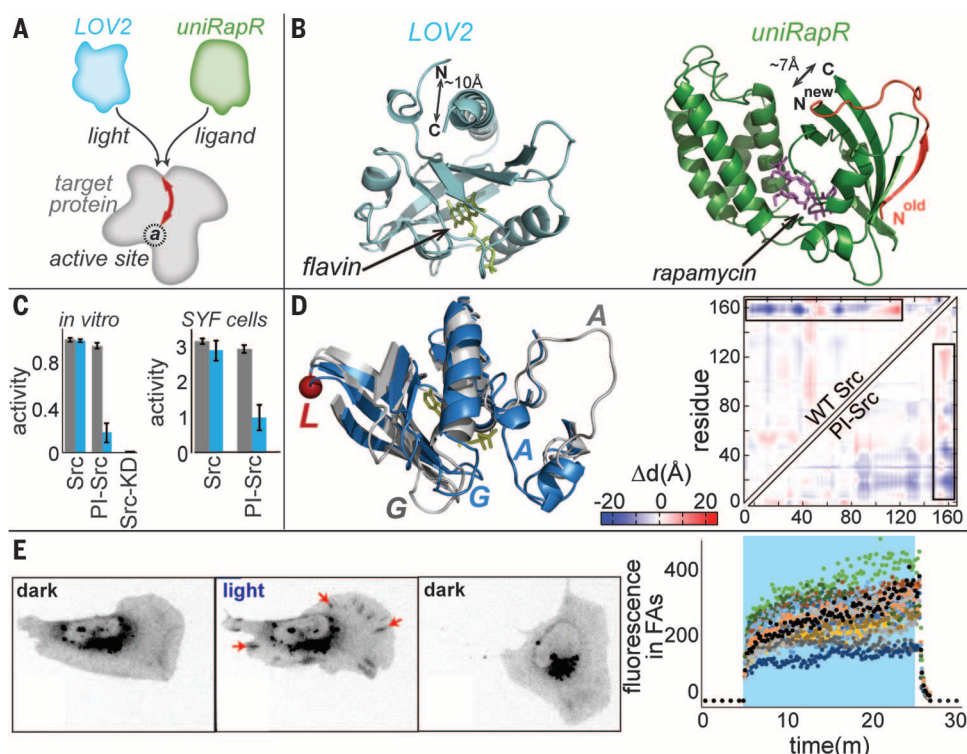
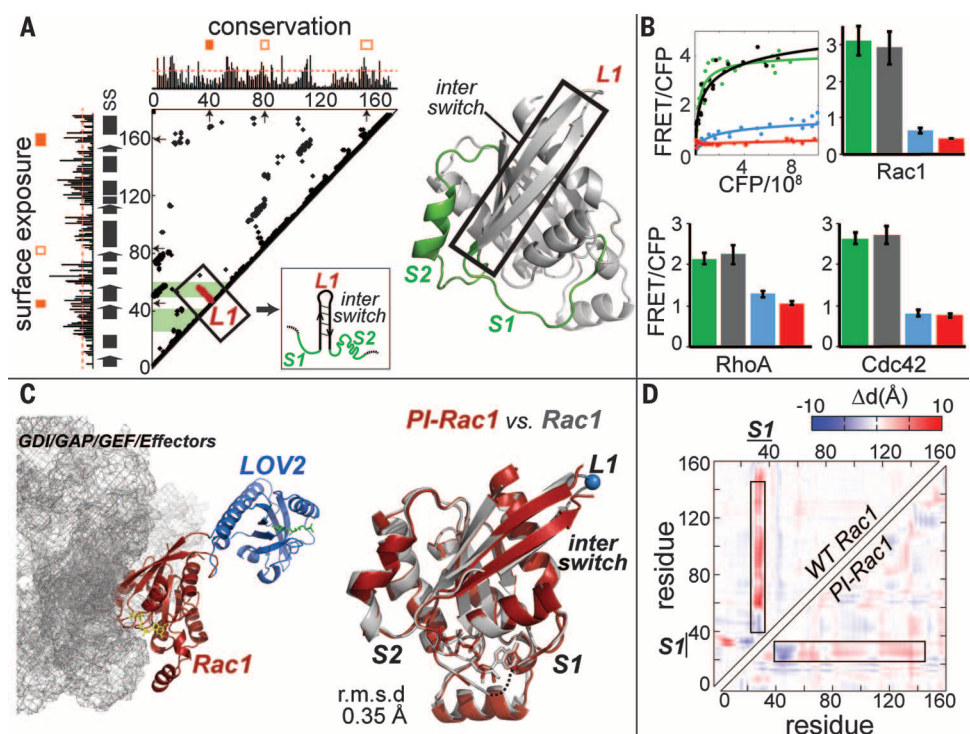


Fig. 2. Designing PI-GTPases. (A) Sequence conservation, surface exposure, loop "tightness," and contact maps were used to select insertion loops (fig. S9). Orange-filled boxes indicate loops fulfilling selection criteria [thresholds (red dashed lines); (box) S_1 and S_2 , secondary structures]. In the scheme, lines extending perpendicular to the diagonal indicate loops (L) that connect tightly interacting elements of secondary structure. When these lines reached the active site (green bands) the loop was selected for testing. For PI-Rac1, we selected L1, which connects strands of the β -pleated sheet in the interswitch region. (B) GTPase activity in HEK293T cells reported using biosensors fused to PI-GTPases in a high-throughput assay. Dark-state mutant (gray); lit-state mutant (blue); T17N (Rac1 and Cdc42) and T19N (RhoA) dominant-negative mutants (red); wild-type GTPase-positive control (green). CFP x axis indicates expression level of biosensor-GTPase fusion. Error bars show SEM ($n = 3$). (C) (Left) Crystal structure of PI-Rac1 with interacting proteins (gray mesh); (right) structures of WT Rac1 (gray) and PI-Rac1 (red) are in excellent agreement. L1 loop is the LOV2 insertion loop. GDI, guanine nucleotide dissociation inhibitor; GAP, GTPase-activating protein. (D) Map showing interresidue distances for WT Rac1 versus PI-Rac1, which suggest that these molecules undergo similar conformational changes.



kinase analogs above, we found that both dynamic coupling analysis (12) and a static contact map analysis (figs. S8 and S9) were effective in identifying mechanically coupled loops. (The latter

offers a simpler approach accessible to many laboratories.) Dynamic coupling and static contact map analyses indicated several loops in Rac1 (Fig. 2A and fig. S10); however, much of

the surface of Rac1 is used to interact with other proteins, which limits the loops appropriate for insertion. Considering all these criteria, we selected loop L1, which connects β -strands between

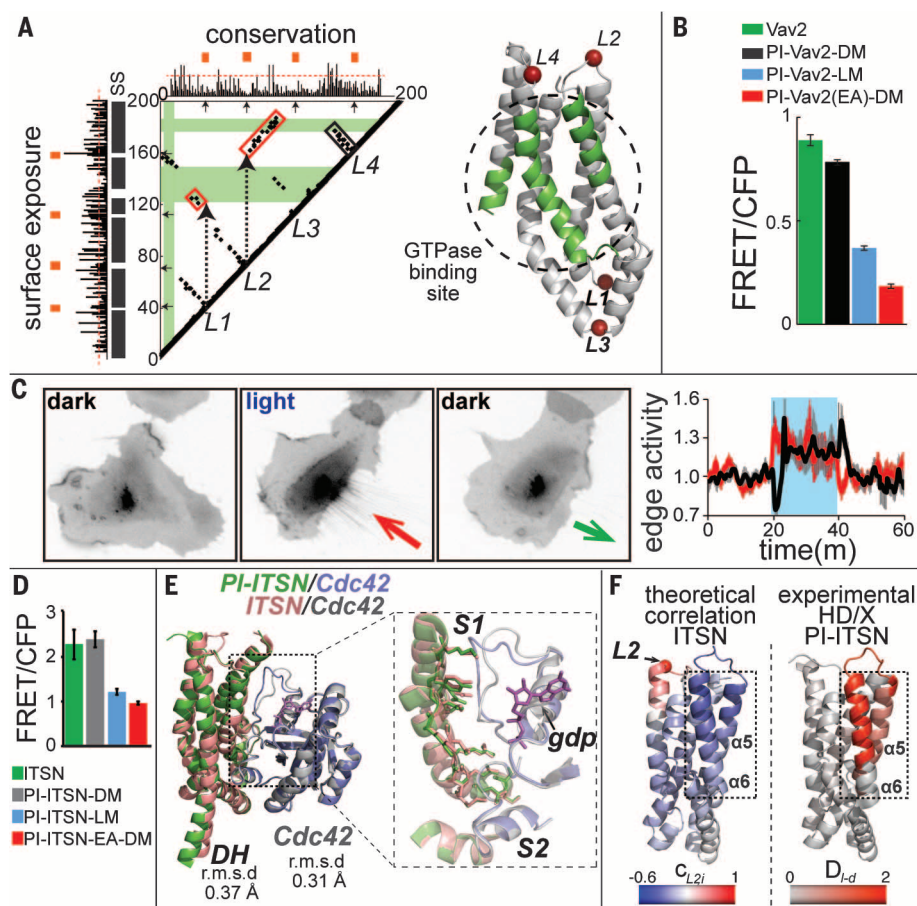


Fig. 3. Designing PI-GEFs. (A) Computational analysis of the Vav2 catalytic DH domain. (Left) Black and red boxes indicate local and nonlocal interactions (fig. S9) that mediate coupling between loops and the active site. (Right) Structural model of the Vav2 DH domain showing insertion loops and the active site (green). (B) In living cells, PI-Vav2 was inhibited in the lit state. DM and LM, dark and lit mutants; EA, E200A/K333A dominant-negative mutant. Error bars show SEM ($n = 3$). (C) (Left) Reversible retraction induced by irradiation of PI-Vav2 in HeLa cells ($n = 9$); retraction (red arrow), protrusion (black arrow). (D) High-content live-cell imaging showed that PI-ITSN was inhibited in the lit state. EA, E1244A catalytically inactive mutant. Error bars show SEM ($n = 3$). (E) (Left) Crystal structure of PI-ITSN (L2) in complex with Cdc42 superimposed on the WT ITSN:Cdc42 complex. (Inset, right) Purple, gdp, guanosine diphosphate. (F) Comparison of deuterium exchange (HD/X) results and dynamic coupling computed using molecular dynamics simulations. $C_{L2,i}$ corresponds to the correlation coefficient between the motion of the L2 loop and the motions of each residue. D_{L-d} corresponds to the differences in relative deuteriation levels in the dark and light.

the S1 and S2 regions (Fig. 2A). L1 was similar to the insertion loop of Src in that it connected interacting secondary structures, enabling efficient propagation of structural changes from the inserted domain to the host protein. All the examples that follow indicate that such “tight loops” are useful insertion sites (figs. S9 and S11).

To test the efficacy of LOV2 insertion into the L1 loop, we incorporated the Rac1 analog into a previously characterized fluorescence resonance energy transfer (FRET) biosensor of Rac1 activity (27) (donor fluorescent protein fused to PI-Rac1 and FRET acceptor fused to a fragment from p21-activated kinase that specifically binds activated Rac1). PI-Rac1 containing a dark-state LOV2 mutation was activated by the upstream guanine exchange factor (GEF) Vav2, whereas activation of a lit-state mutant was substantially reduced (Fig. 2B). Even when an activating mutation (Q61L)

was introduced in Rac1, the lit-state LOV2 mutant showed strong inhibition (fig. S12). For physiologically relevant studies, we used PI-Rac1 to replace endogenous Rac1 in Rac1-depleted fibroblasts. Irradiation produced reversible cell edge retraction, initially as indentations closely spaced along the edge, and then broad retraction of entire lamellae (fig. S12 and movies S4 and S5). We also generated switches from the Rho family GTPases RhoA and Cdc42, using insertion in the same loop. Both showed effective light-induced inhibition in live cells (Fig. 2B, fig. S13, and movies S6 and S7).

To probe the mechanism of photoinhibition, we determined the crystal structure of dark-state PI-Rac1 and examined lit and dark conformational changes using molecular dynamics. The crystal structure showed that LOV2 was placed where it did not interfere with Rac1 binding to regulatory or effector proteins (Fig. 2C, fig. S14, and table S1).

Notably, the dark state-activated structure was almost identical to that of activated WT Rac1, with a root mean square deviation (RMSD) of only 0.35 Å (Fig. 2C). Molecular dynamics showed that the conformational change between dark and irradiated PI-Rac1 manifested mainly in the S1 and S2 switch regions and that the conformational changes of PI-Rac1 and WT Rac1 were remarkably similar (Fig. 2D and fig. S15). Together, these studies suggested that opto-allosteric perturbation of Rac1, like Src, caused switching between naturally occurring active and inactive states.

We next targeted another protein family, GEFs, beginning with the Rac1 activator Vav2. GEFs present a different challenge in that they induce a conformational change through GTPase binding to a broad area involving many relatively weak interactions. Computational analysis of Vav2’s GTPase-binding DH domain revealed three potential insertion loops (Fig. 3A and fig. S16). We used loop L4 for LOV2 insertion because it produced the most effective switch. PI-Vav2 was tested in living cells by examining its effects on a Rac1 biosensor (Fig. 3B). The activities of the PI-Vav2 dark- and lit-state mutants resembled those of different activated and inactivated Vav2 mutants (Fig. 3B and figs. S17 and S18). Pull-down assays confirmed that PI-Vav2 was inhibited upon irradiation (fig. S17) and that irradiation of PI-Vav2 in HeLa cells produced rapid and reversible retraction (Fig. 3C and movie S8). Insertion of LOV2 into L1 or L2 also produced effective PI-Vav2 constructs, but insertion of LOV2 into a loop that was not “tight” produced no switch (fig. S18). The same analysis was used to create two other photoinhibitable GEFs: GEF-H1, a Rho GEF, and Intersectin1 (ITSN), a Cdc42 GEF (Fig. 3D and figs. S19 to S21).

Unlike kinase and GTPase catalytic domains, the GEF catalytic domains do not undergo major intradomain conformational changes. Instead, they are regulated sterically by autoinhibitory domains. To investigate the light-mediated structural changes of PI-ITSN (L2), we determined the crystal structures of PI-ITSN alone and in complex with Cdc42 (Fig. 3E, fig. S22, and table S2). PI-ITSN and WT ITSN were structurally similar, with a backbone RMSD of 0.37 Å. The structure of Cdc42 in the ITSN:Cdc42 complex and in the PI-ITSN:Cdc42 complex were similar, with an RMSD of only 0.31 Å. The interface between ITSN and Cdc42 was also in excellent agreement in the two structures, with an RMSD of 0.36 Å (Fig. 3E). The crystal structure of the PI-ITSN:Cdc42 complex was consistent with the shapes of the PI-ITSN:Cdc42 complex and PI-ITSN in solution, constructed ab initio by small angle x-ray scattering (fig. S23).

Molecular dynamics simulations of ITSN and PI-ITSN revealed that the motions of helices $\alpha 5$ and $\alpha 6$, part of the active site, correlate with the motions of the insertion loop (Fig. 3F), and hydrogen or deuterium exchange coupled to mass spectrometry showed light-induced destabilization of these helices (Fig. 3F and figs. S24 to S26). These results suggest that native ITSN and Cdc42 interactions are maintained in PI-ITSN

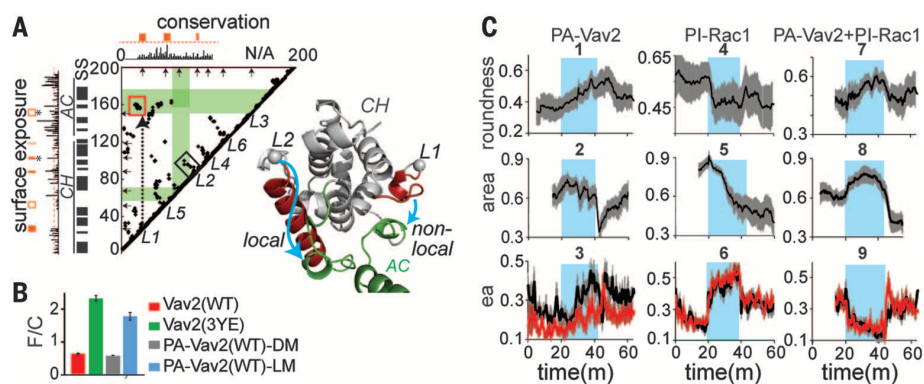


Fig. 4. Designing PA-Vav2 and multiplexed control in living cells. (A) (Left) Computational analysis of Vav2's AID indicated that loops L1 and L2 are coupled to the active site (green) through nonlocal (red box) and local (black box) interactions. CH and AC denote calponin-homology and acidic motifs. (Right) A structural model of the AID showing the connection of L1 and L2 to the active site. (B) PA-Vav2 is activated in the lit state, assayed as in Fig. 2B. Error bars show SEM ($n = 3$). (C) Effects of irradiation and cessation of irradiation on cells expressing PA-Vav2 alone, PI-Rac1 alone, or both in the same cell. Blue box denotes irradiation, ea denotes edge activity, and envelopes show SEM ($n = 15$ for PA-Vav2; $n = 18$ for PI-Rac1; $n = 17$ for PA-Vav2+PI-Rac1).

and support an allosteric connection between the insertion loop and important active-site residues.

We also inserted the uniRapR domain in GEFs, to activate GEFs with rapamycin. Vav2, ITSN, Asef, p115, and Tiam1 all showed rapamycin-induced GTPase binding in pull-down assays (fig. S27). Titrating uniRapR-Vav2 with saturating rapamycin in human embryonic kidney-293T (HEK293T) cells produced dose-dependent activation of a Rac1 biosensor (fig. S27), and fibroblasts stably expressing uniRapR-Vav2 or uniRapR-ITSN produced protrusions and ruffles upon rapamycin addition (fig. S27 and movie S9).

Successful photoinhibition suggested that we might also use allosteric control to activate proteins with light. GEFs, and many other proteins, are regulated by intramolecular interactions of autoinhibitory domains (AIDs), which might be turned on and off allosterically. Analyzing the CH portion of Vav2's AID showed two potential insertion loops (Fig. 4A and fig. S28). We inserted LOV2 in these and in three additional loops not predicted to control activity (fig. S29). In live-cell assays using Rac1 biosensor activity as a readout, only the computed insertion sites produced robust switches (Fig. 4B and fig. S29). In fibroblasts, Vav2 photoactivation induced rounding and lamellae formation rather than the retractions produced by photoinhibition. Upon removal of light, PA-Vav2 cells underwent marked contractions (panels 1 and 2 in Fig. 4C, fig. S30, and movie S10). These results demonstrated that a protein can be allosterically activated by light through control of its AID.

With optogenetics, effects of protein manipulation can be assayed rapidly, before the cell has a chance to compensate as it does with genetic manipulations. We tested whether photoactivation

and photoinhibition could be combined, to assay how photoactivation of one protein is affected by downstream inhibition of another. Unlike the rounding and large lamellae produced by irradiating PA-Vav2 (panel 1 in Fig. 4C and movie S10), irradiating PI-Rac1 cells (produced via knockdown and rescue of Rac1) caused retraction (panels 4 and 5 in Fig. 4C and movie S5), with formation of a complex perimeter and increased velocity of both retractions and protrusions (panel 6 in Fig. 4C). When PA-Vav2 and PI-Rac1 were irradiated in the same cell, area and roundness responded similarly to PA-Vav2 alone, but the cell edge showed a phenotype clearly different from that produced by the individual proteins, with a strong reduction in edge dynamics during irradiation (panels 7 to 9 in Fig. 4C, movie S11, and fig. S30). Thus, PI-Rac1 was being activated and affecting results of Vav2 activation. Interpretation will require further study, but these results are consistent with recent work showing that Vav2 can act independent of Rac1 (28–30).

In summary, we have controlled proteins with light or small molecules in living cells by harnessing order/disorder transitions. Sensory domains were inserted into tight, nonconserved, surface loops that are allosterically coupled to active sites. Engineered proteins switched between naturally occurring, physiologically relevant active and inactive states, generating effective tools to manipulate living cells.

REFERENCES AND NOTES

1. M. Weitzman, K. M. Hahn, *Curr. Opin. Cell Biol.* **30**, 112–120 (2014).
2. L. A. Banaszynski, T. J. Wandless, *Chem. Biol.* **13**, 11–21 (2006).
3. A. Levskaya, O. D. Weiner, W. A. Lim, C. A. Voigt, *Nature* **461**, 997–1001 (2009).
4. M. J. Kennedy *et al.*, *Nat. Methods* **7**, 973–975 (2010).

5. H. Yumerefendi *et al.*, *Nat. Chem. Biol.* **12**, 399–401 (2016).
6. D. Niopek *et al.*, *Nat. Commun.* **5**, 4404 (2014).
7. Y. I. Wu *et al.*, *Nature* **461**, 104–108 (2009).
8. X. X. Zhou, H. K. Chung, A. J. Lam, M. Z. Lin, *Science* **338**, 810–814 (2012).
9. J. H. Choi, A. H. Laurent, V. J. Hilsner, M. Ostermeier, *Nat. Commun.* **6**, 6968 (2015).
10. M. Ostermeier, *Curr. Opin. Struct. Biol.* **19**, 442–448 (2009).
11. J. Lee *et al.*, *Science* **322**, 438–442 (2008).
12. A. V. Karginov, F. Ding, P. Kota, N. V. Dokholyan, K. M. Hahn, *Nat. Biotechnol.* **28**, 743–747 (2010).
13. O. Dazliyan *et al.*, *Proc. Natl. Acad. Sci. U.S.A.* **110**, 6800–6804 (2013).
14. B. L. Oakes *et al.*, *Nat. Biotechnol.* **34**, 646–651 (2016).
15. C. L. Tucker, S. Fields, *Nat. Biotechnol.* **19**, 1042–1046 (2001).
16. P. H. Chu *et al.*, *Proc. Natl. Acad. Sci. U.S.A.* **111**, 12420–12425 (2014).
17. S. M. Harper, L. C. Neil, K. H. Gardner, *Science* **301**, 1541–1544 (2003).
18. A. S. Halavaty, K. Moffat, *Biochemistry* **46**, 14001–14009 (2007).
19. X. Yao, M. K. Rosen, K. H. Gardner, *Nat. Chem. Biol.* **4**, 491–497 (2008).
20. A. R. Fersht, L. Serrano, *Curr. Opin. Struct. Biol.* **3**, 75–83 (1993).
21. M. P. Playford, M. D. Schaller, *Oncogene* **23**, 7928–7946 (2004).
22. Y. Zhou, M. Karplus, *Nature* **401**, 400–403 (1999).
23. F. Ding, D. Tsao, H. Nie, N. V. Dokholyan, *Structure* **16**, 1010–1018 (2008).
24. V. J. Fincham, M. C. Frame, *EMBO J.* **17**, 81–92 (1998).
25. V. G. Branton *et al.*, *Cancer Res.* **65**, 1335–1342 (2005).
26. H. Wang *et al.*, *Nat. Methods* **13**, 755–758 (2016).
27. M. Machacek *et al.*, *Nature* **461**, 99–103 (2009).
28. G. L. Razidlo, B. Schroeder, J. Chen, D. D. Billadeau, M. A. McNiven, *Curr. Biol.* **24**, 86–93 (2014).
29. K. Abe *et al.*, *J. Biol. Chem.* **275**, 10141–10149 (2000).
30. T. Samson, C. Welch, E. Monaghan-Benson, K. M. Hahn, K. Burridge, *Mol. Biol. Cell* **21**, 1629–1642 (2010).

ACKNOWLEDGMENTS

This work was supported by NIH grants P01-GM103723 and P41-EB002025 (K.M.H.), R01GM080742 (N.V.D.), and by Deutsche Forschungsgemeinschaft grant FOR1279 (I.S.). O.D. is a Howard Hughes Medical Institute International Student Research Fellow. X-ray data were collected at the Swiss Light Source, beamline X10SA and X12SA, Paul Scherrer Institute, Villigen, Switzerland. We thank A. Menzel and T. Barends for collecting the small angle x-ray scattering data, and M. Shobair for his help with PI-Vav2 simulations. Atomic coordinates and structure factors have been deposited in the Protein Data Bank under accession codes: 5HZJ (PI-ITSN1-WT), 5HZI (PI-ITSN1-C450M), 5HZK (PI-ITSN1-WT: Cdc42), and 5HZH (PI-Rac1-C450A). O.D., N.V.D., and K.M.H. designed the research; M.T. performed the crystallographic work and conducted hydrogen-deuterium exchange coupled to mass spectrometry assays under the directions of I.S. who collected the x-ray data; P.-H.C. helped the characterization of PI-Src; D.S. conducted the simulations of PI-Src; O.D. performed all experiments and computations not listed above; O.D. and K.M.H. wrote the manuscript with input from all authors. The constructs described in this paper are available from K.M.H. under a material transfer agreement with the University of North Carolina-Chapel Hill.

SUPPLEMENTARY MATERIALS

www.sciencemag.org/content/354/6318/1441/suppl/DC1
Materials and Methods
Tables S1 to S3
Figs. S1 to S30
References (31–63)
Movies S1 to S11

12 June 2016; accepted 16 November 2016
10.1126/science.aah3404

Keystone Symposia 2017 Conference Series

Cell Plasticity within the Tumor Microenvironment (A1)

January 8–12, 2017 | Big Sky, Montana | USA

Precision Genome Engineering (A2)

Jan 8–12, 2017 | Breckenridge, Colorado | USA

Transcriptional & Epigenetic Control in Stem Cells (J1)

joint with **Neurogenesis during Development & in the Adult Brain (J2)**

Jan 8–12, 2017 | Olympic Valley, California | USA

TGF- β in Immunity, Inflammation & Cancer (A3)

January 9–13, 2017 | Taos, New Mexico | USA

Mitochondria Communication (A4)

January 14–18, 2017 | Taos, New Mexico | USA

New Developments in Our Basic Understanding of Tuberculosis (A5)

January 14–18, 2017 | Vancouver, British Columbia | Canada

PI3K Pathways in Immunology, Growth Disorders & Cancer (A6)

Jan 19–23, 2017 | Santa Fe, New Mexico | USA

Biobetters & Next-Generation Biologics:

Innovative Strategies for Optimally Effective Therapies (A7)

Jan 22–26, 2017 | Snowbird, Utah | USA

Diabetes (J3) *joint with* Obesity & Adipose Tissue Biology (J4)

January 22–26, 2017 | Keystone, Colorado | USA

Omics Strategies to Study the Proteome (A8)

January 29–February 2, 2017 | Breckenridge, Colorado | USA

Epigenetics & Human Disease:

Progress from Mechanisms to Therapeutics (A9)

January 29–February 2, 2017 | Seattle, Washington | USA

Hematopoiesis (B1)

January 31–February 4, 2017 | Banff, Alberta | Canada

Noncoding RNAs: From Disease to Targeted Therapeutics (J5)

joint with **Protein-RNA Interactions: Scale, Mechanisms, Structure & Function of Coding & Noncoding RNPs (J6)**

February 5–9, 2017 | Banff, Alberta | Canada

Inflammation-Driven Cancer: Mechanisms to Therapy (J7)

joint with **Microbiome in Health & Disease (J8)**

February 5–9, 2017 | Keystone, Colorado | USA

Autophagy Network Integration in Health & Disease (B2)

February 12–16, 2017 | Copper Mountain, Colorado | USA

Asthma: From Pathway Biology to Precision Therapeutics (B3)

February 12–16, 2017 | Keystone, Colorado | USA

Viral Immunity: Mechanisms & Consequences (B4)

February 19–23, 2017 | Santa Fe, New Mexico | USA

Malaria: From Innovation to Eradication (B5)

February 19–23, 2017 | Kampala | Uganda

Lipidomics & Bioactive Lipids in Metabolism & Disease (B6)

February 26–March 2, 2017 | Tahoe City, California | USA

Bile Acid Receptors as Signal Integrators in Liver & Metabolism (C1)

March 3–7, 2017 | Monterey, California | USA

Rare & Undiagnosed Diseases:

Discovery & Models of Precision Therapy (C2)

March 5–8, 2017 | Boston, Massachusetts | USA

mRNA Processing & Human Disease (C3)

March 5–8, 2017 | Taos, New Mexico | USA

Synapses & Circuits: Formation, Function & Dysfunction (X1)

joint with **Connectomics (X2)**

March 5–8, 2017 | Santa Fe, New Mexico | US

Tumor Metabolism: Mechanisms & Targets (X3)

joint with **Adaptations to Hypoxia in Physiology & Disease (X4)**

March 5–9, 2017 | Whistler, British Columbia | Canada

Engineered Cells & Tissues as Platforms for Discovery & Therapy (K1)

March 9–12, 2017 | Boston, Massachusetts | USA

Kinases: Next-Generation Insights & Approaches (C4)

March 5–9, 2017 | Breckenridge, Colorado | USA

Frontiers of NMR in Life Sciences (C5)

March 12–16, 2017 | Keystone, Colorado | USA

Sex & Gender Factors Affecting Metabolic Homeostasis, Diabetes & Obesity (C6)

March 19–22, 2017 | Tahoe City, California | USA

Cancer Immunology & Immunotherapy:

Taking a Place in Mainstream Oncology (C7)

March 19–23, 2017 | Whistler, British Columbia | Canada

Pattern Recognition Signaling: From Innate Immunity to Inflammatory Disease (X5) *joint with* Type I Interferon: Friend & Foe Alike (X6)

March 19–23, 2017 | Banff, Alberta | Canada

Injury, Inflammation & Fibrosis (C8)

March 26–30, 2017 | Snowbird, Utah | USA

HIV Vaccines (C9)

March 26–30, 2017 | Steamboat Springs, Colorado | USA

Immune Regulation in Autoimmunity & Cancer (D1)

March 26–30, 2017 | Whistler, British Columbia | Canada

Molecular Mechanisms of Heart Development (X7)

joint with **RNA-Based Approaches in Cardiovascular Disease (X8)**

March 26–30, 2017 | Keystone, Colorado | USA

Genomic Instability & DNA Repair (Z1)

joint with **DNA Replication & Recombination (Z2)**

April 2–6, 2017 | Santa Fe, New Mexico | USA

B Cells & T Follicular Helper Cells: Controlling Long-Lived Immunity (D2)

April 23–27, 2017 | Whistler, British Columbia | Canada

Mononuclear Phagocytes in Health, Immune Defense & Disease (D3)

April 30–May 4, 2017 | Austin, Texas | USA

Modeling Viral Infections & Immunity (E1)

May 1–4, 2017 | Estes Park, Colorado | USA

Angiogenesis & Vascular Disease (Z3)

joint with **Mitochondria, Metabolism & Heart (Z4)**

May 8–12, 2017 | Santa Fe, New Mexico | USA

Neuronal Control of Appetite, Metabolism & Weight (Z5)

joint with **Gastrointestinal Control of Metabolism (Z6)**

May 9–13, 2017 | Copenhagen | Denmark

Aging & Mechanisms of Aging-Related Disease (E2)

May 15–19, 2017 | Yokohama | Japan

Single Cell Omics (E3)

May 26–30, 2017 | Stockholm | Sweden

Integrating Metabolism & Immunity (E4)

joint with **Cell Death & Inflammation (K2)**

May 29–June 2, 2017 | Dublin | Ireland

Vectors, Pathogens & Diseases: Current Trends & Emerging Challenges (T1)

September 10–14, 2017 | Durban, KwaZulu-Natal | South Africa

Maternal-Fetal Cross Talk: Harmony vs. Conflict (T2)

October 4–8, 2017 | Washington, DC | USA

Regenerative Biology & Applications: Cell Differentiation, Tissue Organization & Biomedical Engineering (T3)

October 15–19, 2017 | Pok Fu Lam, Hong Kong | China

Antimicrobials and Resistance: Opportunities and Challenges (T4)

October 29–November 1, 2017 | Santa Fe, New Mexico | USA

Frontiers of Serotonin Beyond the Brain (T5)

November 12–15, 2017 | Park City, Utah | USA

Abstract and discounted registration deadlines are three months and two months, respectively, before conferences begin. Abstracts submitted by the abstract deadline will be considered for short talks on the program. Information shown subject to possible change.

www.keystonesymposia.org/meetings | 1.800.253.0685 | 1.970.262.1230

KEYSTONE SYMPOSIA™
on Molecular and Cellular Biology
Accelerating Life Science Discovery

EXPLORE



Interested in the human cell?

Order a free copy of this poster to learn about the most detailed mapping of the human cell ever done. The Human Protein Atlas project is presenting a high-resolution map of the human cell. The proteins have been localized with high precision to cellular organelles, structures and sub-structures, with high-resolution images freely available for you to explore.

The antibodies used are Triple A Polyclonals provided by Atlas Antibodies.

MADE IN SWEDEN



ATLAS ANTIBODIES
Totally human



Gas Chromatography System

Researchers in the fields of food safety, ecology, industry, forensics, and anti-doping can now expand their analytical capabilities using a system designed to enable powerful qualitative and quantitative analysis for GC-MS applications. The Exactive GC Orbitrap GC-MS system delivers sensitive, routine-grade performance for both targeted and nontargeted analysis, along with powerful quantitation. The system offers the quantitative power of a GC triple quadrupole mass spectrometer, combined with the unique advantages of Orbitrap's high-resolution, accurate mass technology, and features new options for routine laboratories to advance their workflows. When using Thermo Scientific TraceFinder software and mass spectral libraries, researchers can benefit from intelligent data-processing workflows for analyte screening and quantitation. Also new, the Orbitrap GC-MS Contaminants Library features more than 700 compounds significant to food and environmental analysis, and allows users to perform target quantitation, target screening, and nontarget screening workflows.

Thermo Fisher Scientific

For info: 800-955-6288
www.thermofisher.com

Air Condenser

In two independent reports, the Asynt CondensSyn waterless air condenser displayed performance comparable to even the most efficient water-driven condensers, and outperformed the alternative designs tested. For low-boiling solvents such as dichloromethane, the CondensSyn was seen to work better than the water-driven condensers. Given the advantages of the CondensSyn, such as eliminating water consumption, taking up less work space, and facilitating setup and cleanup of reactions, both reports conclude that it is the optimal choice for an air condenser. In addition, by combining the CondensSyn with a heating block system, reflux setups can be prepared quickly and easily with no chance of water or oil spillages.

Asynt

For info: +44-(0)-1638-781709
www.asynt.com



Gel Imaging System

The Omega Fluor is a powerful yet simple tool for gel documentation and for generating publication-quality, 16-bit images. The Omega Fluor comes completely assembled for a quick startup. It includes Omega Fluor Acquisition software, which is fully Windows compatible; a clean user interface; simple tools for annotation and contrast adjustments; and a 302-nm UV transilluminator on a pull-out tray. Samples can be viewed directly through the UV-protected viewport, which includes an orange filter for improved visual contrast. The cabinet also includes an Epi white light. The camera in this system boasts a 5-megapixel resolution, which puts the Omega Fluor on a par with systems from a much higher price bracket for image quality. Users can choose UV or white light across a large range of commonly used dyes. The Omega Fluor accommodates large-format protein and nucleotide gels and has a large imaging area of 24 cm × 20 cm.

Eikonix

For info: +44-(0)-1223-515440
www.eikonix.com

Water Purification System

The Elix High-Throughput water purification system provides laboratories with a reliable water purification solution for daily water volumes of up to 9,000 L. It offers full connectivity, providing authorized users real-time remote monitoring—via computer, tablet, or smartphone—with access to all important water-quality data. The system combines MilliporeSigma's Elix electro-deionization technology with advanced purification, including Progard pretreatment cartridges, reverse osmosis, and bactericidal UV lamp treatment. New models include MilliporeSigma's E.R.A. (Evolutive Reject Adjustment) technology, which automatically optimizes water recovery and reduces water usage costs by taking feed-water quality into account. The system can also be linked to a laboratory information management system or building management system for enhanced efficiency and productivity. A large color touchscreen features storage level and dispensing information, water production, and the status of system consumables, including step-by-step instructions from a system wizard for effortless replacement.

MilliporeSigma

For info: 800-645-5476
www.emdmillipore.com

Evaporator

The Genevac Rocket Synergy evaporator enhances chiral separation protocols. Recently there has been considerable interest in the synthesis and separation of enantiomers of organic compounds, especially because of their growing importance in the natural products, biotechnology, and pharmaceutical industries. The chiral analytes of interest are typically separated in large

volumes of solvent. Concentration or drying of these large solvent volumes using a rotary evaporator is time-consuming and may risk thermal degradation of valuable separated chiral products. Rocket Synergy evaporator achieves fast evaporation with precise temperature control, thereby accelerating the safe production of chiral separation samples. Fitted with a six-place rotor, the evaporator can dry or concentrate up to six 400-mL flasks or six 18-mL × 50-mL tubes simultaneously. Replace the flask rotor with a 5-L stainless-steel bowl rotor, and batch volumes of up to 5 L can be evaporated in a single run.

Genevac

For info: +44-(0)-1473-240000
www.genevac.com

Electronically submit your new product description or product literature information! Go to www.sciencemag.org/about/new-products-section for more information.

Newly offered instrumentation, apparatus, and laboratory materials of interest to researchers in all disciplines in academic, industrial, and governmental organizations are featured in this space. Emphasis is given to purpose, chief characteristics, and availability of products and materials. Endorsement by *Science* or AAAS of any products or materials mentioned is not implied. Additional information may be obtained from the manufacturer or supplier.

Publish your research in ***Science Immunology***

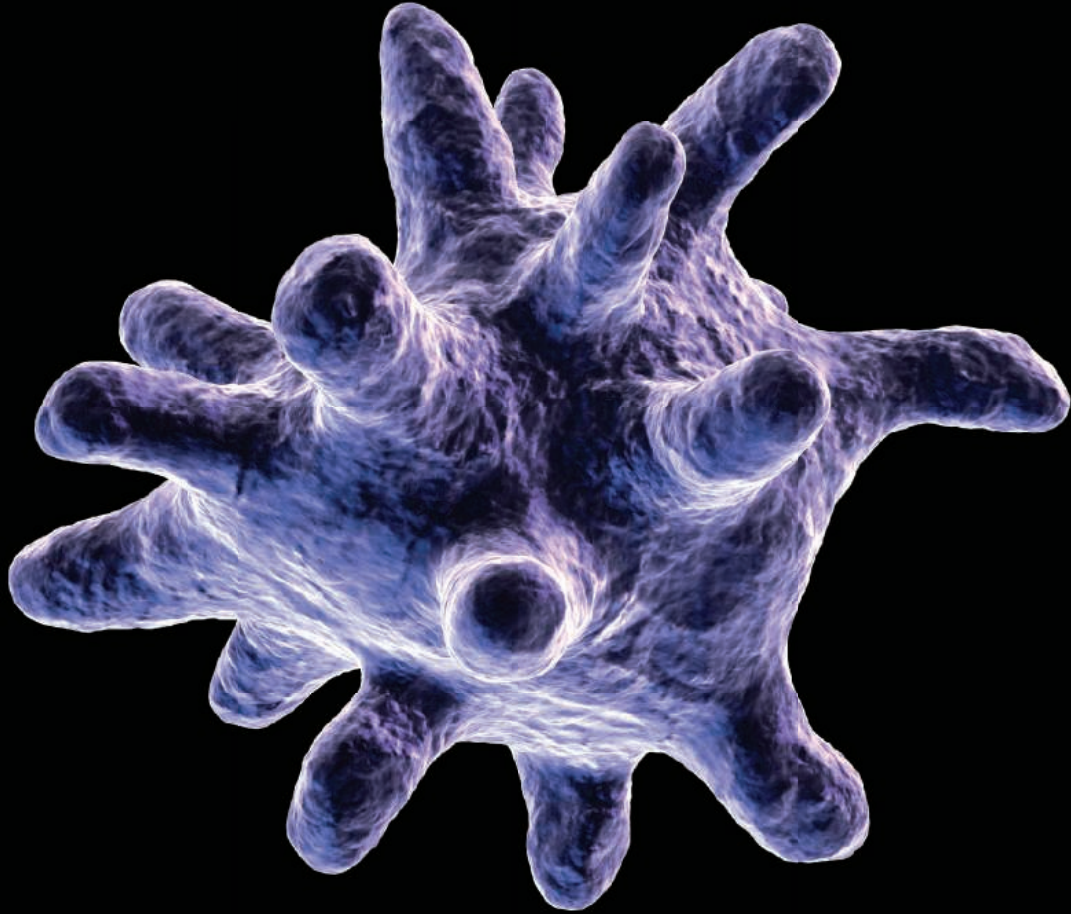


Image: Eraxion / iStockPhoto

— NOW ACCEPTING PAPERS —

Science Immunology, the newest member in the *Science* family of journals, provides original, peer-reviewed research articles that report critical advances in all areas of immunological research, including studies that provide insight into the human immune response in health and disease. Share your research with *Science Immunology*'s global readership and submit your manuscript today!

What will your discovery be?

Submit your manuscript today at
ScienceImmunology.org

ScienceImmunology

AAAS

Science Careers Job Fair at the AAAS Annual Meeting

February 17, 2017

11:00 AM - 4:00 PM EST



A Day of Recruiting Opportunities and Career Workshops

Science Careers and **AAAS** offer an exciting career event at the 2017 AAAS Annual Meeting in Boston, Massachusetts.

- **JOB SEEKERS:** Join us for a chance to meet with recruiters from top scientific organizations and to get valuable advice from career experts. The combination of valuable career development content and exciting career opportunities makes this a free “must-attend” event for scientists.

*For more details and to register, visit
sciencemag.org/careers/jobfair*

- **EMPLOYERS:** Save time and money by meeting hundreds of scientists in person.

*For information and to reserve your exhibit
space package please contact us today.*

Space is limited.

202 326-6577

advertise@sciencecareers.org



Hynes Convention Center

Room 210
Boston, MA

To book your booth, contact:

US: 202-326-6577

Europe: +44 (0) 1223 326528

advertise@sciencecareers.org

Science Careers

FROM THE JOURNAL SCIENCE  AAAS

SCIENCECAREERS.ORG



There's only one **Science**

Science Careers Advertising

For full advertising details, go to ScienceCareers.org and click For Employers, or call one of our representatives.

Tracy Holmes

Worldwide Associate Director
Science Careers
Phone: +44 (0) 1223 326525

THE AMERICAS

E-mail: advertise@sciencecareers.org
Fax: +1 (202) 289 6742

Tina Burks

Phone: +1 (202) 326 6577

Nancy Toema

Phone: +1 (202) 326 6578

Online Job Posting Questions

Phone: +1 (202) 312 6375

EUROPE / INDIA / AUSTRALIA / NEW ZEALAND / REST OF WORLD

E-mail: ads@science-int.co.uk
Fax: +44 (0) 1223 326532

Sarah Lelarge

Phone: +44 (0) 1223 326527

Kelly Grace

Phone: +44 (0) 1223 326528

Online Job Posting Questions

Phone: +44 (0) 1223 326528

JAPAN

Katsuyoshi Fukamizu (Tokyo)

E-mail: kfukamizu@aaas.org
Phone: +81 3 3219 5777

Hiroyuki Mashiki (Kyoto)

E-mail: hmashiki@aaas.org
Phone: +81 75 823 1109

CHINA / KOREA / SINGAPORE / TAIWAN / THAILAND

Danny Zhao

E-mail: dzhao@aaas.org
Phone: +86 131 4114 0012

All ads submitted for publication must comply with applicable U.S. and non-U.S. laws. *Science* reserves the right to refuse any advertisement at its sole discretion for any reason, including without limitation for offensive language or inappropriate content, and all advertising is subject to publisher approval. *Science* encourages our readers to alert us to any ads that they feel may be discriminatory or offensive.

Science Careers

FROM THE JOURNAL *SCIENCE* AAAS

ScienceCareers.org



AAAS Mass Media Science and Engineering Fellows Program

Applications accepted
through January 15
aaas.org/mmfellows



AMERICAN ASSOCIATION FOR THE
ADVANCEMENT OF SCIENCE

POSITIONS OPEN



Research Geneticist (Plants)

The U.S. Department of Agriculture, Agricultural Research Service, Plant Gene Expression Center (PGEN) in Albany, California invites applications for a **RESEARCH SCIENTIST** position with expertise in plant genetics, GS-0440-12/13. PGEN research is conducted through a close collaborative partnership with the University of California, Berkeley. The successful candidate will be responsible for developing a research program that uses modern molecular genetic, genomic and/or computational technologies, including large-scale datasets and novel analytical approaches, to understand how genes govern plant traits of agronomic importance. Areas of research interest are related to plant adaptation and response to the environment, including disease resistance, abiotic stress tolerance and their relationship to plant development and architecture. This is a permanent, full time position. The salary range is \$84,302 to \$130,325/per year. A comprehensive Federal benefits package is available. For application instructions see website: <http://www.usajobs.gov> Keyword: ARS-S17W-0127. Announcement closes January 10, 2017. U.S. Citizenship is required.

The USDA/ARS is an Equal Opportunity Employer and Provider.

Wildlife Ecologist & Lake Fish Biologist Northern Michigan University (Marquette MI)

Applications are invited for two tenure-earning faculty positions at the **ASSISTANT PROFESSOR** level beginning August 2017. The positions will be posted until January 17, 2017. Submit application materials to website: <https://employe.nmu.edu>, where a description and requirements are posted. *Northern Michigan University is an Equal Opportunity Employer including protected veterans and individuals with disabilities.*

Get jobs &
career advice!



@ScienceCareers



/ScienceCareers



Science Careers

Science Careers

sciencecareers.org



South China: A rising power in science

Guangzhou city on the Pearl River

After emerging as a trade superpower, China aims to become a leading force in scientific research and applications ranging from cosmology and spaceflight to genomics and medicine. Universities across south China are stepping up the recruitment of scientists with advanced degrees gained in Europe or the United States. This strategy has yielded prestigious science prizes and papers, and generated the growth of scientific research clusters in the region.

By Kevin Holden

When China's leaders decided a generation ago to experiment with opening the People's Republic to global market forces, they created an archipelago of special economic zones (SEZs) along the nation's southern coast. South China's resulting transformation into an export powerhouse has helped make the country a world trade titan. Now the region is part of a new round of reforms aimed at reshaping China into a globally connected pioneer in the sciences.

China's universities, along with the National Natural Science Foundation and the Chinese Academy of Sciences (CAS), have created award schemes aimed at attracting scientists trained in the United States or Europe to take positions across southern China and to help spur the next stage of the region's metamorphosis. These strategies are helping power research breakthroughs in the spheres of space science, physics, genomics, and medicine.

From rice paddies to space stations

The drive to transmute the country's burgeoning economic might into scientific prowess is evident across southern China. Shenzhen, crisscrossed by rice paddies when it was designated an SEZ, is now one of the world's fastest growing cities and hosts one of China's leading genomics outfits. Similarly, the tropical island of Hainan, ringed by fishing villages when it too became an SEZ, opened its new space launch center this summer.

Thousands of visitors watched the premier liftoff of the new Long March 7 rocket, along with the prototype of a next-generation human space capsule that it carried into orbit.

CAS leaders say spaceflight is a high-priority sector for heightened international cooperation. China recently signed an agreement with the United Nations Office for Outer Space Affairs, outlining Beijing's pledge "to enable United Nations member states, particularly developing countries, to conduct space experiments onboard China's space station, as well as to provide flight opportunities for astronauts and payload engineers."

CAS is stepping up its twin drives to boost collaboration on transborder science projects and to increase its standing in worldwide science. One area in which it has made headway is in studies encompassing the formation of the universe, the earliest galaxies, and the solar system.

Planetary scientist **Yuan Li**, a postdoctoral researcher at Rice University in Houston, says he was persuaded to accept a position at the CAS Guangzhou Institute of Geochemistry through a Global Youth Experts award. Li is the lead author of a recent *Nature Geoscience* study, cowritten with colleagues at Rice, which posited that the life-enabling carbon in the Earth's crust might be the result of a collision between the proto-Earth and a Mercury-like planet about 4.4 billion years ago. That collision was distinct from the interplanetary smashup that scientists believe gave birth to the Moon during the early formation of the solar system.

"During the accretion of our Earth, there were probably numerous collisions between the proto-Earth and small planetary embryos," says Li. This early period in the solar system's evolution, he adds, might have resembled a massive billiards game involving the inner protoplanets crashing into each other before entering stabilized orbits around the sun.

Li's paper is part of a steady rise of articles written by Chinese scholars and published in the world's leading academic journals. He says China's expanding constellation **cont.**



Upcoming Features

Faculty Careers—February 10 ■ Postdoc Careers—March 17 ■ Postdoc Careers—August 25

“Shenzhen has repositioned itself as one of the world’s leading centers for genetics research.”

—Bicheng Yang



of incentives for scientists is a powerful attraction for scholars trained in the West. “In the past five years, thousands of young scientists like me have returned to China,” he says.

Particle physics breakthroughs

China is interested not only in the macroworld, it is also keen on the microworld. Scientists with an advanced degree in physics who have accepted positions at south China universities are helping track and explain how neutrinos morph into different types, or generations, as they fly through space at nearly the speed of light.

These physicists have joined an international team of scientists who are studying nuclear reactor-produced neutrinos in the southern Chinese seaside resort of Daya Bay. Collaboration on these experiments involves universities and physicists stretching across four continents, says **Kam-Biu Luk**, a professor of physics at the University of California, Berkeley, and a distinguished visiting scholar at the University of Hong Kong.

Luk, who heads the international participation in the project, says this exploration of the long-shrouded world of neutrinos is one of the most outstanding experiments in particle physics ever conducted by joint groups of universities based in China and the United States. Physicists at the University of Hong Kong, the Chinese University of Hong Kong, Shenzhen University, Dongguan University of Technology, and Sun Yat-sen University have joined counterparts at Yale, Princeton, and other laboratories in this expanding experiment.

Chinese scientists involved in these neutrino observations, along with the international team headed by Luk, were awarded the prestigious Breakthrough Prize in Fundamental Physics in 2016, for outlining how neutrinos transform as they speed through the cosmos. They won, according to the prize citation, for “revealing a new frontier beyond, and possibly far beyond, the standard model of particle physics.”

Due to the rapidly growing neutrino physics programs in China, **Jiajie Ling**, a postdoctoral researcher at the University of Illinois who is now a professor in physics at Sun Yat-sen University, opted to take a position there with start-up funding support from the Thousand Talents Program for Distinguished Young Scholars. He is helping to guide a new series of experiments at Daya Bay: the search for the hypothesized “sterile neutrino.” This proposed fourth type of neutrino could be a form of the elusive dark matter that scientists have been searching for since the last century, says Ling.

Future home of particle colliders

According to Ling, the massive neutrino study he is working on is helping China move closer to realizing its plans to host an international coalition of elite physicists around its proposed supercollider projects. China’s top-echelon physicists, in tandem with leading scientists worldwide, are designing a ringed particle smasher measuring up to 100 kilometers in circumference that would initially be configured as an electron-positron collider, and would later also host a proton-proton accelerator.

“After so many years of preparation and joining worldwide experiments, now is a fantastic time for China to host the Circular Electron-Positron Collider and the Super Proton-Proton Collider,” Ling says. “More importantly, it is also China’s responsibility to contribute to advancing high-energy physics and humanity’s knowledge about the universe.”

Jie Gao, one of the leaders of the twin circular collider projects at the CAS Institute of High Energy Physics, says southern Guangdong Province is a leading contender to host the ringed accelerators. Chinese and American scientists who are laying the groundwork for what would be the largest and most sophisticated particle physics lab in history predict it could attract thousands of the world’s experimental physicists to take up positions in China’s planned “collider city.”

Alain Blondel, one of the primary shapers of the Future Circular Collider being mapped out by CERN (the European Organization for Nuclear Research) in Switzerland, says “it would be fantastic” if the leaders of CERN and of the Chinese supercollider program wind up competing to attract the globe’s foremost physicists.

Tao Liu, a physicist at Hong Kong University of Science and Technology, echoes this sentiment. He says China’s planned collider project is the most exciting ever to capture the attention of leading physics professors and science students across Hong Kong.

The supercolliders, Liu adds, will “boost development in science and society in the coming decades, [and] will inspire young talents of this and future generations to devote themselves to the exploration of basic science.”



Mining the genome

Just across the border from Hong Kong, universities and the local government in Shenzhen are channeling their expanding funds into making globally recognized advances in life science research and applications.

“Shenzhen has repositioned itself as one of the world’s leading centers for genetics research,” says **Bicheng Yang**, communications director at the genomics outfit BGI, which is moving forward with plans to create a specialized life science college in partnership with the South China University of Technology (SCUT) and the University of Copenhagen.

Four years ago, BGI signed a cooperation pact with the Gates Foundation to set up joint training programs with the University of the Chinese Academy of Sciences and SCUT. “The aim is to integrate the new college more and more into scientific research that stretches across the continents,” she explains.

Xin Jin, a genomics expert with dual research positions at BGI and at the SCUT, says, “One of the most exciting projects we are working on is the Chinese Million-ome Project, aimed at decoding one million Chinese genomes across the entire country.”

The university and BGI are also exploring the use of genomics to map the genetic evolution of current populations dating back to the early modern humans who trekked to Asia more than 40,000 years ago, and their admixture with more archaic species, adds Jin, who coauthored a study on this topic published in *Nature*.

At the frontier of human genome editing

The potential use of genomic engineering to eradicate the genetic bases for diseases is also being explored by groups of university researchers in the southern mega-city of Guangzhou. One of these groups recently reported conducting a leading-edge experiment, but with only limited success, in editing the genomes of human embryos to confer genetic resistance to HIV infections. A similar paper published in 2015 by researchers at Sun Yat-sen University ignited a global debate over whether this type of research should be conducted on human embryos because of its potential to trigger genetic changes that ripple across future generations.

Since then, leaders of the national science academies in the United States, the United Kingdom, and China have met and reached a consensus that while this type of research could continue, any applications should be prohibited. The lead organizer of the summit involving the three science academies was **David Baltimore**, president emeritus of the California Institute of Technology. He adds that Chinese researchers can move forward with embryonic genome editing studies as long as “experiments are limited to 14 days of in vitro growth and no implantation is attempted.”

The genomics teams at Sun Yat-sen University and at Guangzhou Medical University, says Baltimore, represent “an effort of two labs to move into the forefront of the research.”

Some scholars suggest that China’s support for these studies, in view of the U.S. Congressional ban on federal funding for research involving modifying the genomes of human embryos, could help scientists across Chinese universities move ahead in this realm of gene editing.

FEATURED PARTICIPANTS

BGI
www.bgi.com/us

California Institute of Technology
www.caltech.edu

CERN Future Circular Collider Study
fcc.web.cern.ch/pages/default.aspx

Daya Bay Reactor Neutrino Experiment
dayabay.ihep.ac.cn/twiki/bin/view/Public

Guangdong University of Foreign Studies
english.gdufs.edu.cn

Guangzhou Institute of Geochemistry, Chinese Academy of Sciences
english.gig.cas.cn

Hong Kong University of Science and Technology
www.ust.hk

Institute of High Energy Physics, Chinese Academy of Sciences
english.ihep.cas.cn

South China University of Technology
en.scut.edu.cn

Sun Yat-sen University
iso.sysu.edu.cn

University of California, Berkeley
physics.berkeley.edu

University of Copenhagen
www.ku.dk/english

University of Hong Kong
www.hku.hk

Reversing “brain drain”

In another region of south China, at the Guangdong University of Foreign Studies, **Jing Yang** has been conducting research with colleagues at Pennsylvania State University on structural changes in the brain that occur when students begin studying a second language.

Yang, formerly a postdoctoral fellow at Penn State, says she joined Guangdong University of Foreign Studies because the school “is well known for cultivating international talent.” She says she aims to help transform the university’s language center into “a leading research center for linguistics and applied linguistics,” and adds that the government is providing large-scale grant support to reach that goal.

China’s economic ascent and the increasingly attractive recruitment packages offered by its universities are becoming extremely appealing to Chinese scholars who have studied in the West, Yang says, and are beginning to help reverse a decades-long brain drain, during which scholars left the country to pursue their careers elsewhere.

While many Chinese scientists still opt to stay in Europe or the United States after obtaining an advanced degree there, Yang observes that “some scholars, like me, chose to go home to work for a brighter future for ourselves and also for our country.” These scholars, she adds, are helping create clusters of excellent scientific research across China.

“The rise of China definitely is not limited to the economy,” Yang explains. “We hope our country can excel in science, culture, and technology too. It is a double win for China and the world.”

Kevin Holden is a freelance writer based on the east coast of China and the west coast of the United States.

DOI: 10.1126/science.opms.r1600172

WE ARE SEEKING OUTSTANDING RESEARCHERS IN MOLECULAR MEDICINE

The Wallenberg Centres for Molecular Medicine are key elements in a national effort to reposition Sweden as a world-leading life science nation. The initiative was taken by the Knut and Alice Wallenberg Foundation, and is a joint venture with the Universities and University Hospitals of Gothenburg, Lund, Umeå and Linköping. SciLifeLab in Stockholm and Uppsala serves as a research partner and unique core facility for the four Centres.

Through repeated calls in the upcoming years with **tenure track research positions – Wallenberg Molecular Medicine Fellows** – we will recruit translationally oriented research groups. The groups will be centered on internationally recruited young scientists of outstanding potential and funded at a globally competitive level through **very generous starting packages** with the possibility of promotion to Senior Lecturer within four years. Each of these groups will synergize with pre-existing excellent research environments as well as strong clinical collaborators, promoting ground-breaking research in molecular and translational medicine. Together, we will rise to future challenges within molecular life science in order to improve human health.

Note that the application deadline at the four Centres may vary.

www.wcmm.se



Umeå University



LINKÖPING
UNIVERSITY



UNIVERSITY OF
GOTHENBURG

LUND UNIVERSITY:

We are recruiting up to three tenured faculty members at the level of Senior Lecturer (Associate Professor) within the area **Molecular Medicine - Regenerative Medicine (Regeneration, Replacement, and Repair)**. Successful candidates will receive a generous career package, will work in a translational environment including clinical scientists at Skåne University Hospital and have access to cutting-edge infrastructure at one of the largest Universities in Scandinavia. Between December 1, 2016 and February 15, 2017 candidates are invited to submit Declarations of Interest as described on our homepage. **www.med.lu.se/wcmm**

UMEÅ UNIVERSITY:

Several tenure track research positions are advertised in the areas of **cancer, infection biology, metabolism/diabetes and neuroscience**. The positions are at Associate Senior Lecturer (Assistant Professor) level. The successful candidates will work in association with strong research environments and have access to excellent research infrastructures including unique collections of longitudinal samples in existing biobanks. **www.wcmm.umu.se**

LINKÖPING UNIVERSITY:

With a medicine-technology interface and extending from a biomedical engineering profile, onwards to basic biomedical and clinical research, we plan to recruit a number of tenure track faculty members, at the level of Assistant/Associate Professor. Currently, we are especially interested in researchers working in the area of **Digital Pathology**. The successful candidates will be expected to develop a dynamic, extramurally funded, internationally recognized research program, and to integrate with existing strengths in medical technology, materials science and bioengineering. **www.liu.se/wcmm**

UNIVERSITY OF GOTHENBURG:

The scope of the Centre in Gothenburg is molecular medicine aspects of **metabolic and degenerative diseases, neuroscience, inflammation and cancer**. Successful candidates will become part of strong research environments with excellent infrastructure and enjoy close collaboration with AstraZeneca and clinical/translational research platforms at one of the largest University hospitals in northern Europe. Read more about our present and coming calls at **www.wcmm.gu.se**

**WALLENBERG CENTRES FOR
MOLECULAR MEDICINE
SWEDEN**

*Knut och Alice
Wallenbergs
Stiftelse*



RICHARD D. GREEN DEAN College of Natural Sciences and Mathematics

California State University, Long Beach (CSULB) invites nominations and letters of application for the Richard D. Green Dean of the College of Natural Sciences and Mathematics. CSULB seeks outstanding, publicly engaged leaders to join a dedicated leadership team that is committed to advancing the University's broad and forward-seeking mission.

The Position: The Richard D. Green Dean of the College of Natural Sciences and Mathematics is the chief academic officer of the College and reports to the Provost and Senior Vice President for Academic Affairs. The Dean is expected to exercise vision, ethical leadership, and advocacy in academic affairs, research and scholarly activities, and curricular matters in the College, placing emphasis on the continuing development of the finest undergraduate and graduate educational programs possible. He/she is required to lead the associate deans, department chairs, director of development, and faculty in efforts (such as public-private sector partnerships and federal/state programs) to develop, effectively manage, and enhance on-going funding for the support of the College's academic programs and research activities for faculty and students, especially those that increase success of students in underserved and underrepresented groups. He/she is expected to work with leadership on institutional awards (such as NIH BUILD and HSI-STEM) to help support, carry out, and institutionalize programmatic elements. The Dean is responsible for management of the fiscal and personnel resources of the College, including recruitment, evaluation and retention of a well-qualified and highly diverse faculty and staff. He/she will work with college/department leadership and academic advisors to develop and carry out initiatives for student success leading to increased retention and graduate rates (particularly 4-year) and a reduction in the achievement gap. Distributions from the Richard D. Green endowment provide discretionary funds for the Dean to support college initiatives.

For further information, please see position description **1012756** at **web.csulb.edu/divisions/aa/personnel/jobs/admin/**. Review of applications to begin no sooner than **December 19, 2016**. Position open until filled.

CSULB is an Equal Opportunity Employer.



RESEARCH IS A COLLECTIVE WORK

Come and join us and discover how our research team plays a round the clock in furthering the advance of medical science.

INSERM IS RECRUITING: 93 TENURE POSITIONS ARE OFFERED TO RESEARCHERS M/F DEDICATED TO BIOMEDICAL RESEARCH

- Research Associates: January 12th, 2017 - 4.00.pm (GMT+1)
- Research Directors: February 2nd, 2017 - 4.00.pm (GMT+1)

Candidates to Research Associates and Research Directors positions must have a PhD (or equivalent degree). There is no nationality restriction.

Inserm is the only French public research institute to focus entirely on human health.

Its researchers are committed to studying all diseases, whether common or rare. Through its diversity of approaches, Inserm provides a unique environment for researchers.

More than 13 000 researchers, engineers and technicians work in the 281 Inserm laboratories housed in hospitals, universities and research campuses, all over France.

Visit our website : <http://www.eva3.inserm.fr>



Inserm

Institut national
de la santé et de la recherche médicale



Government of India Ministry of Science & Technology Department of Biotechnology

RAMALINGASWAMI RE-ENTRY FELLOWSHIP : 2016-17

Applications are solicited from Indian Nationals working in overseas research institutions for the "Ramalingaswami Re-entry Fellowship", a re-entry scheme of the Department of Biotechnology (DBT), Ministry of Science & Technology, Government of India.

Aim of the Fellowship

The scheme is conceptualized with the aim of attracting highly skilled researchers (Indian Nationals) working overseas in various cutting edge disciplines of biotechnology (agriculture, health sciences, bio-engineering, energy, environment, bioinformatics and other related areas), by providing them an attractive avenue to pursue their R&D interrests in Indian institutions.

Who is eligible to apply ?

The applicant should possess a Ph.D., M.D., M. Tech, M.V.Sc. or equivalent degree with an outstanding track record as reflected in publications and other recognitions and with at least three years of post-doctoral research experience of which last two years should be from overseas laboratory. OnlyCandidates (Indian Nationals) working overseas are eligible to apply. Those who have already returned to India within one year of the closing date of this advertisement are also eligible. Researcher's upto 45 years of age as determined on closing date of application are eligible to apply.

Incentives of being a Ramalingaswami Fellow

1. This is a senior fellowship programme, and awardees are to be considered synonymous to the faculty/scientists at the level of scientist-D. They are entitled to take up teaching/research assignments and supervising Doctoral/MS students.
2. The scheme provides a consolidated monthly remuneration of Rs.85,000/- p.m. In addition, a house rent allowance of Rs. 7,500/- p.m. is given to fellows. In case host institute provides accommodation to the fellow, no house rent allowance is admissible.
3. Fellows will receive a research/contingency grant of Rs. 10.00 lakhs for the 1st year, Rs. 7.50 lakhs for the 2nd years Rs. 5.00 lakhs for the subsequent 3 years for purchase of consumables, minor equipment, international and domestic travel, engaging manpower and other contingent expenditure to be incurred for the implementation of research proposal.
4. DBT encourages host institutions to provide medical benefits, transport allowance, leave travel allowance and other benefits as per their prevailing norms as applicable to their employees of the rank equivalent to scientist D out of their own resources/ funds.
5. Fellows retain an option for drawing either the fellowship or salary if they are appointed at a suitable permanent scientific position. Fellows opting for salary can continue to avail the research /contingency grant with prior approval of DBT.
6. Ramalingaswami Re-entry Fellows could take up fellowship at any of the scientific institutes/ universities in the country. However, application should be duly forwarded by the competent authority of the host Institute. Fellows/Awardee can change his/her host institute only once during the tenure of the fellowship.
7. Awardees are eligible to apply for research grants to any of the funding agencies towards accomplishment of research proposal. However, the Co-PI has to be a permanent employee of the host institution.

Tenure of fellowship

Fellows can draw fellowship for a term of five years. Fellowship is further extendable for another term on fresh appraisal of performance of the fellow. Those who are able to secure permanent positions will not be considered for 2nd term.

How to apply

Applications may be sent as per Proforma downloadable from DBT website (www.dbtindia.nic.in) and duly forwarded by the competent authority to

Dr. Meenakshi Munshi, Director, Department of Biotechnology, Block-2, 7th Floor, CGO Complex, Lodhi Road, New Delhi -110 003, both as a hard copy as well as **soft copy**. The applications not forwarded by the host institution will not be considered. **Soft copy to be mailed at**

Email : rlsfellowship.dbt@nic.in only a single file latest by 31st January, 2017.

UCLA Institute for Quantitative and Computational Biosciences

A partnership between the UCLA College, Health Sciences and Engineering

Faculty Positions in the Quantitative and Computational Biosciences

UCLA has established the interdepartmental Institute for **Quantitative and Computational Biosciences (QCBio)** to lead the transformation of biology and biomedicine into a data-rich and math-based, predictive science.

QCBio is partnering with academic departments across Life Sciences, Physical Sciences, the David Geffen School of Medicine, and the Henry Samueli School of Engineering to recruit multiple faculty spanning diverse areas of the Quantitative and Computational Biosciences: Big Data Analytics and Machine Learning, Systems Biology and Multi-scale Modeling, Dynamics, Stochasticity, Robustness

These may intersect with life and biomedical science research areas such as: Epidemiology, Wireless and Public Health, Genomics, Proteomics, Metabolomics, Cancer, Signaling, Metabolism Infection, Microbiome, Immunity, Stem Cells, Development, Cell fate decisions Plants, Ecosystems, Sustainability

We are seeking candidates for any faculty rank. Competitive candidates will have a Ph.D. in a biomedical or computational sciences field with a strong biosciences research program that involves the development and use of novel computational methodologies. They will also share a sense of mission in the ongoing QCBio revolution of the biosciences.

Applicants should submit a cover letter, curriculum vitae, a list of referees, a research statement, a teaching statement, and a diversity statement on-line to <https://recruit.apo.ucla.edu/apply/JPF02718>. Review of applications will begin **January 6, 2017**.

As a campus with a diverse student body, we encourage applications from women, minorities, and individuals with a history of mentoring under-represented minorities in the sciences.

The University of California is an Equal Opportunity/Affirmative Action Employer. All qualified applicants will receive consideration for employment without regard to race, color, religion, sex, sexual orientation, gender identity, national origin, disability, age or protected veteran status. For the complete University of California nondiscrimination and affirmative action policy, see: UC Nondiscrimination & Affirmative Action Policy. (<http://policy.ucop.edu/doc/4000376/NondiscrimAffirmAct>)

UCLA is California's largest university, with an enrollment of nearly 38,000 undergraduate and graduate students. The UCLA College of Letters and Science and the university's 11 professional schools feature renowned faculty and 323 degree programs and majors. The Biosciences at UCLA include more than 300 faculty members, many top-ten ranked departments, and is consistently in the top ten in NIH funding.

Professor and Director

Itasca Biological Station and Laboratories

The College of Biological Sciences (CBS) at the University of Minnesota Twin Cities invites applications for the position of **Professor and Director of Itasca Biological Station and Laboratories**. We seek an outstanding scientist with a national reputation to lead research, education, and public interaction at Itasca. The ideal candidate will have a Ph.D. or equivalent, a strong record of publication, externally funded research, experience mentoring undergraduate and/or graduate students, excellence in teaching, and be qualified for appointment at the level of full professor in a CBS department.

Learn more about this position at the college's faculty hiring website.

z.umn.edu/cbsfacultyhiring



College of
Biological Sciences
UNIVERSITY OF MINNESOTA
Driven to Discover

UCLA

Tenure track Assistant Professor Position In Quantitative Ecology or Evolution of Microbes

The Department of Ecology and Evolutionary Biology and the new Institute for Quantitative and Computational Biosciences (QCBio) at the University of California, Los Angeles are searching for a joint faculty appointment at the level of Assistant Professor. Candidates must have a PhD within the field of Biology, Microbiology and/or Computational Sciences.

Quantitative and computational biologists working on the ecology or evolution of terrestrial or aquatic (including marine) microbiomes, microbial symbionts, and/or pathogens, at the level of populations or communities, are invited to apply. The competitive applicant will conduct conceptually oriented research that uses quantitative or computational approaches such as mathematical modeling, genomics/metagenomics, or network science. Research on naturally-occurring or laboratory systems will be considered, and experimental approaches and use of emerging technologies are encouraged.

UCLA boasts thriving research communities in ecology and evolutionary biology, as well as in genomics, bioinformatics and computational systems biology. There is a strong and growing community of microbiology and microbiome researchers on campus, and excellent opportunities to interface with biomedical or environmental science programs. The joint position will support the new faculty member to contribute to educational programs at the undergraduate and graduate level and to develop new synergies between the missions of QCB and the Department of Ecology and Evolutionary Biology.

UCLA is California's largest university with a diverse student body. Successful applicants should convey their commitment to excellence in research, teaching, mentoring, and contributions to diversity. Questions regarding the position should be sent to Alexander Hoffmann, ahoffmann@ucla.edu. Materials should be submitted online and contain a (1) cover letter, (2) CV, (3) research statement covering both past accomplishments and future plans, (4) teaching statement, (5) a contribution to diversity statement, (6) three key and relevant publications, and (7) names and contact information for at least three references. Applications should be submitted through <https://recruit.apo.ucla.edu/apply/JPF02745>. Review of applications will begin on **January 15, 2017**.

As a campus with a diverse student body, we encourage applications from women, minorities, and individuals with a history of mentoring under-represented minorities in the sciences.

The University of California is an Equal Opportunity/Affirmative Action Employer. All qualified applicants will receive consideration for employment without regard to race, color, religion, sex, sexual orientation, gender identity, national origin, disability, age or protected veteran status. For the complete University of California nondiscrimination and affirmative action policy, see: UC Nondiscrimination & Affirmative Action Policy. (<http://policy.ucop.edu/doc/4000376/NondiscrimAffirmations>), and is consistently in the top ten in NIH funding.



University of
Zurich ^{UZH}

Faculty of Science

The Faculty of Science (www.mnf.uzh.ch) of the University of Zurich invites applications for a

Professor of Evolutionary Anthropology (tenured)

in order to join our team of experts at the Department of Anthropology.

We seek innovative applicants with a strong record in research and teaching, who will strengthen our existing expertise in biological/evolutionary anthropology. Applicants with an internationally competitive research profile in any field of biological/evolutionary anthropology, and demonstrating potential for innovative transdisciplinary research are particularly encouraged to apply.

The successful applicant is expected to develop a complementary and independent research program in biological/evolutionary anthropology, ideally including fieldwork on humans and/or non-human primates. Research should be aimed at understanding the evolution of our own species in a broad sense, encompassing the biological foundations of human behavior and culture. Contributing to the existing undergraduate and graduate teaching efforts in biological anthropology will also constitute an integral part of the position. The successful applicant will be located at the University of Zurich and is further expected to acquire external funding.

The University of Zurich provides generous research support, including dedicated funds for personnel and running expenses and competitive start-up packages. Zurich's scientific environment includes a rich spectrum of research activities in the life sciences and provides extensive opportunities for collaborations with research groups at the University of Zurich, as well as teams at the nearby ETH Zurich. The University of Zurich and the city of Zurich also offer a stimulating cultural environment and are family-friendly.

Application packages should include a motivation letter, a full curriculum vitae, a vision statement of research and teaching interests outlining major unsolved problems and how they could be tackled and the names and addresses of three potential referees. Documents should be addressed to Prof. Dr. Michael Schaepman, Dean of the Faculty of Science, University of Zurich, and uploaded as a single PDF file to <http://www.mnf.uzh.ch/EA> by 31 January 2017. A brief questionnaire will have to be filled out at the beginning of the upload process. For further information, please contact Prof. Dr. Christoph Zollikofer at zolli@aim.uzh.ch.

The University of Zurich is an equal opportunities employer.

By Barbara Gastel

Living up to my mentors

When the holiday letter failed to arrive last December, I worried. And I recalled two letters from decades earlier. I received the first during my sophomore year of high school. In it, an early-career scientist I'll call Dr. E told me another candidate had received the summer research opportunity I had sought. He ended the letter by saying he hoped he could accept me the next year. I took that as an empty pleasantry. Yet a year later, the second letter arrived, offering me the spot. Little did I realize that remembering others and following through on commitments were typical of Dr. E. Nor did I imagine that those letters would start relationships that would last much of a lifetime and shape my own mentoring.

Arriving that summer to work with Dr. E, I found laboratory benchtops nearly up to my chin and glassware cabinets beyond my reach—the lab had been built to suit 6-foot-7-inch Dr. E. I learned to look atop the refrigerator for protocols and appreciated the kick stools located throughout the lab. Even more, I appreciated how Dr. E helped us students reach a higher level in science. As well as instructing us himself, Dr. E had senior trainees guide junior ones, reinforcing their own knowledge and boosting their teaching proficiency. He trusted us, giving us room to develop our problem-solving abilities, technical dexterity, and communication skills.

Dr. E also integrated us into the lab's social life. At the department picnic, I met Dr. E's wife, also a scientist, and we quickly bonded. The next year, to broaden my learning, I applied for a summer research program at her institution, where she arranged for me to work in her lab.

Those summers, I developed not only my scientific skills, but also a valued relationship with the Drs. E. One Dr. E or the other often gave me a ride to or from work. Sometimes we talked science, but often we simply talked about everyday things. I enjoyed my first taste of lime pie when the Drs. E invited students to their home. My glimpses of their lives as a two-career couple reassured me that, with kindness and flexibility, a marriage of two professionals can flourish.

After heading to college and beyond, I stayed in touch with the Drs. E. When visiting my parents, I would call or see them. I watched as their careers developed and their family grew. Soon after I married, Mr. Dr. E met my husband and me for lunch—even though for medical reasons he was restricted to fluids. He also came to pay his respects



"Those letters [started] relationships that would last much of a lifetime."

after my father died. The Drs. E stayed interested in my work even after I chose a career that employed mainly the pen rather than the pipette. They became true mentors rather than simply advisers.

I have been privileged to return some of what the Drs. E gave me. During college, Mr. Dr. E's university asked me to write a letter on his behalf, probably for tenure or a teaching award. I knew little of such things then, but I valued the chance to reciprocate after the recommendations he had written for me. Likewise, I felt honored when Mrs. Dr. E called to request my advice about a family member's education.

Now, as a mentor myself, I try to live up to the example of the Drs. E. I see reflections of their mentorship in mine—whether I am supervising

trainees, hosting students for dinner (with a special dessert, of course), supporting mentees regardless of career path, or just trying to follow through on what I say.

Over the years, my contact with the Drs. E came to consist largely of exchanging holiday letters. When last December passed without a letter from them, an internet search confirmed what I had feared. As I prepared to send Mrs. Dr. E a condolence card, an abbreviated holiday letter arrived from her, from a new address, near offspring. Now, as I send my holiday letter this year, I am thankful to have known the Drs. E—as scientists, as individuals, and as a couple—and I try to honor their example as I exchange good wishes with current and former trainees of my own. ■

Barbara Gastel is a professor of veterinary integrative biosciences and of humanities in medicine at Texas A&M University in College Station. Send your career story to SciCareerEditor@aaas.org.